A MODELING STUDY OF LAND SURFACE PROCESSES AND SURFACE ENERGY BUDGETS USING THE MAXIMUM ENTROPY PRODUCTION THEORY

A Dissertation
Presented to
The Academic Faculty

by

Shih-Yu Huang

In Partial Fulfillment
of the Requirements for the Degree
Doctor of Philosophy in the
School of Civil and Environmental Engineering

Georgia Institute of Technology
December, 2017

A MODELING STUDY OF LAND SURFACE PROCESSES AND SURFACE ENERGY BUDGETS USING THE MAXIMUM ENTROPY PRODUCTION THEORY

Approved by:

Dr. Jingfeng Wang, Advisor
School of Civil and Environmental Engineering
Georgia Institute of Technology

Dr. Satish Bastola
School of Civil and Environmental Engineering
Georgia Institute of Technology

Dr. Aris P. Georgakakos
School of Civil and Environmental Engineering
Georgia Institute of Technology

Dr. Yi Deng
School of Earth and Atmospheric Sciences
Georgia Institute of Technology

Dr. Jian Luo
School of Civil and Environmental Engineering
Georgia Institute of Technology

Date Approved: September 28, 2017

To my lovely parents, Chia-Sheng Huang and Tsung-Chao Yen

ACKNOWLEDGEMENTS

First and foremost, I would like to express my sincere gratitude to my advisor, Dr. Jingfeng Wang, who has guided me during my doctoral education with his thorough knowledge, strictly scientific attitude, and immense enthusiasm. I could not have successfully completed my dissertation without his enlightment and support. My grateful thanks also go to my dissertation committee members, Dr. Aris Georgakakos, Dr. Jian Luo, Dr. Yi Deng, and Dr. Satish Bastola, who provided insightful comments that kept me on the right track.

I gratefully appreciate my current and previous labmates, Husayn El Sharif, Yao Tang, Yue Zhao, Yiming Chen. Thank you for the stimulating discussions and sage advice. Special thanks go to Chia-Jeng Chen and Yi Lu, who graciously share their knowledge and technical skills. I would also like to thank friends outside of civil engineering, Wei-Ya Chen, I-Ting Chuang, Wei-Fang Sun, Hao-Lin Hu, and Robert Gillespie – for the invaluable assistance, firm friendship, and good times throughout these years. In particular, Hsin-Chieh Peng and Tica Lin deserve special thanks for the mutual support along the way. There are too many people to list individually who provided invaluable assistance during my path toward earning my PhD. My acknowledgement goes to them all.

Last, but not least, my sincerest gratitude goes to my loving parents, Chia-Sheng Huang and Tsung-Chao Yen, and my sisters, Pei-Yu Huang and Yi-Han Huang. Your endless faith in me and unparalleled support has given me strength throughout this venture. I am so grateful for all you have done for me. Without your love, understanding, and encouragement, I would not have achieved this monumental goal. This dissertation is dedicated to you.

TABLE OF CONTENTS

LIST OF TABLES

LIST OF FIGURES

LIST OF SYMBOLS

A_T	Diurnal amplitude of surface skin temperature
A_θ	Diurnal amplitude of surface soil moisture
$B(\sigma)$	Reciprocal Bowen ratio (MEP model)
C_1, C_2	Surface layer stability factor (MEP model)
C_E, C_H	Bulk transfer coefficient of water vapor and heat
D_s	Dissipation function (MEP model)
D	Hydraulic diffusivity
E	Latent heat flux
E_{OBS}	Observed E
E_{BTM}	The bulk transfer modeled E
E_{MEP}	The MEP modeled E
ESI	Evaporation over snow-ice surfaces (sublimation/deposition)
F_w	Soil water flux
H	Sensible heat flux
H_{OBS}	Observed H
H_{BTM}	The bulk transfer modeled H
H_{MEP}	The MEP modeled H
HSI	Sensible heat flux over snow-ice surfaces
I	Infiltration rate
I_0	The "apparent" thermal inertia parameter of air
I_a	Thermal inertia parameter of sensible heat
I_e	Thermal inertia parameter of latent heat
I_s	Thermal inertia of the soil
I_{ds}	Thermal inertia of dry soil
I_w	Thermal inertial of liquid water
I_{wsi}	Thermal inertia of water-snow-ice
K_H	Turbulent eddy diffusivity of heat
$K(\theta)$	Unsaturated hydraulic conductivity
K_{sat}	Saturation hydraulic conductivity

L_v	Latent heat of vaporization of liquid water
LWd	Surface downward longwave radiation
LWu	Surface upward longwave radiation
P	Precipitation
Q	Ground/soil heat flux or water-snow-ice surface conductive heat flux
Q_{OBS}	Observed Q
Q_{BTM}	The bulk transfer modeled Q
Q_{MEP}	The MEP modeled Q
QSI	Snow-ice surface conductive heat flux
Q_1	Soil heat flux leaving the top soil layer
Q_{wg1}	Net gravitational drainage rate from the bottom of the top soil layer
R_0	Net solar radiation entering the media
R_n	Surface net radiation
R_n^L	Net surface longwave radiation
R_n^S	Net surface shortwave radiation
R_v	Gas constant of water vapor
SWd	Surface downward shortwave radiation
SWu	Surface upward shortwave radiation
T	Soil temperature
$\overline{T}$	Deep soil temperature/Daily average soil temperature
$\overline{T_a}$	Air temperature far from the surface/Daily average near-surface air temperature
T_0	Reference temperature
T_1	Air temperature at the lowest model level
T_a	Air temperature
T_g	Ground surface temperature
T_s	Surface skin temperature
U	Wind speed
ΔT_s, ΔT_a, ΔQ, ΔH	Diurnal amplitude of T_s, T_a, Q, and H
ΔX	Uncertainty of a flux X
b	Pore size distribution parameter
c_p	Specific heat of air under constant pressure
c_s	Specific heat of the soil

c_{snow}	Specific heat of snow
c_w	Specific heat of water
c_{wsi}	Specific heat of water-ice-snow media
d_T	Damping depth of the surface temperature
d_θ	Damping depth of the surface moisture
g	Gravitational acceleration
q_a	Air specific humidity
q_s	Surface specific humidity
$q_{sat}(T_s)$	Saturation specific humidity at T_s
r	Correlation coefficient
t	Time
u	Slope of the unsaturated hydraulic conductivity with respect to θ
z	Vertical coordinate
ΔR_n, $\Delta\sigma$, $\Delta\beta_s$	Uncertainties of R_n, σ, and $\beta_s \equiv I_s/I_0$
Δt	Model time step
z_1	Top soil layer thickness
α	Priestley-Taylor parameter/Wetness function for estimating q_s
β	Soil texture dependent empirical parameter
γ	Psychrometric constant
δ	Soil layer depth
ϵ	Initial phase of surface temperature wave
θ	Soil moisture
$\bar{\theta}$	Daily averaged soil moisture
θ_1	Averaged soil moisture of the top soil layer
θ_s	Surface soil moisture
θ_r	Residual soil water content
κ	von Kármán constant
λ_s	Thermal conductivity of the soil
λ_{snow}	Thermal conductivity of snow
λ_w	Thermal conductivity of liquid water
λ_{wsi}	Thermal conductivity of water-ice-snow media
ρ_a	Air density

ρ_s	Density of the soil
ρ_{snow}	Density of snow
ρ_w	Density of water
ρ_{wsi}	Density of water-ice-snow media
σ	Dimensionless parameter (MEP model)
ϕ	Soil porosity
$\psi(\theta)$	Soil water potential
ψ_{ae}	Air entry water potential
ω_0	Fundamental diurnal frequency
Δ	Slope of the saturation water vapor pressure curve at certain temperature

LIST OF ABBREVIATIONS

ALMIP	AMMA Land Surface Model Intercomparison Project
AMIP II	The Second Phase of the Atmospheric Model Intercomparsion Project
AMMA	African Monsoon Multidisciplinary Analysis
AMSR-E	Advanced Microwave Scanning Radiometer – Earth Observing System
A-Train	Afternoon Constellation
AVHRR	Advanced Very High Resolution Radiometer
BSRN	Baseline Surface Radiation Network
BTM	Bulk Transfer Model
CALIPSO	Cloud–Aerosol Lidar and Infrared Pathfinder Satellite Observations
CAM	The Community Atmosphere Model
CCCM	CALIPSO-CloudSat-CERES-MODIS
CCMP	Cross-Calibrated Multi-Platform
CERES	NASA Clouds and the Earth's Radiant Energy System
CFSR	NASA Climate Forecast System Reanalysis
CI	Confidence Interval
CLM	The Community Land Model
CMIP3 (5)	Phase 3 (5) of the Coupled Model Intercomparison Project
DAS	Data Assimilation System
DJF	December–January–February
EC	Eddy Covariance
ECMWF	European Centre for Medium-Range Weather Forecasts
ERA-15/-40/	ECMWF 15-/40-year reanalysis
ERA-Interim	ECMWF Interim reanalysis
ERBE	Earth Radiation Budget Experiment
FRM	Force-Restore Method
FRM_{Ta}	Force-Restore Model of T_a
FRM_{Ts}	Force-Restore Model of T_s
FRM_{Ta}^{O}	FRM_{Ta} driven by observed heat flux
FRM_{Ts}^{O}	FRM_{Ts} driven by observed heat flux
FRM_{Ta}^{B}	FRM_{Ta} driven by the BTM heat flux

FRM_{Ts}^{B}	FRM_{Ts} driven by the BTM heat flux
$FRM_{\theta s}$	Force-Restore Model of θ_s
$FRM_{\theta s}^{O}$	$FRM_{\theta s}$ driven by observed heat flux
$FRM_{\theta s}^{B}$	$FRM_{\theta s}$ driven by the BTM heat flux
FRMEP	The Force-Restore-MEP Model
FRMEP-ND	The FRMEP model neglecting the drainage term in the $FRM_{\theta s}$
GCM	Global Circulation Model
GDAS	NCEP Global Data Assimilation System
GEOS	NASA GMAO Goddard Earth Observing System
GEOS-4/-5	GMAO GEOS GCM/DAS version 4/version 5
GEBA	Global energy balance Archive
GEWEX-SRB	Global Energy and Water Exchanges Project–Surface Radiation Budget
GHM	Global Hydrological Model
GIMMS NDVI	Global Inventory Monitoring and Modeling System Normalized Difference Vegetation Index
GLASS	Global Land-Atmosphere System Study
GLDAS	Global Land Data Assimilation System
GMAO	NASA Global Modeling and Assimilation Office
GPCC	Global Precipitation Climatology Centre
GPCP	Global Precipitation Climatology Project
GPM	The Global Precipitation Measurement
GSSTF	Goddard Satellite-based Surface Turbulent Fluxes
GSSTF2	GSSTF2 version 2
GSWP	Global Soil Wetness Project
GSWP-2	The second Global Soil Wetness Project
HDE	Heat Diffusion Equation
HOAPS	Hamburg Ocean Atmosphere Parameters and Fluxes from Satellite Data
IGBP	International Geosphere-Biosphere Programme
IPCC	Intergovernmental Panel on Climate Change
IPCC-AR4/-AR5	IPCC – the Fourth/Fifth Assessment Report
ISCCP	International Satellite Cloud Climatology Project
ISCCP-FD	ISCCP FD version

JJA	June–July–August
JMA	Japan Meteorological Agency
JMA-MRI	JMA – Meteorological Research Institute
JRA	Japanese Reanalysis
JRA-25/-55	JRA 25-/55-year reanalysis
LSM	Land Surface Model
MAM	March–April–May
MEP	Maximum Entropy Production
MERRA	Modern Era Retrospective-analysis for Research and Applications
MERRA-2	MERRA reanalysis version 2
MERRA-Land	MERRA Land only offline simulations
MODIS	Moderate-Resolution Imaging Spectroradiometer
MOSE	Monin-Obukhov Similarity Equations
MOST	Monin-Obukhov Similarity Theory
NASA	National Aeronautics and Space Administration
NASA NEWS	NASA Energy and Water Cycle Study
NCDC	National Climatic Data Center
NCEI	National Centers for Environmental Information
NCEP	National Centers for Environmental Prediction
NCEP-NCAR	NCEP – National Center for Atmospheric Research
NCEP-DOE	NCEP – Department of Energy
NOAA	National Oceanic and Atmospheric Administration
NoSI	MEP simulation without considering snow and sea-ice extent
NPSC	Non-polar-region-snow-covered area
OAFlux	Objectively Analyzed Air-sea Fluxes
OHC	Ocean heat content
ORCHIDEE	Organising Carbon and Hydrology In Dynamic Ecosystems
OSM	Ocean Surface Model
PCMDI	Program for Climate Model Diagnosis and Intercomparison
PILPS	Project for the Intercomparison of Land-Surface Parameterization Schemes
PMM	Penman-Monteith method
PoRs	Polar Regions
PTM	Priestley-Taylor method

QuickSCAT	Quick Scatterometer
SMAP	Soil Moisture Active Passive
SOP	September–October–November
SRL	Surface Roughness Length
SSMI	Special Sensor Microwave Imager
SST	Sea Surface Temperature
SnP	Snow presence
SVAT	Soil-Vegetation-Atmosphere Transfer
TOA	Top of atmosphere
TOGA COARE	Tropical Ocean Global Atmosphere Coupled Ocean-Atmosphere Response Experiment
TRMM	Tropical Rainfall Measuring Mission
WaterMIP	Water Model Intercomparison Project
WHOI	Woods Hole Oceanographic Institution
3D/4D-VAR	Three-/Four-Dimensional Variational assimilation
tiu	thermal inertia unit $\equiv$ J m^{-2} K^{-1} $s^{-1/2}$

SUMMARY

Land surface model (LSM) plays an important role in numerical simulation of weather and climate. The existing LSMs have been found to produce inconsistent surface energy and water budgets due to the deficiencies in the parameterization of surface temperature, surface soil moisture, and surface heat fluxes. Specifically, surface heat flux parameterizations based on the conventional gradient-flux methods (e.g., the bulk transfer model, BTM) are subject to large modeling errors and uncertainties. Performance of LSMs may be enhanced by improving surface heat flux parameterizations. A new approach, the maximum entropy production (MEP) model of surface heat fluxes, was recently developed to overcome the drawbacks of existing flux models. Compared to the BTM-based heat fluxes, the MEP modeled heat fluxes close the surface energy budget using fewer model inputs and parameters with reduced uncertainties.

In this study, a coupled model of surface temperature, surface soil moisture, near-surface air temperature, and surface heat fluxes, for use in a LSM as well as GCM, was formulated built on the classical force-restore method (FRM) incorporating the MEP model of surface heat fluxes, referred to as the FRMEP model. The FRMEP model is driven by surface net radiation and precipitation without explicitly using other meteorological variables and location specific empirical tuning parameters benefited by the unique features of the MEP model. The proposed FRMEP model was evaluated using observations from field experiments with contrasting climate and soil wetness conditions. The modeling errors of the FRMEP are smaller than those of the classical FRMs, which are forced by observed or BTM-parameterized surface heat fluxes. Diurnal and seasonal variations of

surface temperature, surface soil moisture, near-surface air temperature, and surface heat fluxes are well captured by the FRMEP model. Analysis of the FRMEP suggests that the gravitational drainage, which was excluded in the classical FRM of surface soil moisture, cannot be neglected under wet soil condition.

With the theoretical and technical advantages, the MEP model is a promising new method to tackle one major challenge in the study of global climate change, that is, modeling and monitoring of surface energy budgets. In this study, the climatology of global surface energy budgets together with the corresponding trend and uncertainty estimates are re-estimated using the MEP model utilizing the input data from remote sensing observations and reanalysis data products during 2001-2010. The MEP estimates of land and ocean surface heat fluxes at continental and ocean basin scales are examined separately to quantify the corresponding global contributions. The MEP model produces the first dataset of global ocean surface conductive heat flux, which is not available from the existing data products. The MEP model provides a new estimate of global land snow-ice and sea ice surface heat fluxes. An analysis of the influence of snow and sea ice presence on the estimates global surface energy budgets is also conducted by excluding snow and sea ice extent in the MEP simulations.

The MEP produced new estimates of global annual mean terrestrial evapotranspiration and sensible heat fluxes are in close agreement with previous estimates, while the corresponding ground heat flux is higher than the existing estimates. The MEP modeled global land surface heat fluxes have increasing trends during 2001-2010 consistent with that of observed net radiation. The new estimates of ocean evaporation and surface conductive heat flux based on the MEP model are smaller than the existing

estimates, while MEP estimated ocean surface sensible heat fluxes are higher than those reported previously. The MEP modeled ocean surface heat fluxes have negative trends globally. The regional and seasonal trends of MEP heat fluxes are consistent with the global and annual trends, respectively. Analysis of the MEP modeled snow-ice surface heat fluxes suggests that global land sublimations and snow-ice surface sensible heat fluxes are mostly contributed by the non-polar regions, while the global contributions of land snow-ice surface conductive heat flux over polar and non-polar regions are comparable. The global annual means of MEP modeled snow-ice surface heat fluxes have positive trends during 2001-2010. Over oceans, the global contributions of sea ice surface heat fluxes are small compared to ocean (open-water) surface heat fluxes. The MEP estimates of global annual mean sea ice sublimation and surface conductive heat flux have opposite trends, while those of global annual mean sea ice surface sensible heat flux remain stationary. The MEP modeled global surface heat flux budgets are not sensitive to snow and sea ice presence.

The results presented in this study suggest the potential applications of the MEP model in climatic and hydrological studies. The encouraging tests of the FRMEP model justify the possibilities of enhancing the performance of LSMs and hydrological models by improving heat flux parameterizations using the MEP model. Upon further tests, the FRMEP model has potential to serve as an attractive data retrieval algorithm for downscaling and gap-filling satellite remote sensing observations. The MEP model also offers an alternative approach to meet the challenge of monitoring and modeling global surface energy budgets. The new estimates of global/regional surface energy budgets based on the MEP model presented in this study lead to a broader view of global energy and water cycles from a surface perspective.

CHAPTER 1. INTRODUCTION

Global Circulation Models (GCMs), or simply, climate models, are vital tools for quantitatively understanding the global climate system and its variability (e.g., Sen Gupta et al., 2012). In recent decades, climate models have been extensively used for analyzing the impacts of climate change on hydrology, agriculture, and socioeconomics and investigating the corresponding mitigation strategies (Markoff and Cullen, 2008; Golombek et al., 2012; Seneviratne et al., 2012; Hirabayashi et al., 2013; McDonald and Girvetz, 2013; Wada et al., 2013; Dankers et al., 2014). For example, GCMs have been used to investigate regional and global water availability (Gregory et al., 1997; Burke et al., 2006; Wetherald and Manabe, 2003; Manabe et al., 2004). GCM outputs coupled with hydrological and crop models are now used routinely for assessing the impacts of climate change on water resources, food security and ecosystems (Hay et al., 2002; Salathé, 2005; Hanson and Dettinger 2005; Ines et al., 2011; Yang et al., 2015).

Climate model simulations are usually sensitive to the diurnal and seasonal variations of surface forcing parameterized by a land surface model (LSM) (Mintz, 1984; Rowntree, 1983; Rowntree and Bolton, 1983; Chen and Dudhia, 2001; Zeng et al., 2015). LSMs describe the fundamental surface processes regulating the exchange of energy and water as well as chemical compounds such as CO_2 between the land surface and the atmosphere (Zhang et al., 1996; Collatz et al., 2000; Bounoua et al., 2002; Chen et al., 2003; Gao et al., 2004; Yang, 2004). More specifically, LSMs provide estimates of surface latent E, sensible H, and ground Q heat fluxes partitioned from surface radiative fluxes representing the transport of energy and water at the surface into the soil or atmosphere

(Rowntree, 1991; Dickinson et al., 1991). The importance of LSM for both weather forecasting and climate models has been increasingly recognized in recent decades (Dickinson et al., 1993; Ek et al., 2003; Friend and Kiang, 2005). Numerous studies have demonstrated the significant efficacy of LSM estimated surface energy and water conditions on the GCM as well as regional atmospheric simulations in predicting atmospheric motion, temperature, and rainfall fields (Ookouchi et al., 1984; Mahfouf et al., 1987; Avissar and Pielke, 1989; Chen and Avissar 1994a, b).

LSMs have developed rapidly over the past two decades in terms of improving mechanistic structures and numerical techniques (Sellers, et al., 1997; Pitman, 2003; Zhao and Li, 2015). Intercomparisons of LSMs have been reported in previous publications with the main objectives of (1) assessing the model sensitivity to different parameterizations, forcing inputs, and spatial scales, (2) determining the model adequacy for simulating key land surface processes over various regions, and (3) developing an ensemble climatology of surface energy and water budgets (e.g., Garratt, 1993; Rowntree, 1991; Dickinson et al., 1991; Dirmeyer et al., 1999, 2006; Henderson-Sellers et al., 1993, 1995; Viterbo, 2002; Boone et al., 2009; Zeng et al., 2015). In particular, the earlier Project for the Intercomparison of Land-Surface Parameterization Schemes (PILPS) (Henderson-Sellers et al., 1993, 1995), the Global Soil Wetness Project (GSWP) (Dirmeyer et al., 1999, 2006), and the more recent AMMA (African Monsoon Multidisciplinary Analysis) Land surface Model Intercomparison Project (ALMIP) have led to better understanding and significant improvements of LSMs (Boone et al., 2009).

Despite the potential usefulness of LSMs for the climatic studies aforementioned, challenges related to the reliability of LSMs remain resulting from the variety of model

parameterizations in terms of structure and complexity, especially in the parameterizations of (1) primary surface state variables such as surface temperature T_s, surface soil moisture θ_s, and near-surface air temperature T_a, and (2) surface heat fluxes. T_s, θ_s, and T_a are good indicators of climatic states at seasonal to centennial and local to global scales (Jones et al., 1999, 2012; Seneviratne and Stöckli, 2008; Wang and Zeng, 2013; Frey and Kuenzer, 2014; Ji et al., 2014). T_s and θ_s dominate the partition of surface radiative energy into turbulent/conductive heat fluxes (E, H, and Q) on a diurnal time scale (Jacobs et al., 2000; Hirota et al., 2002; Gao et al., 2008). Henderson-Sellers et al. (1995) obtained a global annual mean T_s ranging from ~6 to 12 ^{o}C produced by various LSMs involved in PILPS even though most of the models predicted a positive trend of T_s over the study period (1979-1988). The researchers also indicate that the discrepancies of surface water budgets among LSMs are presumably caused by the parameterization of soil moisture dynamics.

T_a is one of the widely used variables for characterizing recent climate change. T_a estimated by LSMs is often compared to ground observations to evaluate the performance of LSMs (e.g., Dickinson et al., 1986; Zhang and Zheng, 2004; Oleson et al., 2010). T_a referred to in this study is the air temperature at screen height (i.e., about 2 to 10 m) rather than at the lowest level of the climate models T_1 (about 30 to 50 m, e.g., Zhang and Anthes, 1982; Hong and Pan, 1996). In current LSMs, T_a is usually diagnosed from other state variables such as T_s and T_1 using empirical approaches (e.g., Dickinson et al., 1986; Bonon, 1996; Zhang and Zheng, 2004; Oleson et al., 2010). Moreover, multiple model layer with fine resolution within the planetary boundary layer is often required to resolve a T_1 close to the surface (e.g., Zhang and Zheng, 2004). Thus, the parameterization of T_a in the existing LSMs appears to be either oversimplified or computationally costly.

The existing LSMs have been found to produce inconsistent estimates of global surface energy and water budgets resulting from the parameterizations of surface heat fluxes as well as T_s and θ_s. The inconsistencies increase considerably in fully coupled LSM-GCM simulations (compared to offline LSM simulations) further amplifying the discrepancies among the GCM simulations (Henderson-Sellers et al., 1995; Boone et al., 2009). Henderson-Sellers et al. (1995) found an imbalance of global surface energy budgets ranging from -0.4 to 13.2 W m^{-2} estimated by various combinations of LSM-GCM simulations. Furthermore, the LSMs under comparison obtained an overall scatter of 40 W m^{-2} in monthly mean E over tropical forests and mid-latitude grasslands. Sato et al. (1989) obtained a greater H and less E over vegetated land using the LSM developed by Seller et el. (1986) compared to those using a conventional hydrological model (Sela, 1980). Boone et al. (2009) indicates that the spatial and temporal variabilities of simulated surface longwave radiation between LSMs are attributed to discrepancies in the simulated T_s.

Most of the existing LSMs and ocean surface models (OSM) parameterize surface heat fluxes using "gradient-based" methods. A commonly used method is known as the bulk transfer model (BTM), which parameterizes surface heat fluxes as functions of temperature/humidity gradient between the surface and air, wind speed, and site-dependent parameter such as surface roughness lengths (SRLs) (e.g., Noilhan and Planton, 1989; Dickinson et al., 1991; Lee and Pielke, 1992). A major advantage of BTM is that the model inputs are obtained from routine meteorological variables including near-surface air temperature, humidity, wind speed as well as surface temperature and humidity. However, the formulations of BTM differ largely among LSMs (also OSMs) (e.g., Lee and Pielke, 1992; Brunke et al., 2003). More importantly, previous research indicates that the BTM

estimated heat fluxes are subject to large errors and uncertainties resulting from several drawbacks of the models including (1) not closing the surface energy budget (2) the uncertainty caused by the model inputs and parameters such as gradient variables, wind speed, and SRLs, and (3) the inherent bias and uncertainty from the model formalism with no obvious solution (e.g., Stull, 1988; Brunke et al., 2003, 2011).

The flux parameterizations in the existing LSMs/OSMs with the aforementioned weaknesses are closely related to one of the unsolved issues in present climatic and hydrological research, i.e., estimating global climatology, trend, and variability of surface heat fluxes. Surface heat fluxes vary greatly at different spatial and temporal scales in response to local and non-local physical and dynamical processes (Roberts et al., 2012). The geographical distributions of surface heat fluxes are important as they are the primary driving force of planetary hydrological cycle and ocean circulations (Stephens et al., 2012a; Katul et al., 2012; Herman, 2015). Recent studies have summarized the current knowledge about global and regional surface energy budgets (radiative and turbulent fluxes) (Trenberth et al., 2009; Stephens et al., 2012a; L'Ecuyer, et al., 2015). These previous studies have shown that the existing estimates of global surface energy budgets, especially surface heat fluxes, are still subject to large uncertainties.

Further improvements of large-scale surface heat flux estimates face difficulties from both modeling and observational perspectives given existing technology and theory. Previous studies showed that different flux algorithms produce wide range of surface heat flux estimates and no single algorithm is universally recommended (Henderson-Sellers et al., 1995; Jiménez et al., 2011; Mueller et al., 2011, 2013). Heat flux estimates over oceans remain highly uncertain due to the lack of direct measurements and great diversity of

parameterization schemes. As a result, reliable estimates of surface heat fluxes at large spatial and temporal scales are imperatively needed for characterizing the long-term climate change in response to surface forcing conditions and quantifying the role of lands and oceans in global climate change and variability (Beltrami, 2001; Roberts et al., 2012).

An innovative approach, the maximum entropy production (MEP) model of surface heat fluxes (Wang and Bras, 2009, 2011; Wang et al. 2014), was recently developed to overcome the drawbacks of the existing flux models. The foundation of the MEP model is the contemporary non-equilibrium thermodynamics built on the Bayesian probability theory, information theory and well-established atmospheric boundary layer turbulence theory (i.e. the Monin-Obukhov similarity theory, MOST, Monin and Obukhov, 1954). In the MEP model, surface turbulent and/or conductive heat fluxes are derived from the partition of surface radiative fluxes, thus automatically balance the surface energy budget. Compared to the BTM heat fluxes, the MEP parameterized surface heat fluxes (1) close the surface energy budgets by definition at all space-time scales, (2) avoid explicit use of temperature and moisture gradients, wind speed and SRLs as model inputs and parameters, (3) are free of location specific tuning (empirical) parameters, (4) are applicable to the full range of soil moisture conditions from residual water content to saturation., and (5) have reduced sensitivity to the uncertainties of model inputs and parameters.

With its theoretical and technical advantages, the MEP model provides a unique and so far unexplored opportunity for enhancing the performance of LSMs by providing improved parameterization of surface heat fluxes. The MEP model also provides a promising new method to meet the challenges of monitoring and modeling global surface heat fluxes as remote sensing observation missions now provide high resolution

observations of surface radiative fluxes (e.g., National Aeronautics and Space Administration – Clouds and the Earth's Radiant Energy System or NASA CERES, Wielicki et al., 1996).

1.1 Objectives and Scope

This study is motivated by the following scientific question:

How does the MEP model, as an innovative surface heat flux parameterization with enhanced physical constraints and reduced uncertainty, benefit the modeling of land surface processes and estimates of surface energy budgets?

To answer the scientific question, this study, by applying the MEP model, aims to (1) improve predictions of surface temperature, surface soil moisture, and near-surface air temperature for use in LSMs as well as hydrological and atmospheric models and (2) provide new estimates of global surface heat fluxes with reduced uncertainties, by overcoming the aforementioned weaknesses in the existing estimates. Specifically, the research objectives and scope are listed as follows:

- To develop a coupled model for predicting surface state variables including surface temperature, surface soil moisture, and near-surface air temperature by incorporating the MEP model of surface heat fluxes;
- To demonstrate the value of the proposed model for reproducing key land surface processes under various climatic and soil wetness conditions that meet the demand of climate models;

- To reconstruct the climatology of global/regional and inter-annual variabilities of surface heat flux budgets using the MEP model along with the corresponding trend and uncertainty estimates;
- To compare the MEP-based estimates with the existing flux products and justify the new estimates from both physical and numerical aspects.

1.2 Thesis Organization

The dissertation is organized as follows: Chapter 2 reviews essential concepts and research relevant to this study starting with the surface energy balance equations over land and ocean surfaces followed by the parameterizations of surface temperature, surface soil moisture, near-surface air temperature, and surface heat fluxes in the existing LSMs, and previous estimates of global surface energy budgets. Chapter 3 presents the development and validation of the new model. Predictions of the proposed model are compared with those of conventional models to demonstrate the improvements achieved by the new model. Chapter 4 provides the detailed operational framework of applying the MEP model at global scale. Comparison of the MEP and earlier estimates will be given along with explanations of the discrepancies. Chapter 5 summarizes the major findings and recommendations for future research.

CHAPTER 2. LITERATURE REVIEW

This chapter reviews earlier and contemporary literatures done in areas relevant to this study. Section 2.1 introduces the surface energy balance equations over land (non-transparent) and ocean (transparent) surfaces, which are core concepts in climate research and important constraints in LSMs/OSMs and climate models. Sections 2.2 and 2.3 review the commonly used models of surface temperature T_s, soil moisture θ_s, near-surface air temperature T_a, and surface heat fluxes, which are the main outputs of LSMs. Section 2.4 summarizes the previously reported estimates of global surface energy budgets (radiative and heat fluxes) obtained through various methods and data products.

2.1 Surface Energy Balance Equations

The energy budget at the Earth's surface, where most solar heating takes place, accounts the exchanges of energy between the Earth's surface and atmosphere which are important determinants of micro, regional, and global climates. The surface radiative energy must be balanced by (dissipated through) the turbulent/conductive heat flux, the primary drivers of the Earth's energy and water cycle (Kleidon et al., 2014).

Over lands where surface media are non-transparent to sunlight (Figure 2.1(a)), the conservation of energy at the land-atmosphere interface is expressed as,

$$R_n \equiv SWd - SWu + LWd - LWu = E + H + Q \tag{2.1}$$

where R_n, SWd, SWu, LWd, LWu (W m^{-2}) are the net radiation, incoming solar, reflected solar, downward atmospheric longwave, and surface emitted longwave radiation, respectively. Radiative fluxes toward the surface are defined as positive. Latent E and sensible H heat fluxes entering the atmosphere and ground heat flux Q (W m^{-2}) entering the soil layer are defined as positive.

(a) Land Surface Energy Budget

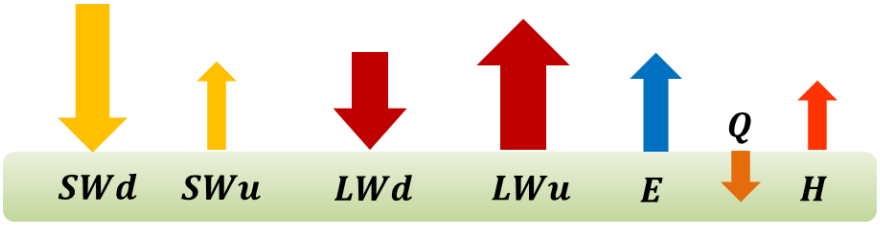

$$R_n \equiv SWd - SWu + LWd - LWu = E + H + Q$$

(b) Ocean Surface Energy Budget

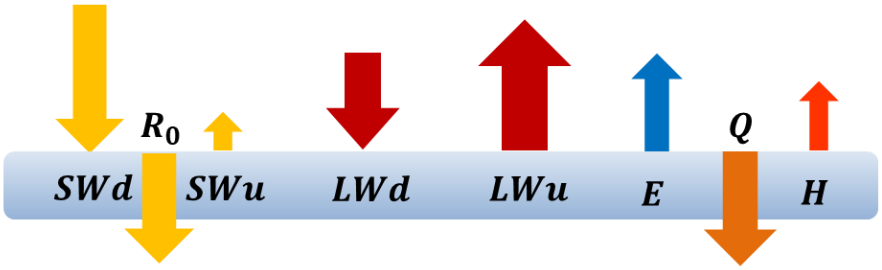

$$R_n^S \equiv SWd - SWu = R_0$$
$$R_n^L \equiv LWd - LWu = E + H + Q$$
$$\text{Net Water Heat Flux (Water Heat Uptake)} \equiv R_n - E - H = R_0 + Q$$

Figure 2.1: Surface energy balance equations over (a) land and (b) water-snow-ice surfaces. SWd, SWu, LWd, and LWu are downward shortwave, upward shortwave, downward longwave, upward longwave radiation; R_n the net radiation; R_n^S and R_n^L the net shortwave and longwave radiation; E, H, Q the latent, sensible, and ground/water-snow-ice surface conductive (within the cool skin layer) heat flux; R_0 the (net) solar radiation entering the (water-snow-ice) media. Radiation fluxes are positive when entering the surface media. Thermal energy fluxes are positive when entering the atmosphere or leaving the surface media.

Over water, snow, and ice surfaces, where the media are transparent to sunlight (Figure 2.1(b)), the conservation of energy is expressed as (e.g., Badgley, 1966; Saunders, 1967; Weller, 1968; Fairall et al., 1996a; Wang et al., 2014),

$$\begin{aligned} R_n^L &\equiv LWd - LWu = E + H + Q \\ R_n^S &\equiv SWd - SWu = R_0 \end{aligned} \tag{2.2}$$

where R_n^S and R_n^L are the net surface shortwave and longwave radiations (W m^{-2}), R_0 the (net) solar radiation entering the (water-snow-ice) media (W m^{-2}), and Q the water-snow-ice surface conductive heat flux analogous to ground heat flux (W m^{-2}). Eqs. (2.2) and (2.1) are identical when solar radiation vanishes (i.e., nighttime). Specifically, the net water heat flux or water heat uptake is defined as $R_n - E - H$ equal to $R_0 + Q$ according to Eq. (2.2). Solar radiation enters the surface energy balance equation through Q. An analytical expression of Q in terms of R_0 and T_s is given in (Wang et al., 2014).

Note that the usually assumed long-term surface energy balance expressed as

$$R_n = R_n^S + R_n^L = E + H \tag{2.3}$$

does not hold over either land or ocean surface. Over sunlight transparent surfaces (ocean, snow, and ice), $R_n = E + H$ or $R_0 + Q = 0$ implies that all solar radiation entering, e.g., the ocean, is transferred back into the atmosphere to balance net long-wave radiation and turbulent heat fluxes as shown in Eq. (2.2). This is physically unrealistic since part of solar radiation absorbed by the water must be dissipated through a number of physical, chemical and biological processes in the ocean including the thermal energy transport down to deeper ocean indicated by the decreasing ocean water temperature with depth (Liu et al.,

2010; Kuhlbrodt and Gregory, 2012), the conversion of thermal energy to kinetic energy for sustaining the global ocean general circulations (Laurent and Simmons, 2006; Toggweiler and Samuels, 1998), the energy consumed by chemical reactions such as photosynthesis (Behrenfeld and Falkowski, 1997; Falkowski and Raven, 2007; Pisciotta et al., 2010) among others. These previous studies suggest that the thermal energy responsible for the observed increase in ocean water temperature (increasing ocean heat content, e.g., Levitus et al., 2012), used to evaluate the imbalance between R_n and $E + H$ (e.g., Stephens et al., 2012a), is only a portion of the solar radiation absorbed by the oceans.

Over land surfaces, $R_n = E + H$ implies that $Q = 0$ representing a (quasi) steady-state of soil temperature for a long-term (annual) average. In fact, (quasi) steady-state of soil temperature does not necessarily lead to vanishing Q even at annual (or longer) time scale. The annual mean Q over lands would be zero if (1) soil temperature has no trend at inter-annual timescales (no change of thermal energy storage), (2) annual mean soil heat flux at the bottom of the top soil layer vanishes, and (3) annual mean soil temperature profile is uniform. These conditions rarely occur (e.g., Gilichinsky et al., 1998; Qian et al., 2011; Bai et al., 2014) indicating that Q over lands is likely non-zero at annual scale. Thermal energy entering the land surface (Q) is transferred through several mechanisms not limited to heat conduction. For example, Heitman et al. (2008, 2010) showed that part of thermal energy entering the soil is used for subsurface evaporation (subsurface latent heat sink). Thermal energy in the soil may also be transferred downward by infiltrating rainwater reaching groundwater aquifers much deeper than the top soil layer.

2.2 Modeling of Surface State Variables

Specification of T_s and θ_s in LSMs plays an essential role in numerical climatic and hydrological models as T_s and θ_s dominate the energy and moisture exchange between the land surface and the atmosphere (Jacobs et al., 2000; Gao et al., 2008; Seneviratne and Stöckli, 2008). T_a is one of commonly used variables for evaluating changing climates and LSM performance. An overview of commonly used parameterizations of T_s, θ_s, and T_a in the existing LSMs together with the corresponding strengths and weaknesses is given in this section.

2.2.1 Modeling of Surface Temperature T_s

Deardorff (1978) and Henderson-Sellers et al. (1995) summarized the parametrizations of T_s in the existing LSMs, which can be classified into the following three categories:

(1) Discretized Heat Diffusion Equation (HDE)

In the HDE model, soil temperature profile is solved by one-dimensional heat diffusion equation using finite difference schemes (e.g., Carlslaw and Jaeger, 1959; Benoit, 1976; Verseghy, 1991; Oleson et al., 2010). T_s is described by the conservation of energy within a top soil layer in the form of the continuity equation (Pan and Mahrt, 1987; Avissar and Pielke, 1989; Verseghy, 1991; Liang et al., 1994; Smirnova et al, 1997; Oleson et al., 2010). A general form of the energy conservation equation can be expressed as

$$\rho_s c_s \frac{T_s^{n+1} - T_s^n}{\Delta t} = \frac{Q^n - Q_1^n}{z_1} \tag{2.4}$$

where T_s^{n+1} and T_s^n are the surface temperature (K) between two time steps, n and $n+1$ the two consecutive time steps, respectively, ρ_s the soil bulk density (kg m^{-3}), c_s the specific heat of soil (J kg^{-1} K^{-1}), Δt the model time step (s), Q the ground surface flux (W m^{-2}), Q_1 the soil heat flux leaving the top soil layer (W m^{-2}), z_1 the thickness of top soil layer (m). Q and Q_1 are estimated based on the surface energy equation (Eq.(2.1)) and the Fick's first law of diffusion, respectively (e.g., Smirnova et al, 1997; Oleson et al., 2010).

The HDE model has been widely applied in the existing LSMs as it directly deals with the governing equation of heat transfer in the soil with no theoretical simplifications (e.g., Benoit et al., 1976; Chen and Dudhia, 2001; Dai et al., 2003). Yet, several issues associated with the HDE model may affect its accuracy and reliability. First, the model time step is required to be sufficiently small for the sake of accuracy (Benoit, 1976; Deardorff, 1978). Second, the HDE model often requires a small z_1 close to surface for resolving the sharp gradient of soil temperature near the surface, which is computationally costly. Third, the HDE model predicted T_s is always subject to the errors and uncertainties from the poorly calibrated multi-layer soil thermal parameters. Moran et al. (2004) state that although the HDE model have been extensively tested, the operational applications of these models are generally limited as the detailed soil thermal properties are difficult to obtain. On the other hand, increasing the number of soil layers is needed for more accurate numerical solution, while the modeling error may increase by introducing additional uncalibrated soil thermal parameters.

(2) Insulated Surface Model

As its name suggests, the insulated surface model predicts T_s solely at the surface without using soil temperature information from below by neglecting or simplifying Q. In some earlier LSMs, T_s is solved iteratively through the surface energy balance equation (Eq. (2.1)), while T_s appears in LWu (through the Stefan–Boltzmann law) and H (parameterized as a function of near-surface temperature gradient). Q is either assumed to be zero (i.e., ground surface stores no heat) (Gate et al., 1971; Manabe et al., 1974; Robock et al., 1995) or a fixed portion of H or R_n. For example, Kasahara and Washington (1971) set Q as one-third of H. Nickerson and Smiley (1975) assumed Q being 0.19 or 0.32 of R_n depending on atmospheric stability.

By assuming zero heat conduction from below, T_s can be solved by the conservation of energy at the surface expressed as (e.g., Arakawa, 1972; Corby et al., 1972; Rowntree, 1975; Sellers et al., 1986; Oleson et al., 2010),

$$\rho_s c_s \frac{\partial T_s}{\partial t} = R_n - E - H = Q \tag{2.5}$$

where the variables are defined the same as those in Eq. (2.4). Eq. (2.5) is sometimes called the "ground heat flux forcing model" as the time variation of T_s is function of Q alone (Deardorff, 1978). However, Corby et al. (1972) pointed out that Eq. (2.5) has difficulty properly reproducing diurnal variation of T_s. The oversimplification of Q limited the applications of this model. Additionally, Deardorff (1978) argued that Eq. (2.5) does not consider the effect of deep soil temperature on T_s.

(3) Force-Restore Method

Improving parameterizations of T_s to overcome the weaknesses of the HDE and insulated surface model have been the goal of many previous studies. The force-restore method (FRM), first proposed by Bhumralkar (1975) and Blackadar (1976), was one approach. The FRM was originally developed to predict the "ground surface temperature T_g" (i.e., the averaged soil temperature within a thin soil layer with a depth of δ) through an ordinary differential equation, which is derived from the one-dimensional heat diffusion equation driven by surface forcing, as an approximate solution of heat transfer equation (Bhumralkar, 1975; Blackadar, 1976; Deardorff, 1978; Lin, 1980; Dickinson, 1988; Hu and Islam, 1995; Gao et al., 2008).

Various versions of FRMs were formulated for different definitions of T_g (e.g., Bhumralkar, 1975; Deardorff, 1978; Lin, 1980). Bhumralkar (1975) set $T(\delta, t) = T_g$, while Lin (1980) defined $T_g = 0.5[T(\delta, t) + T_s]$ by assuming a linear variation of soil temperature within a thin layer from surface to depth δ. To predict T_s, Deardorff (1978) applied the FRM to a limiting case by letting δ approach zero (i.e., $T_g \longrightarrow T_s$), referred to as FRM_{Ts}. In the FRM_{Ts}, time variation of T_s is determined by the sum of a forcing term due to ground heat flux Q and a restoring term expressed as the difference between T_s and a reference temperature $\bar{T}$.

The FRM_{Ts} modifies the insulated surface method by adding a restoring term, which represents the effect of $\bar{T}$ on T_s. Deardorff (1978) compared several methods for predicting T_s to show that the FRM_{Ts} improves the simulations of T_s compared to other methods including the HDE and insulated surface (surface energy balance)-based methods

(e.g., Gates et al., 1971; Manabe et al., 1974; Nickerson and Smiley, 1975; Benoit, 1976). The FRM_{Ts} has been widely used in climate and hydrological models (Dickinson et al., 1986, 1993; Wetzel and Chang, 1987; Noilhan and Planton, 1989; Cogley et al., 1990; Xue et al., 1991; Pitman et al., 1991; Sellers et al., 1996; Jacobs et al., 2000; Margulis and Entekhabi, 2001; Gao et al., 2004; Luce and Tarboton, 2010).

The extended applications of FRM have also been investigated by previous studies owing to its parameter-parsimonious and explicit physical interpretation. Hirota et al. (1995) applied the FRM at daily scale to estimate daily mean T_g. Hu and Islam (1995) proposed a generalized version of FRM for predicting T_s and T_g derived from minimizing the errors between the solutions of FRM and HDE. Hirota et al. (2002) applied the FRM to estimate daily mean soil temperature, soil temperature at depth in frozen soils, and T_g under a snow cover. Gao et al. (2008) revised the FRM_{Ts} to take heterogeneous soil layer and conductive and advective heat transfer into account.

2.2.2 Modeling of Surface Soil Moisture θ_s

θ_s in LSMs is usually solved numerically based on the (1) mass conservation (2) discretized Richards equation, and (3) FRM. The following gives a brief review of the three approaches along with the corresponding features and limitations. Note that the first two methods usually estimate an averaged soil moisture of top soil layer (θ_1) rather than θ_s as being defined at the surface in this study.

(1) Mass Conservation

Mass conservation-based models predict θ_1 as a residual of surface water balance equation using a general expression given as (e.g., Laio et al., 2001; Guswa et al., 2002),

$$z_1 \frac{d\theta_1}{dt} = I - E - Q_{wg1} \tag{2.6}$$

where θ_1 and z_1 are the soil moisture and the thickness of top soil layer, I the infiltration, E the evapotranspiration rate, Q_{wg1} the net gravitational drainage rate from the bottom of top soil layer.

Several types of mass conservation-based models were developed over the years. The bucket model, first proposed by Manabe et al. (1969), is the simplest one. The bucket model is a lumped model for a single soil layer. The soil layer is conceptualized as a bucket receiving and retaining all flow-in water until its storage capacity is filled. The excess water above the soil layer's capacity becomes runoff. Note that the bucket model ignores the gravitational drainage (Q_{wg1} in Eq. (2.6)). Over the years, Manabe's original bucket model was expanded to address multiple soil layers (e.g., Hansen et al., 1983; Xue et al., 1991), runoff generation from dry soils (e.g., Gates and Schlesinger, 1977), and gravitational drainage (Laio et al., 2001; Guswa et al., 2002).

The bucket model is still used in some LSMs owing to its simple description of hydrological cycle (e.g., Milly, 1992; Famiglietti and Wood, 1994; Robock et al., 1995; Liao et al., 2001; Guswa et al., 2002; Romano et al., 2011). However, the bucket model often overestimates E and potential evapotranspiration compared to other schemes because it does not have adequate vegetation parameters that describe effects of plant physiology

on the E estimates (e.g., Henderson-Sellers et al., 1996; Seneviratne et al., 2002; Seneviratne et al., 2010). Furthermore, Romano et al. (2011) state that the bucket model have a short memory for soil water storage as water transferring at different rates along vertical soil profile is virtually ignored. They also indicate that the bucket model cannot describe the system response to rapid change in atmospheric forcing accurately due to the direct feedback between soil water storage and evapotranspiration. Also, runoff being simply parameterized by the further incident water after reaching soil capacity was found to be incapable of reproducing observed surface energy and water budgets (e.g., Bowen ratio and run-off ratio) (Liang et al., 1998; Wood et al., 1998; Schlosser et al., 2000).

A number of studies attempted to improve the modeling of soil moisture by improving the parameterization of evapotranspiration and gravitational drainage in Eq. (2.6). These improved soil moisture models were incorporated into a group of later generations of LSMs known as the Soil-Vegetation-Atmosphere Transfer (SVAT) models (e.g., Sellers et al., 1986; Dickinson et al., 1986; Ács et al., 1991; Xue et al., 1991). In SVAT models, soil column is divided into two to three layers with a top soil layer ranging from 5-10 cm. SVAT models have better physical parameterizations compared to the bucket model. For example, E in SVAT models is commonly parameterized using the bulk transfer or the Penman-Monteith method (e.g., Sellers et al., 1986; Koster and Suarez, 1996), while E in the bucket model is usually formulated as potential evapotranspiration multiplied by a limiting factor expressed as a linear function of soil moisture between two thresholds (i.e., field capacity and wilting point) (e.g., Guswa et al., 2002; Seneviratne et al., 2010).

Previous studies have shown that the simulated soil moisture as well as surface energy and water fluxes from different SVAT models disagree with each other (Shao and Henderson-Sellers., 1996; Wetzel et al., 1996; Koster and Milly, 1997; Liang et al., 1998; Wood et al., 1998; Pitman et al., 1999). The discrepancies are caused by the various complexities of evapotranspiration and runoff parameterizations among models. Intercomparisons of SVAT models are well summarized in international comparison projects such as PILPS (Henderson-Sellers et al., 1993; 1995) and GSWP (Dirmeyer et al., 1999, 2006). Excellent overviews of the SVAT model performance with respect to soil moisture predictions are given by Shao and Henderson-Sellers (1996) and Koster and Milly (1997).

Some other mass conservation-based models were developed independently. The conceptual model first proposed by Georgakakos and Baumer (1996) and later used in Venkatesh et al. (2011) estimates soil moisture of a 150 cm soil column with a 50 cm top soil layer. Sheikh et al. (2009) developed a two-layer soil water balance model for a distributed hydrological model. The top soil layer was set to be 20 cm to analyze daily soil moisture variation. A major limitation of these models is the requirments of other components of water cycle, such as infiltration, surface runoff, and drainage, which need to be parameterized with empirical and site-dependent parameters. Additionally, these models are applied at larger temporal scales (i.e., daily).

(2) Discretized Richards Equation

The discretized Richards equation (Richards, 1931) describes the vertical soil water movement in unsaturated soil, and is used in previous studies to predict θ_s and soil

moisture profile (e.g., Mahrt and Pan, 1984; Abramopoulos et al., 1988; Avissar and Pielke, 1989; Entekhabi and Eaglesom, 1989; Verseghy, 1991). Mahrt and Pan (1984) showed that the model often underestimates the soil water flux within the soil due to truncation errors. They suggest that a sufficiently thin upper soil layer and a small grid size are required to reduce the truncation errors. Celia et al. (1990) applied the discretized Richards equation in the form of pressure head (h-form) to solve water flow within unsaturated soil layer. The results showed that the h-form of Richards equation, in general, produces large error on mass conservation and infiltration depth.

Kumar et al. (2013) developed a non-linear root water uptake model by applying the Richards equation with an additional sink term representing the water uptake by roots. The results showed that the model tends to underestimate the depletion of the top layer soil moisture. They also found that the model is highly sensitive to crop parameters, which have large uncertainties. Furthermore, similar to the HDE model of T_s, multi-layer models need many soil parameters (e.g., soil hydraulic conductivity and shape parameters in soil water retention curve), which are difficult to accurately obtain from field observations (e.g., Gallage et al., 2013; Wassar et al., 2016). Specification of large numbers of model parameters introduces additional modeling errors and uncertainties.

(3) Force-Restore Method

The success of the FRM_{Ts} (Section 2.2.1) motivated the development of FRM to predict θ_s based on a simplified Richards equation. Deardorff (1977) proposed a FRM of θ_s ($FRM_{\theta s}$) as an analogy of FRM_{Ts} but without providing a derivation. Noilhan and Planton (1989) and Hu and Islam (1995) formulated a $FRM_{\theta s}$ by neglecting the

gravitational drainage term in the Richards equation. The $FRM_{\theta s}$ has been applied in some LSMs (Wetzel and Chang, 1987; Noilhan and Planton, 1989; Kowalczyk et al., 1991). However, Hu and Islam (1995) point out that the assumptions and approximations limit the applicability of these $FRM_{\theta s}$s. These classical $FRM_{\theta s}$s are only applicable to relatively dry soil conditions where soil water movement is dominated by the gradient of soil water potential (Jacobs et al., 2000). Neglecting the drainage term introduces large modeling error under wet soil conditions where gravitational drainage dominates soil water flow.

2.2.3 Modeling of Near-surface Air Temperature T_a

In current LSMs, T_a (screen level, about 2-10 m) is commonly diagnosed from other state variables and is not involved in either the LSM or climate model predictions. Dickinson et al. (1986) estimated T_a at two meters high by a weighted average of T_s and air temperature at the lowest (climate) model level T_1 with the weights determined by the drag coefficient. Zhang and Zheng (2004) estimated T_a using a simple empirical equation ($0.45\ T_s + 0.55\ T_1$) without justification. Pleim and Xiu (1995) estimated T_a using H and T_1 based on the Blackadar boundary layer scheme (Blackadar, 1976, 1979), which requires a high resolution model layer within the atmospheric boundary layer for obtaining T_1 close to the surface.

Alternatively, the Community Land Model (CLM) (Bonan, 1996; Oleson et al., 2010) incorporated into the Community Atmosphere Model (CAM) (Neale et al., 2012) estimates T_a through T_s with a log-profile relationship established from the well-known surface layer similarity theory (i.e., Monin-Obukhov similarity theory, MOST, Monin and

Obukhov, 1954) and with the parameters obtained from the Kansas experiment (Businger et al., 1971). However, the log-profile approaches rely heavily on site dependent parameters, i.e., surface roughness lengths (SRLs), which are difficult to estimate accurately and subject to large uncertainty (Wieringa, 1993). Moreover, the appearance of SRLs in the log-profile-based formulations of T_a is a mathematical artifact. SRLs are not included in the original Monin-Obukhov similarity equations (MOSE) derived using the Buckingham π theorem in the dimensional analysis (e.g., Arya 1988). They are only introduced by integrating the MOSE down to close-to-surface levels beyond the domain within which the premises underlying the MOSE hold.

2.3 Modeling of Surface Heat Fluxes

2.3.1 Conventional Models of Surface Heat Fluxes

Surface heat fluxes in existing LSMs (also OSM) are usually parameterized by gradient-based method known as the bulk transfer method (BTM). The BTM parameterizes latent E and sensible H heat fluxes as functions of near-surface temperature/humidity gradient, wind speed, and bulk transfer coefficients (e.g., Arya, 1988; Deardorff, 1978; Maykut, 1982; Andreas and Murphy, 1986; Noilhan and Planton, 1989; Schröder et al., 2003). The bulk transfer coefficients are often derived from the integrated forms of the dimensionless wind and temperature profile from the MOST (e.g., Paulson, 1970; Andreas and Murphy, 1986; Beljaars and Holtslag, 1991; Zeng et al., 1998) with the atmospheric stability parameter ζ written as a (empirical) function of temperature gradient, wind speed, and SRLs (e.g., Deardorff, 1968; Businger et al., 1971; Andreas and Murphy, 1986;

Businger, 1988; Rutgersson et al., 2001; Zhang et al., 2011). Bulk transfer coefficients may also be directly estimated using meteorological measurements with the BTM (e.g., Leovy, 1969; Pond et al., 1974; Sadhuram, 1991).

The BTM estimated E and H are subject to substantial errors and uncertainties mainly resulting from the drawbacks of model formalism and uncertainties in model inputs and parameters. Specifically, the bulk transfer coefficients depending on SRLs introduce substantial uncertainties and errors into the BTM heat fluxes (e.g., Zeng et al., 1998; Brunke et al., 2002, 2003, 2011). Lüers and Bareiss (2010) found that modeling errors of BTM are mostly caused by the empirical transfer coefficients. Brunke et al. (2002) evaluated eight different BTMs in terms of SRL parameterizations. They obtained notably different E and H under weak and strong wind as well as strongly unstable conditions. Renfrew et al. (2002) showed that the SRL formula used to compute bulk transfer coefficients in the National Centers for Environmental Prediction (NCEP) bulk algorithm leads to overestimations of E and H under moderate to high wind speed conditions.

Strub and Powell (1987) indicate that even though the performance of BTM can be improved by stability corrections over shorter time scale (daily to weekly) simulations, the BTM still consistently underestimate both E and H under stable atmospheric conditions. Sadhuram (1991) estimated a bulk transfer coefficient of E over Arabian Sea different from the values reported by Kondo (1975) and Bunker (1976). The differences, as stated by Sadhuram (1991), are caused by the temporal and spatial variations of the transfer coefficients. Also, the use of different dimensionless wind/temperature profiles, suggested by several research groups (reviewed by e.g., Högström, 1988), may introduce additional

uncertainties into the BTM heat fluxes as the dimensionless profiles directly change the formulation of bulk transfer coefficients.

The effects of wind speed biases on the BTM estimated heat fluxes have been shown to be most pronounced in winter months (Moore and Renfrew, 2002). Wind speed also affects the BTM estimated heat fluxes through SRLs. Earlier studies (Zeng et al., 1998; Renfrew et al., 2002) suggest that commonly used formulae of SRLs have difficulties producing consistent estimates of surface momentum and heat fluxes, especially heat fluxes, under weak wind and moderate to high wind conditions. Additionally, measurements of wind speed and SRLs over large regions are difficult to make. Previous studies have shown that remote sensing retrieved surface wind speed contains high uncertainties and biases (Katzberg et al., 2001; Komjathy et al., 2004; Katzberg and Dunion, 2009; Clarizia et al., 2012).

Large measurement errors in bulk gradient of temperature/humidity directly introduce uncertainties into the BTM heat fluxes (via bulk transfer coefficients). Rutgersson et al. (2001) compared E and H estimated by two BTMs in terms of different forms of bulk transfer coefficients with observations at two marine sites. The results showed that both models overestimate E and H, which are largely attributed to the errors in the measured temperature and humidity gradient. Friedl (2002) showed that the BTM overestimates both E and H under large temperature gradients and low wind speeds.

Further improvements of the BTM heat fluxes face theoretical and technical obstacles. The measurement error of a bulk gradient computed from the difference of two close numbers is difficult to reduce given existing technology. Additionally, even if all

bulk gradient variables are free of measurement errors, the BTM heat fluxes have inherent modeling errors since the BTM are based on the first-order closure of the Reynolds decomposition of turbulent flows subjected to substantial and unknown modeling errors. Furthermore, it is well understood that the use of SRLs in the parameterization of bulk transfer coefficients based on the MOST is a mathematical artifact as discussed in Section 2.2.3. More importantly, the BTM estimated E and H are not constrained by the conservation of energy, and hence do not automatically close the surface energy budget. Lack of energy conservation is a fundamental drawback of BTM with no obvious solution. The closure problem in turbulence models remains "one of the unsolved problems in classical physics" (Stull, 1988). Thus, estimation errors of the BTM heat fluxes are theoretically unbounded.

In addition to the BTM, the Penman-Monteith (PMM) (Monteith, 1965) and Priestley-Taylor method (PTM) (Priestley and Taylor, 1972) are also frequently used to estimate E (e.g., Sheffield et al., 2010; Zhang et al., 2010a; Miralles et al., 2011; Fisher et al., 2008). The PMM was developed to use surface net radiation, temperature, humidity, and wind speed data to estimated E. The PMM can be viewed as the BTM constrained by the surface energy balance. The PMM overcomes some weaknesses of the BTM such as the failure of closing surface energy budget and the dependence of temperature and humidity gradient. However, the PMM estimated E is still affected by the uncertainties from the aerodynamic resistance parameters expressed as a function of wind speed and SRLs (e.g., Alves and Pereira, 2000; Monteith and Unsworth, 2013).

The PTM was developed as a simplification of the PMM by assuming that the "atmospheric demand" term is proportional to the "available energy" term represented by

an empirical constant α, the so-called Priestley-Taylor parameter. Therefore, the PTM does not include vapor pressure deficit and aerodynamic resistance explicitly. The range of α, reported by previous studies, differs largely for both water unstressed and stressed conditions. Under water unstressed conditions, α lies between 1.0 and 1.5 obtained from several field experiments (Singh and Taillefer, 1986; Brutsaert and Chen, 1995; Chen and Brutsaert, 1995). Under water stressed conditions, α is usually assumed to be a linear function of root zone soil moisture (e.g., Fisher et al., 2005). The function is formulated using the soil moisture below the surface (e.g., 20 cm) rather than surface soil moisture, which is more relevant to evapotranspiration.

Ground heat flux Q is commonly estimated using near-surface soil temperature gradient according to the Fick's first law of diffusion (e.g., Chen et al., 1996; Pan and Mahrt, 1987; Bosilovich and Sun, 1995; Koster et al., 2000). The estimated Q in current LSMs is potentially underestimated resulting from the underestimated soil temperature gradient. For example, the catchment-based LSM in the Modern Era Retrospective-analysis for Research and Applications (MERRA) reanalysis (Koster et al., 2000) and the Noah LSM in the NCEP reanalysis system (Chen et al., 1996; Chen and Dudhia, 2001; Ek et al., 2003) estimate Q using temperature gradient between T_s and the averaged soil temperature of top soil layer (0-5 cm for the catchment-based LSM and 0-10 cm for the Noah LSM, respectively). The use of an averaged soil temperature below the surface may not capture the sharp gradient of soil temperature near the surface thus leading to an underestimation of Q. Furthermore, temperature gradient in the Fick's first law of diffusion is in fact local rather than bulk gradient. Alternatively, Q may be estimated by the residual of surface energy balance equation (Eq. (2.1)), while E and H are obtained by the BTM

(e.g., Deardorff, 1978; Noilhan and Planton, 1989; Gentine et al., 2012). Q estimated using this method is subject to large modeling errors and uncertainties from the errors and uncertainties of R_n, E, and H. For example, positive biases of wind speed and temperature/humidity gradient during daytime may lead to an overestimation of $E + H$ that is greater than R_n with unrealistic negative daytime Q. On the other hand, the error and uncertainty of Q cause those of E when E is estimated using the PMM (Gavilán et al., 2007).

2.3.2 Maximum Entropy Production (MEP) Model of Heat Fluxes

The MEP model of surface heat fluxes recently proposed by Wang and Bras (2009, 2011) and Wang et al. (2014) is an unconventional dynamic-statistical model built on the Bayesian probability theory, information theory and atmospheric boundary layer turbulence theory. The MEP model allows E, H, and Q over the Earth-atmosphere interface to be simultaneously solved in terms of analytical functions of surface radiation fluxes, temperature and/or humidity as the most probable partition of radiation fluxes while closing the surface energy budget (satisfying the conservation of energy). Instead of focusing on fundamental physical laws, the MEP model seeks an answer to the question: What is the best prediction of energy partitioning of surface radiation fluxes into surface heat fluxes based on the available surface energy and moisture states?

The formulation of the MEP model is described in (Wang and Bras, 2011) for the case of land surfaces, and in (Wang et al., 2014) for the case of water-snow-ice surfaces. As the first humidity (and temperature)-gradient independent, physically-based model of

surface heat fluxes, the MEP model does not make explicit uses of near-surface temperature, humidity gradient (and water vapor deficit) data thus avoiding the substantial measurement errors of bulk gradient variables. The MEP model also uses fewer model parameters (than existing models) that are independent of wind speed and SRLs. The modeling errors of the MEP heat fluxes are bounded by the measurement errors of surface radiative fluxes.

Tests of the MEP model using field observations reported previously by the model developers (Wang and Bras, 2009, 2011; Wang et al., 2014) provide evidence that the MEP model accurately predicts surface heat fluxes over both land and water-snow-ice surface at field scales. Also, the MEP model applies to the full range of soil moisture conditions from residual water content to saturation. Independent tests of the MEP model have been reported (e.g., Nearing et al., 2012; Yang and Wang, 2014; Shanafield et al., 2015) and show that the MEP model matches, or outperforms, other existing models. These early applications of the MEP model justified its potential as an alternative approach for modeling the surface heat fluxes at regional and global scales.

2.4 Estimation of Global Surface Energy Budgets

The first study of global surface energy budget can be traced back to early 1900s (Dines, 1917). Over the years, the estimates of global annual mean surface energy budgets have been substantially improved due to the advancement of satellite observations. The reduced uncertainty of planetary albedo estimate, over the past century, greatly improves our understanding of surface energy budget (e.g., Hunt et al., 1986). The satellite-derived

global precipitation also helps the estimation of global annual mean E (e.g., Trenberth et al., 2007). Numerous studies have attempted to reconstruct global long-term (annual) surface energy budgets using different methods by combining progressively improved observations made over the past several decades (e.g., National Academy of Sciences, 1975; Budyko, 1982; Liou, 1992; Kiehl and Trenberth 1997; Trenberth et al., 2009; Stephens et al., 2012a; L'Ecuyer, et al., 2015).

The estimates of global surface energy budgets are now available from many data products, and are classified into three categories: the observation-based products (satellite and in situ observations), model simulations based products, and reanalysis products (e.g., Mueller et al., 2013). Although more advanced observations and models have been introduced, global surface energy budgets estimated by various datasets differ largely, even when they are of the same category (e.g., Jiménez et al., 2011; Mueller et al., 2011, 2013; Wild et al., 2015). Considerable uncertainties result from, e.g., the lack of reliable measurements with global coverage (observation-based) and the different parameterizations among LSMs (model based and reanalysis outputs) (Kiehl and Trenberth 1997; Jiménez et al., 2011; Stephens et al., 2012a; Mueller et al, 2013; Wild et al., 2013, 2015). Wild et al. (2013) showed that the uncertainties of surface radiation budgets are generally larger than those at the top of atmosphere (TOA). Uncertainties of surface turbulent fluxes are in general twice as large as those of surface radiative fluxes, which indicate that there are still challenges for monitoring and modeling global surface energy budgets, especially surface turbulent heat fluxes. More importantly, all the existing global data products report an exactly/nearly zero Q at annual scale over both global land and ocean according to Eq. (2.3), which is questionable as discussed in Section 2.1.

The following sections provide a brief summary of previous works regarding the estimations of global surface energy budgets by discussing the features of each category.

2.4.1 Observation-based Estimates

In observation-based estimates, surface radiations (shortwave and longwave) are usually derived from the radiation observations at TOA using a radiation transfer model that accounts for atmospheric attenuation and emission through the atmosphere (e.g., Li et al., 2013; Wild et al., 2013). Global annual mean E is generally derived from (1) global annual precipitation amount assuming E is equal to precipitation for a long-term average at global scale (e.g., Legates and Willmott, 1990; Kiehl and Trenberth, 1997; Trenberth et al., 2009; Stephens et al., 2012a), (2) upscaling of global network of continuous in-situ E measurements (e.g., Jung et al., 2010), or (3) physical or empirical models such as the PMM, PTM, and BTM (e.g., Fisher et al., 2008; Wang and Liang, 2008, Sheffield et al., 2010). The first two approaches estimate global annual mean E directly from in-situ and/or satellite observations, while the third method derives global annual mean E from meteorological observations with global coverage. Global annual mean H is commonly estimated as a residual of global annual mean of R_n and E according to Eq. (2.3) (Kiehl and Trenberth, 1997) or by the BTM using global data products of meteorological variables (e.g., Fisher et al., 2008; Sheffield et al., 2010).

Several recent studies (Kiehl and Trenberth, 1997; Trenberth et al., 2009; Stephens et al., 2012a; L'Ecuyer, et al., 2015) provide comprehensive summaries of the current knowledge about global annual mean surface energy budgets using satellite observations.

Kiehl and Trenberth (1997) constructed the global surface radiation budgets based on the Earth Radiation Budget Experiment (ERBE) data and compared it to earlier studies (during the 1990s) using earlier generation of satellite observations, such as the International Satellite Cloud Climatology Project (ISCCP, Rossow and Zhang, 1995). The global annual mean E is estimated by the earlier Global Precipitation Climatology Project (GPCP) data (Adler et al., 2003), while that of H is deduced as $R_n - E$.

Trenberth et al. (2009) updated the values based on the improved satellite radiation measurements from the National Aeronautics and Space Administration – Clouds and the Earth's Radiant Energy System (NASA CERES) and more recent GPCP precipitations observations. CERES estimates the surface radiation fluxes using improved cloud properties observations from Moderate-Resolution Imaging Spectroradiometer (MODIS) compared to ISCCP, which is used in ERBE (Wielicki et al., 1996, 2006). They further examined the surface energy budgets over lands and oceans separately to understand the sources of discrepancies between different estimates. Contrary to Kiehl and Trenberth (1997), which leaves H as the final quantity to be computed as a residual, Trenberth et al. (2009) estimated global annual mean of R_n^L as a residual of surface energy balance equation, while that of H is estimated from reanalysis products.

Stephens et al. (2012a) further revised the estimates of global mean surface energy budgets using more data products. The global surface radiation budgets are obtained from the ensemble average of multiple data products including CERES, ISCCP-FD version (Zhang et al., 2004), NASA Global Energy and Water Exchanges Project – Surface Radiation Budget (GEWEX-SRB), and Afternoon Constellation (A-Train) with the uncertainties estimated from direct comparison with surface observations. The global

annual mean of E is derived from the more recent GPCP data, while that of H is estimated from multiple land flux products (Jiménez et al., 2011) and SeaFlux datasets (Curry et al., 2004; Clayson et al., 2012, 2013).

L'Ecuyer et al. (2015) reconstructed the global and regional (continental and ocean basin) annual mean surface energy budgets using the satellite observations during 2000-2009. The surface radiation data are from GEWEX-SRB, ISCCP-FD, and CERES supplemented by the latest cloud and aerosol properties from the A-Train Constellation including the Cloud-Aerosol Lidar and Infrared Pathfinder Satellite observation (CALIPSO) satellite, the CloudSat Cloud Profiling Radar, and MODIS known as the CALIPSO-CloudSat-CERES-MODIS (CCCM) merged dataset (Kato et al., 2010, 2011). Surface turbulent heat fluxes are estimated using the Princeton ET (Sheffield et al. 2010; Vinukollu et al., 2011b) and MERRA reanalysis data products (Rienecker et al., 2011; Bosilovich et al., 2011) and the Global Land Data Assimilation System (GLDAS) (Rodell et al., 2004). The uncertainties are evaluated using either the range or the standard deviation of estimates from various products. The atmospheric and surface water and energy balance equations are incorporated as constraints through a variational method (Rodgers, 2000; Kalney, 2003) that reduces the energy imbalance and uncertainties of each component. The estimates of global annual mean surface energy budgets reported by these articles as well as other independent studies are summarized in Table 2.1.

The aforementioned works indicate that current observation-based estimates of global surface energy budgets have large uncertainties. For example, the uncertainties in aerosol and cloud properties significantly affect both surface downward and upward radiation retrievals and E (through precipitation) (Kato et al., 2013), while those in T_s, air

temperature, and water vapor dominate the biases in R_n^L (L'Ecuyer and Stephens 2003; Zhang et al., 2004, 2006, 2007, 2010b). Kiehl and Trenberth (1997) suggest an uncertainty of 20-25 W m^{-2} in global annual mean R_n^S primarily caused by an exclusion of aerosol effects and potentially underestimated cloud absorption in the radiation transfer model. Stephens et al. (2012a) estimated an overall uncertainty of 9 W m^{-2} in global annual mean R_n^S by direct comparison with surface observations. However, the seemingly smaller uncertainty of R_n^S, reported by Stephens et al. (2012a), as compared to Kiehl and Trenberth (1997)), results from a large error cancellation of random sampling error.

Kiehl and Trenberth (1997) and Trenberth et al. (2009) showed that the estimates of global annual mean R_n^L between various estimates could differ by ~20 W m^{-2}. They conclude that the discrepancies are presumably caused by the strong dependence of R_n^L retrieval on cloud-base height and low cloud amount, which are difficult to retrieve accurately from satellite observations. Kiehl and Trenberth (1997) state that R_n^L retrieved from satellite observations is more likely to be underestimated as a result of the missing view of low clouds from satellites. However, Wild and Roeckner (2006) argue that R_n^L derived from satellite observations is typically higher than that estimated by climate models. Alternatively, Stephens et al. (2012a) reported an uncertainty of 14 W m^{-2} in global annual mean R_n^L with the main source of errors from the uncertainties in temperature and water vapor information required for flux retrieval.

Among the observation-based estimates of surface radiation fluxes, the CERES data are known to have better accuracy. The increase in efficacy is a result of improved instruments and spatial resolution as compared to the previous generation of observations

such as ERBE products (Wielicki et al., 1996, 2006). CERES data have been used to construct the global surface radiation budgets mentioned previously (Trenberth et al., 2009; Stephens et al., 2012a, b; Kato et al., 2011, 2012). Kato et al. (2012) did a comprehensive analysis of the uncertainty estimates of CERES surface radiations. The uncertainties in global annual mean CERES R_n, R_n^S, and R_n^L were estimated to be 12, 10, and 7 W m^{-2}, respectively. Their study also showed that the uncertainty of R_n^S over land surfaces is greater than that over oceans, while that of R_n^L over land and ocean are comparable. The uncertainties of global surface radiation budgets reported by previous studies, if available, are summarized in Table 2.1.

Before the era of satellite remote sensing, global annual mean E was commonly estimated by upscaling the gauge-measured precipitation to global scale. This approach has been shown to have considerable uncertainties resulting from sparse data points over oceans and the upscaling errors (Legates, 1995). For example, Legates (1995) showed a spread of ~350 (780 to 1130) mm per year (~27 W m^{-2}) in the global precipitation estimated by earlier studies (e.g., Schutz and Gates, 1972a, b, 1973, 1974; Jaeger, 1976, 1983). In recent times, the consensus on estimating the global annual mean E is using information from satellite-based global precipitation measurements (e.g., Kiehl and Trenberth, 1997, Trenberth et al., 2009; Stephens et al., 2012a), which are still subject to the uncertainty of precipitation retrieval, especially over oceans. Stephens et al. (2012a) suggest an overall uncertainty of 10 W m^{-2} in global annual mean E derived from the uncertainty in GPCP global precipitation. The largest uncertainties are over oceans lying between 10% and 20% (L'Ecuyer and Stephens, 2002; Haynes et al., 2009), or approximately 8 to 16 W m^{-2}, with the global ocean precipitation estimated to be ~82 W m^{-2} (Adler et al., 2003). Adler et al.

(2012) and Behrangi et al. (2014) suggest that the latest global precipitation datasets have biases as large as 9% (~7 W m^{-2}). Arbitrary adjustments may also make the E estimates less reliable. For example, Trenberth et al. (2009) imposed a 5% global increase of precipitation over oceans to reduce the surface energy imbalance.

Jung et al. (2010) estimate a global annual mean E by integrating the E observations from eddy covariance (EC) measurements, geospatial information from satellite remote sensing, and surface meteorological data using a machine-learning algorithm (i.e., Model Tree Ensemble). The reported low uncertainty of ~2 W m^{-2} is, however, evaluated using the standard deviation over 25 ensemble trees rather than the uncertainty of E. Additionally, this method may not be applied to oceans due to the lack of high quality EC data over oceans.

The estimates of global annual mean E using physical (e.g., PMM, PTM, and BTM) or empirical (statistical) models have been conducted by a number of studies. Mueller et al. (2011) estimated an ensemble mean of global land E from six data products derived based on the PTM/PMM, GPCP precipitation, and Jung et al. (2010). The standard deviation of the six products is approximately 6 W m^{-2}. Mueller et al. (2013) included seven additional estimates to determine a short-term (1989-1995) and long-term (1989-2005) global land E with an interquartile range of ~6 W m^{-2}. Jiménez et al. (2011) showed a spread of ~20 W m^{-2} in the global land E that was obtained by five estimates using the PMM, PTM and empirical approaches. Vinukollu et al. (2011a) obtained a range of ~10 W m^{-2} of the global land E estimated by the PMM, PTM, and a surface-energy-balance-based method (Su, 2002) even though all the estimates used the same meteorological inputs.

The BTM is used to estimate E over oceans. Global ocean E estimates are now available from several datasets including the SeaFlux (Curry et al., 2004; Clayson et al., 2012, 2013), Objectively Analyzed Air-sea Fluxes (OAFlux) project (Yu and Weller, 2007, 2012) from Woods Hole Oceanographic Institution (WHOI), Goddard Satellite-based Surface Turbulent Fluxes (GSSTF) products from the Goddard Earth Sciences Data and Information Services Center (Chou et al., 2003), and Hamburg Ocean Atmosphere Parameters and Fluxes from Satellite Data (HOAPS) (Grassl et al., 2000, Bentamy et al., 2003; Andersson et al., 2010). SeaFlux, OAFlux, and HOAPS use the BTM algorithm developed by the Tropical Ocean Global Atmosphere Coupled Ocean–Atmosphere Response Experiment (TOGA COARE) (Fairall et al., 1996b, 2003). Chou et al. (2003) showed that the global ocean E estimated by GSSTF version 1 (GSSTF1) is 12.7 W m^{-2} larger than that estimated by GSSTF version 2 (GSSTF2). The discrepancy is caused by the effect of salinity on surface saturated humidity and the use of different von Kármán constants (included in bulk transfer coefficient). Schlosser and Houser (2007) showed that the global ocean E estimated by GSSTF accounts for ~91% of global precipitation, while that estimated by HOAPS is only ~76%.

The quality of BTM-based E estimates is strongly affected by that of model inputs as discussed in Section 2.3.1. For example, Clayson and Bogdanoff (2013) showed that neglecting the diurnal sea surface temperature (SST) warming leads to a global-averaged error of roughly 4.5 W m^{-2}. Brunke et al. (2011) indicate that the uncertainties of bulk gradient variables dominate the discrepancies among products. Clayson et al. (2013) showed that the global ocean E and H estimated by SeaFlux have biases of 14 and 6 W m^{-2}, respectively, when compared with ship observations. The main source of uncertainty is

an attribute of the uncertainties in satellite retrievals of near-surface air temperature and humidity. Andersson et al. (2011) showed that the discrepancies of global ocean E estimates between HOAPS and other satellite-derived products primarily results from those of near-surface humidity among data products. The low uncertainties of OAFlux estimated global ocean E and H reported by Yu et al. (2008) are, however, computed by comparing with only 107 buoy measurements. On the other hand, Gleckler and Weare (1997) estimated a zonal mean error of 25 W m^{-2} in the BTM estimated E over oceans obtained by direct comparison with ship observations.

Kiehl and Trenberth (1997), as well as earlier studies, estimated global annual mean H as a residual of surface energy balance equation (Eq.(2.3)). These H estimates remain highly uncertain resulting from the uncertainties of R_n^S, R_n^L, and E. The global annual mean H estimated by Kiehl and Trenberth (1997) is 24 W m^{-2}, while other earlier estimates ranges from 16 to 27 W m^{-2}. Trenberth et al. (2009) reported a lower global mean H of 17 W m^{-2}, which mainly results from the lower estimates of R_n^S, as compared to Kiehl and Trenberth (1997). Jiménez et al. (2011) showed a spread of ~20 W m^{-2} in the global land H obtained from different datasets.

Most recent observation-based estimates of global annual mean H are obtained by the BTM using observed temperature gradient and wind speed. The errors and uncertainties of BTM estimated H are considerable due to those of model inputs and parameters as discussed in Section 2.3.1. For example, Gleckler and Weare (1997) estimated a systematic error greater than 10 W m^{-2} in global ocean H against ship measurements largely resulting from the utilized parameterizations. Stephens et al. (2012a) reported an uncertainty of 7 W

m^{-2} in global annual mean H evaluated by the range of multiple estimates. They further concluded that "No definitive measure of the uncertainty of this flux exists and the uncertainty range given merely reflects a judgement on where the value most likely lies.". Table 2.1 lists the reviewed estimates of global annual mean E and H with the corresponding uncertainties (if available).

Table 2.1: Observation-based estimates of global annual mean surface energy budgets reviewed in this study (mean ± uncertainty / [min max] in W m^{-2}). *: See list of abbreviations for the source datasets.

Reference or Products Name	R_n^S	R_n^L	E	H	Source Datasets or Model Information
Global					
Kiehl and Trenberth (1997)	168±20	-66±21	78±25	24±10	ERBE, GPCP
Trenberth et al. (2009), 1985-1989	165	-51	-	-	ISCCP-FD
Trenberth et al. (2009), 2000-2004	161	-63	80	17	CERES, GPCP
Stephens et al. (2012a)	165±9	-52±14	88±10	24±7	CERES, ISCCP-FD, GEWEX-SRB, A-train, Cloudsat, GPCP, SeaFlux
L'Ecuyer et el. (2015)	164±7	-58±9	81±4	25±4	CCCM, ISCCP-FD, GEWEX-SRB, GPCP, SeaFlux, Princeton ET, MERRA, GLDAS
Legates (1995)	-	-	78 / [62 89]	-	Gauge Measurements
Ohmura and Gilgen (1993)	142	40	-	-	GEBA
Rossow and Zhang (1995)	165	46	-	-	ISCCP
Zhang et al. (2004)	166	49	-	-	ISCCP-FD
Kato et al. (2012)	169±10	53±7	-	-	CERES
Land					
Trenberth et al. (2009), 1985-1989	147	-58	-	-	ISCCP-FD, GPCP
Trenberth et al. (2009), 2000-2004	145	-80	39	27	CERES, GPCP
L'Ecuyer et el. (2015)	140±12	-69±17	39±4	39±7	CCCM, ISCCP-FD, GEWEX-SRB, Princeton ET, MERRA, GLDAS
Jung et al. (2010)	-	-	38±2	-	*FLUXNET, GIMMS NDVI
Jiménez et al. (2011)	-	-	42 / [37 58]	45 / [31 58]	PMM, PTM, MTE, Empirical
Mueller et al. (2011)	-	-	48±5	-	PMM, PTM, MTE, Empirical
Vinukollu et al. (2011a)	-	-	42 / [37 47]	-	PMM, PTM, SEB
Mueller et al. (2013)	-	-	41±6	-	PMM, PTM, MTE, Empirical
Ocean					
Trenberth et al. (2009), 1985-1989	172	-48	-	-	ISCCP-FD, GPCP
Trenberth et al. (2009), 2000-2004	168	-57	97	12	CERES, GPCP
L'Ecuyer et el. (2015)	178±6	-47±8	89±8	16±4	CCCM, ISCCP-FD, GEWEX-SRB, GPCP, SeaFlux
SeaFlux (Clayson et al., 2013)	-	-	90±14	18±6	*AVHRR, SSMI, CCMP
OAFlux (Trenberth et al., 2009)	-	-	94±7	11±1	*QuickSCAT, AVHRR, SSMI AMSR-E
HOAPs (Trenberth et al., 2009)	-	-	104	15	*AVHRR, SSMI
GSSTF-2 (Chou et al., 2003)	-	-	108	-	*SSMI, NCEP-NCAR

2.4.2 Model-simulation-based Estimates

In this category, global surface energy budgets are estimated via offline LSM (or OSM) or coupled GCM simulations driven by meteorological forcing from atmospheric reanalysis/climate model outputs. Surface radiative fluxes are computed from the given solar constant with a radiation transfer model applied down to the surface. E is commonly parametrized using the PMM (e.g. Liang et al., 1994; Meigh et al., 1999; Balsamo et al., 2009), PTM (e.g., Bondeau et al., 2007; Rost et al., 2008), and BTM (e.g., Takata et al., 2003; Hanasaki et al., 2008; Koirala, 2010). H is estimated by the BTM using the temperature gradient between surface and the lowest level of climate model (e.g., Chen and Dudhia, 2001; Takata et al., 2003). A number of independent model-based estimates of global mean E and H have been provided by several groups, and well reviewed by e.g., Haddeland et al. (2011), Jiménez et al. (2011), Mueller et al. (2013), and Wild et al. (2015). These previous works showed that the model-based estimates are still afflicted with considerable uncertainties for all energy budget components indicated by the wide spread of estimates among products. The main reason responsible for the inter-model discrepancy is the use of different parameterizations and inputs among models (e.g., Kato et al., 2007; Wild, 2008; Muller et al., 2013; Wild et al., 2015). These estimates also have substantial biases relative to ground observations (e.g., Wild, 2008; Wild et al., 2015).

Several studies and international projects sought to determine representative values for each of the surface energy budget component and quantify the corresponding uncertainties. In particular, the Program for Climate Model Diagnosis and Intercomparison (PCMDI) collected outputs from multiple GCMs during 2005-2006. These archived data

constitute phase 3 of the Coupled Model Intercomparison Project (CMIP3) and was released in 2010 (Meehl et al., 2007). The CMIP3 products have been used for preparing the Fourth Assessment Report of the Intergovernmental Panel on Climate Change (IPCC-AR4) (IPCC, 2007).

Wild (2008) verified the current estimates of global annual mean surface radiation fluxes produced by 14 GCMs in CMIP3. The results showed a large variability of global annual mean R_n^S and R_n^L among the 14 GCMs. The ensemble means of global R_n^S and R_n^L as well as the range of the estimates are listed in Table 2.2. The obtained biases of 6 and -5.6 W m^{-2} for R_n^S and R_n^L, respectively, are estimated by the comparison with field observations from 760 sites of the Global Energy Balance Archive (GEBA) and 44 sites of the GEBA/Baseline Surface Radiation Network (BSRN). In the same paper, he also includes the estimates from 20 earlier GCMs provided by the second phase of the Atmospheric Model Intercomparsion Project (AMIP II) (Wild et al., 1998; Wild, 2005). The global mean R_n^S and R_n^L estimated by AMIP II are both lower (in magnitude) than those estimated by CMIP3 (see Table 2.2). Trenberth and Fasullo (2010) point out several key deficiencies in the climate model simulations of CMIP3. For example, CMIP3 overestimates the absorption of solar radiation at mid and high latitudes, but underestimate it in tropics of the Southern Hemisphere caused by the errors of cloud fields.

A new version of CMIP products was released in 2013 known as the phase 5 of the CMIP (CMIP5) (Taylor et al., 2012). CMIP5 uses different climate scenarios from those of CMIP3 for describing the amount of future greenhouse gas. CMIP5 is used in the fifth assessment report of IPCC (IPCC-AR5) (IPCC, 2013). Compared to CMIP3, CMIP5 contains more advanced GCMs. Evaluation of the CMIP5 historical experiments shows

that the simulations of modern climate were improved compared with CMIP3 simulations (Harrison et al., 2015). However, the biases of solar radiation absorption in CMIP3 also present in CMIP5 (Ceppi et al., 2012; Chang et al., 2012; Grise and Polvani, 2014).

Wild et al. (2013) evaluated the global mean surface energy budgets produced by 22 GCMs compiled in the CMIP5 and found that the estimates from different GCMs vary. The mean and range of the reported estimates are listed in Table 2.2. By comparing with ground observations from BSRN, it was demonstrated that most of the models overestimate the downward solar radiation and underestimate the downward longwave radiation. The best estimates from their results are the one that fits best to previous studies (e.g., Stephens et al., 2012a, see Table 2.1). Wild et al. (2015) further expanded the study of Wild et al. (2013) by including more GCMs (total 43) outputs in CMIP5 and examining the global land and ocean surface energy budgets separately. Comparison of results from the two studies are close as shown in Table 2.2. The estimates vary greatly among CMIP5 simulations, for example, with substantial spread in surface radiative fluxes over lands and E and H over oceans (see Table 2.2).

The Global Soil Wetness Project (GSWP) is an ongoing modeling research of the Global Land-Atmosphere System Study (GLASS), a contributing project of the GEWEX (Dirmeyer et al., 1999). A major goal of GSWP includes producing global land surface fluxes, state variables, and other hydrological quantities. Dirmeyer et al. (2006) reported a global surface energy budget produced by 13 LSMs involved in the Second Global Soil Wetness Project (GSWP-2). Table 2.2 clearly shows that the estimates of all surface energy budget components differ largely among models resulting from the utilized model parameterizations.

Many studies provide independent estimates of individual surface energy budget components at global scales, especially E. Mueller et al. (2011) reported an ensemble mean of global land E averaged from 19 LSMs outputs including those from GSWP and the Organising Carbon and Hydrology In Dynamic Ecosystems (ORCHIDEE) and 11 GCMs from IPCC-AR4. The ensemble means estimated from GSWP/ORCHIDEE and IPCC-AR4 LSMs differ by ~5 W m^{-2}. The standard deviations of the two groups of estimates are both ~5 W m^{-2} (see Table 2.2). Haddeland et al. (2011) compared the global land E simulated by six LSMs and five global hydrological models (GHMs) involved in the Water Model Intercomparison Project (WaterMIP) for a 15-year period (1985-1999). The results showed a range of 33 to 46 W m^{-2} even all models were run at the same spatial resolution and driven by the same meteorological data. Jiménez et al. (2011) showed a spread of ~9 and ~15 W m^{-2} for global land E and H produced by four offline LSM simulations. Previous estimates reviewed in this study are listed in Table 2.2.

Table 2.2: Global annual mean surface energy budgets estimated by offline land surface model simulations reviewed in this study (mean ± uncertainty / [min max] in W m^{-2})

Name	R_n^S	R_n^L	E	H	Reference
Global					
AMIP II	154	-51	-	-	Wild (2008)
CMIP3	162 / [149 172]	-56 / [-64 -40]	-	-	Wild (2008)
CMIP5 (22 GCMs)	161 / [159 169]	-55 / [-65 -49]	85 / [78 92]	20 / [14 27]	Wild et al. (2013)
CMIP5 (43 GCMs)	160 / [153 171]	-57 / [-64 -49]	82 / [79 93]	21 / [14 27]	Wild et al. (2015)
Land					
CMIP5	136 / 33 [121 153]	-66 / [-83 -57]	38 / [32 46]	32 / [16 43]	Wild et al. (2015)
GSWP, ORCHIDEE	-	-	43±5	-	Mueller et al. (2011)
IPCC-AR4	-	-	48±5	-	Mueller et al. (2011)
GSWP-2	140 / [103 177]	-66 / [-71 -60]	39 / [27 55]	33 / [20 47]	Dirmeyer et al. (2006)
WaterMIP, GHMs	-	-	- / [33 46]	-	Haddeland et al. (2011)
GLASS, NCAR	-	-	- / [36 45]	- / [31 46]	Jiménez et al. (2011)
Ocean					
CMIP5	170 / 21	-53 / [-59 -45]	100 / [94 113]	16 / [6 21]	Wild et al. (2015)

2.4.3 Atmospheric Reanalysis Products

In recent years, global gridded reanalysis datasets produced by incorporating available observations into climate models using data assimilation system (DAS) technique provide an alternative way of comprehensive estimates of global surface energy budgets. Since the first generation of reanalysis systems developed in the mid-1990s, global atmospheric reanalysis data have become indispensable for climate studies (Wang et al., 2011). Four major reanalysis products are currently available, National Oceanic and Atmospheric Administration (NOAA) NCEP, NASA Global Modeling and Assimilation Office (GMAO), European Centre for Medium-Range Weather Forecasts (ECMWF), and Japanese reanalysis (JRA). These reanalysis products are independently and periodically updated using more advanced satellite observations, climate models, and DAS. Below is a brief overview of these reanalysis datasets and the corresponding estimates of global surface energy budgets.

NCEP released its first generation of reanalysis product in the mid-1990s known as the NCEP – National Center for Atmospheric Research (NCEP-NCAR) (Kalnay et al., 1996). The NCEP-NCAR dataset is continuously updated using near real-time observations. The major limitation of the NCEP-NCAR product is its coarse spatial resolution (T62, ~210 km) compared to other reanalysis products. Trenberth et al. (2009) also found an overestimation of global land E in NCEP-NCAR reanalysis as compared to other estimates. The second NCEP reanalysis product, known as the NCEP – Department of Energy (NCEP-DOE), was completed around 2002 using an updated forecast model and DAS (Kanamitsu et al., 2002). The improvements include better physical parameterizations in the forecast model, corrections of assorted errors in the DAS, and

inclusion of additional observations. The NCEP-DOE reanalysis still belongs to the first generation products as it uses a similar DAS and the same GCM (upgraded version) as those used in NCEP-NCAR reanalysis (Kanamitsu et al., 2002; Higgins et al., 2010).

Recently, NCEP released its latest generation of reanalysis product, the climate forecast system reanalysis (CFSR) (Saha et al., 2006, 2010). CFSR is an improved version of NCEP-NCAR and NCEP-DOE as it couples ocean-atmosphere-land system at higher spatial resolution (T382, ~38 km) (Higgins et al., 2010). Other new features and improvements in CFSR have been summarized in (Higgins et al., 2010; Saha et al., 2010; Wang et al., 2011). The NCEP reanalysis products apply three-dimensional variational assimilation (3D-VAR) for the gridpoint statistical interpolation. Wang et al. (2011) provided a comparison of the global surface energy budgets produced by the NCEP reanalysis data products during 1979 to 2008 (see Table 2.3).

The Modern Era Retrospective-Analysis for Research and Applications (MERRA) reanalysis is provided by NASA GMAO with two primary objectives: to incorporate the satellite observations from NASA Earth Observing System and to improve the hydrological simulations in earlier reanalysis products (Lucchesi, 2008, 2012; Rienecker et al., 2011). The MERRA reanalysis data were produced using the GMAO Goddard Earth Observing System (GEOS) version 5 (GEOS-5) (Rienecker et al., 2008; Molod et al., 2012). The GEOS-5 GCM is executed at $0.5^{o} \times 0.67^{o}$ resolution. An incremental analysis updates procedure is applied in the DAS to slowly adjust the model states toward the observed state (Bloom et al., 1996; Rienecker et al., 2011). Previous studies indicate that MERRA has improved skills of reproducing spatial distribution of precipitation, especially related to the tropical oceanic regions as compared to earlier reanalysis products (Bosilovich et al., 2008,

2011). On the other hand, the MERRA-Land, the post processing of MERRA land fields, was produced using corrected precipitation forcing from GPCP data and modified rainfall interception model (Reichle et al., 2011; Reichle, 2012). The results showed that MERRA-Land corrects some known errors in the MERRA surface meteorological fields (e.g., downward shortwave radiation).

The MERRA-2, an updated NASA reanalysis, was recently released with numerous updates and improvements on the DAS, model parameterizations, and observing systems (Bosilovich et al., 2015). For instance, MERRA-2 assimilates observations that are not available to MERRA during the 2010s. Another notable change in MERRA-2 is the assimilation of aerosol observations. An extensive review of the MERRA-2 can be found in (Bosilovich et al., 2015). They also provided a comparison of global surface energy budgets between MERRA and MERRA-2 estimates for the period of 2000 to 2010 (see Table 2.3).

The ERA-15, which is the first generation of ECMWF and was completed in 1996, provides 15 years of reanalysis data from 1979 to 1993 (Gibson et al., 1999). ERA-15 was produced using earlier version of the ECMWF Integrated Forecast Model. As the first generation of reanalysis product, there are several key deficiencies in ERA-15 include the coarse spatial resolution (T106, ~190 km), dry bias over land, excessive precipitation over tropical oceans, and failure of closing global hydrological budget (Rudolf et al., 1996). The ERA-40 completed in 2003 provides a global atmospheric reanalysis of the 45-year period from 1957 to 2002 with higher spatial resolution compared to ERA-15 (T159, ~125 km) (Uppala et al., 2005). Several major improvements were achieved in ERA-40 as it uses updated climate model and directly assimilates satellite radiation data. For example, ERA-

40 estimated precipitation is closer to the Global Precipitation Climatology Centre (GPCC) observations than ERA-15 over South America and Central Africa. The imbalance of global hydrological budgets is significantly reduced in ERA-40. Yet the wet bias of precipitation over tropical oceans remains (Andersson et al., 2005).

The third generation of ECMWF reanalysis, known as the ERA-Interim, uses an improved atmospheric model and DAS than those used in ERA-40 (Simmons et al., 2007; Uppala et al., 2008; Dee et al., 2011). Unlike ERA-40, which is limited to a 45-year period (1957-2002) without further update, ERA-Interim is extended back to 1979 and continuously updated in near-real-time. ERA-Interim has higher spatial resolution (T255, ~80 km) compared to ERA-40. The DAS in ERA-Interim is based on a 12-hourly four-dimensional variational analysis (4D-VAR), while 3D-VAR was used in ERA-40. The too-strong precipitation over oceans from the early 1990's in ERA-40 was reduced but still greater than GPCP observations, especially over tropical regions (Dee et al., 2011). The estimates of global surface energy budgets from ERA-40 and ERA-Interim are listed in Table 2.3. The estimates from ERA-15 were excluded as it only covers a short period (15 years) with several well-documented issues mentioned previously (Kallberg, 1997; Uppala et al., 2005).

The first generation of JRA reanalysis is the JRA-25 providing 25-year products from 1979 to 2004 with T106 spatial resolution (~110 km) (Onogi et al., 2007). JRA-25 was completed using the numerical assimilation and forecast system from Japan Meteorological Agency (JMA). The observational and satellite data used in JRA-25 were collected from multiple sources including ECMWF, the NOAA National Climatic Data Center (NCDC, now National Centers for Environmental Information, NCEI), and the

Meteorological Research Institute of JMA (JMA-MRI). JMA continued the production on a real-time basis until January 2014 using the same DAS as used for JRA-25. Trenberth et al. (2009) showed that the global ocean E estimated by JRA is 14 W m^{-2} greater than that estimated by NCEP-NCAR reanalysis product. They also found that JRA produces higher E, H, and LWu when compared with other reanalysis products, which results in a negative net surface flux over oceans (i.e., ocean gains energy at annual scale). Onogi et al. (2007) indicate that one of the unsolved problems of JRA-25, as with all reanalysis products, are the jumps in the analyzed meteorological fields caused by absence/sudden change of available observations and large inconsistency between forecast and observed fields. For example, JRA-25 precipitation has a stepwise shift when the Special Sensor Microwave Imager (SSMI) retrieved total column water vapor becomes available for assimilation (Onogi et al., 2005).

The second generation of Japan reanalysis, JRA-55, provides a 55-year data from 1958 to 2012 using a more sophisticated atmospheric model and newly available and reprocessed past observations (Kobayashi et al., 2015; Harada et al., 2016). JRA-55 has been continuing in near-real-time since 2013. Compared to JRA-25, JRA-55 uses more advanced DAS (4D-VAR vs. 3D-VAR) and an increased model resolution (T319, ~55 km). Major improvements in JRA-55 (e.g., reduced bias in Amazonian rainfall) and several notable persist biases (e.g., dry bias in the upper and middle troposphere) are summarized in Kobayashi et al. (2015) and Harada et al. (2016). The estimates of global surface energy budgets from JRA-25 and JRA-55 have been reported in previous publications (Trenberth et al., 2009; Kobayashi et al., 2015) and summarized in Table 2.3. Note that the estimates

of global surface energy budgets from JRA-25 are adapted from Kobayashi et al. (2015) using the more recent data (2002-2008).

In addition to the four reanalysis products listed above, GLDAS is another important reanalysis product that provides estimates of land surface fluxes and water and energy storage (Rodell et al., 2004). The GLDAS products contain the assimilated outputs from four offline simulations of LSMs (Chen et al., 1996; Ek et al., 2003; Dai et al., 2003; Liang et al., 1994; Koster and Suarez, 1996) using satellite and ground-based observations with the NCEP Global Data Assimilation System (GDAS) (Derber et al., 1991). GLDAS currently has 39 (17) years data from 1979 (2000) to present with $1^{o}\times1^{o}$ ($0.25^{o}\times0.25^{o}$) resolution. The estimates of global surface energy budgets from GLDAS were reported by Mueller et al. (2011) and listed in Table 2.3.

Intercomparisons and validation of the existing reanalysis products have been well-summarized (e.g., Hagemann et al., 2005; Trenberth et al., 2009; Vinukollu et al., 2011a; Zaitchik et al., 2010; Berrisford et al., 2011; Bosilovich et al., 2011; Jiménez et al., 2011; Kennedy et al., 2011; Mueller et al., 2011, 2013; Rienecker et al., 2011; Reichle et al., 2011; Yi et al., 2011; Wang et al., 2011; Reichle, 2012; Roberts et al., 2012; Wang and Dickinson, 2012; Bosilovich et al., 2015; Kobayashi et al., 2015). These studies showed that different reanalysis products yield very different estimates of surface energy components arguably resulting from the great diversity of GCMs, meteorological forcing data, and DAS. No one reanalysis is representative of all products for all surface energy budget components. The reanalysis estimates are consistently associated with considerable biases and errors when compared with observations at various spatial and temporal scales, especially for surface heat fluxes.

Table 2.3: Global annual mean surface energy budgets estimated by reanalysis data products reviewed in this study (mean ± uncertainty in W m-2)

Data Products	R_n^S	R_n^L	E	H	Resolution	Period	References
Global							
NCEP-NCAR	161	-61	81	16			
NCEP-DOE	160	-57	91	8			
CFSR	167	-57	84	16	0.5°×0.5°		
MERRA	169	-63	76	18		2000-2010	
MERRA-2	163	-63	86	19		2000-2010	
ERA-40	155	-54	82	16	1.125°×1.125°	1989-2001	
ERA-Interim	164	-57	84	17	0.75°×0.75°	1989-2008	
JRA-25	172	-72	91	20	1.125°×1.125°	2002-2008	
JRA-55	164	-62	93	20	0.5°×0.5°	2002-2008	
Land							
NCEP-NCAR	153	-73	51	26			
NCEP-DOE	143	-71	52	13			
CFSR	140	-66	38	35	0.5°×0.5°		
MERRA	150	-70	45	33	0.5°×0.67°	2000-2004	Bosilovich et al. (2011)
ERA-40	134	-65	41	26	1.125°×1.125°	1985-1989	Trenberth et al. (2009)
JRA-25	156	-87	39	27	1.125°×1.125°	2000-2004	Trenberth et al. (2009)
GLDAS	-	-	37	-	0.25°×0.25°	1989-1995	Mueller et al. (2011)
NCEP-NCAR, JRA-25, MERRA, MERRA-Land, ERA-Interim	-	-	50±5	-	-	1989-1995	Mueller et al. (2011)
JRA, MERRACFSR, ERA-Interim	-	-	45±4	-	-	1989-2005	Mueller et al. (2013)
Ocean							
NCEP-NCAR	165	-56	94	11			
NCEP-DOE	167	-51	106	6			
CFSR	178	-54	103	9	0.5°×0.5°		
MERRA	177	-62	90	12	0.5°×0.67°	2000-2004	Bosilovich et al. (2011)
ERA-40	164	-51	102	16	1.125°×1.125°	1985-1989	Trenberth et al. (2009)
JRA-25	175	-68	109	17	1.125°×1.125°	2000-2004	Trenberth et al. (2009)

CHAPTER 3. A COUPLED MODEL OF SURFACE TEMPERATURE, SURFACE SOIL MOISTURE, AND NEAR-SRUFACE AIR TEMPERATURE BASED ON THE FORCE-RESTORE AND MEP MODEL

3.1 Motivation

The performance of LSMs can be enhanced by improving the predictions of surface temperature T_s, soil moisture θ_s, and surface heat fluxes, which provide the information of surface energy and water budgets. An improved parameterization of near-surface air temperature T_a is useful for more quantitative understanding of recent climate change. However, the existing parameterizations with well-documented drawbacks (Sections 2.2 and 2.3) leave more room for further improvement.

The force-restore method (FRM) for predicting T_s and θ_s has been incorporated into LSMs owing to its computational efficiency and realistic physical interpretation compared to other methods as discussed in Section 2.2.1. Mihailović et al., (1999) showed that the FRM of T_s (FRM_{Ts}) are highly sensitive to the model inputs and parameters, especially (ground) heat flux Q which is difficult to measure/estimate accurately given existing technologies/methods. Gao et al. (2004) and Kahan et al. (2006) found that the current FRM_{Ts}s tend to overestimate the diurnal variation of T_s resulting from the biased Q estimates. Gao et al. (2008) pointed out that using a Q estimated by the residual of surface energy balance equation as in Eq. (2.1) in the FRM_{Ts} may lead to more modeling errors caused by the uncertainties in surface net radiation R_n, latent heat E, and sensible

heat H fluxes. On the other hand, neglecting the gravitational drainage in the current $FRM_{\theta s}$s could produce significant modeling error under high soil moisture conditions as discussed in Section 2.2.2. These previous works suggest that the performance of FRMs may be enhanced by improving the parameterization of surface heat fluxes.

In this study, a coupled FRM of T_s, θ_s, and T_a will be formulated where the surface heat fluxes are parameterized using the MEP model (Wang and Bras, 2009, 2011), referred to as the FRMEP model. The classical FRM of θ_s ($FRM_{\theta s}$) was reformulated based on the Richards equation taking the gravitational drainage into account to improve the prediction of θ_s under wet soil conditions. A FRM of T_a (FRM_{Ta}) will be derived based on a one-dimensional heat diffusion equation analogous to the FRM of T_s (FRM_{Ts}). By incorporating the MEP model of surface heat fluxes, the FRMEP model simulates the dynamics of T_s, θ_s, and T_a driven by surface net radiation and precipitation or infiltration without relying on other atmospheric variables. The expected improvement of the FRMEP model, as compared to the classical FRMs forced by observed or BTM parameterized heat fluxes, results from the advantages of the MEP parameterized surface heat fluxes as discussed in Section 2.3.2. Specifically, the MEP modeled heat fluxes are expressed as functions of the state variables of the FRMs. The measurement error of surface net radiations is on the order of 10% (Michel et al., 2008) or 10-25 W m^{-2} (Kohsiek et al., 2007) less than those of measured and BTM estimated surface heat fluxes that drive classical FRMs.

The model formalisms of FRM_{Ts}, revised $FRM_{\theta s}$, and FRM_{Ta} are given in Section 3.2. The MEP model of surface heat fluxes over land surfaces is given in Section 3.3. The

BTM of surface heat fluxes used in the classical FRM simulations is given in Section 3.4. Section 3.5 provides the site information of the two field experiments used to evaluate the FRMEP model with contrasting climate and soil wetness conditions. Section 3.6 presents validation of the FRMEP model. The predictions of the FRMEP model are compared with those of the classical FRM_{Ts} and $FRM_{\theta s}$ forced by observed and BTM heat fluxes. The effect of neglecting the gravitational drainage term in $FRM_{\theta s}$ is analyzed by replacing the revised $FRM_{\theta s}$ by the classical $FRM_{\theta s}$ (neglecting the gravitational drainage) in the coupled model simulations. A one-year simulation of the FRMEP model is also presented to test the FRMEP model for capturing the seasonal variations of T_s, θ_s, and T_a. Section 3.7 gives a brief summary of the FRMEP model.

3.2 Force-Restore Model (FRM) of Primary Surface State Variables

3.2.1 The FRM of Surface Temperature (FRM_{Ts})

The heat transfer in a vertically homogeneous soil is usually described by a one-dimensional heat diffusion equation:

$$\rho_s c_s \frac{\partial T}{\partial t} = \lambda_s \frac{\partial^2 T}{\partial z^2} \tag{3.1}$$

where $T = T(z,t)$ is the soil temperature (K) at depth z and time t, ρ_s the soil bulk density (kg m^{-3}), c_s the specific heat of soil (J kg^{-1} K^{-1}), λ_s the thermal conductivity of the soil (J m^{-1} K^{-1} s^{-1}), and z the vertical coordinate positive downward (m) with the ground at z = 0. Assuming a sinusoidal function of surface soil temperature,

$$T(0,t) = \bar{T} + A_T sin(\omega_0 t + \epsilon) \tag{3.2}$$

where $\bar{T}$ is the reference temperature set to be the deep soil temperature or daily mean surface temperature (K) according to the assumption of homogeneous soil temperature profile (Bhumralkar, 1975; Hu and Islam, 1995), A_T the amplitude of diurnal variation at the surface (K), ω_0 the fundamental diurnal frequency (= $2\pi/\tau$ (s^{-1}), τ the length of day), and ϵ the initial phase. Based on Eq.(3.2), the solution of Eq. (3.1) may be written as

$$T(z,t) = \bar{T} + A_T e^{-\frac{z}{d_T}} sin\left(\omega_0 t + \epsilon - \frac{z}{d_T}\right) \tag{3.3}$$

where $d_T = (2\lambda_s/\rho_s c_s \omega_0)^{1/2}$ is the damping depth of diurnal temperature wave (m) (Sellers, 1965; Hu and Islam, 1995).

The heat flux into the soil is given by Fourier's law:

$$Q(z,t) = -\lambda_s \frac{\partial T(z,t)}{\partial z} \tag{3.4}$$

Substituting Eq. (3.3) into Eq. (3.4) leads to

$$Q(z,t) = \frac{\lambda_s A_T}{d_T} e^{-\frac{z}{d_T}} \left[sin\left(\omega_0 t + \epsilon - \frac{z}{d_T}\right) + cos\left(\omega_0 t + \epsilon - \frac{z}{d_T}\right)\right] \tag{3.5}$$

or

$$Q(z,t) = \frac{\lambda_s}{d_T}\left[\frac{1}{\omega_0}\frac{\partial T(z,t)}{\partial t} + T(z,t) - \bar{T}\right] \tag{3.6}$$

An averaged "ground surface temperature" T_g for a thin soil layer δ is defined as

$$T_g = \frac{1}{\delta}\int_0^{\delta} T(z,t)dz \tag{3.7}$$

Integrating Eq. (3.1) over depth δ and using Eq. (3.4) and (3.7) leads to

$$\rho_s c_s \delta \frac{dT_g}{dt} = Q(0,t) - Q(\delta,t) \tag{3.8}$$

Combining Eq. (3.6) with Eq. (3.8), the time evolution of T_g is obtained as

$$\rho_s c_s \delta \frac{dT_g}{dt} = Q(0,t) - \frac{\lambda_s}{d_T}\left[\frac{1}{\omega_0}\frac{\partial T(\delta,\ t)}{\partial t} + T(\delta,t) - \bar{T}\right] \tag{3.9}$$

Assuming $T(\delta,t) \cong T_g$ for a thin soil layer, Eq. (3.9) is re-written as

$$\alpha_T \frac{dT_g}{dt} = \frac{2Q(0,t)}{\rho_s c_s d_T} - \omega_0(T_g - \bar{T}) \tag{3.10}$$

where $\alpha_T = 1 + 2\delta/d_T \cong 1$ when $\delta \ll d_T$. Let δ approach zero (Deardorff, 1978) so that $T_g \longrightarrow T_s$ and expand d_T by its definition, the force-restore equation of T_s governing the variation of T_s at sub-diurnal time scale is obtained as

$$\frac{dT_s}{dt} = \frac{\sqrt{2\omega_0}Q(0,t)}{I_s} - \omega_0(T_s - \bar{T}) \tag{3.11}$$

where $I_s = \sqrt{\rho_s c_s \lambda_s}$ is the thermal inertia of the soil (J m^{-2} K^{-1} s$^{-1/2}$ also known as the thermal inertia unit or tiu). I_s may be parameterized as a function of soil moisture:

$$I_s = \sqrt{I_{ds}^2 + \theta I_w^2} \tag{3.12}$$

where θ is the volumetric soil moisture ($m^3\ m^{-3}$), I_{ds} the thermal inertia of dry soil (tiu), $I_w = \sqrt{\rho_w c_w \lambda_w}$ the thermal inertia of liquid water (tiu) with ρ_w the density (10^3 kg m^{-3}), c_w the specific heat (4.18×10^3 J kg^{-1} K^{-1}), and λ_w the heat conductivity of liquid water (0.58 W m^{-1} K^{-1}). Eq. (3.11) is referred as the force-restore method as the forcing of change T_s by the Q term is modified by the restoring term ($T_s - \bar{T}$). Eq. (3.11) is a linear ordinary differential equation of T_s for given Q. In Eq. (3.11), the forcing term due to Q dominates the amplitude of the diurnal variation of T_s, while the restoring term due to $\bar{T}$ determines the magnitude of T_s.

Specification of $\bar{T}$ has an appreciable effect on the performance of FRM_{Ts} (Mihailović et al., 1999). Both deep soil temperature and daily mean surface temperature were used in previous studies (e.g., Bouttier et al., 1993; Boone et al., 2000; Noilhan and Planton, 1989; Mahfouf and Noilhan, 1991; Noilhan and Mahfouf, 1996). Various selections of $\bar{T}$ in previous studies are related to the assumption of homogeneous soil temperature profile, which are rarities in nature (Ren and Xue, 2004). $\bar{T}$ was usually given as a constant for short-term simulation (e.g., Bouttier et al., 1993; Calvet et al., 1998). For long-term simulations, a time varying $\bar{T}$ is desired to provide the information on temperature seasonality. Mihailović et al. (1999) suggest that it is always possible to select a minimum value of $\bar{T}$ among all possibilities in the restoring force to minimize the deviation of estimated surface energy partitioning from the observations. In this study, $\bar{T}$ is set to be the minimum of deep soil and daily mean surface temperature, which is readily available from either directly measurements or climatological archives.

3.2.2 The FRM of Surface Soil Moisture ($FRM_{\theta s}$)

One-dimensional unsaturated flow in a soil column is described by the Richards equation:

$$\frac{\partial \theta}{\partial t} = \frac{\partial}{\partial z}\left[K(\theta)\frac{\partial \psi(\theta)}{\partial z}\right] - \frac{\partial K(\theta)}{\partial z} \tag{3.13}$$

where θ is the volumetric soil moisture (m^3 m^{-3}), $K(\theta)$ the unsaturated hydraulic conductivity (m s^{-1}), $\psi(\theta)$ the soil water potential (m), and z the vertical coordinate with the same directionality as that defined in Section 3.2.1. The first term represents the unsaturated flow induced by the diffusion process, while the second term is the gravitational drainage. A common parameterization of $K(\theta)$ and $\psi(\theta)$ is (Campbell, 1974; Clapp and Hornberger, 1978; van Genuchten, 1980):

$$K(\theta) = K_{sat}\left(\frac{\theta}{\phi}\right)^{2b+3} \tag{3.14}$$

$$\left|\frac{\psi(\theta)}{\psi_{ae}}\right| = \left[\left(\frac{\theta - \theta_r}{\phi - \theta_r}\right)^{-\frac{1}{m}} - 1\right]^{\frac{1}{n}},\ n = 1 + \frac{1}{b},\ m = 1 - \frac{1}{n} \tag{3.15}$$

where K_{sat} is the saturation hydraulic conductivity (m s^{-1}), ϕ the soil porosity (m^3 m^{-3}) with θ/ϕ the degree of saturation, b the pore size distribution parameter, ψ_{ae} the air entry water potential (m), with θ_r being the residual soil water content (m^3 m^{-3}). The (empirical) estimates of soil hydraulic parameters are adopted from the representative values reported by Clapp and Hornberger (1978). Alternative forms of $K(\theta)$ and $\psi(\theta)$ have been suggested by other studies based on various experiements (e.g., Brooks and Corey, 1964;

Davidson et al., 1969; Tzimopoulos and Sakellariou-Makrantonaki, 1996; Assouline, 1998, 2001; Brutsaert, 2000; Valiantzas, 2011), but they are all empirical.

Deardorff (1977) proposed an FRM of $\theta_s = \theta(0,t)$ as an analogy of FRM_{Ts} (Eq. (3.11)) but without giving the derivation. By neglecting the gravitational drainage term and assuming constant soil parameters, Hu and Islam (1995) provided a derivation of $FRM_{\theta s}$ using simplified Eq. (3.13):

$$\frac{\partial \theta}{\partial t} = D\frac{\partial^2 \theta}{\partial z^2} \tag{3.16}$$

where $D = K(\theta)[\partial\psi(\theta)/\partial\theta]$ is the hydraulic diffusivity ($m^2\ s^{-1}$). By assuming periodic boundary condition similar to Eq. (3.3), a solution of θ is obtained as

$$\theta(z,t) = \bar{\theta} + A_\theta e^{-\frac{z}{d_\theta}} sin\left(\omega_0 t + \epsilon - \frac{z}{d_\theta}\right) \tag{3.17}$$

where $\bar{\theta}$ is a reference soil moisture, A_θ the amplitude of diurnal variation of $\theta(0,t)$, and $d_\theta = (2D/\omega_0)^{1/2}$ the damping depth of diurnal soil moisture fluctuation (m). According to Darcy's law, the water flux F_w associate with the simplified Richards equation (ignoring the drainage term) written as

$$F_w(z,t) = -D\frac{\partial \theta(z,t)}{\partial z} \tag{3.18}$$

Following the same derivation of Eqs. (3.5)-(3.11) and introducing the surface water flux as precipitation less evapotranspiration $F_w(0,t) = P - E$ lead to a force-restore equation of θ_s:

$$\frac{d\theta_s}{dt} = \sqrt{\frac{2\omega_0}{D(\theta_s)}}[P(t) - E(t)] - \omega_0(\theta_s - \bar{\theta}) \tag{3.19}$$

In this study, a revised $FRM_{\theta s}$ is proposed by keeping the drainage term in Eq. (3.13). Eq. (3.13) can be re-written as

$$\frac{\partial \theta}{\partial t} + u\frac{\partial \theta}{\partial z} = D\frac{\partial^2 \theta}{\partial z^2} \tag{3.20}$$

where $u = \partial K(\theta)/\partial\theta$ is the slope of the unsaturated hydraulic conductivity (m s^{-1}). Then the solution of Eq. (3.20) becomes

$$\theta(z,t) = \bar{\theta} + A_\theta e^{-\frac{z-ut}{d_\theta}} sin\left(\omega_0 t + \epsilon - \frac{z-ut}{d_\theta}\right) \tag{3.21}$$

According to Eq. (3.13), the water flux $F_w(z,t)$ keeping the gravitational drainage term becomes

$$F_w(z,t) = -D\frac{\partial \theta(z,t)}{\partial z} + K\big(\theta(z,t)\big) \tag{3.22}$$

Note that a modification of surface water flux $F_w(0,t)$ is made in this study by using infiltration $I - E$ instead of $P - E$ in previous studies since infiltration is not equal to rain rate under ponding condition when the rainfall rate exceeds infiltration. $I - E$ is defined as positive entering the soil. Substituting Eq. (3.21) into Eq. (3.22) and following the same derivations of Eqs. (3.5)-(3.11) with $F_w(0,t) = I - E$ leads to the new $FRM_{\theta s}$:

$$\frac{d\theta_s}{dt} = \left(\frac{u(\theta_s)}{D(\theta_s)} + \sqrt{\frac{2\omega_0}{D(\theta_s)}}\right)[I - E - K(\theta_s)] - \omega_0(\theta_s - \bar{\theta}) \tag{3.23}$$

Similar to the FRM_{Ts}, the forcing term due to surface water flux dominates the amplitude of the diurnal variation of θ_s, while $\bar{\theta}$ determines the magnitude of θ_s. In Eq. (3.23), $\bar{\theta}$ is set to be the daily mean of θ_s. Note that unlike the FRM_{Ts} where $\bar{T}$ can also be set as deep soil temperature according to the assumption of homogeneous soil temperature profile, $\bar{\theta}$ may not be taken as deep soil moisture as the mean soil moisture often increases with depth and reaches saturation when close to groundwater table. $\bar{\theta}$ set equal to saturation tends to "restore" the modeled θ_s toward saturation, which is unrealistic as surface soil moisture does not have that tendency.

The newly derived $FRM_{\theta s}$ includes two additional terms u/D and $K(\theta_s)$ compared to the classical formulation shown in Eq. (3.19) proposed by Deardorff (1977) and Hu and Islam (1995). In fact, Eq. (3.19) is a special case of Eq. (3.23) under the condition of low soil moisture whenever the effect of gravitational drainage is negligible. Contrary to the FRM_{Ts} (Eq. (3.11)), the $FRM_{\theta s}$ (Eq. (3.23)) is a nonlinear differential equation of θ_s for given I and E. Note that the formulations of u and D are based on Eqs. (3.14) and (3.15). Using different formulae of $K(\theta)$ and $\psi(\theta)$ may affect the predictions of $FRM_{\theta s}$. Introducing effective degree of saturation, $(\theta - \theta_r)/(\phi - \theta_r)$ (e.g., Mualem, 1976; Brutsaert, 2000) as a substitute of θ/ϕ, for Eq. (3.14), is one example. Furtehr tests of the sensitivity of the $FRM_{\theta s}$ predictions to various parameterizations of u and D (through $K(\theta)$ and $\psi(\theta)$) are required but not included in this study.

3.2.3 The FRM of Near-Surface Air Temperature (FRM_{Ta})

Previous studies have demonstrated that the diurnal variation of T_a results from the divergence of turbulent transport of sensible heat within the atmospheric surface layer (e.g., Taylor, 1915; Beers, 1944). Over a homogeneous surface, turbulent heat transport is predominantly vertical and described by the Fick's law. As a result, the heat transfer within the atmospheric surface layer may be described by a one-dimensional diffusion equation (e.g., Priestley, 1959; Wang and Bras, 1998):

$$\frac{\partial T_a}{\partial t} = \frac{\partial}{\partial z}\left(K_H \frac{\partial T_a}{\partial z}\right) \tag{3.24}$$

associated with the sensible heat flux H expressed as

$$H(z,t) = -\rho_a C_p K_H \frac{\partial T_a(z,t)}{\partial z} \tag{3.25}$$

where K_H is the turbulent transfer coefficient or eddy diffusivity for heat. A model proposed by Wang and Bras (1998) derived from Eqs. (3.24) and (3.25) and later used in Moghim et al. (2015) estimates T_a diagnostically in terms of a weighted time average (i.e., half-order integral) of H.

The analogy between the heat transfer within the atmospheric surface layer and in the soil can be easily seen by comparing Eqs. (3.24) and (3.25) with Eqs. (3.1) and (3.4). This opens a possibility of utilizing Eqs. (3.24) and (3.25) to develop a FRM of T_a (FRM_{Ta}), which has enhanced physical foundation compared to previous formulae. By following the same derivations of the FRM_{Ts} (Section 3.2.1), a FRM_{Ta} can be formulated as

$$\frac{dT_a(0,t)}{dt} = \frac{\sqrt{2\omega_0}H(0,t)}{I_a} - \omega_1(T_a(0,t) - \overline{T_a}) \tag{3.26}$$

where $\overline{T_a}$ is the air temperature far from the surface or daily mean near-surface air temperature, and I_a the thermal inertia for turbulent heat transfer in the air (tiu) defined as (Wang and Bras, 2009)

$$I_a \equiv \rho_a C_p \sqrt{K_H} \tag{3.27}$$

where K_H is the turbulent diffusivity of the air ($m^2\ s^{-1}$). Similar to FRM_{Ts} (Eqs. (3.27)), the diurnal fluctuation of T_a is dominated by H, while $\overline{T_a}$ specifies the magnitude of T_a. The analogies between FRM_{Ts} and FRM_{Ta} suggest that

$$\frac{\Delta T_s}{\Delta T_a} = \frac{\Delta Q / I_s}{\Delta H / I_a} \tag{3.28}$$

where ΔT_s, ΔT_a, ΔQ, and ΔH are the diurnal amplitude of T_s, T_a, Q, and H, respectively. In practical applications, I_a may be estimated by rearranging Eq. (3.28), which yields

$$I_a = \frac{\Delta T_s}{\Delta T_a} \frac{\Delta H}{\Delta Q} I_s \tag{3.29}$$

Similar to I_s having seasonality dominated by that of soil moisture, I_a in Eq. (3.29) is expected to have seasonal cycle because T_s, T_a, H, and Q all have seasonality. Alternatively, I_a may also be parameterized using the extremum solution of the Monin-Obukhov similarity equations (MOSE) (Wang and Bras, 2010, see also Eq. (3.31)).

Similar to the $\overline{T}$ in FRM_{Ts}, the specification of $\overline{T_a}$ is expected to affect the FRM_{Ta} predicted T_a significantly. A given constant of $\overline{T_a}$ may be good for short-term simulation,

while a time varying $\overline{T_a}$ may be required to provide the information of temperature seasonality. Yet there are no theoretical methods available for specifying $\overline{T_a}$ from previous studies. Therefore, in this study, $\overline{T_a}$ is determined by applying similar strategies as those used for specifying $\bar{T}$ in the FRM_{Ts} based on the analogy between FRM_{Ts} and FRM_{Ta}. Consequently, $\overline{T_a}$ is set to be either daily mean T_a (analogous to daily mean T_s used as $\bar{T}$ in the FRM_{Ts}) or the air temperature far from the surface (e.g., above the top of surface layer analogous to the deep soil temperature used as $\bar{T}$ in the FRM_{Ts}). $\overline{T_a}$ can be estimated offline using the FRM_{Ta} with observed meteorological inputs.

3.2.4 Heat Flux Forcing of the FRMs

The classical FRM_{Ts} and $FRM_{\theta s}$ are forced by ground heat flux Q and net surface water flux, $I - E$ ($P - E$ in previous studies) that are usually obtained from either field measurements (e.g., Lin, 1980; Jacobs et al., 2000; Ren and Xue, 2004; Gao et al., 2008) or model parameterizations (e.g., Deardorff, 1977, 1978; Noilhan and Planton, 1989; Xue et al., 1991; Gao et al., 2004).

The measured Q is usually obtained by combining the soil heat flux directly measured at a certain depth using a heat flux plate with the soil heat storage above the plate obtained by measuring soil temperature (e.g., heat flux plate instruction manual, available at https://s.campbellsci.com/documents/ca/manuals/hfp01_man.pdf). The measurements of soil heat flux are subject to errors caused by the contrasting thermal conductivities of the plate and the surrounding soil, the poor contact between heat flux plate and the soil, the presence of subsurface latent heat sink, and the heat flux bias resulting from liquid and

vapor water movement in the soil (Philip, 1961; Fuchs and Hadas, 1973; Kimball et al., 1976; Mayocchi and Bristow, 1995; Sauer et al., 2003; Sauer et al., 2008; Heitman et al., 2008, 2010). Ochsner et al. (2006) showed that in situ measurements of Q by heat flux plate were in general underestimated caused by the systematic negative sensor bias ranging from 18 to 66% even the heat flux plate is carefully installed. Additionally, the measurement error of soil heat flux increases rapidly with the installation depth of heat flux plate with the maximum error comparable to the magnitude of soil heat flux (Gentine et al., 2012). Measured Q may also be biased by neglecting the time derivative of soil heat capacity as well as the sampling error of the temperature profile for estimating heat storage (Ochsner et al., 2007; Gentine et al., 2012). The overall measurement errors of Q can reach up to 100 W m^{-2} (Foken, 2008).

Measurement error of Q (and H) causes measurement error of E when E is computed from the surface available energy (net radiation $R_n - Q$) using e.g., Bowen-ratio method (Ohmura, 1982; Lewis, 1995) or Penman equation (Penman, 1948). Using in-situ measurements of $R_n - E - H$ as the model forcing in FRM_{Ts} also introduces large uncertainty resulting from the uncertainties of R_n, E, and H measurements (Gao et al., 2008). Although the EC system provides more accurate measurements of E (and H), it is well known that EC measurements in general underestimate the surface available energy by 10-30% (Wilson et al., 2002; Culf et al., 2004; Barr et al., 2006; Mauder and Foken, 2006; Foken et al., 2006; Mauder et al., 2006; Oncley et al., 2007; Foken, 2008).

The modeled Q is often obtained as a residual of the surface energy balance equation, $R_n - E - H$ (Eq. (2.1)), where E and H are parameterized using the BTM (e.g.,

Noilhan and Planton, 1989; Dickinson et al., 1991; Lee and Pielke, 1992). The modeling errors of BTM estimated E and H caused by those of model inputs and parameters (humidity/temperature, wind speed, and transfer coefficients) as well as the failure of closing surface energy budget lead to unrealistic Q as discussed in Section 2.3.1. Thus, the performance of FRM_{Ts} and $FRM_{\theta s}$ may be enhanced by improving the parameterization of surface heat fluxes.

3.3 The MEP Model of Surface Heat Fluxes over Land Surfaces

The MEP theory (Wang and Bras, 2009, 2011) solves latent E, sensible H, and ground Q heat fluxes as the most probable partitioning of R_n while satisfying conservation of energy. According to the MEP theory, the most likely partitioning of surface heat fluxes over land surfaces can be obtained through extremizing the dissipation function D_s expressed as

$$D_s = \frac{2Q^2}{I_s} + \frac{2H^2}{I_a} + \frac{2E^2}{I_e} \tag{3.30}$$

where I_s is the thermal inertia of soil or leaf matrix of canopy (tiu), I_a, and I_e are the thermal inertia parameters related to H and E (tiu). I_a can be parameterized as a function of H through the extremum solution of MOSE (Wang and Bras, 2010) as

$$I_a = \rho_a c_p \sqrt{C_1 \kappa z} \left(C_2 \frac{\kappa z g}{\rho_a c_p T_0} \right)^{\frac{1}{6}} |H|^{\frac{1}{6}} = I_0 |H|^{\frac{1}{6}} \tag{3.31}$$

where ρ_a is the air density (kg m^{-3}), κ the von Kármán constant ~0.4, g gravitational acceleration (m s^{-2}), T_0 a reference temperature (K) set to be 300 K in this study, and z the vertical distance (m) from the material surface above which the MOSE hold. Based on the tests over land surfaces, z may be chosen as 2-3 m for the case of flat bare soil, 4-5 m for the case of short vegetation, and 9-10 m for the case of tall trees. c_p is the specific heat of air under constant pressure (10^3 J kg^{-1} K^{-1}), C_1 and C_2 the parameters related to the universal constant in the empirical functions characterizing the atmospheric stability of the surface layer (Businger et al., 1971), I_0 the "apparent" thermal inertia of the air as an eddy-diffusivity dependent parameter characterizing the boundary layer turbulence. Note that Eqs. (3.31) and (3.27) become identical when K_H in Eq. (3.27) is parameterized using the extremum solution of MOSE.

Assuming the same turbulent mixing process is responsible for both heat and moisture transport in the atmospheric surface layer, I_e can be parameterized as (Wang and Bras, 2011)

$$I_e = \sigma I_a = \frac{L_v^2 q_s}{c_p R_v T_s^2} I_a \tag{3.32}$$

where q_s is the surface specific humidity (kg kg^{-1}), σ a dimensionless parameter characterizing the surface thermal and moisture condition on the partition of surface net radiation into the heat fluxes, L_v the latent heat of vaporization of liquid water (2.5×10^6 J kg^{-1}), and R_v the gas constant of water vapor (461 J kg^{-1} K^{-1}).

By extremizing Eq. (3.30) with the parameterization of I_a and I_e in Eqs. (3.31) and (3.32) under the constraint of surface energy balance as in Eq. (2.1) leads to a unique solution of Q, E, and H as (implicit) analytical functions of R_n, T_s, and q_s expressed as

$$\begin{cases} \left[1 + B(\sigma) + \dfrac{B(\sigma)}{\sigma}\dfrac{I_s}{I_0}|H|^{\frac{-1}{6}}\right]H = R_n \\ E = B(\sigma)H \\ Q = R_n - E - H \end{cases} \tag{3.33}$$

with

$$B(\sigma) = 6\left(\sqrt{1 + \frac{11}{36}\sigma} - 1\right) \tag{3.34}$$

where $B(\sigma)$ is recognized as the reciprocal Bowen ratio. For the limiting case of dry soil, for example, vanishing σ ($q_s = 0$) from zero soil moisture leads to $E = 0$ (as $B(\sigma) = 0$), i.e., the obvious solution of zero evaporation over dry soil. For the limiting case of saturated soil, q_s becomes the saturated specific humidity at T_s and σ becomes Δ/γ with Δ the slope of the saturation water vapor pressure curve at T_s, and γ the psychometric constant (e.g., Allen et al., 1998). The corresponding E is the potential evapotranspiration by definition. For soil surface, I_s is estimated using Eq. (3.12). For canopy or dense forest land cover, I_s is negligible since the thermal inertia of leaf matrix is two orders of magnitudes smaller than that of soil. Note that the MEP model only uses R_n and T_s data for the case of saturated land surfaces (e.g., saturated soils, irrigated farm lands and canopy under no water stress) where q_s is a function of T_s alone according to the Clausius-Clapeyron equation. It can be shown that the solutions of E, H, and Q, from the nonlinear algebraic equations in Eq. (3.33), are unique.

The MEP modeled heat fluxes, as the partition of given radiative fluxes automatically, close the surface energy budget by definition. In addition, the effect of horizontal advection of thermal energy, momentum and moisture on the surface energy budgets is represented by the given surface variables R_n, T_s, and q_s in the MEP model. Therefore, the MEP model, as an inference algorithm as well as a physical principle, allows the heat fluxes to be retrieved from surface net radiation, temperature, and/or humidity without using temperature and humidity gradients, wind speed, and surface roughness data. However, *its independence of these variables should not be interpreted as temperature/humidity gradients, wind speed and surface roughness playing no role in the corresponding transport processes*. The absence of these variables in the MEP formalism reflects strong and effective surface-atmosphere interactions so that the surface radiation fluxes together with surface temperature and/or humidity contain essential and sufficient information for the retrieval of surface heat fluxes. Using the extremum solution of MOSE (Wang and Bras, 2010), the temperature gradient and wind speed (or wind shear) are expressed as analytical functions of sensible heat and momentum fluxes, hence can be eliminated in the parameterization of eddy-diffusivity (through I_0 in Eq.(3.31)) in the MEP formalism.

The MEP modeled Q and E may be expressed as functions of R_n, T_s, and θ_s when q_s is parameterized in terms of θ_s and/or T_s. A general expression of q_s is

$$q_s = \alpha(\theta_s, T_s) q_{sat}(T_s) \tag{3.35}$$

where $q_{sat}(T_s)$ is the saturation surface specific humidity at T_s (kg kg^{-1}), and α the wetness function characterizing water transport from inner soil pores to the soil surface. Lee and

Pielke (1992) summarized various formulations of α. The most commonly used parameterization of q_s is the Philip's formula derived from the thermal equilibrium of vapor-liquid water in the soil (Philip, 1957). The Philip's formula had been shown unable to represent the effect of the resistance of water transport from the soil pores to the soil-atmosphere interface (Wetzel and Chang, 1987; Avissar and Mahrer, 1988; Kondo et al., 1990). Theoretically, the assumption of thermal equilibrium does not hold because of the latent heat processes over land surfaces. Other formulae of q_s are mostly obtained empirically for specific soil types or by assuming a simple linear relationship between α and the ratio of soil moisture to field capacity (e.g., Deardorff, 1978; Noilhan and Planton, 1989; Lee and Pielke, 1992).

In this study, an alternative parameterization of α is proposed based on an analogy of soil moisture dependence on the ratio of actual evapotranspiration to potential evapotranspiration (e.g., Mintz and Walker, 1993; Seibert, 1997),

$$\alpha = \left(\frac{\theta}{\phi}\right)^{\beta} \tag{3.36}$$

where β is a soil texture dependent parameter. Eq. (3.36) represents the relative soil wetness that determines the corresponding deduction of q_s from saturation condition $q_{sat}(T_s)$. Parameterization of α as in Eq. (3.36) satisfies the physical constraints of q_s, that is, q_s reaches its upper limit $q_{sat}(T_s)$ when soil is saturated ($\theta = \phi$) and becomes zero when soil is completely dry (e.g., Lee and Pielke, 1992). Since direct observations of q_s (i.e., specific humidity right above the surface) are currently unavailable, β may be

estimated offline by fitting the MEP modeled fluxes to the observed fluxes with q_s and α parameterized using Eqs. (3.35) and (3.36), respectively.

Incorporating the MEP model of surface heat fluxes (Eq. (3.33)) into the FRM equations (Eqs. (3.11), (3.23), and (3.26)) leads to a fully coupled model for predicting T_s, θ_s, T_a as well as surface heat fluxes, i.e., the FRMEP model. Figure 3.1 shows the framework of the FRMEP model.

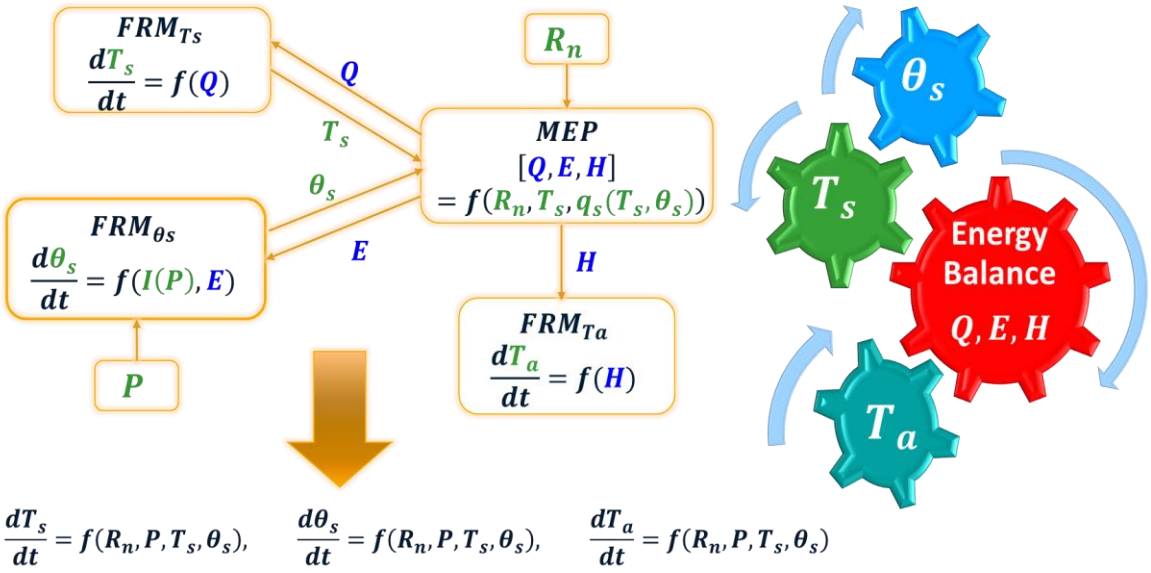

Figure 3.1: The framework of the FRMEP Model

3.4 The Bulk Transfer Model of Surface Heat Fluxes

The BTM of E and H are formulated as (e.g., Leovy, 1969; Lee and Pielke, 1992)

$$E_{BTM} = L_v \rho_a C_E U (q_s - q_a) \tag{3.37}$$

$$H_{BTM} = \rho_a c_p C_H U (T_s - T_a) \tag{3.38}$$

where C_E and C_H are the bulk transfer coefficients of water vapor and heat (-) assumed to be identical, and U the wind speed (m s^{-1}). C_E and C_H are parameterized following (e.g., Andreas and Murphy, 1986; Beljaars and Holtslag, 1991) with the stability functions and the empirical constants given by (Paulson, 1970; Businger et al., 1971), q_a and T_a the air specific humidity (kg kg^{-1}) and temperature (K), respectively. Q_{BTM} is computed as the residual term of the surface energy balance equation

$$Q_{BTM} = R_n - E_{BTM} - H_{BTM} \tag{3.39}$$

The T_s, θ_s, and T_a predicted by the classical FRMs using BTM heat fluxes can be obtained by substituting Eqs. (3.37), (3.38), and (3.39) into Eqs. (3.11), (3.26), and (3.23), respectively.

3.5 Datasets

Tests of the FRMEP model were conducted using field experimental data from two sites with contrasting climatic and soil wetness conditions. The Lucky Hills Site (LH) is located in the Walnut Gulch Experimental Watershed in southern Arizona (Keefer et al., 2008). The climate is semiarid with a three-month monsoon season from July to September. The dominant soil type is sandy loam covered with open shrubs of about one-meter height. The soil moisture remains low (< 0.2 m^3 m^{-3}) except for rainy seasons. $\beta \cong 2$ in Eq. (3.36) was obtained for this site through minimizing the root mean square error (RMSE) between the MEP modeled heat fluxes and observed surface heat fluxes. The soil thermal inertia I_s was estimated as ~1000 tiu according to Eq. (3.12) with the dry soil thermal inertia $I_{ds} \cong$

830 tiu estimated from observed T_s and Q (Wang et al., 2010). I_a was estimated as ~2500 tiu according to Eq. (3.29).

An automatic weather station collected meteorological data with a net radiometer installed at 2.96-meter height since 1990. An EC system was mounted at 6.5-meter height that has collected surface fluxes and hydro-meteorological data since 2008. T_s was measured by an infrared thermometer. Soil temperature and moisture were measured at multiple depths ranging from 5 to 200 cm. Soil heat flux measured at 8 cm depth was used to estimate Q . Long-term (since 1990) datasets are publicly available at www.tucson.ars.ag.gov/dap/ and http://cdiac.esd.ornl.gov/programs/ameriflux/-data_system/aamer.html#Lucky_Hills_Shrubland. Data products with 30-minute resolution over the periods of August 10 to August 28, 2009 with multiple wetting-drying cycles are used. The data spanning year 2009 was selected for the one-year simulation due to its higher data quality.

The Brooks Field site 10 (BF10) is located in central Iowa with temperate continental climate and surrounded by corn/soybean fields. The dominant soil type is silty clay loam with $\beta \cong 0.6$ in Eq. (3.36). An EC system was mounted at 5 m height. T_s was measured by an infrared thermometer. Soil moisture measured at 5 cm depth at this site is relatively high during the growing season (> 0.2 m^3 m^{-3}). More details about the data products can be found online (https://fluxnet.ornl.gov/site/806 and http://cdiac.esd.ornl.-gov/programs/ameriflux/data_system/-aamer.html#BrooksField10). Thirty-minute data products over the periods of June 9 to June 29, 2011 with several major rainy events are used in this study. The thermal inertia of the soil was estimated as $I_s \cong 1250$ tiu using the same method as that for estimating I_s at the LH site. I_a was estimated as ~2000 tiu

according to Eq. (3.29). On the other hand, I_a was estimated as ~1000 tiu for both sites according Eq. (3.31). Thus, to analyze the sensitivity of FRM_{Ta} with respect to the I_a parametrization, the two I_a estimates will be both applied to the FRMEP model.

3.6 Model Validation

3.6.1 Diurnal Variability

3.6.1.1 Dry Condition – Lucky Hills Site, Arizona

Figures 3.2 to 3.4 show the predictions of the FRMEP model and those of the classical FRMs, which are forced by observed and BTM surface heat fluxes, against field observations. The corresponding scatter plots are shown in Figures 3.5 and 3.6. Soil moisture measured at 5 cm depth, θ_{OBS}, was used as the surrogate of θ_s when computing I_s in the FRM_{Ts}^{O} using Eq. (3.12). Soil temperature measured at 200 cm was adapted for $\overline{T}$ in Eq. (3.11) as described in Section 3.2.1. The infiltration rate I in Eq. (3.23) was set to be equal to precipitation rate P obtained from measurements; however, the upper limit for θ_s is set at saturation when modeled θ_s is greater than saturation due to large P (i.e., ponding/runoff presents). $\overline{T_a}$ was set to be ~21 ^{o}C estimated by an offline test of FRM_{Ta} as discussed in Section 3.2.3.

Figure 3.2(a) compares T_s predicted by the FRMEP model and the classical FRM_{Ts} as in Eq. (3.11) forced by observed Q (Q_{OBS}) and Q_{BTM}, denoted as FRM_{Ts}^{O} and FRM_{Ts}^{B}, respectively. Q_{OBS}, Q_{BTM} and the Q predicted by the FRMEP model (Q_{MEP}) are shown in Figure 3.2(b). Figure 3.2(a) shows that the FRMEP modeled T_s agrees more closely with

the observed T_s compared to that by the FRM_{Ts}^{O}. The error statistics of the FRMEP and FRM_{Ts}^{O} are summarized in Table 3.1. The bias of the FRMEP modeled T_s is about 2.0 ºC compared to the bias of -4.3 ºC of the FRM_{Ts}^{O} modeled T_s. The negative bias of FRM_{Ts}^{O} is presumably caused by the large negative nighttime Q_{OBS}. The RMSE of the FRMEP modeled T_s of 5.6 ºC is also lower than that of the FRM_{Ts}^{O} 6.0 ºC. The correlation coefficients, designated as r, between the two modeled T_ss and observations are both high (0.87 for the FRMEP model and 0.92 for the FRM_{Ts}^{O}) indicating that the diurnal variation of T_s is well captured by the FRM_{Ts}.

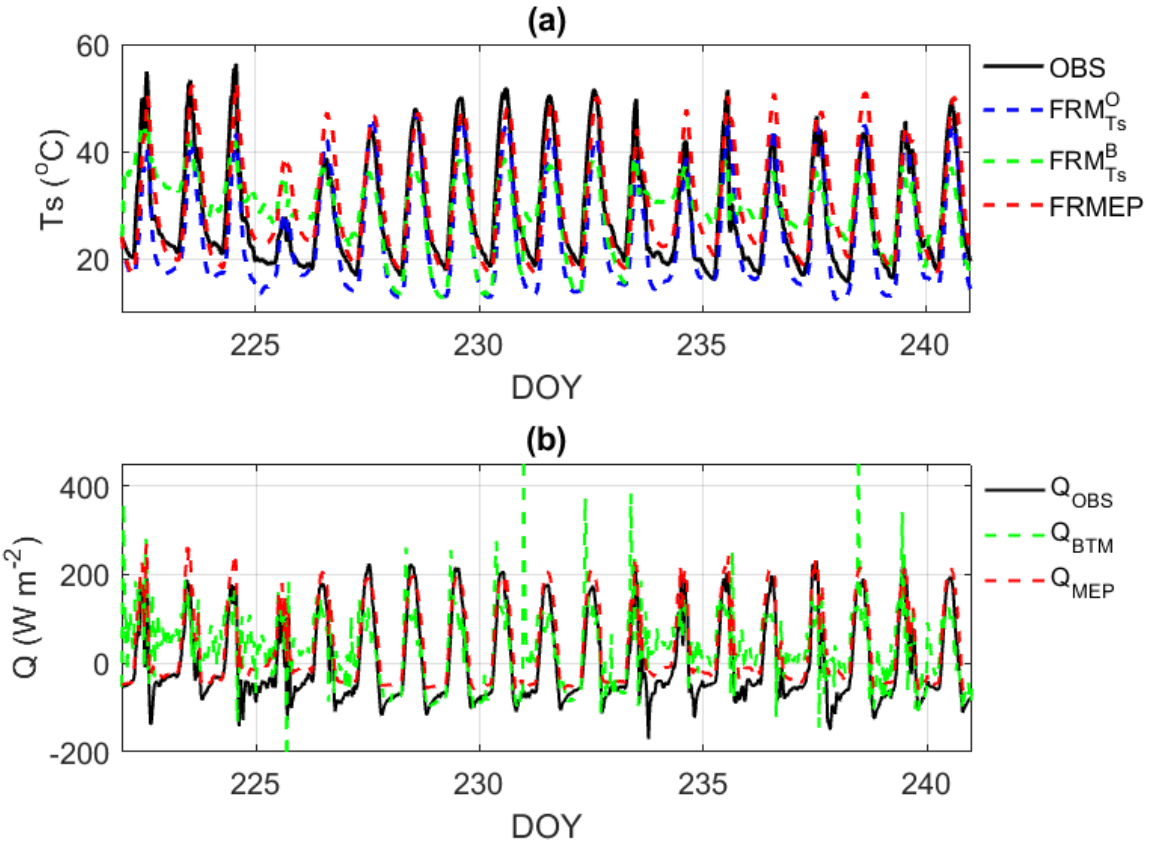

Figure 3.2: (a) T_s predicted by the FRM_{Ts}^{O} (dashed blue), FRM_{Ts}^{B} (dashed green), and the FRMEP model (dashed red) versus observations (solid black), and (b) the modeled Q_{BTM} (dashed green) and Q_{MEP} (dashed red) versus Q_{OBS} (solid black) of the LH site, August 10 to August 28, 2009.

Table 3.1: Error statistics of the FRMEP, FRMEP-ND, and classical FRMs predictions, Lucky Hills Site, Arizona (Unit: T_s(K), θ_s(m^3 m^{-3}), T_a(K), Q, E, and H (W m^{-2}))

	Bias	RMSE	Correlation coef. (r)
T_s	2.0[a] / 2.0[b] / -4.3[c] / 0.4[d]	5.6[a] / 5.6[b] / 6.0[c] / 7.1[d]	0.87[a] / 0.87[b] / 0.92[c] / 0.71[d]
θ_s	0.02[a] / 0.02[b] / -0.01[c] / 0.11[d]	0.03[a] / 0.03[b] / 0.03[c] / 0.12[c]	0.86[a] / 0.86[b] / 0.78[c] / 0.69[d]
T_a	-0.40[a] / -0.41[b] / -0.34[c] / 3.1[d]	2.76[a] / 2.76[b] / 2.76[c] / 6.15[d]	0.81[a] / 0.81[b] / 0.81[c] / 0.30[d]
Q	38.1[a] / 38.0[b] / - / 35.1[d]	49.5[a] / 49.4[b] / - / 85.1[d]	0.95[a] / 0.95[b] / - / 0.64[d]
E	-19.8[a] / -19.6[b] / - / -123.3[d]	40.3[a] / 40.3[b] / - / 243.9[d]	0.85[a] / 0.85[b] / - / 0.59[d]
H	-1.0[a] / -1.0[b] / - / 50.5[d]	36.0[a] / 36.0[b] / - / 193.2[d]	0.93[a] / 0.93[b] / - / 0.66[d]

a: FRMEP vs. OBS
b: FRMEP-ND vs. OBS
c: FRM^O vs. OBS
d: FRM^B vs. OBS

Q_{MEP} is in close agreement with Q_{OBS} as shown in Figure 3.2(b). Q_{MEP} is, in general, slightly greater than Q_{OBS} as shown in Figure 3.6(a) resulting in an overall bias and RMSE of 38.1 and 49.5 W m^{-2}, even though the diurnal variations are well captured (r = 0.95). It is noted that nighttime Q_{MEP} is constrained by R_n, while nighttime Q_{OBS} is greater than the corresponding R_n, violating the surface energy balance. Several possibilities may be responsible for the discrepancy between Q_{MEP} and Q_{OBS}. First, Q_{OBS} is likely underestimated owing to the negative bias of soil heat flux measured by the heat flux plate as discussed in Section 3.2.4. The bias of measured soil heat flux could reach 20% for specific type of heat flux plate, e.g., the HFT3 used at the LH site (Sauer et al., 2003; Scott et al., 2006). Second, the sampling error of temperature profile could lead to an estimation error of heat storage on the order of 10 W m^{-2} (Gentine et al., 2012). Third, the measurement error of Q_{OBS} due to neglecting the time derivative of soil heat storage (calorimetric correction) is about 10 W m^{-2} (Ochsner et al., 2007). Fourth, the heat storage tends to be overestimated (in magnitude) resulting from the overestimation

(underestimation) of the change rate of soil temperature during daytime (nighttime). The use of measured soil temperature at certain depth to estimate heat storage implies a linearly interpolated soil temperature profile extending from surface to the depth of the heat flux plate. It has been shown that the linearly interpolated temperature profile overestimates (in magnitude) the actual rate of soil temperature change, which leads to an approximate 10% overestimation on Q_{OBS} (Yang and Wang, 2008). The effect of heat storage estimation on Q_{OBS} is expected to be stronger during nighttime due to the relatively small magnitude of soil heat flux. More importantly, part of the thermal energy entering the soil for subsurface soil evaporation (subsurface latent heat sink) leads to a consistently underestimated soil heat flux measurements using heat flux plate (Heitman et al., 2008, 2010).

Figure 3.2(a) also shows that the FRMEP modeled T_s agrees more closely with the observed T_s than the FRM_{Ts}^{B} modeled T_s (see also Figures 3.5(a) and 3.5(b)). The FRM_{Ts}^{B} modeled T_s has a comparable magnitude but reduced diurnal amplitude as compared to the observed T_s. The bias of FRM_{Ts}^{B} modeled T_s (0.4 ^{o}C) appears to be smaller compared to that of the FRMEP predicted T_s (2.0 ^{o}C), which is due to the error cancellation as the corresponding RMSE of the FRM_{Ts}^{B} modeled T_s (7.1 ^{o}C) is higher than that of the FRMEP modeled T_s (5.6 ^{o}C). Table 3.1 shows the error statistics of the FRMEP model and the FRM_{Ts}^{B}. The FRMEP modeled T_s has higher correlation with the observed T_s than the FRM_{Ts}^{B} modeled T_s (0.87 vs. 0.71). The FRM_{Ts}^{B} predicted T_s driven by Q_{BTM} has unrealistic fluctuations on day 222 to 225 and day 234 to 237 (Figures 3.2(b) and 3.6(b)). The modeling errors of Q_{BTM}, calculated using Eq. (3.39), are caused by those of E_{BTM} and H_{BTM} according to Eqs. (3.37) and (3.38). The modeling errors of E_{BTM} and H_{BTM} in Eqs. (3.37) and (3.38) is attributed to the uncertainties of bulk gradients of

temperature/humidity, wind speed and transfer coefficients C_E and C_H. Compared to Q_{BTM}, Q_{MEP} has bounded modeling errors, which are less than the measurement errors of R_n.

Figure 3.3(a) shows the θ_s predicted by the FRMEP model and that by Eq. (3.23) driven by observed E (E_{OBS}) and E_{BTM} against θ_{OBS} with the 30-min rainfall P displayed on the top of the figure. The terms $FRM_{\theta s}^{O}$ and $FRM_{\theta s}^{B}$ denote the FRMs as in Eq. (3.23) driven by E_{OBS} and E_{BTM}, respectively. The corresponding scatter plots of the FRMEP and the $FRM_{\theta s}^{B}$ predicted θ_s versus observations are shown in Figures 3.5(c) and 3.5(d), respectively. $\bar{\theta}$ was taken as the daily mean of θ_s prior to the current simulation time. The comparison of the FRMEP modeled E (E_{MEP}) and E_{OBS} is shown in Figure 3.3(b). The FRMEP modeled θ_s agrees closely with θ_{OBS} and accurately captures the wetting-drying cycles with r = 0.86 (see also Figure 3.5(c)). Table 3.1 shows that the bias and RMSE of the FRMEP modeled θ_s are 0.02 and 0.03 m^3 m^{-3}, respectively, within the measurement error ~0.02-0.05 m^3 m^{-3} (Keefer et al., 2008).

The good agreement between E_{MEP} and E_{OBS} is evident in Figures 3.3(b) and 3.6(c). The bias of -19.8 W m^{-2} of E_{MEP} is likely caused by the potentially overestimated E_{OBS} during nighttime, dry soil condition, and rainy period. The nighttime E_{OBS} was positive most of the time, which is inconsistent with the corresponding negative nighttime R_n. A negative nighttime R_n corresponds to a strong radiative cooling of land surfaces that favors dew formation or negative E. It is well known that EC measurements during nighttime may not fully capture the turbulent fluxes under low winds and stable surface layer condition (Burda, 2013). EC measured E under dry soil condition (θ_{OBS} < 0.1 m^3 m^{-3} below the wilting point) is likely to be overestimated as eddy fluxes of water vapor in

such a condition do not come from evapotranspiration. EC measured E usually produces significant errors during rain events (e.g., Berbigier et al., 2001; Nordbo et al., 2012). In addition, EC measured E during rain events is likely a result of high atmospheric humidity (and its fluctuations) instead of high evaporation rates.

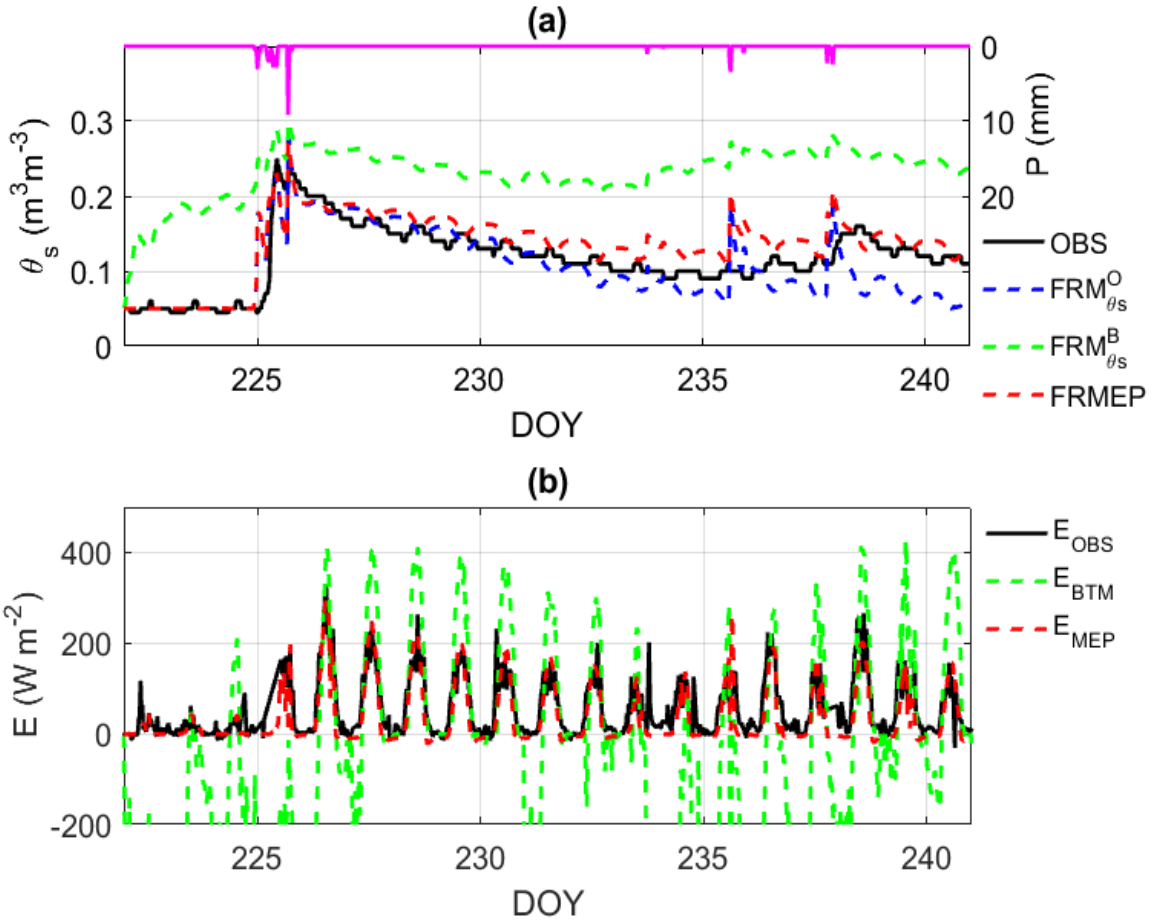

Figure 3.3: (a) θ_s predicted by the $FRM^O_{\theta s}$ (dashed blue), $FRM^B_{\theta s}$ (dashed green), and the FRMEP model (dashed red) versus observations (solid black) with precipitation P on the top, and (b) the modeled E_{BTM} (dashed green) and E_{MEP} (dashed red) versus E_{OBS} (solid black) of the LH site, August 10 to August 28, 2009.

Compared to the FRMEP model, the $FRM^O_{\theta s}$ predicted θ_s begins deviating from θ_{OBS} on day 235 as shown in Figure 3.3(a). The growing discrepancy between the $FRM^O_{\theta s}$ predicted θ_s and θ_{OBS} appears to be caused by the potentially overestimated E_{OBS}, leading

to the negative bias of the θ_s predicted by the $FRM_{\theta s}^{O}$. The effect of using overestimated E_{OBS} in the $FRM_{\theta s}^{O}$ accumulates with time and eventually dominates the dynamics of θ_s after day 236, leading to a significant underestimation of modeled θ_s against θ_{OBS} as shown in Figure 3.3(a). The smaller bias of the θ_s predicted by the $FRM_{\theta s}^{O}$ compared to that predicted by the FRMEP model is mainly attributed to its closer agreement with θ_{OBS} before day 235. However, the goodness of the FRMEP and $FRM_{\theta s}^{O}$ modeled θ_s against θ_{OBS} before day 235 is difficult to quantify because the discrepancies between the two modeled θ_ss and θ_{OBS} are both within the measurement errors (0.02-0.05 m^3 m^{-3}). It is noted that the classical $FRM_{\theta s}$ predicted θ_s starts to deviate from θ_{OBS} after a longer no-rain period (after day 235 in Figure 3.3(a)), while the FRMEP modeled θ_s follows θ_{OBS} more closely.

Figure 3.3(a) shows that both the $FRM_{\theta s}^{O}$ and the FRMEP model capture the rain events as indicated by the rapid increase of modeled θ_s. The increase of modeled θ_s during rainy periods is generally greater than that of θ_{OBS}. For example, one millimeter of rainfall on day 234 leads to a 0.05 m^3 m^{-3} increase in modeled θ_s, while θ_{OBS} remains unchanged. Two possible reasons may be responsible for the different sensitivities of modeled θ_s and θ_{OBS} to precipitation. First, the $FRM_{\theta s}$ theoretically simulates the "skin" soil moisture, while θ_{OBS} is always an averaged soil moisture over a certain depth/region due to the finite size of soil moisture sensors. For example, θ_{OBS} at the LH site is measured by the TDR100 and Steven's Hydra Probe centered at 5 cm below the surface with a 3 cm of sensing volume (cylindrical measurement region). As a result, the variation of θ_s is expected to be greater than that of θ_{OBS} for the same rainfall as the depth of θ_s is closer to surface. Second,

the soil moisture change due to low rain rates may not be detected by a soil moisture sensor buried beneath the surface. For example, one millimeter rainfall increases the averaged soil moisture by 0.02 m^3 m^{-3} for a 5 cm soil column, which is smaller than the accuracy of soil moisture sensor.

θ_s predicted by the $FRM_{\theta s}^{B}$ is overestimated compared to θ_{OBS} as shown in Figures 3.3(a) and 3.5(d) caused by the bias of E_{BTM} (see Figures 3.3(b) and 3.6(d)). At the start of simulation period, the large negative E_{BTM} (condensation), as a result of large negative humidity gradient ($q_s \approx 0$ at low soil moisture), becomes an unrealistic source of θ_s in the $FRM_{\theta s}^{B}$ and leads to a large positive bias of θ_s. The error statistics shown in Table 3.1 indicate that the FRMEP model gives a more accurate prediction of θ_s compared to the $FRM_{\theta s}^{B}$ as E_{MEP} agrees more closely with E_{OBS} compared to E_{BTM}.

Figure 3.3(a) shows that the modeled θ_ss have an opposite phase to that of θ_{OBS}. θ_s is expected to decrease during daytime due to soil evaporation. The opposite phase of daytime θ_{OBS} to that of θ_s is likely caused by the measurement error of the time domain reflectometry method known to be strongly affected by soil temperature (Schanz et al., 2011). High soil temperature leads to an overestimation of bulk soil dielectric constant, thus resulting in a bias of the retrieved soil moisture. The bias can be as large as 0.08 m^3 m^{-3} when soil temperature reaches 40 ^oC. The daytime peaks of soil temperature measured at the same level of θ_{OBS} are 40-45 ^oC at the LH site. The diurnal amplitude of θ_{OBS} is about 0.03 m^3 m^{-3} less than the temperature effect. Therefore, the temperature effect is the most likely cause of the opposite phase between modeled and observed surface soil moisture.

Figure 3.4(a) shows the T_a predicted by the FRMEP model and that by Eq. (3.26) driven by observed H (H_{OBS}) and H_{BTM} against θ_{OBS}. The FRM_{Ta}^{O} and FRM_{Ta}^{B} denote the FRMs of T_a, as in Eq. (3.26), driven by H_{OBS} and H_{BTM}, respectively. The corresponding scatter plots of the FRMEP and FRM_{Ta}^{B} simulations are shown in Figures 3.5 and 3.6. The FRMEP modeled T_a agrees closely with observations as show in Figure 3.4(a) (see also Figure 3.5(e) for the scatter plot). The bias and RMSE of the FRMEP modeled T_a are about -0.4 and 2.76 ^{o}C during the model period (see Table 3.1). A high correlation of 0.81 between FRMEP predicted and observed T_a indicates that the FRMEP model well captures the diurnal variation of T_a. Larger discrepancies of the FRMEP modeled T_a against observations occurred in, e.g., day 225 and 235-238. These discrepancies are found to be caused by the prescribed reference temperature $\overline{T_a}$ in the FRM_{Ta}, which is difficult to capture the abrupt drop of observed T_a due to episodic events. The close agreement of the FRMEP estimated H (H_{MEP}) and H_{OBS} are evident as shown in Figure 3.4(b) also indicated by the low modeling error (e.g. bias ~ -1 W m^{-2}) and high correlation (r = 0.93). The T_a predicted by the FRM_{Ta}^{O} are comparable with that predicted by the FRMEP model resulting from the close agreement between the two model forcings (i.e., H_{OBS} and H_{MEP}). The error statistics of the FRMEP and FRM_{Ta}^{O} are summarized in Table 3.1.

The T_a predicted by the FRMEP model agrees more closely with the observed T_a when compared to that by the FRM_{Ta}^{B} as shown in Figure 3.4(a) (see also Figures 3.5(e) and 3.5(f) for the scatter plots). The smaller modeling error and higher correlation of the FRMEP predicted T_a (bias -0.4 ^{o}C, RMSE 2.76 ^{o}C, correlation 0.81) compared to those of FRM_{Ta}^{B} predicted T_a (bias 3.1 ^{o}C, RMSE 6.15 ^{o}C, correlation 0.3) are obvious as H_{MEP} agrees more closely with H_{OBS} than H_{BTM} (see Table 3.1). The H_{BTM} has unrealistic

fluctuations throughout the model period as shown in Figure 3.4(b). The unrealistic fluctuations of H_{BTM} are attributed to the uncertainties of estimated transfer coefficients C_H similar to those of E_{BTM}. The modeling errors of H_{MEP} are always bounded by the measurement errors of R_n, while those of H_{BTM} are theoretically unbounded.

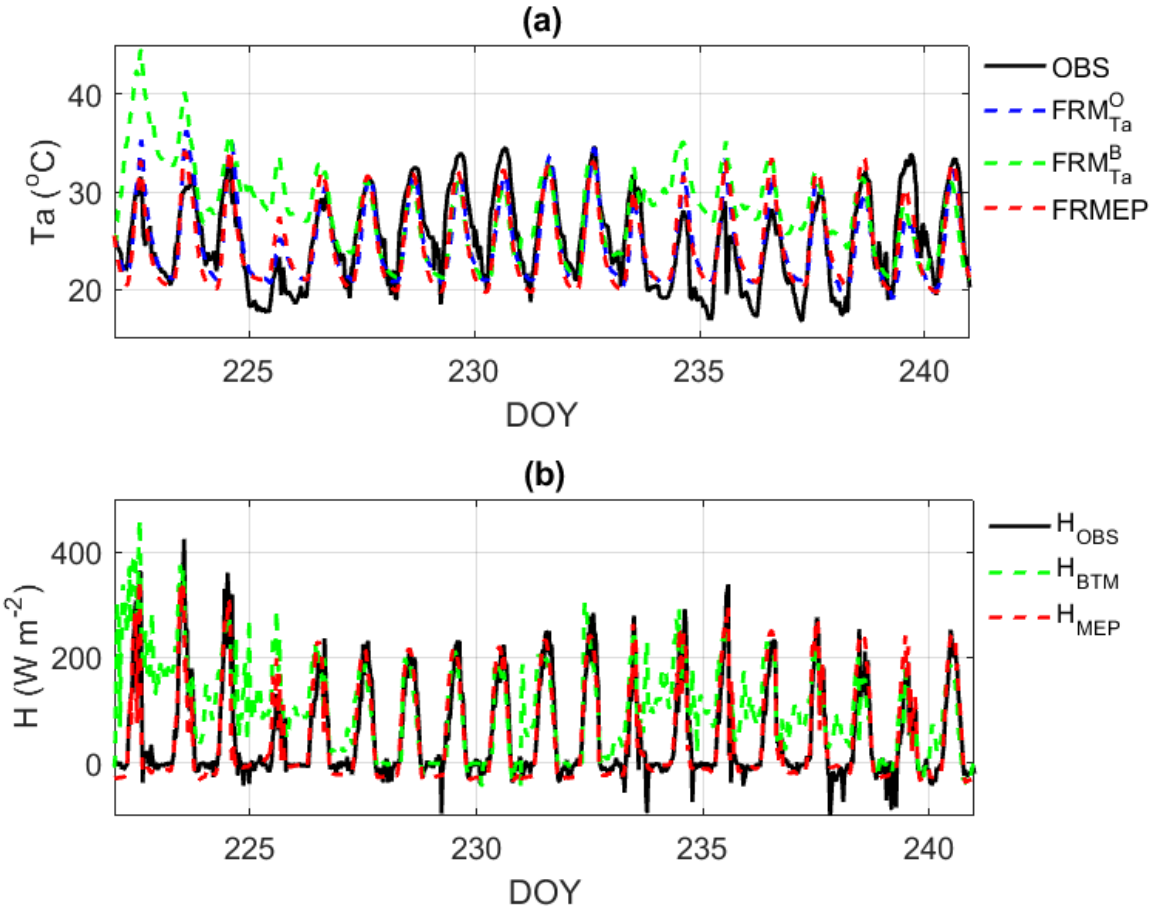

Figure 3.4: (a) T_a predicted by the FRM^{O}_{Ta} (dashed blue), FRM^{B}_{Ta} (dashed green), and the FRMEP model (dashed red) versus observations (solid black), and (b) the modeled H_{BTM} (dashed green) and H_{MEP} (dashed red) versus H_{OBS} (solid black) of the LH site, August, 10 to August 28, 2009.

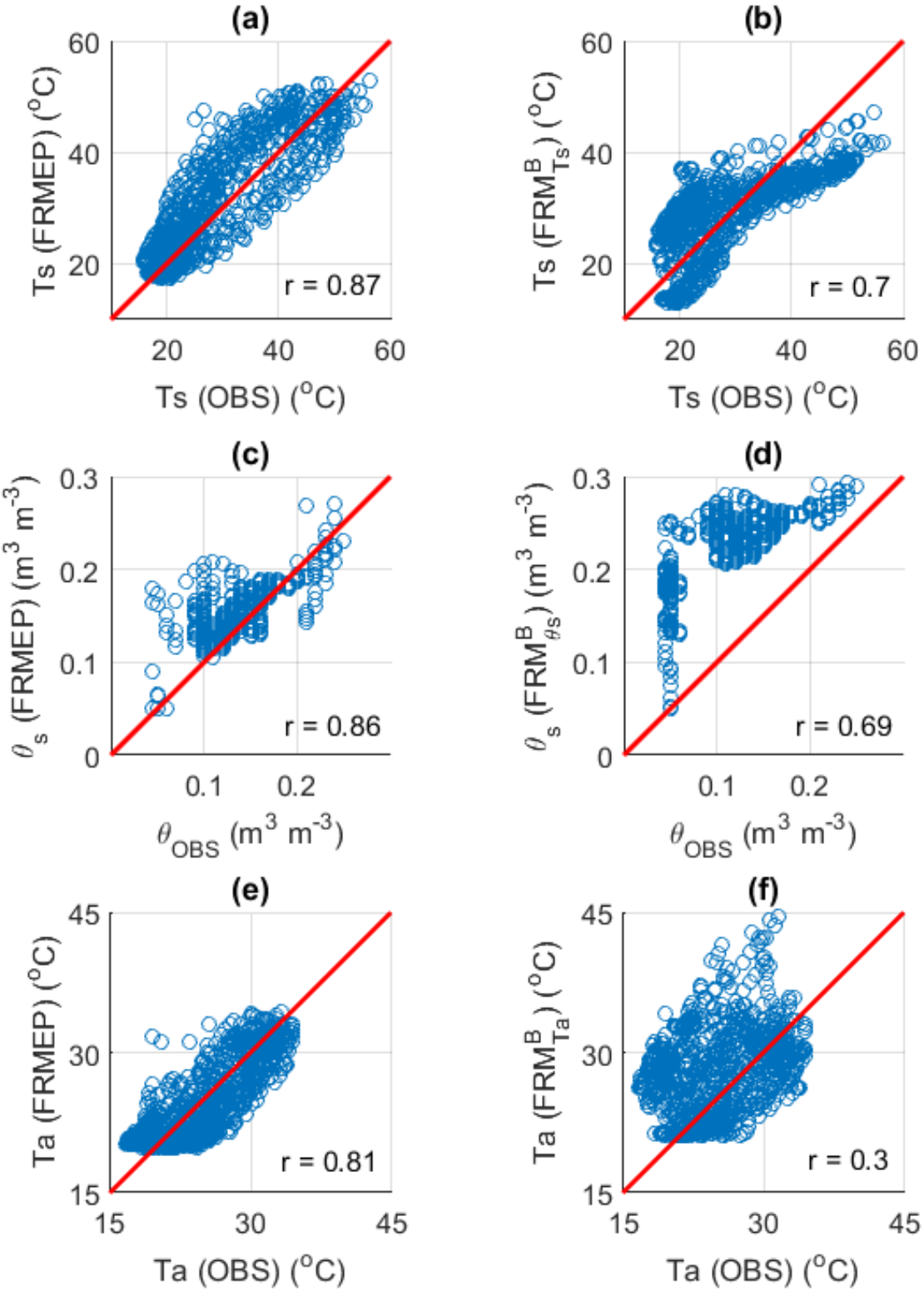

Figure 3.5: The scatter plots of Figures 3.2 to 3.4 showing the comparison of the FRMEP and classical FRMs predicted T_s , θ_s , and T_a versus observations.

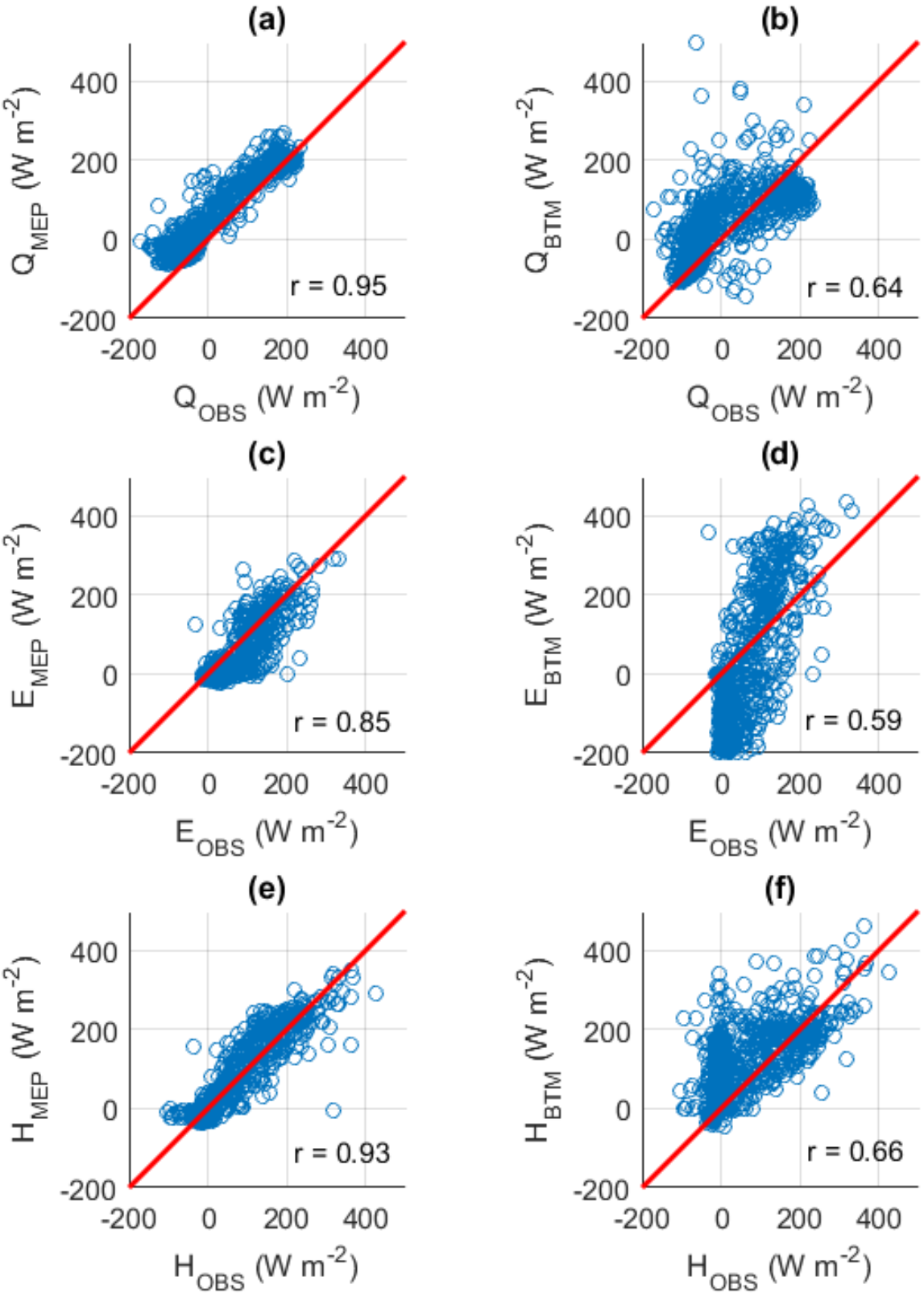

Figure 3.6: The scatter plots of Figures 3.2 to 3.4 showing the comparison of the MEP and BTM estimated *Q*, *E* and *H* versus observations.

The effect of gravitational drainage term in the $FRM_{\theta s}$ was evaluated by replacing the equation of θ_s (Eq. (3.23)) in the FRMEP model with Eq. (3.19), referred to as the FRMEP-ND model (neglecting gravitational drainage term in the $FRM_{\theta s}$). The simulated T_s, θ_s, T_a as well as surface heat fluxes from the FRMEP and FRMEP-ND models are nearly identical at the LH site (figures not shown). The consistency between the FRMEP and the FRMEP-ND predictions is expected as the soil moisture at the LH site is low (< 0.2 m^3 m^{-3}) so that the drainage term is not important. This supports the argument (Section 3.2.2) that the applicability of the classical $FRM_{\theta s}$ is limited to low soil moisture conditions. The error statistics of the FRMEP and FRMEP-ND model simulations against the observations are shown in Table 3.1.

Tests of the sensitivity of I_a to the FRMEP predicted T_a are conducted by applying the I_a parameterized using Eq. (3.31) (derived from the MOSE, ~1000 tiu), while I_a in Eq. (3.29) (~2500 tiu) was used in the performed analysis shown in Figures 3.4 to 3.6. A comparison of T_as predicted by the FRMEP model using different $I_a s$ is shown in Figure 3.7(a). The diurnal amplitude of FRMEP modeled T_a with I_a ~1000 tiu are apparently greater than that with I_a ~2500 tiu as shown in Figure 3.7(a). The FRMEP modeled T_a with I_a ~1000 tiu is nearly identical to the FRMEP modeled T_s (see Figure 3.7(b)) and agree closely with the observed T_s. One reasonable explanation is that Eq. (3.31) evaluates the I_a right above the evaporating surface theoretically even though the MOST is known to be only applied to certain level above the surface. I_a at the surface is expected to be smaller than I_a above the surface as turbulent diffusivity increases with height. In other words, the FRMEP with I_a parameterized using Eq. (3.31) predicts a T_a at the surface, which is expected to be close to T_s according to the continuity of temperature across the land surface

and atmosphere (i.e., $T_a = T_s$ at $z = 0$). The encouraging results suggest that the FRM_{Ta} with I_a derived based on the MOST (Eq. (3.31)) may be applied as an alternative way for verifying the FRMEP predicted T_s.

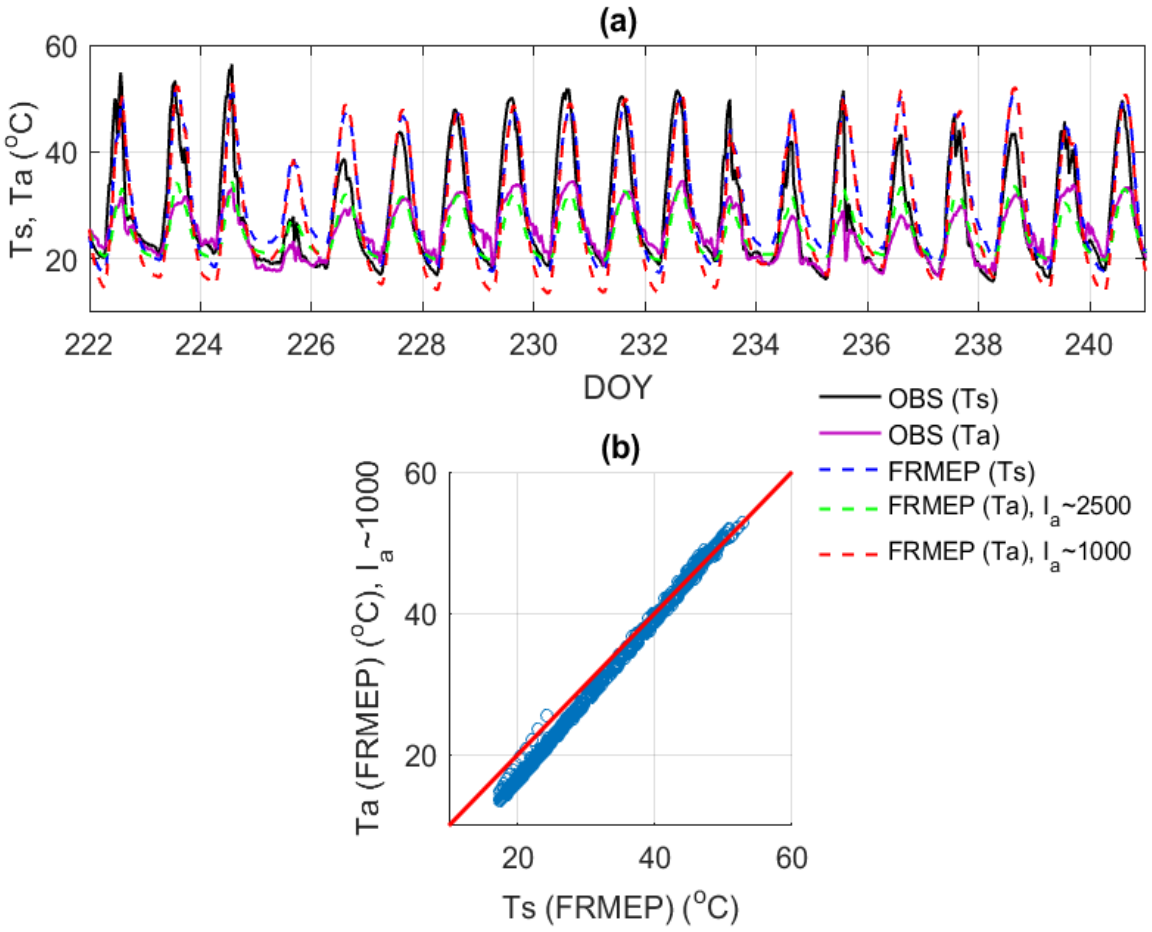

Figure 3.7: (a) The comparison of the FRMEP modeled T_s (dashed blue), T_a with I_a estimated using Eq. (3.29) (dashed green), T_a with I_a estimated using Eq. (3.31) (dashed red) versus observed T_s (solid black) and T_a (solid purple) of the LH site, August 10 to August 28, 2009, and (b) the scatter plot of the FRMEP modeled T_s and T_a with I_a estimated using Eq. (3.31).

3.6.1.2 Wet Condition – Brooks Field Site, Iowa

The predictions of the FRMEP and the classical FRMs, forced by observed and BTM surface heat fluxes, against observations at the BF10 site are shown in Figures 3.8 to 3.10. The corresponding scatter plots for the state variables and heat fluxes are presented in Figures 3.12 and 3.13, respectively. $\bar{T}$ in Eq. (3.11) was estimated to be about 16 ^{o}C obtained from the average of observed T_s over unfrozen periods due to lack of deep soil temperature measurements. $\bar{\theta}$ and $\overline{T_a}$ were computed using the same method as those at the LH site.

The performances of the FRMEP model and the FRM_{Ts}^{O} are comparable to that at the LH site. The FRMEP modeled T_s has a close agreement with observed T_s as shown in Figure 3.8(a) (see also Figure 3.12(a)). In contrast, the FRM_{Ts}^{O} tends to underestimate T_s during nighttime caused by the underestimated Q_{OBS} inconsistent with the observed R_n. The bias and RMSE of the FRMEP modeled T_s are -1.2 ^{o}C and 2.7 ^{o}C, respectively, lower than those of the FRM_{Ts}^{O} predicted T_s (-4.2 ^{o}C and 5.0 ^{o}C) as shown in Table 3.2. The correlation coefficients between the two modeled T_ss with observations are comparable (0.87 and 0.92 for the FRMEP and FRM_{Ts}^{O}, respectively). Figures 3.8(b) and 3.13(a) show that Q_{MEP} agrees closely with Q_{OBS} except for nighttime. The bias of 22.9 W m^{-2} is mainly due to the potentially underestimated nighttime Q_{OBS} as discussed previously.

The FRMEP modeled T_s agrees more closely with observed T_s when compared to the FRM_{Ts}^{B} modeled T_s as shown in Figure 3.8(a) (see also Figures 3.12(a) and 3.12(b)). Table 3.2 shows that the FRMEP predicted T_s has lower model bias, RMSE, and higher correlation with observations than the FRM_{Ts}^{B} predicted T_s. The FRM_{Ts}^{B} predicted T_s has

spurious spikes (e.g., day 164, 172, 178, and 180) resulting from the unrealistic Q_{BTM} (see Figures 3.8(b) and 3.13(b)), which is caused by the large fluctuations of E_{BTM} (also H_{BTM}) discussed previously (see Figures 3.9(b) and 3.10(b) for E_{BTM} and H_{BTM}). The sum of E_{BTM} and H_{BTM} being greater (smaller) than R_n on those days leads to a large negative (positive) Q_{BTM} according to Eq.(3.39). Q_{MEP} has closer agreement with Q_{OBS} than Q_{BTM} throughout the period as shown in Figure 3.8(b) (see also Figures 3.13(a) and 3.13(b)). The corresponding error statistics are listed in Table 3.2.

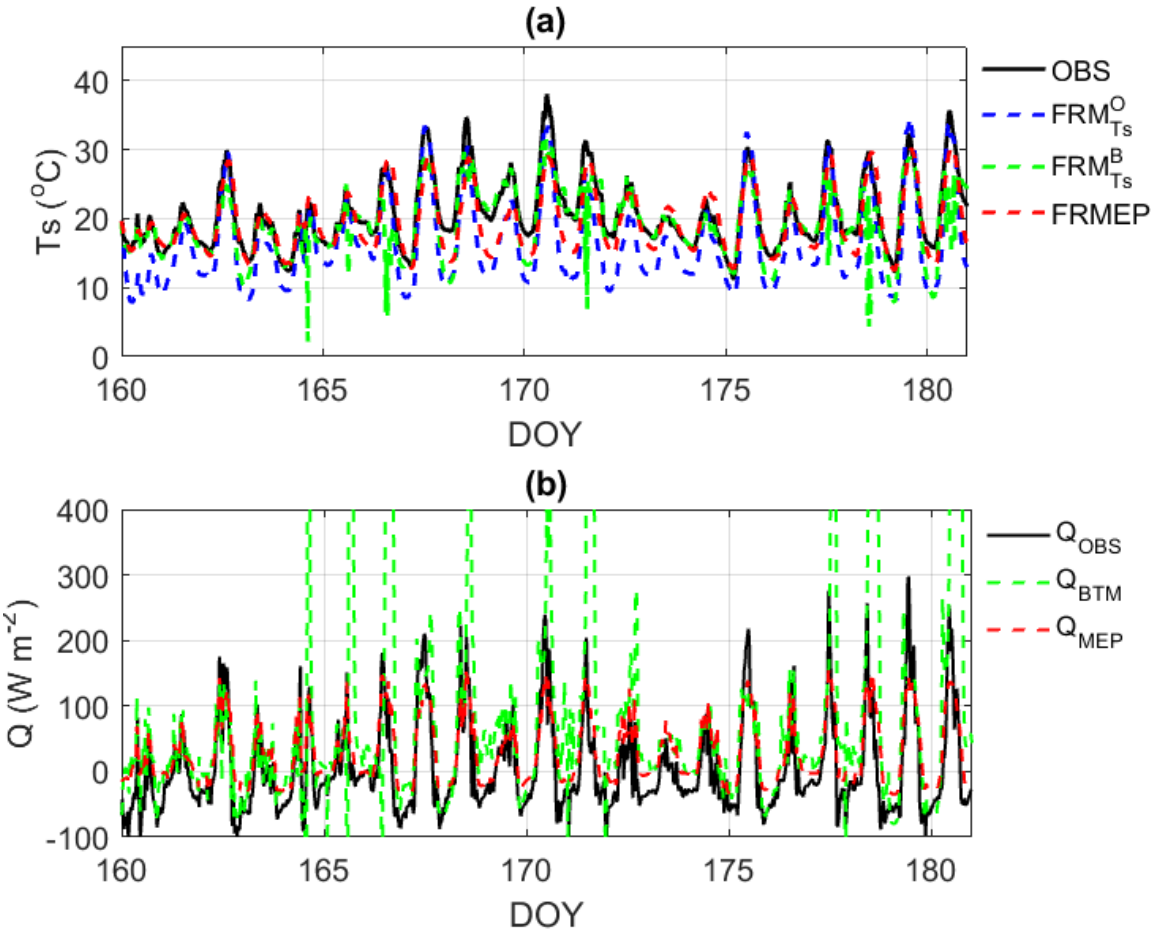

Figure 3.8: (a) T_s predicted by the FRM^{O}_{Ts} (dashed blue), the FRM^{B}_{Ts} (dashed green), and the FRMEP model (dashed red) versus observed T_s (solid black), and (b) the modeled Q_{BTM} (dashed green) and Q_{MEP} by the FRMEP model (dashed red) versus Q_{OBS} (solid black) of the BF10 site, June 9 to June 29, 2011.

Table 3.2: Error statistics of the FRMEP, FRMEP-ND, and classical FRMs predictions, Brooks Field Site 10, Iowa (Unit: T_s(K), θ_s(m^3 m^{-3}), T_a(K), Q, E, and H (W m^{-2}))

	Bias	RMSE	Correlation coef. (r)
T_s	-1.2[a] / -1.4[b] / -4.2[c] / -1.6[d]	2.7[a] / 2.8[b] / 5.0[c] / 3.7[d]	0.87[a] / 0.87[b] / 0.92[c] / 0.78[d]
θ_s	-3.6×10^{-4} [a] / 0.05[b] / -0.01[c] / -0.02[d]	0.02[a] / 0.06[b] / 0.03[c] / 0.04[d]	0.71[a] / 0.33[b] / 0.72[c] / 0.66[d]
T_a	-0.29[a] / -0.41[b] / -2.01[c] / -0.44[d]	2.34[a] / 2.40[b] / 3.66[c] / 2.09[d]	0.81[a] / 0.81[b] / 0.65[c] / 0.88[d]
Q	22.9[a] / 22.9[b] / - / 90.7[d]	41.7[a] / 41.7[b] / - / 245.8[d]	0.90[a] / 0.90[b] / - / 0.43[d]
E	-16.7[a] / -15.1[b] / - / -59.9[d]	71.7[a] / 72.2[b] / - / 172.6[d]	0.84[a] / 0.84[b] / - / 0.36[d]
H	24.3[a] / 22.6[b] / - / -7.4[d]	50.3[a] / 48.2[b] / - / 92.3[d]	0.70[a] / 0.70[b] / - / 0.04[d]

a: FRMEP vs. OBS
b: FRMEP-ND vs. OBS
c: FRM^O vs. OBS
d: FRM^B vs. OBS

The FRMEP modeled θ_s agrees closely with θ_{OBS} as shown in Figures 3.9(a) and 3.12(c) with a bias -3.6×10^{-4} m^3 m^{-3} and a RMSE 0.02 m^3 m^{-3} as shown in Table 3.2. Rain events are well captured indicated by the rapid increase of θ_s. Figure 3.9(a) further shows a greater increase of θ_s than θ_{OBS} during rain events owing to the higher sensitivity of θ_s than θ_{OBS} to precipitation. The largest discrepancy between the FRMEP modeled θ_s and θ_{OBS} is only about 0.03 m^3 m^{-3}, less than the measurement error of soil moisture caused by the temperature effect discussed previously. The correlation coefficient of 0.71 between the FRMEP modeled θ_s with θ_{OBS} shown in Table 3.2 may also be related to the uncorrected θ_{OBS} due to the temperature effect on measurements. The close agreement between E_{MEP} and E_{OBS} is evident as shown in Figures 3.9(b) and 3.13(c) with the exception of those unrealistic fluctuations of E_{OBS} during rain events (e.g., day 160, 172, and 173).

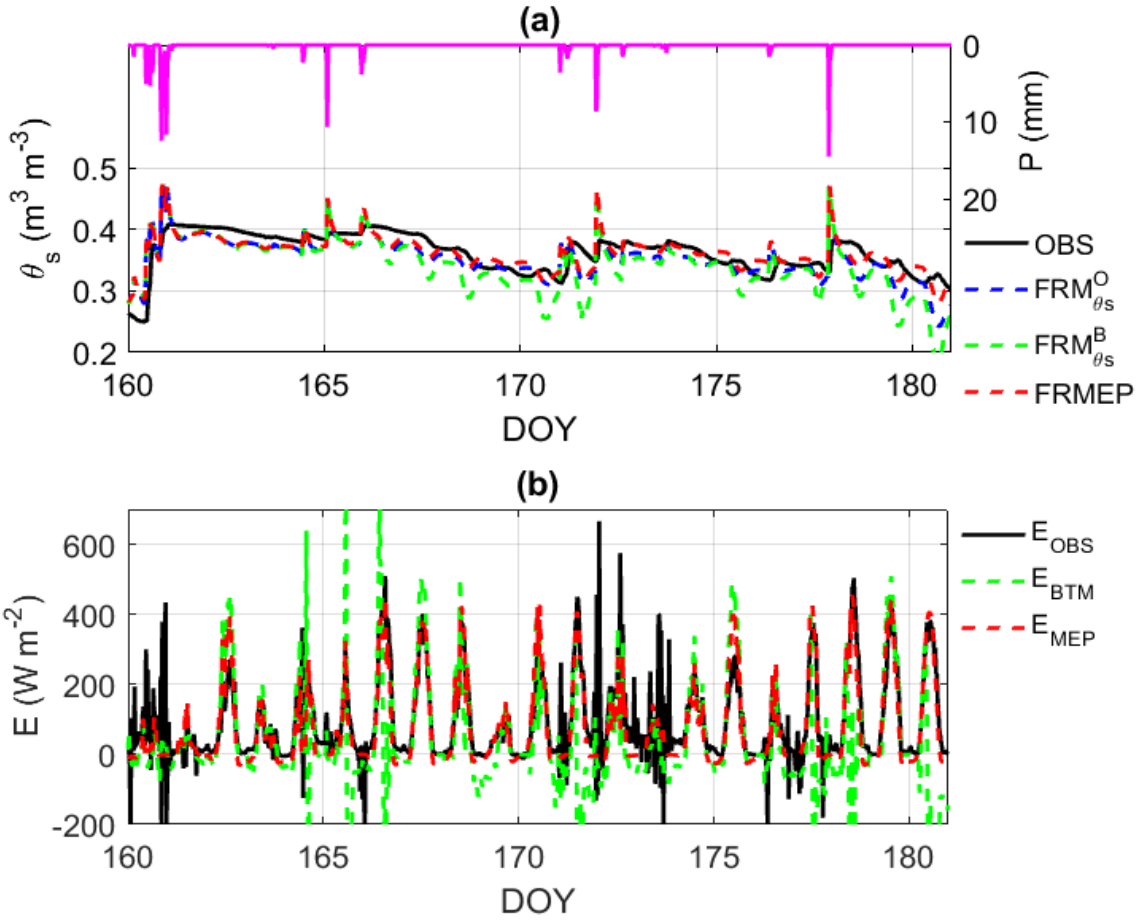

Figure 3.9: (a) θ_s predicted by the $FRM^O_{\theta s}$ (dashed blue), the $FRM^B_{\theta s}$ (dashed green), and the FRMEP model (dashed red) versus θ_{OBS} (solid black) with precipitation on the top, and (b) the modeled E_{BTM} (dashed green) and E_{MEP} by the FRMEP model (dashed red) versus E_{OBS} (solid black) of the BF10 site, June 9 to June 29, 2011.

The FRMEP and $FRM^O_{\theta s}$ predicted θ_ss are in close agreement with each other as shown in Figure 3.9(a), even though the two models are driven by unequal E_{OBS} and E_{MEP}. The similar error statistics of the two models are shown in Table 3.2. The effect of using potentially overestimated nighttime E_{OBS} seems to be weaker at the BF10 site than that at the LH site caused by the frequent rain that keeps the θ_s high. Precipitation causes a more rapid change in soil moisture than evaporation does. A light rain event, for example, with a rate of 1 mm hr^{-1} is equivalent to ~700 W m^{-2} of negative E. Figure 3.9(a) clearly shows

that the FRMEP model performs better than the $FRM_{\theta s}^{B}$ for predicting θ_s (see also Figures 3.12(c) and 3.12(d)). The $FRM_{\theta s}^{B}$ predicted θ_s has greater negative bias compared to the FRMEP predicted θ_s resulting from the unrealistic fluctuations of E_{BTM} discussed previously (see Figures 3.9(b) and 3.13(d)).

The FRMEP predicted T_a agree closely with the observed values as shown in Figure 3.10(a). The corresponding overall bias is -0.29 ^{o}C. The diurnal fluctuation of T_a is well captured by the FRMEP model indicated by the high correlation between FRMEP modeled and observed T_a (r = 0.81) as shown in Figure 3.12(e). The diurnal amplitudes of the simulated T_a agree closely with those of observed T_a. The larger discrepancies between the FRMEP modeled and observed T_a are presumably caused by the prescribed $\overline{T_a}$ in the FRM_{Ta} as discussed in Section 3.6.1.1.

The H_{MEP} is, in general, greater than H_{OBS} as shown in Figure 3.10(b). The H_{OBS} may be potentially underestimated as it is consistently lower than the residual of other surface energy budget components, i.e., $R_n - Q_{OBS} - E_{OBS}$ as shown in Figure 3.11. The potentially underestimated H_{OBS} leads to reduced diurnal amplitude of the FRM_{Ta}^{O} predicted T_a as shown in Figure 3.10(a). The FRMEP modeled T_a has lower error statistics (bias -0.29 ^{o}C, RMSE 2.34 ^{o}C) and higher correlations (r = 0.81) with observations as compared to the FRM_{Ta}^{O} modeled T_a (bias -2.01 ^{o}C, RMSE 3.66 ^{o}C, r = 0.65) as shown in Table 3.2. The close agreement between the FRMEP modeled T_a and observations also suggests that the FRMEP model has potential to be applied as a tool for verifying the consistency between measured surface state variables (e.g., T_a) and forcing (e.g., H).

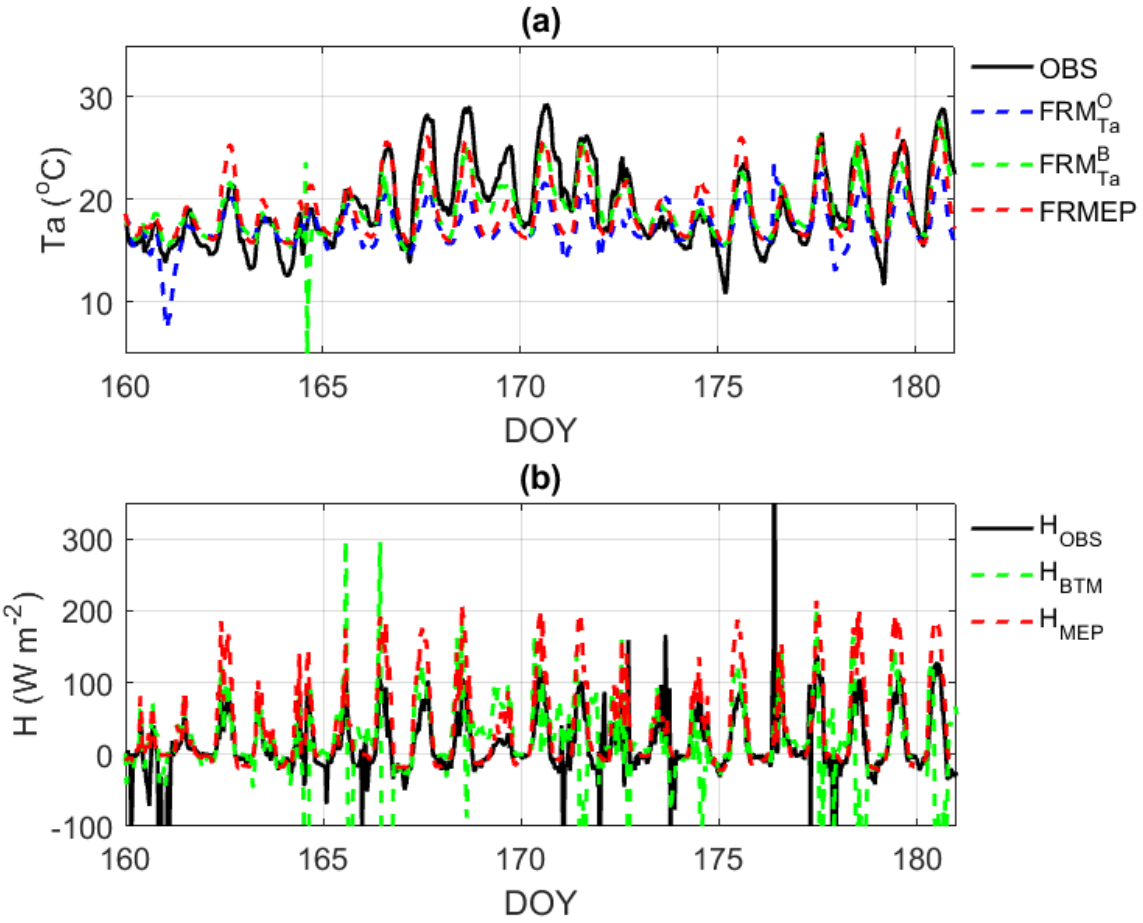

Figure 3.10: (a) T_a predicted by the FRM^{O}_{Ta} (dashed blue), the FRM^{B}_{Ta} (dashed green), and the FRMEP model (dashed red) versus observed T_a (solid black), and (b) the modeled H_{BTM} (dashed green) and H_{MEP} by the FRMEP model (dashed red) versus H_{OBS} (solid black) of the BF10 site, June 9 to June 29, 2011.

The T_a predicted by the FRMEP model has smaller bias compared to that predicted by the FRM^{B}_{Ta} (-0.29 ºC vs. -0.44 ºC). The FRM^{B}_{Ta} predicted T_a has seemingly smaller RMSE and comparable correlation with observations (RMSE 2.09 ºC, r = 0.88) compared to the FRMEP model (RMSE 2.34 ºC, r = 0.81) as shown in Table 3.2 (see aslo Figures 3.12(e) and 3.12(f)). However, the FRM^{B}_{Ta} predicted T_a has unrealistic peaks (e.g., day 164) and fluctuations (e.g., day 178 and 179) resulting from the corresponding erroneous estimates of H_{BTM}, which contains unrealistic fluctuations as shown in Figure 3.10(b).

H_{MEP} outperforms the H_{BTM} as indicated by the much improved error statistics and correlations with observations as shown in Table 3.2 (see also Figures 3.13(e) and 3.13(f)). The lower bias of H_{BTM} (-7.4 W m^{-2}) compared to H_{MEP} (24.3 W m^{-2}) is, again, mainly due to (1) the potentially biased H_{OBS}, as discussed previously, and (2) the error cancellation as the RMSE of H_{BTM} is much higher than that of H_{MEP}.

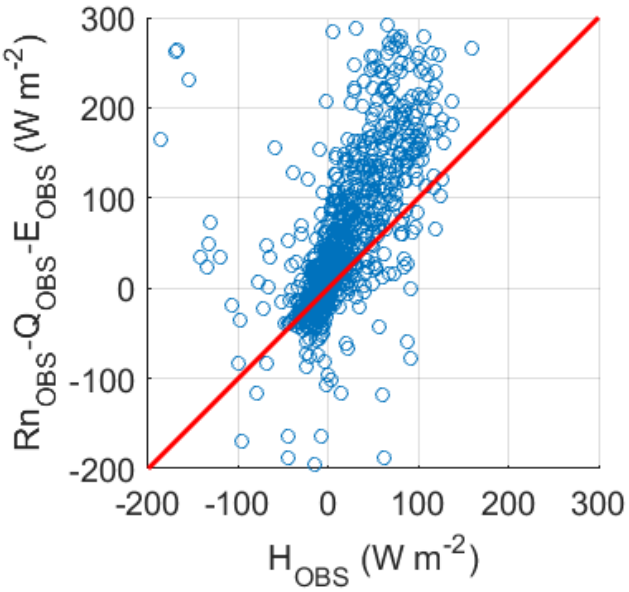

Figure 3.11: $R_n - Q_{OBD} - E_{OBS}$ versus H_{OBS} of the BF10 site, June 9 to June 29, 2011.

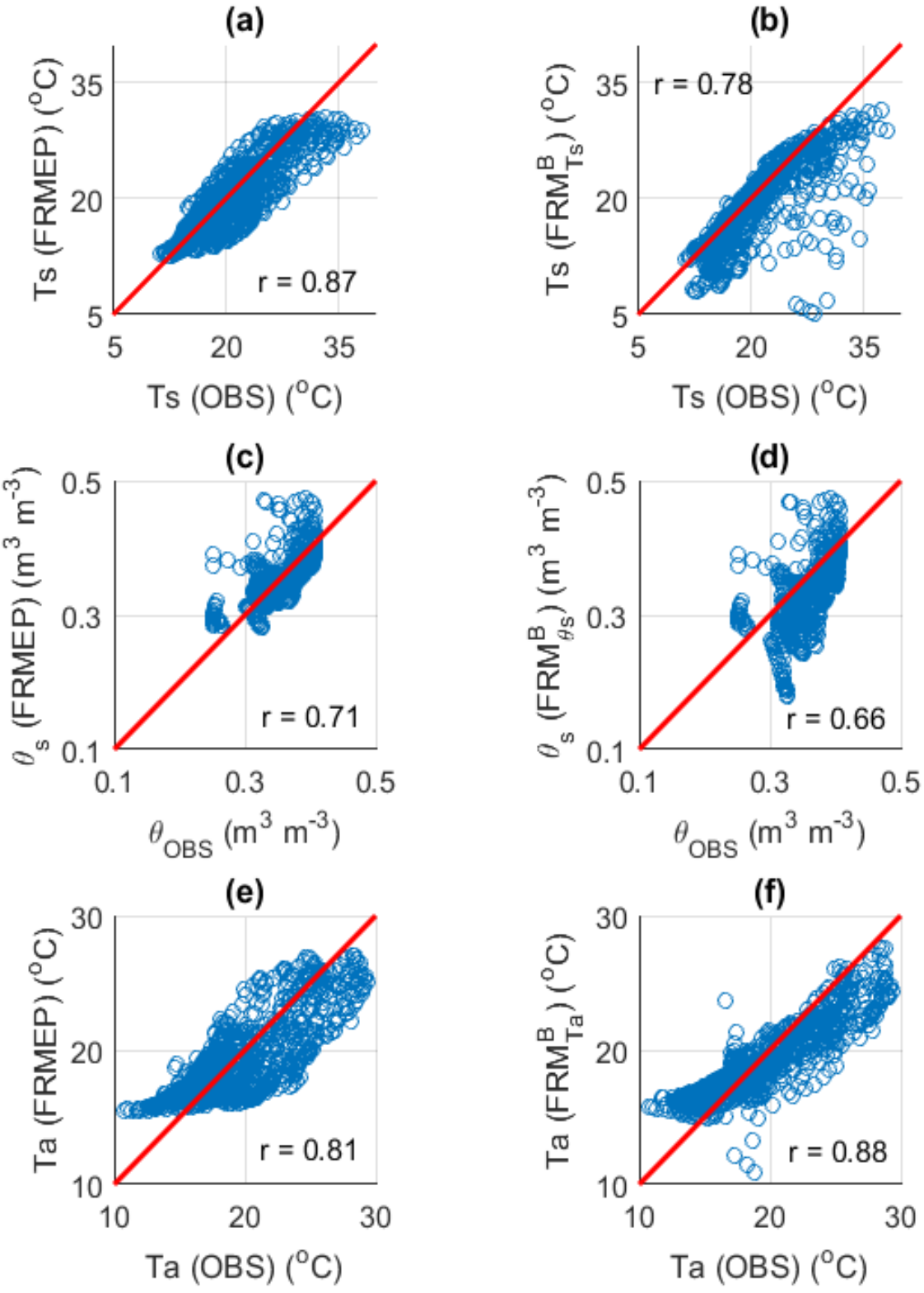

Figure 3.12: The scatter plots of Figures 3.8 to 3.10 showing the comparison of the FRMEP and classical FRMs predicted T_s , θ_s , and T_a versus observations.

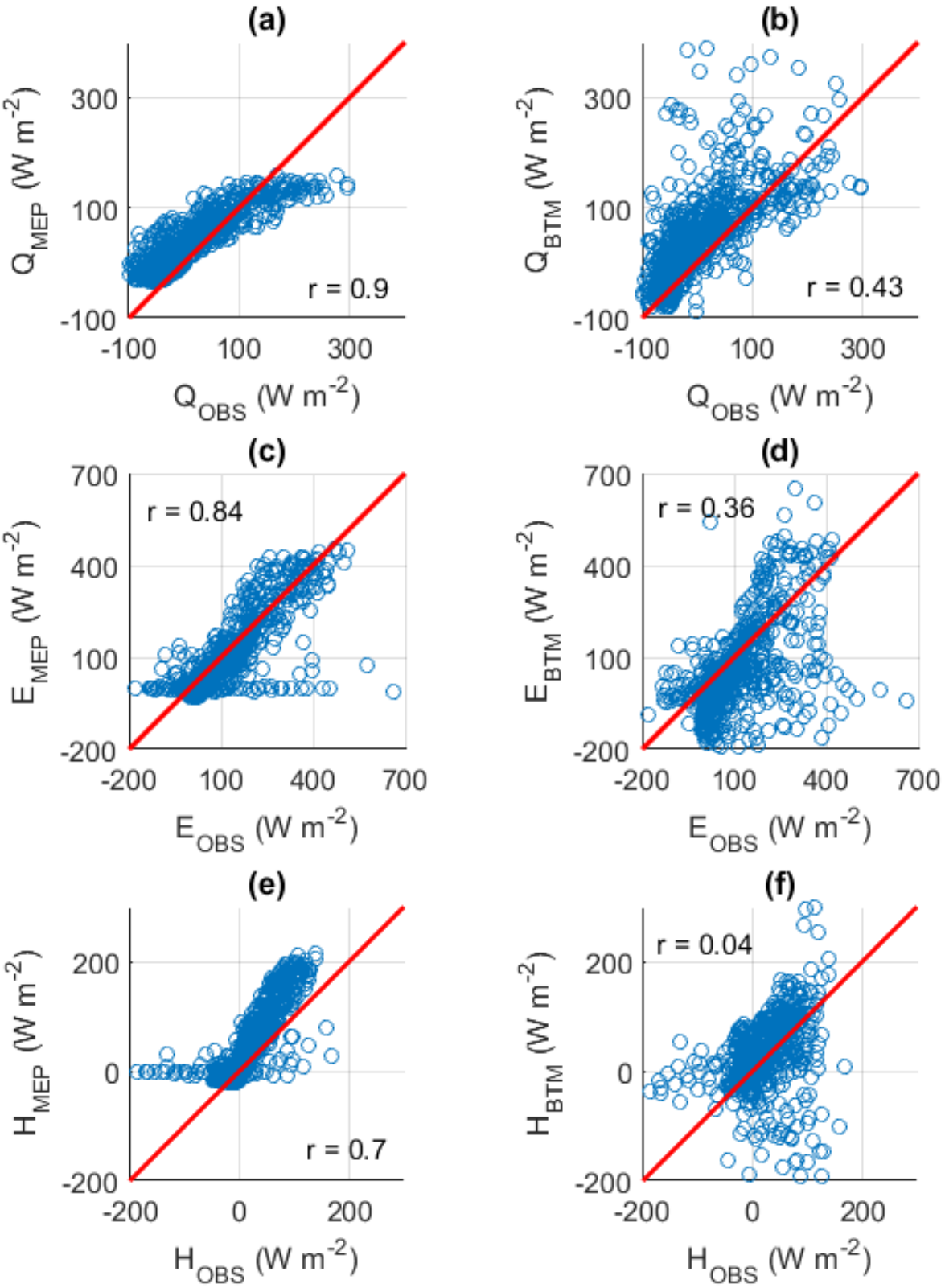

Figure 3.13: The scatter plots of Figures 3.8 to 3.10 showing the comparison of the MEP and BTM estimated *Q*, *E* and *H* versus observations

The comparison of the FRMEP and FRMEP-ND predictions is shown in Figure 3.14. Figure 3.14(c) shows that the FRMEP-ND model apparently overestimates θ_s, while the FRMEP with the drainage term predicts θ_{OBS} relatively well. The corresponding error statistics of the FRMEP-ND model are given in Table 3.2. The T_s, T_a, and three surface heat fluxes simulated by the FRMEP with and without the gravitational drainage term are nearly identical as shown in Figure 3.14. It turns out that the gravitational drainage term in the FRMEP affects θ_s more strongly than other variables under high soil moisture condition (e.g., > 0.3 m^3 m^{-3}). This is due to the reduced sensitivity of σ and q_s to soil moisture for wet soils in the MEP modeled heat fluxes according to Eqs. (3.32) and (3.36). The gravitational drainage term would be equally important in the FRMEP model when soil moisture is between the extremes.

The results of FRMEP predicted T_as using different parameterizations of I_a (Eq. (3.29) vs. (3.31)) are shown in Figure 3.15. The FRMEP modeled T_a with I_a parameterized using Eq. (3.31) (~1000 tiu) is higher than that with I_a parameterized using Eq. (3.29) (~2000 tiu). The FRMEP modeled T_a with I_a ~1000 tiu agrees closely with observed T_s, which is physically realistic according to the continuity of temperature across the land surface and atmostphere as discussed in Section 3.6.1.1.

The two case studies demonstrate the following advantages of the FRMEP model: (1) improved parameterization of surface heat fluxes with the closure of surface energy balance, (2) independent of bulk gradient and other atmospheric variables, and (3) reduced sensitivity to model input and parameters compared to the BTM of heat fluxes in classical

FRMs as the dynamics of T_s are inversely related to T_s^2 through the parameter σ shown in Eq. (3.32).

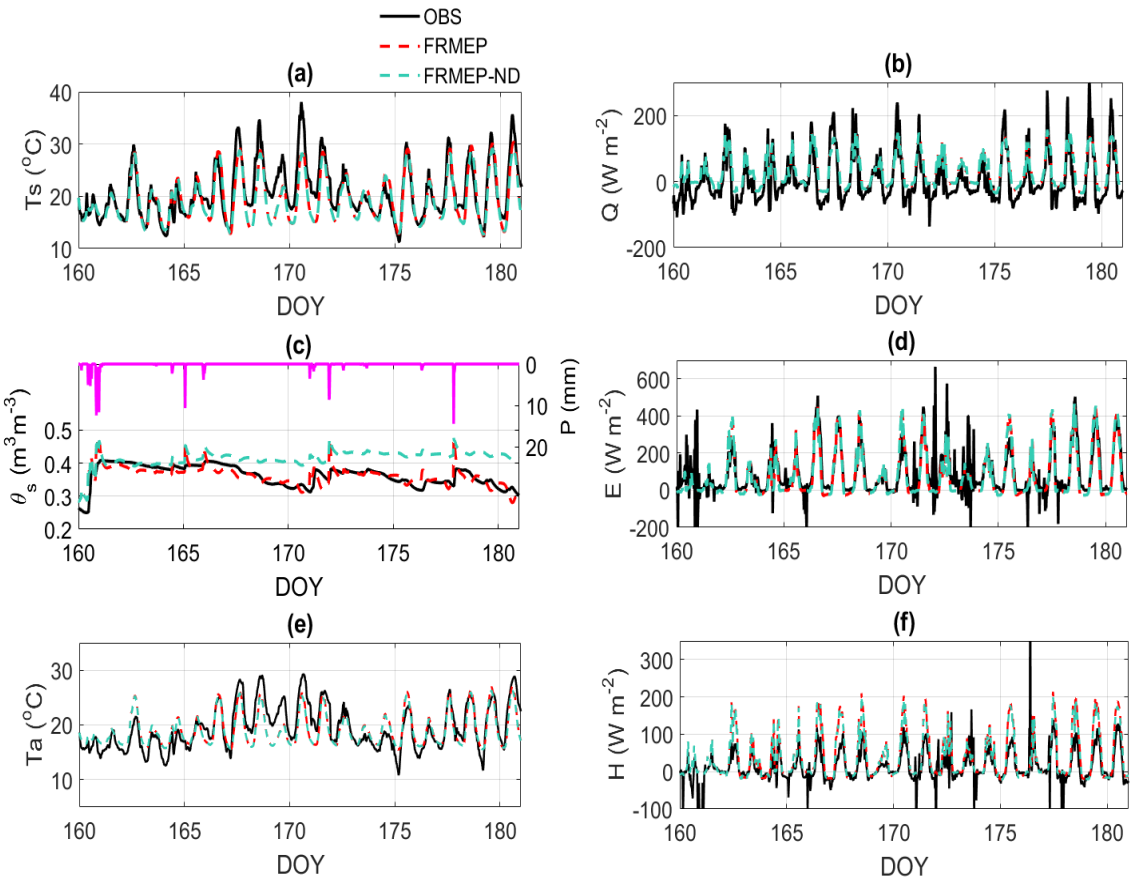

Figure 3.14: The FRMEP (dashed red) and the FRMEP-ND (dashed cyan) predicted (a) T_s, (b) Q_{MEP}, (c) θ_s (d) E_{MEP}, (e) T_a, and (f) H_{MEP} versus observations (solid black) of the BF10 site, June 9 to June 29, 2011.

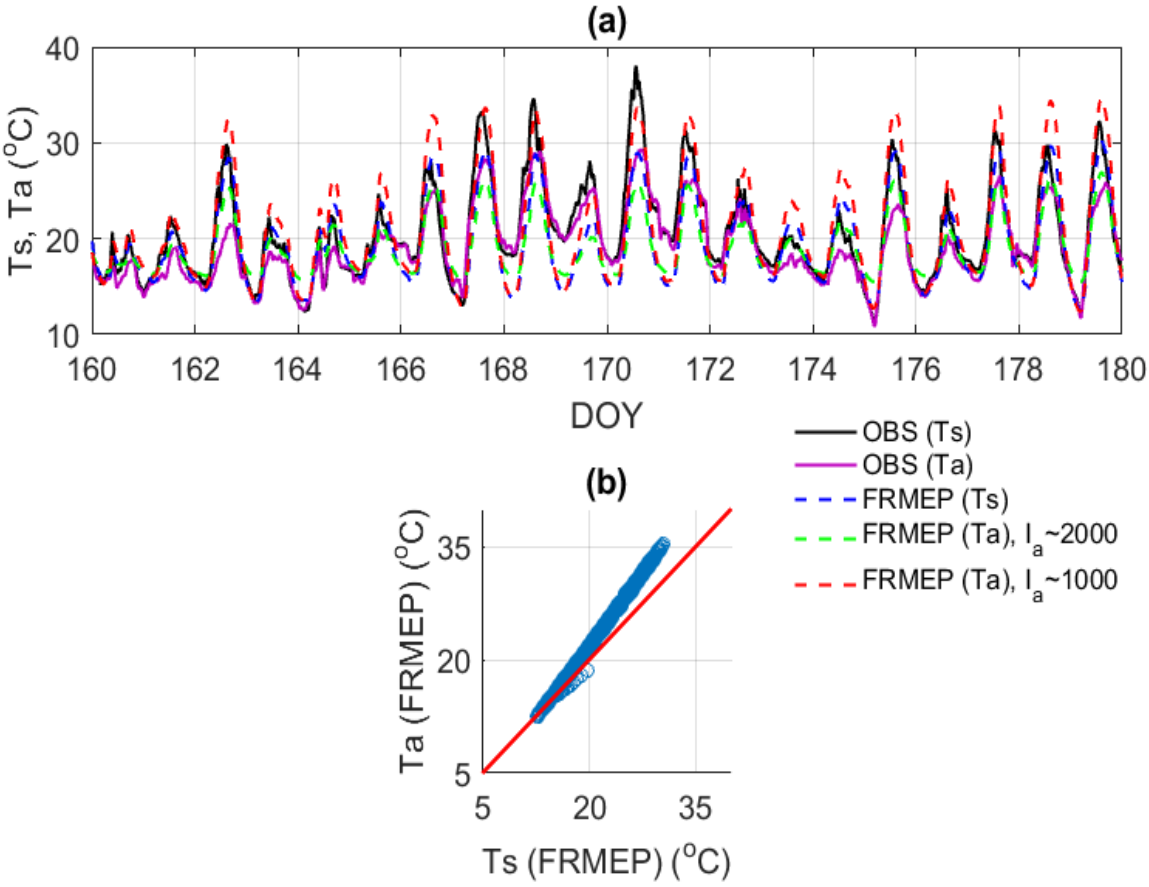

Figure 3.15: (a) The comparison of the FRMEP modeled T_s (dashed blue), T_a with I_a estimated using Eq. (3.29) (dashed green), T_a with I_a estimated using Eq. (3.31) (dashed red) versus observed T_s (solid black) and T_a (solid purple) of the BF10 site, June 9 to June 29, 2011, and (b) the scatter plot of the FRMEP modeled T_s and T_a with I_a estimated using Eq. (3.31).

3.6.2 Seasonal Variability

The FRMEP model was tested to simulate the seasonal/annual cycle of T_s and θ_s. The data products from the LH site during 2009 were selected for the one-year simulation. Unlike the short-term simulations presented in Section 3.6.1 that use a constant or deep soil temperature as $\bar{T}$, $\bar{T}$ in the one-year simulation is set as the daily mean climatology of

T_s obtained from the meteorological records since 2001 or deep soil temperature, whichever is lower (see discussions in Section 3.2.1). Consequently, for this specific site, deep soil temperature was used through day 60 to 280 (March to September), while daily mean T_s was used for the rest of year. Similarly, $\overline{T_a}$ is set as the daily mean climatology of T_a obtained from observations since 1990 during cold season (October to February), while the daily mean climatology T_a less 3.5 ^{o}C, representing an air temperature far from the surface, is adopted to the warm season (March to September) determined by the offline test of FRM_{Ta} as discussed in Section 3.2.3. I_a was estimated as ~2500 and ~2000 tiu for the warm and cold seasons according to Eq. (3.29).

The daily-averaged FRMEP predicted T_s, θ_s, and T_a over 2009 versus observations are shown in Figure 3.16, while those of modeled surface heat fluxes against observations are shown in Figure 3.17. The simulations between day 250 to 280 are removed due to the unrealistic R_n data (positive or downward during nighttime). Figures 3.16(a) and 3.16(e) showed that the FRMEP modeled T_s and T_a well capture the seasonal cycles with daily mean biases of 1.7 ^{o}C and 0.49 ^{o}C and correlations of 0.93 and 0.87, respectively (see also Figures 3.16(b) and 3.16(f)). The FRMEP modeled T_s and T_a agree more closely with observations during the warm season than the cold season. Larger discrepancies between the simulated and observed daily mean T_s and T_a are mostly during the cold season when observed values abruptly drops (e.g., day 40-45 in Figures 3.16(a) and 3.16(e) for T_s and T_a, respectively, see also Figures 3.18(a) and 3.18(e) for the diurnal plots of selected period from January 30 to March 1). This is caused by the large deviation of the prescribed reference temperature $\bar{T}$ and $\overline{T_a}$ from the observed daily mean of T_s and T_a in the FRMEP model.

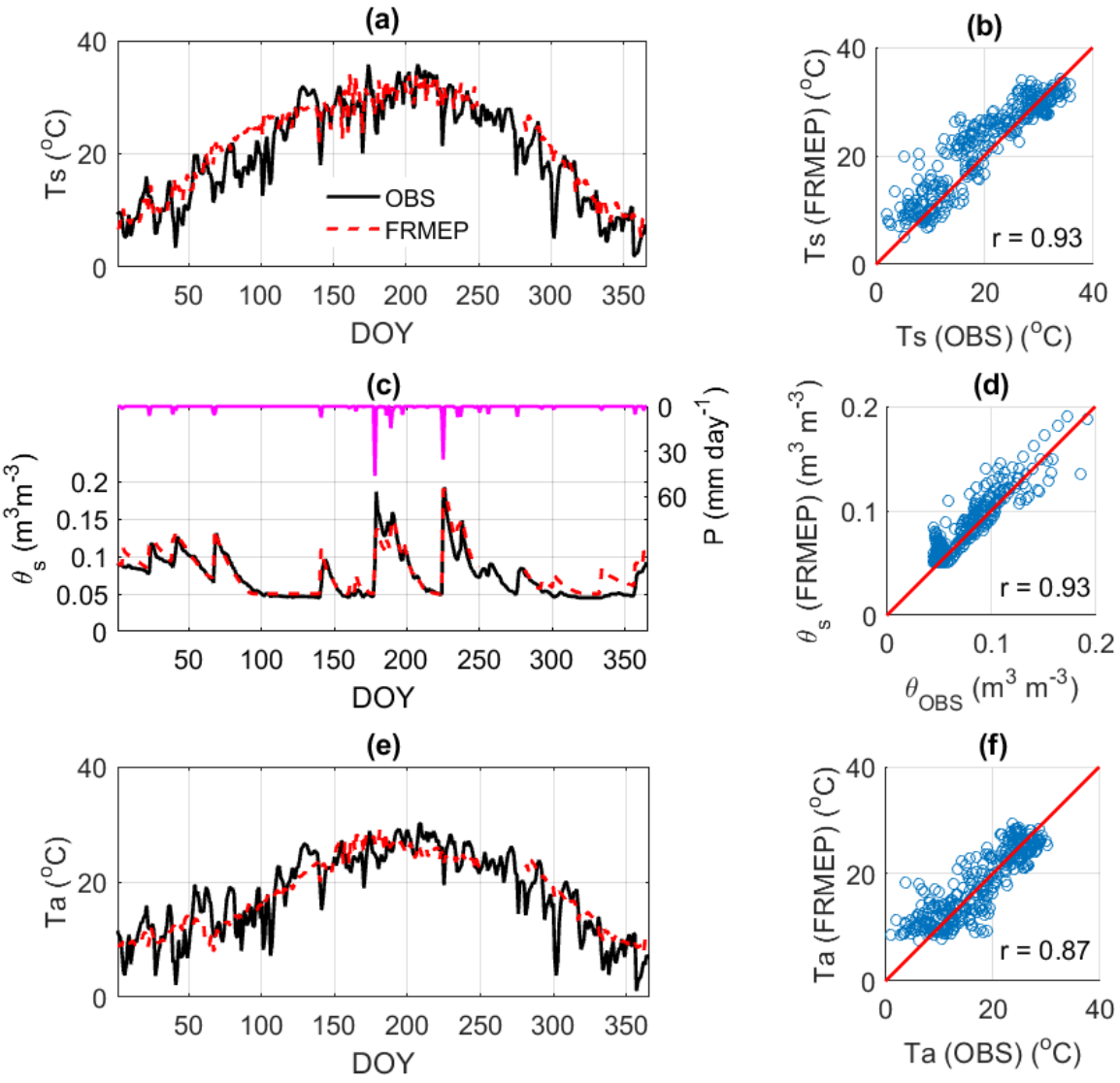

Figure 3.16: Daily-averaged (a) T_s, (c) θ_s, (e) T_a (solid red) predicted by the FRMEP model versus observations (solid black) over 2009 at the LH site. The corresponding scatter plots are shown on the right panel. Precipitation P is shown on the top of (c).

In the force-restore models at diurnal time scale, $\overline{T}$ and $\overline{T_a}$ are theoretically equal to the daily mean T_s and T_a, respectively. Accurate simulation of daily mean T_s and T_a requires $\overline{T}$ and $\overline{T_a}$ to be equal or close to actual daily mean T_s and T_a. Setting $\overline{T}$ and $\overline{T_a}$ as the climatologies of daily mean T_s and T_a in the FRMEP model will not capture the episodic events, thus leading to a relativly large difference between the simulated and

observed values. Note that the amplitudes of simulated T_s and T_a both agree closely with the observations (Figures 3.18(a) and 3.18(e)) as long as the modeled Q and H agree with the observations (Figures 3.18(b) and 3.18(f)). This demonstrates the feature of the FRM_{Ts} and FRM_{Ta} that the heat flux forcings dominates the amplitude of the diurnal variation of T_s and T_a, respectively.

The results suggest that the specification of $\overline{T}$ and $\overline{T_a}$ has stronger impacts on long-term simulations than short-term simulations. This is a major limitation of the force-restore model for long-term simulations. A possible solution to this problem is to restart the simulations periodically using observed T_s and T_a as initial condition, which implicitly specifies the reference temperature in the FRM_{Ts} and FRM_{Ta}, respectively. Figure 3.16(c) shows the FRMEP modeled θ_s with the corresponding scatter plot shown in Figure 3.16(d). The close agreement between the FRMEP predicted θ_s and θ_{OBS} is evident (bias 7×10^{-3} m^3 m^{-3}, r = 0.93). The FRMEP modeled θ_s reproduces the wetting-drying cycles at sub-diurnal to seasonal/annual time scales and captures the rapid variations of soil moisture in response to rain events as shown in Figures 3.18(c) and 3.16(c), respectively.

The magnitude of Q_{MEP} is higher than Q_{OBS}, as shown in Figures 3.17(a) and 3.17(b), mainly resulting from multiple sources of measurement errors as discussed in Section 3.2.4. Figure 3.17(c) shows that E_{MEP} agrees closely with E_{OBS} most of time except for when E_{OBS} has large aberrations that are presumably caused by the measurement errors during rain events (e.g., see also the peaks on days 39 to 42 due to rainfall in Figure 3.18(d)). H_{MEP} agrees more closely with H_{OBS} during the monsoon season (July to September) than outside the monsoon season as shown in Figure 3.17(e). This implies that

the energy partitioning in the MEP model may be biased presumably resulting from the calibration of the wetness function (Eq. (3.36)) for estimating q_s (Eq. (3.35)). The soil texture dependent parameter β in Eq. (3.36), obtained as ≈ 2 and used for the one-year simulation, was calibrated by fitting the MEP modeled surface heat flux to the observations using the data over the entire year. However, the calibrated β with the best overall fitting does not guarantee its universal applicability. The β may also be seasonal dependent due to the change of surface type (e.g., bare soil to vegetated surface and vice versa). For this specific site, using β = 2 yields good agreement between H_{MEP} and H_{OBS} during the monsoon season, while H_{MEP} is underestimated outside the monsoon season. In sum, parameter estimations of the FRMEP model, especially under long-term simulation, requires further tests before applying the FRMEP model to long-term simulation.

Despite the biases in the daily mean values, diurnal variations of Q, E, and H are well captured by the FRMEP model throughout the year (see Figures 3.18 (b), 3.18(d) and 3.18(f)). The correlations between the MEP modeled and observed heat fluxes at sub-daily scale are 0.92, 0.74, and 0.86 for Q, E, and H, respectively. The MEP model also captures the seasonal variations of E and H validated by the high correlations with observations (0.86 and 0.89 for E and H) as shown in Figures 3.17(d) and 3.17(f), respectively. The seemingly lower correlation between daily mean Q_{MEP} and Q_{OBS} (r = 0.58) is mainly caused by the potentially underestimated daily mean Q_{OBS} (Figure 3.17(b)).

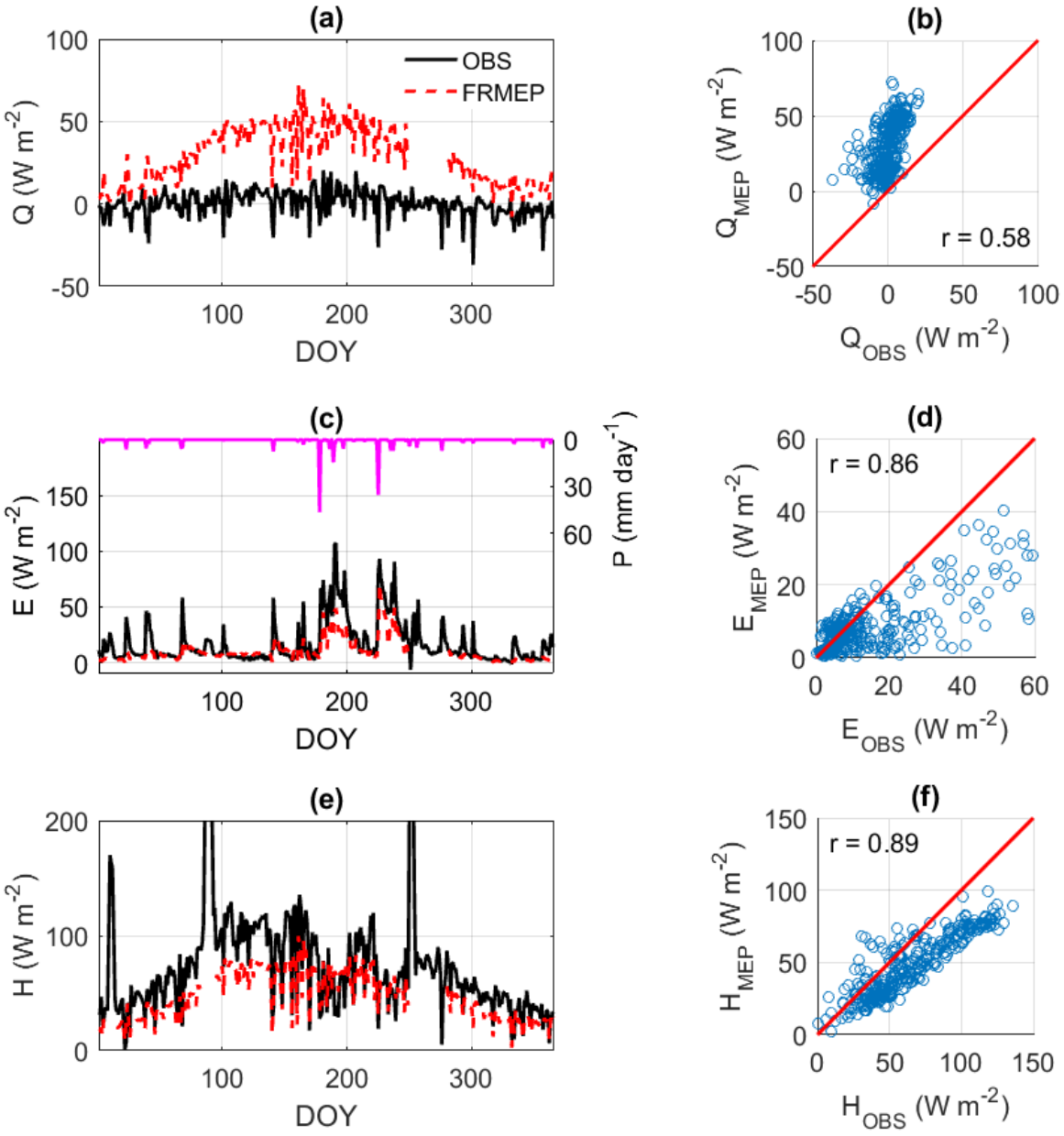

Figure 3.17: Daily-averaged (a) Q_{MEP}, (c) E_{MEP}, (e) H_{MEP} (solid red) predicted by the FRMEP model versus observations (solid black) over 2009 at the LH site. The corresponding scatter plots are shown on the right panel. Precipitation P is shown on the top of (c).

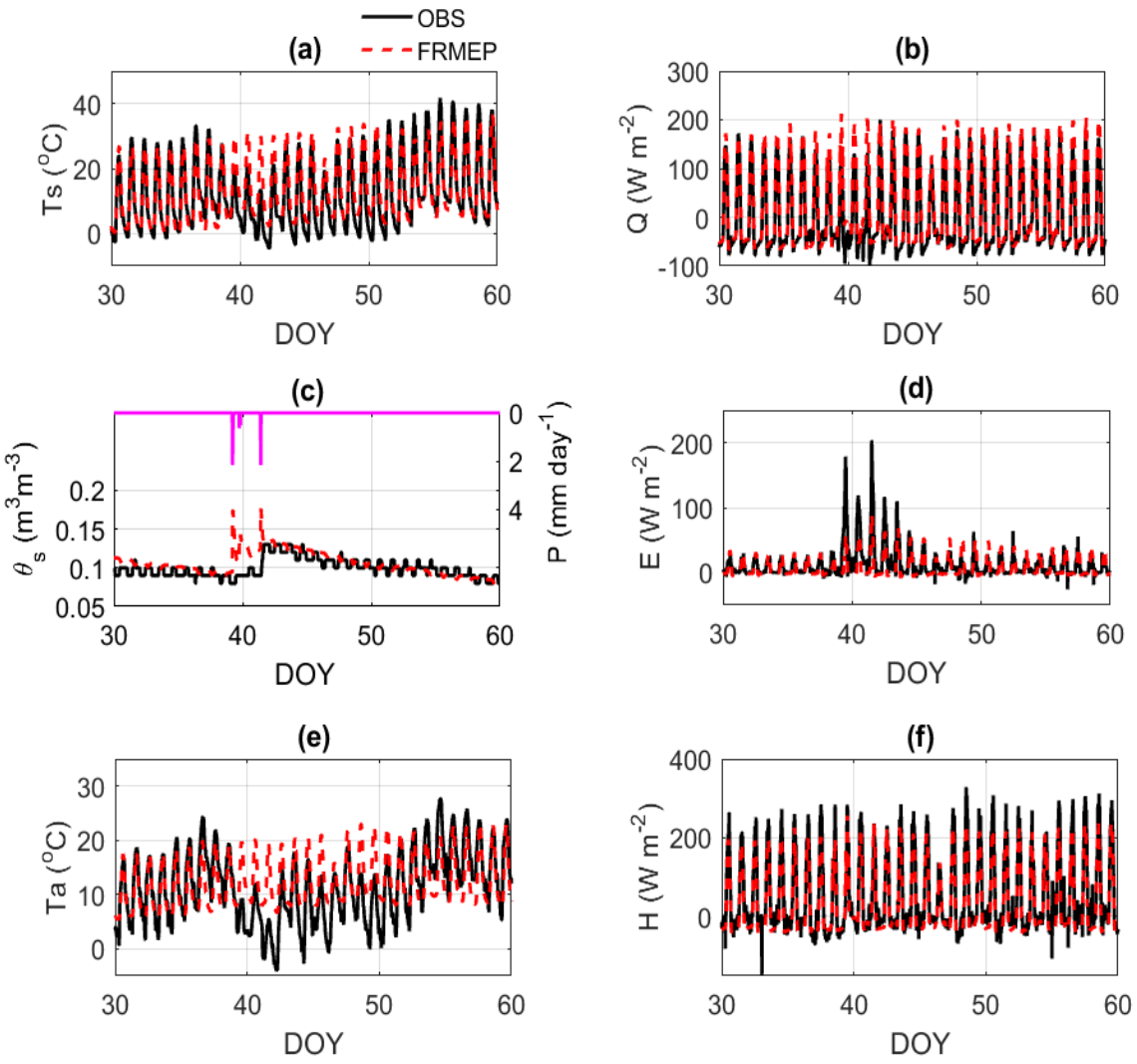

Figure 3.18: 30-minutes (a) T_s, (b) Q_{MEP}, (c) θ_s, (d) E_{MEP}, (e) T_a, and (f) H_{MEP} predicted by the FRMEP model (dashed red) versus observations (solid black) of the LH site, January 30 to March 1, 2009. Precipitation P is shown on the top of (c).

3.7 Summary

In this study, a coupled force-restore model of surface temperature, soil moisture, and near-surface air temperature (FRMEP) is formulated by incorporating the MEP model of surface heat fluxes and including the gravitational drainage term. The FRMEP model is

driven by surface radiation and precipitation data without using other meteorological variables, such as air temperature, humidity, wind speed and surface roughness lengths among others. The FRMEP model has reduced sensitivity to the uncertainties of model inputs and parameters compared to the classical FRMs.

The newly formulated FRMEP model was evaluated using observations from two field experiments with contrasting climate and soil moisture conditions. The case studies suggest that the FRMEP model predicted surface temperature, soil moisture, near-surface air temperature, and heat fluxes are in close agreements with observations at the two sites with significant contrasts in climatic and soil wetness conditions. This study shows that the FRMEP model provides more reliable predictions compared to classical FRMs, which are driven by observed or bulk parameterized heat fluxes. For short-term simulations, the modeling errors of the FRMEP predictions are in general lower than those of the classical FRMs, which are forced by observed or bulk formula based surface heat fluxes (bias 1~2 ^{o}C vs. ~4 ^{o}C for surface temperature, 0.02 m^3 m^{-3} vs. 0.05 m^3 m^{-3} for surface soil moisture, less than 1 ^{o}C vs. 2~3 ^{o}C for near-surface air temperature). The diurnal variations of surface temperature, soil moisture, near-surface air temperature and surface heat fluxes are well captured by the FRMEP model evidenced by the high correlations between the model predictions and observations (above 0.7). The one-year simulation showed that the FRMEP model well captures the seasonal variations of surface temperature, soil moisture, and near-surface air temperature (correlations 0.93, 0.93, and 0.87, respectively) with mean biases of 1.7 ^{o}C, 6×10^{-3} m^3 m^{-3}, and 0.49 ^{o}C, respectively.

This study also shows that the MEP modeled surface heat fluxes improve the FRMEP model performance during nighttime and rainy period whenever the observed heat

fluxes have large measurement errors. The revised FRM of soil moisture, taking the gravitational drainage term into account, significantly improves the soil moisture predictions under high soil moisture conditions. This suggests that the drainage term cannot be neglected under wet soil condition. The results of the one-year simulation indicate that the specification of model parameters, such as the reference temperatures of the FRMs and the wetness function for determining surface humidity, is the major limitation and source of uncertainty of applying the FRMEP model to long-term simulations.

CHAPTER 4. NEW ESTIMATES OF GLOBAL SURFACE ENERGY BUDGETS BASED ON THE MEP MODEL

4.1 Motivation

One major challenge in the study of global climate change is monitoring and modeling of surface energy and water budgets. Numerous studies (e.g. Trenberth et al., 2009; Jiménez et al., 2011; Mueller et al., 2011, 2013) showed that the existing global data products have difficulties producing consistent estimates of surface energy budgets, especially surface heat fluxes. These difficulties are arguably as a result of the drawbacks of the commonly used BTMs as discussed in Section 2.3.1. The estimates of global surface energy fluxes at regional and sub-annual time scales are expected to have even higher uncertainties. More importantly, there are no estimates of global water-snow-ice surface conductive heat fluxes to balance the surface upward longwave radiation, latent heat, and sensible heat over transparent surface media (Eq. (2.2)).

Another potential source of error and uncertainty in the existing global surface energy budget estimates is the exclusion of contributions from the polar regions and sea ice covered area (e.g., Stephens et al., 2012). Snow-ice surface heat fluxes are fundamental components of surface energy budget in permafrost regions (Strasser et al., 2008; Westermann et al., 2009). Over snow-ice surfaces, the surface energy balance determines the amount of energy that is available for sublimation and melting/freezing, which directly couples the surface energy balance to the surface mass balance (van den Broeke et al., 2011). However, few existing models simulate the full seasonal sublimation (e.g., Grachev

et al., 2007) due to logistical difficulties and extreme environmental conditions. Lynch et al. (1999) showed that the quantification of latent and sensible heat fluxes under arctic conditions still faces challenges from both measurement and modeling aspects.

The MEP model, which has enhanced physical constraints and reduced uncertainty compared to conventional flux models, provides a new promising method to fill the gaps in our current understanding of global surface energy budgets. In this study, global climatology of surface heat fluxes together with the corresponding uncertainty is re-evaluated using the MEP model utilizing the input data from contemporary remote sensing and reanalysis products with global coverage. The corresponding regional and seasonal analyses evaluated at continental and ocean basin scales are examined to quantify their contributions to global surface energy budgets. Global sublimation/deposition, sensible, and surface conductive heat fluxes over land snow-ice and sea ice covered areas are produced separately owing to the unique formulation of the MEP model. The global contributions of polar region heat fluxes to the global surface heat flux budgets is quantified for the first time. Land snow and sea ice cover effects on the estimates of global surface heat flux budgets are also analyzed.

The formulation of the MEP model of heat fluxes over water-snow-ice surface as well as the uncertainty estimates are given in Sections 4.2 and 4.3. A description of remote sensing observations and reanalysis data products used in this study is given in Section 4.4. Section 4.5 compares the MEP-based estimates of global surface energy budgets and previous estimates. The results of regional analysis are given in Section 4.6. Section 4.7 presents an analysis of the MEP estimated global land snow-ice and sea ice surface heat fluxes. Section 4.8 gives a brief summary of the new estimates.

4.2 The MEP Model of Heat Fluxes over Water-snow-ice Surfaces

The MEP model of heat fluxes over land surfaces is described in Section 3.3. For the case of water-snow-ice surfaces (transparent media), the dissipation function D_s is expressed as a function of surface latent E, sensible H, and water-snow-ice conductive Q (within the cool skin) heat flux (Wang et al., 2014):

$$D_s = \frac{2(Q + R_n^S)^2}{I_{wsi}} + \frac{2H^2}{I_a} + \frac{2E^2}{I_e} \tag{4.1}$$

where R_n^S is the surface net solar radiation (W m^{-2}), I_{wsi} the thermal inertia parameter of water-snow-ice media (J m^{-2} K^{-1} s$^{-1/2}$ ≡ tiu). I_a and I_e are identical to those in Eqs. (3.31) and (3.32).

Under the surface energy constraint as in Eq. (2.2), the MEP model predicted E, H, and Q through the following algebraic equations (Wang et al., 2014):

$$\begin{cases} \left[1 + B(\sigma) + \dfrac{B(\sigma)}{\sigma}\dfrac{I_{wsi}}{I_0}|H|^{\frac{-1}{6}}\right]H = R_n \\ E = B(\sigma)H \\ Q = R_n^L - E - H \end{cases} \tag{4.2}$$

where R_n^L is the surface net longwave radiation (W m^{-2}). The definitions of the other variables have been given in Section 3.3. The formulations of σ and $B(\sigma)$ are given in Eqs. (3.32) and (3.34), respectively. The vertical distance z in I_0 (Eq.(3.31)) is set at 2.5 m above the surface where the sensitivity of the MEP model predicted heat fluxes on z is weak. Over water-snow-ice surfaces, q_s is often assumed to be the saturation humidity at T_s. Therefore, σ as well as $B(\sigma)$ is a function of T_s alone according to the Clausius-

Clapeyron equation. Note that over water-snow-ice surfaces, MEP E and H are solved from T_s and R_n only, while MEP Q requires R_n^S or R_n^L ($Q = R_n^L - E - H$) according to Eq. (4.2). In contrast, the MEP Q over land surfaces only need input of R_n (Eq.(3.33)) since soil is non-transparent to sunlight.

The thermal inertia parameter I_{wsi} is defined as

$$I_{wsi} \equiv \sqrt{\rho_{wsi} c_{wsi} \lambda_{wsi}} \tag{4.3}$$

where ρ_{wsi} is the bulk density, c_{wsi} the specific heat, and λ_{wsi} the thermal conductivity of water-snow-ice media. Over water and ice surfaces, I_{wsi} are estimated as 1560 and 1920 tiu (with ρ_w = 10^3 kg m^{-3} the density, c_w = 4.18×10^3 J kg^{-1} K^{-1} the specific heat, λ_w = 0.58 W m^{-1} K^{-1} the heat conductivity of liquid water; ρ_i = 0.92×10^3 kg m^{-3} the density, c_i = 1.82×10^3 J kg^{-1} K^{-1} the specific heat, and λ_i = 2.2 W m^{-1} K^{-1} the heat conductivity of ice). Over snow surfaces, I_{wsi} is expressed as a function of snow density ρ_{snow} with the thermal conductivity λ_{snow} parameterized as (e.g., Mellor, 1977; Fujita and Ageta, 2000)

$$\lambda_{snow} = 0.029(1 + 10^{-4}\rho_{snow}^2) \tag{4.4}$$

and the specific heat of snow c_{snow} set to be identical to that of ice. In this study, sublimation/deposition, sensible heat, and conductive heat fluxes over land snow-ice/sea ice surfaces are denoted by ESI, HSI, and QSI, respectively, to make a distinction between heat fluxes over snow-ice and water surfaces.

It is important to re-emphasize that the MEP model allows the heat fluxes to be retrieved from radiation, temperature and/or humidity without using temperature and humidity gradients, wind speed, and surface roughness length(s) data. The MEP model

parameterizes the same physical processes underlying the fluxes as those in the existing flux models including the bulk transfer model (BTM). The difference is that the MEP method makes a more effective use of the information that is most relevant to heat fluxes provided by the surface variables (radiation, temperature, and/or humidity) than the conventional methods.

4.3 Uncertainty of the MEP Surface Heat Fluxes

The MEP model predicted surface heat fluxes, as in Eqs. (3.33) (land) and (4.2) (water-snow-ice), are mathematically expressed as functions of R_n, the dimensionless variable $\sigma \propto q_s / T_s^2$ and model parameter $\beta_s \equiv I_s / I_0$. The uncertainty of a flux X ($X = E$, H, Q), ΔX, may be expressed as

$$\Delta X = \frac{\partial X}{\partial R_n}\Delta R_n + \frac{\partial X}{\partial \sigma}\Delta\sigma + \frac{\partial X}{\partial \beta_s}\Delta\beta_s \tag{4.5}$$

where ΔR_n, $\Delta\sigma$, and $\Delta\beta_s$, are the uncertainties of R_n, σ, and β_s, respectively. $\Delta\sigma$ and $\Delta\beta_s$ are related to the uncertainties of ΔT_s, Δq_s, ΔI_s, and ΔI_0 through

$$\Delta\sigma = \frac{\partial \sigma}{\partial T_s}\Delta T_s + \frac{\partial \sigma}{\partial q_s}\Delta q_s = \sigma\left(\frac{\Delta q_s}{q_s} - 2\frac{\Delta T_s}{T_s}\right) \tag{4.6}$$

$$\Delta\beta_s = \frac{\partial \beta_s}{\partial I_s}\Delta I_s + \frac{\partial \beta_s}{\partial I_0}\Delta I_0 = \beta\left(\frac{\Delta I_s}{I_s} - \frac{\Delta I_0}{I_0}\right) \tag{4.7}$$

The partial derivatives in Eq. (4.5) are derived from Eqs. (3.33) and (4.2):

$$\frac{\partial H}{\partial R_n} = \left[1 + B + \frac{5B}{6\sigma}\beta\,|H|^{\frac{-1}{6}}\right]^{-1} \tag{4.8}$$

$$\frac{\partial E}{\partial R_n} = B\frac{\partial H}{\partial R_n} \tag{4.9}$$

$$\frac{\partial Q}{\partial R_n} = 1 - \frac{\partial E}{\partial R_n} - \frac{\partial H}{\partial R_n} \tag{4.10}$$

$$\frac{\partial H}{\partial \sigma} = H\left[\frac{-11}{2(B-6)} + \frac{2B(B+6) - 11\sigma}{2\sigma(B+6)}\frac{\beta}{\sigma}|H|^{\frac{-1}{6}}\right]\left[1 + B + \frac{5B}{6\sigma}\,\beta|H|^{\frac{-1}{6}}\right]^{-1} \tag{4.11}$$

$$\frac{\partial E}{\partial \sigma} = \frac{11}{2(B+6)}H + B\frac{\partial H}{\partial \sigma} \tag{4.12}$$

$$\frac{\partial Q}{\partial \sigma} = -\frac{\partial E}{\partial \sigma} - \frac{\partial H}{\partial \sigma} \tag{4.13}$$

$$\frac{\partial H}{\partial \beta_s} = \frac{-11}{2(B+6)}H|H|^{\frac{-1}{6}}\left[1 + B + \frac{5B}{6\sigma}\beta|H|^{\frac{-1}{6}}\right]^{-1} \tag{4.14}$$

$$\frac{\partial E}{\partial \beta_s} = B\frac{\partial H}{\partial \beta_s} \tag{4.15}$$

$$\frac{\partial Q}{\partial \beta_s} = -\frac{\partial E}{\partial \beta_s} - \frac{\partial H}{\partial \beta_s} \tag{4.16}$$

For the cases of water-snow-ice surfaces, Δq_s in Eq. (4.6) drops out as q_s over saturation surface is a function of T_s, while ΔI_s = 0 since the thermal inertia of liquid water, snow, and ice are known constants. $\Delta\sigma$ is dominated by Δq_s due to relatively large uncertainty of humidity measurements (e.g., $\Delta q_s/q_s$~10% vs. $\Delta T_s/T_s$~0.3%). In this study, uncertainty of I_0 is ignored when the empirical coefficients in the MOSE are assumed to be known as fixed constants. Then, the uncertainty of I_s, hence β_s, is caused by that of the thermal inertia of dry soil I_d and soil moisture θ according to Eq. (3.12). The uncertainty of I_s due to the measurement error of soil moisture ~0.04 m^3 m^{-3} is about 50 tiu according to Eq. (3.12) (Yi et al., 2011; Lakshmi, 2013). The dominant soil types of the Earth include sandy loam, loam, silt loam, sandy clay loam, and clay loam (Nachtergaele et al., 2012)

with thermal inertia in the range of 600-1000 tiu (Farouki, 1982; Wang et al., 2010). In this analysis, a constant I_d = 800 tiu is used as a representative value of I_d. Combing the two sources of uncertainties of I_s leads to a maximum $\Delta I_s/I_s \cong 20\%$. Note that I_s and the associated uncertainty only affect the MEP fluxes over two thirds of the land masses which are not covered with dense vegetation.

4.4 Data Products

Surface radiation and temperature data from NASA CERES (Wielicki et al., 1996) during 2001-2010 are used as the input of the MEP model. The CERES is a set of radiometers designed based on the ERBE (Barkstrom et al., 1989). The CERES data is derived from observations made by the Terra and Aqua satellites, which have improved spatial resolution and instrument calibration than previous generation of the ERBE products. The surface radiation from the CERES SYN 1deg-3Hour data product (Edition 3A, Level 3) with 3-hourly 1°×1° resolution is used (http://ceres.larc.nasa.gov/-products.php?product-=SYN1deg). The CERES SYN1deg-3Hour surface radiative fluxes are computed based on the Langley Fu-Liou radiative transfer model (Fu and Liou, 1993) using the cloud properties from Moderate Resolution Imaging Spectroradiometer (MODIS) and geostationary satellite, atmospheric profiles from NASA GMAO, and aerosol properties from MODIS. The modeled radiative fluxes are constrained (tuned) to the observed CERES TOA fluxes. The CERES surface temperature data are obtained using the GMAO GEOS-4 and 5 reanalysis (Rienecker et al., 2008). The uncertainty of CERES global, land, and ocean annual surface net radiation (12, 16, and 14 W m^{-2}, respectively)

estimated based on the observations of cloud and aerosols properties from the CALIPSO, CloudSat, and MODIS (Kato et al., 2012) will be used in the uncertainty analysis of the MEP fluxes in this study.

Surface specific humidity and top layer soil moisture data over the same period are available from the NASA MERRA reanalysis dataset (product tavg1_2d_flx_Nx and tavg1_2d_mld_Nx, available at http://disc.sci.gsfc.nasa.gov/daac-bin/DataHoldings.pl) with hourly $0.5^o \times 0.67^o$ resolution (Bosilovich et al., 2011; Rienecker et al., 2011). The MERRA surface humidity and soil moisture data were converted to 3-hourly $1^o \times 1^o$ resolution consistent with the CERES data products. Snow mass, snow depth, and fractional snow and sea ice coverage data, originally at hourly $0.5^o \times 0.67^o$ resolution from MERRA, are applied at daily $1^o \times 1^o$ resolution in the MEP simulations.

Land-cover data are adopted from the International Geosphere-Biosphere Programme (IGBP) land cover climatology with 1/60 degree resolution (Townshend, 1992) (http://modis-atmos.gsfc.nasa.gov/ECOSYSTEM/-format.html). The IGBP data were converted to $1^o \times 1^o$ resolution providing the fractional coverage of each surface type (e.g., bare soil, vegetated, water, ice). The fractional coverage of each surface type based on the IGBP data (climatology) was updated daily by incorporating fractional snow and sea ice coverage data from MERRA. Snow and sea ice cover changes the surface energy budgets through the change of (1) surface type (from soil to snow) and (2) thermal properties (e.g., from water to ice). Figure 4.1 shows an example of the changes of fractional land and ocean coverages due to snow and sea ice on January 10, 2005. The surface type over Antarctica and Greenland was set to be permanent ice according to the IGBP land cover climatology data since the MERRA snow data are not available over the

polar regions (PoRs). The PoRs are defined as the regions beyond 61.5^{o} latitude (north and south) in this study.

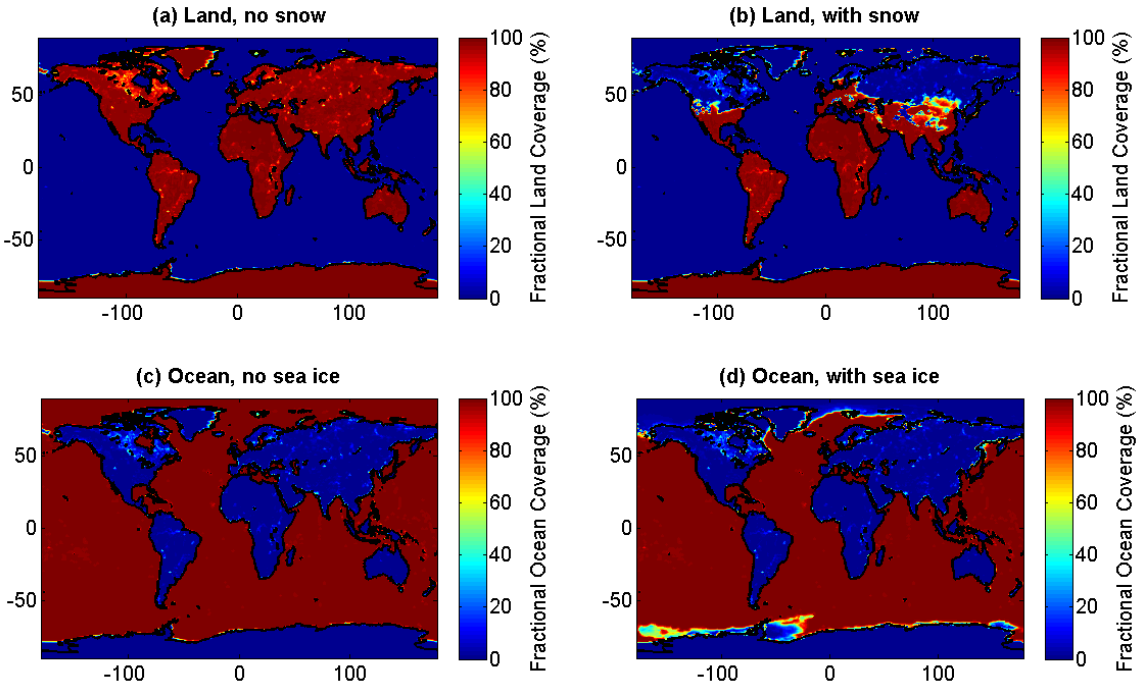

Figure 4.1: Fractional coverage of land (a) without (b) with snow presence and ocean (c) without (d) with sea ice presence on January 10, 2005.

The MEP-based estimates of global and regional surface energy budgets will be compared with other estimates from reanalysis data products and previous studies (see Section 2.4). The delineations of continents and oceans are based on those provided by the NASA Energy and Water Cycle Study (NASA NEWS) - Climatology of the First Decade of the Twenty-first Century Dataset (Rodell et al., 2015). Note that the ocean surface (conductive) heat flux Q from the existing products is computed as a residual of the energy balance equation as in Eq. (2.2) since it is not available from existing products. The data products used for model inputs and validation are list in Tables 4.1 and 4.2. As surface heat flux data over the PoRs are essentially non-existence, the analyses of the MEP surface heat

fluxes exclude the contributions from the PoRs when compared with previous estimates for the purpose of consistency. An analysis of the MEP estimates of surface heat fluxes over the PoRs as well as snow and sea ice covered areas will be given in Section 4.7.

Table 4.1: List of data products used for model inputs of the MEP simulations

Variable	Source of Data	Time Period	Resolution	
			Spatial	Temporal
R_n, R_n^L	NASA CERES	2001-2010	1°×1°	3-hourly
T_s	GMAO GEOS	2001-2010	1°×1°	3-hourly
q_s, θ_s	NASA MERRA	2001-2010	0.5°×0.67°	hourly
ρ_{snow} (Mass/Depth), Snow/Sea ice Coverage	NASA MERRA	2001-2010	0.5°×0.67°	hourly
Land Cover	IGBP	-	1/60 °×1/60 °	-

Table 4.2: List of data products used for validating the MEP estimates of surface heat fluxes

Data Set	Time Period	Resolution	
		Spatial	Temporal
NASA MERRA	2001-2010	0.5°×0.67°	Monthly
NASA GLDAS-NOAH	2001-2010	1°×1°	Monthly
WHOI OAFlux	2001-2010	1°×1°	Monthly
National Climatic Data Center (NCDC) (now National Centers for Environmental Information, NCEI)	2001-2010	-	Yearly

4.5 MEP-based Estimates of Global Surface Heat Fluxes

4.5.1 Global Land Area

Figure 4.2(a) shows the MEP model predicted 2001-2010 climatology (annual mean) of evapotranspiration (or latent heat flux) E over lands using the 3-hourly CERES surface net radiation and temperature data supplemented by the MERRA surface specific humidity and soil moisture data. The MEP estimated annual mean E , 492 mm yr^{-1} (1.35 mm d^{-1} or 39 W m^{-2}), is consistent with earlier estimates including, for example, the 1982-2008 climatology ~478 mm yr^{-1} (Jung et al., 2010, Figure 4.2(b)) based on the analysis combining global ground fluxes network, satellite remote sensing with surface meteorological data. The MEP estimated global annual mean E is consistent with the NASA GLDAS reanalysis data, 467 mm yr^{-1} (37 W m^{-2}) (Rodell et al., 2004; Wang and Dickinson., 2012, see Figure 4.2(d)), but lower than 642 mm yr^{-1} from the MERRA reanalysis data (Figure 4.2(c)) although with similar spatial patterns. The global annual mean of MEP E is also comparable to other existing reports and data products shown in Table 4.3. Other reported estimates, e.g., Figure 1(a) in (Mueller et al., 2011), Table 8 in (Wang and Dickinson, 2012), range from 303 mm yr^{-1} (0.83 mm d^{-1} or 24.1 W m^{-2}) to 730 mm yr^{-1} (2 mm d^{-1} or 58 W m^{-2}). The spatial pattern of the MEP E is consistent with that of R_n and q_s shown in Figures 4.3(a) and 4.3(c) suggesting that the MEP modeled E is dominated by surface radiation energy and humidity conditions.

The uncertainty of the global annual mean MEP E over lands is 126 mm yr^{-1} (0.35 mm d^{-1} or 10 W m^{-2}) according to Eqs. (4.5)-(4.16) (see also Table 4.3). Table 4.4 provides the corresponding representative values of the partial derivatives and model

input/parameter uncertainties of the MEP surface heat fluxes as in Eqs. (4.5)-(4.16) and the relative contributions of R_n, σ, and β_s to the MEP surface heat fluxes. The results show that 57% of the uncertainty of MEP E over lands is attributed to that of the net radiation data, 27% to the parameter σ representing the uncertainties from temperature and humidity data, and 16% to the thermal inertia parameter β_s at annual scale (see Table 4.4(b)).

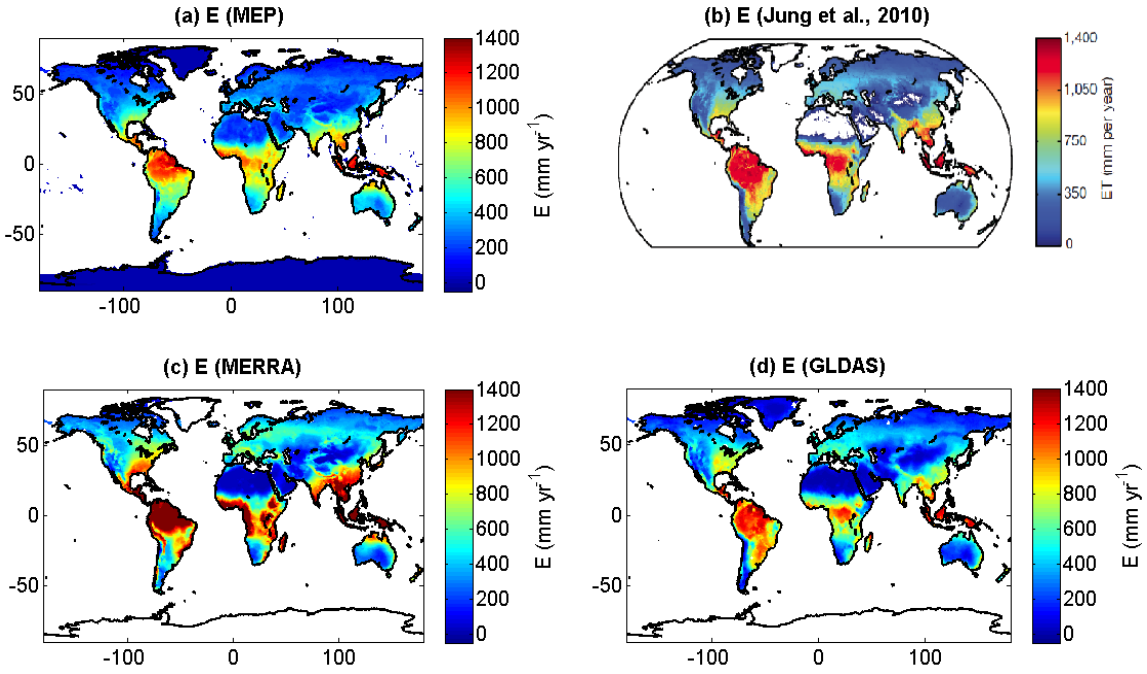

Figure 4.2: Annual mean *E* over land surfaces estimated by (a) MEP model (2001-2010) according to Eq. (3.33) using the 3-hourly CERES SYN1deg-3Hour surface net radiation, GMAO GEOS surface temperature, and the MERRA reanalysis surface specific humidity data; (b) FLUXNET, satellite remote sensing and surface meteorological data over 1982-2008 (Jung et al., 2010); (c) MERRA (2001-2010); and (d) GLDAS (2001-2010) data products

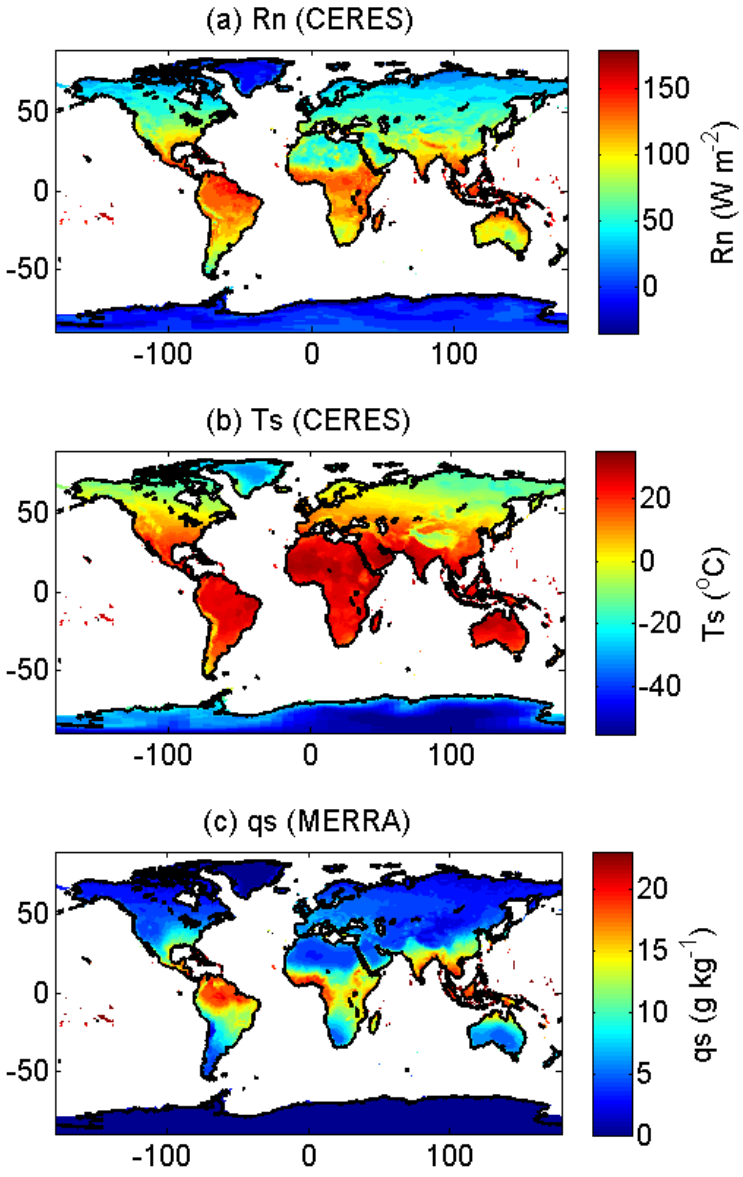

Figure 4.3: Global annual mean of CERES (a) R_n, (b) T_s, and MERRA (c) q_s over 2001-2010.

Figure 4.4 shows the 2001-2010 climatology (annual mean) of MEP modeled H and Q over lands compared with the MERRA and GLDAS reanalysis data. Note that Q is assumed to be zero when land surface is covered with snow/ice due to the insulating effect of snow/ice pack that prevents the soil from both warming and cooling (Zhang, 2005; Iwata et al., 2008). Solar radiation penetrating snow surfaces (R_0) is mostly absorbed by the

snowpack caused by the large extinction coefficient (e-folding length), i.e., rapid irradiance attenuation within snowpacks (e.g., O'Neill and Gray, 1973; Grenfell and Maykut, 1977). The penetration depth of short wave radiation to snow is less than 10 cm with only 3-4% of incoming solar radiation can reach the soil surface below 10 cm of snow (Baker et al., 1991; Järvinen and Leppäranta, 2013). Previous studies have shown that the T_s below snowpacks remains quasi-stationary resulting in a zero Q during snow-covered periods (e.g., Hoelzle et al., 2001; Boike et al., 2003; Iwata et al., 2008; LaMontagne, 2009; Gądek and Leszkiewicz, 2010; Lund et al; 2017). Over permeant ice surfaces (e.g., polar and alpine regions), R_0 is difficult to reach the soil surface as the thickness of ice packs above are easily exceed tens of meters (typical extinction coefficient ~1.5 m^{-1}). In earler snow energy balance models, Q is often neglected (Male and Gray, 1981; Berris and Harr, 1987).

The global annual mean MEP H, 33 W m^{-2}, agrees with several earlier estimates (Table 4.3), but lower than the GLDAS (51 W m^{-2}) and MERRA (41 W m^{-2}) estimates. The spatial pattern of MEP H is consistent with that of CERES R_n but substantially different from the MERRA and GLDAS data. Note that the GLDAS and MERRA H have noticeably different spatial patterns even though they are calculated using the BTM. The uncertainty of the MEP modeled global annual mean H, 7 W m^{-2} (Table 4.3), is attributed to that of R_n (67%), σ (14%), and β_s (19%) as shown in Table 4.4(b).

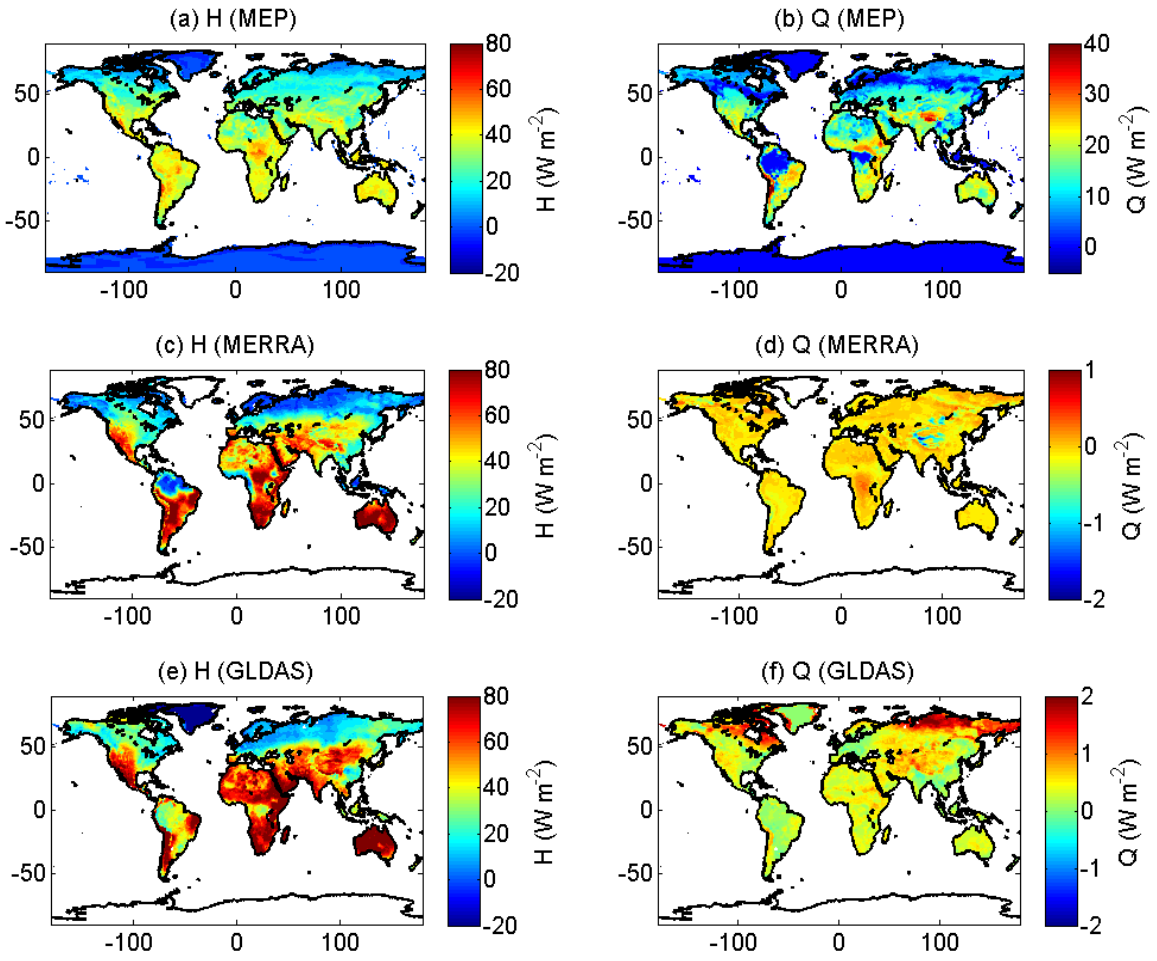

Figure 4.4: The MEP estimated global (a) sensible heat H and (b) ground heat Q versus the MERRA (c) H (d) Q and GLDAS (e) H (f) Q. The MEP modeled H and Q are obtained according to Eq. (3.33) using the 3-hourly CERES SYN1deg-3Hour surface net radiation and surface temperature, and the MERRA surface specific humidity data. All fluxes are annual means over 2001-2010.

The MEP model estimates a global annual mean Q of 14 W m^{-2} over lands shown in Table 4.3. The spatial distribution of the MEP Q depends on land cover with vanishing Q over dense-canopy-covered (Amazonia, high latitude North America, and the Eurasian continent) as shown in Figure 4.4(b). The 14 W m^{-2} of global annual mean MEP Q over lands using the 3-hourly CERES R_n and T_s is likely overestimated caused by the effects of the temporal resolution of the input data on the MEP simulation. A sensitivity analysis

(Huang et al., 2014) on the effects of the temporal resolution of input data on the MEP fluxes using field observations showed that using daily data in the MEP model tends to overestimate daily Q by one third, as compared to that using half-hourly data. 54%, 16%, and 30% of the 10 W m^{-2} uncertainty of global annual mean MEP Q are caused by the uncertainty of R_n, σ, and β_s, respectively (see Table 4.4(b)).

Table 4.3: Global annual means of land surface heat fluxes estimated by the MEP model according to Eq. (3.33), CERES surface net and net longwave radiation, and products from MERRA reanalysis, Global Land Data Assimilation System (GLDAS), NCEP reanalysis, Japanese reanalysis (JRA), and other published studies. (Unit: W m^{-2}).

Variable	E	H	Q	R_n	R_n^L	$R_n - E - H$ $(= R_0 + Q)$
MEP (2001-2010)	39±10	33±7	14±10	88±16	-70±11	-*
MEP (2001-2010, with polar regions)	35	30	13	78	-66	-*
Trenberth et al. (2009)	39	27	0[a]	66	-80	-*
MERRA (2001-2010)	51	41	0[a]	92	-74	-*
GLDAS (2001-2010)	37	51	0.5	88	-65	-*
NCEP/NCAR[1]	51	26	3[a]	80	-73	-*
NCEP/DOE II[1]	52	13	7[a]	72	-71	-*
CFSR[1]	38	35	0[a]	74	-66	-*
JRA[2]	39	27	2[a]	69	-87	-*
Jiménez et al. (2011)	45±15	45±15	0[a]	90±15	-	-*
Mueller et al. (2011)	48±6	-	-	-	-	-
Mueller et al. (2013)	39±12	-	-	-	-	-
Wang & Dickinson (2012)	35±9	-	-	-	-	-
Vinukollu et al. (2011a)	42±5	-	-	-	-	-
Yuan et al. (2010)	33±3	-	-	-	-	-
Zhang et al. (2010a)	43	-	-	-	-	-

a: Q calculated as the residual of the energy balance equation as in Eq. (2.1)
***: $R_n - E - H = Q$ over land surfaces**
1: Wang et al. (2011)
2: Trenberth et al. (2009)

Table 4.4: (a) Representative values of the partial derivatives and uncertainties of variables in Eq. (3.33) calculated at the global annual mean radiation fluxes, temperature and humidity data over lands, and (b) relative contributions of uncertainties (%) of the independent variables R_n, σ, and β_s to the uncertainties of the MEP land surface heat fluxes according to Eqs. (4.5)-(4.16).

	E	H	Q
(a)			
$\lvert\partial X/\partial R_n\rvert$	**0.35**	**0.31**	**0.34**
ΔR_n		**16**	
$\lvert\partial X/\partial\sigma\rvert$	**17.40**	**7.10**	**10.31**
$\Delta\sigma$		**0.15**	
$\lvert\partial X/\partial\beta_s\rvert$	**4.99**	**4.40**	**9.39**
$\Delta\beta_s$		**0.48**	
(b)			
R_n	**57**	**67**	**54**
σ	**27**	**14**	**16**
β_s	**16**	**19**	**30**

The land mass gaining thermal energy at annual scale predicted by the MEP model is consistent with the estimates from NCEP reanalysis products (Table 4.3), while the MERRA and GLDAS reanalysis products have a nearly zero annual mean Q (< 1 W m^{-2} as shown in Table 4.3). In the MERRA and GLDAS LSMs, Q is linearly proportional to the near-surface temperature gradient (Pan and Mahrt, 1987; Chen et al., 1996; Koster et al., 2000; Ek. et al., 2003). However, the temperature gradient calculated using surface temperature and an averaged soil temperature of top soil layer (5-10 cm) tends to be underestimated due to the sharp gradient of soil temperature near the surface leading to underestimated Q.

Table 4.3 further shows that the MEP global annual mean E, H, and Q over lands decrease by about 4, 3, and 1 W m^{-2}, respectively, when including the PoRs. The MEP H over Greenland is small positive (< 10 W m^{-2}), while the GLDAS data give a relatively

large negative H (< -20 W m^{-2}). Several reasons may be responsible for the discrepancies. For example, the MEP and GLDAS (BTM-based) estimates use different surface energy balance equations over snow-ice surfaces (Eq. (2.2) vs. (2.3)). The uncertainties from model inputs (e.g., wind speed) and parameters (e.g., SRLs) are difficult to quantify as they are not explicitly used in the MEP model. Also, the CERES R_n used in the MEP simulations are consistently greater than the GLDAS R_n. The uncertainty of MEP heat fluxes caused by the use of different radiation inputs requires further assessment. The zero MEP Q over Greenland is consistent with the GLDAS estimates, however, due to different reasons. The zero MEP Q are from the snow insulating effect (i.e., snow/ice pack absorbs surface solar radiation and prevents the soil from warming and cooling) resulting in zero amount of thermal energy entering the soil as discussed previously. By contrast, the zero GLDAS Q is a consequence of the assumption of zero surface net thermal energy at annual scale (i.e. Eq. (2.3)).

The global annual mean land surface heat fluxes (2001-2010) estimated by the MEP model and those from MERRA and GLDAS data are shown in Figure 4.5. The corresponding model inputs are shown in the right panel. The global annual mean MEP E over lands has an increasing trend of 5.18 mm yr^{-1} yr^{-1} (0.41 W m^{-2} yr^{-1}) during 2001-2010 with the 95% confidence interval (CI) of 2.90 mm yr^{-1} yr^{-1} (0.23 W m^{-2} yr^{-1}). The increasing trend of MEP E results from the increasing trend of CERES R_n and MERRA q_s as shown in Figures 4.5(b) and 4.5(f), while Jung et al. (2010) reported a decreasing trend of global annual mean E due to the decreasing trend of global soil moisture during 1998-2008 derived from the Tropical Rainfall Measuring Mission's (TRMM) (Owe et al., 2008). Higher R_n and q_s lead to higher E according to the MEP model. Higher R_n implies more

radiation energy for heat fluxes, while higher q_s favors radiation energy dissipated through latent heat of phase change. The increasing trend of global annual mean MEP E is consistent with the MERRA, but opposite to the GLDAS estimates as shown in Figure 4.5(a).

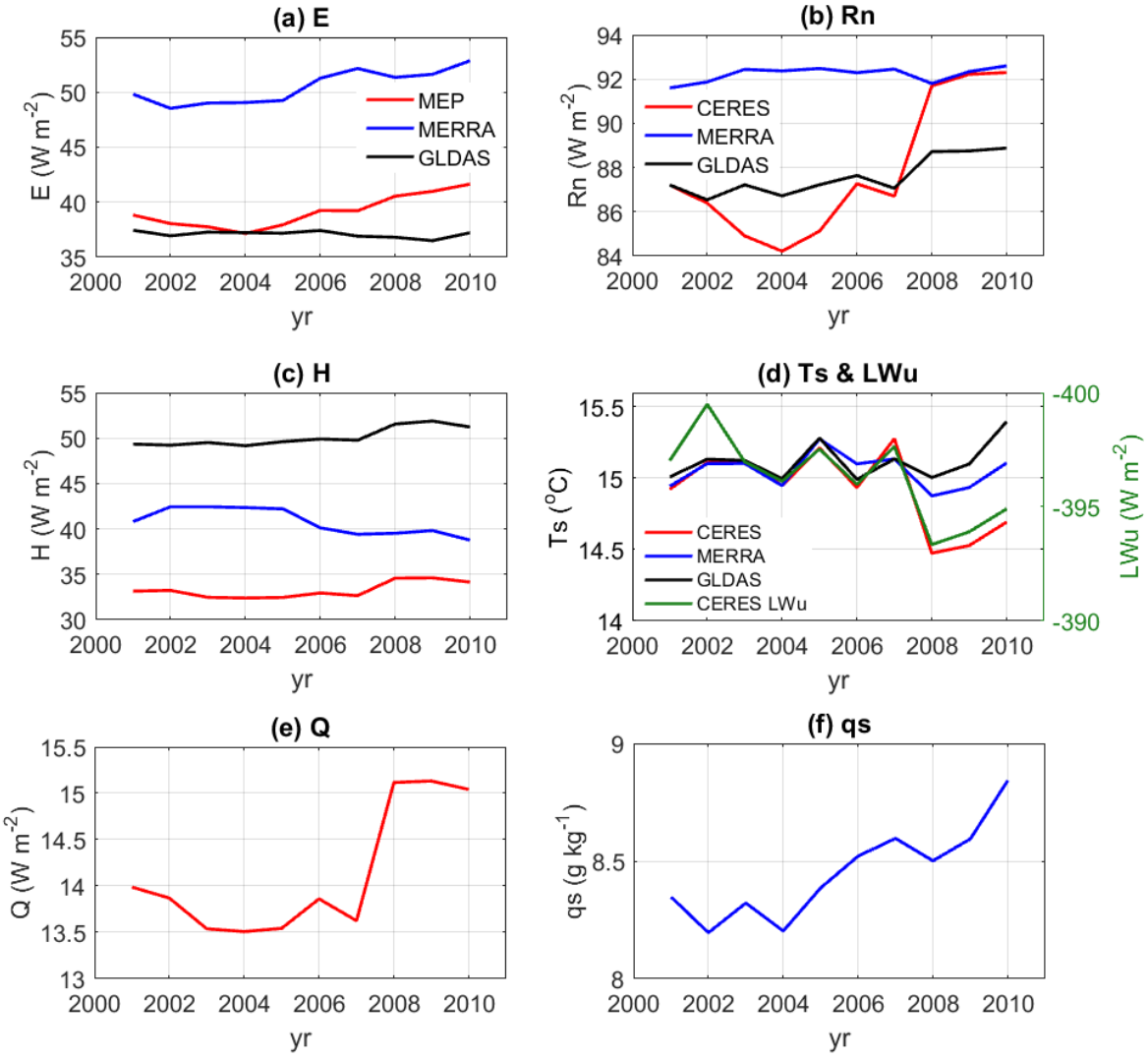

Figure 4.5: Global annual mean land surface (a) E, (c) H, and (e) Q estimated by the MEP (red), MERRA (blue), and GLDAS (black) (MERRA and GLDAS Q are essentially zero, not shown); (b) R_n (d) T_s (with CERES surface upward longwave radiation LWu (green)) data from CERES (red), MERRA (blue), and GLDAS (black); (f) MERRA q_s over 2001-2010.

The global annual mean MEP H over lands has an increasing trend of 0.18 W m^{-2} yr^{-1} (see Figure 4.5(c)) associated with the increasing trend of the CERES R_n as shown in Figure 4.5(b). The uncertainty of the trend is estimated as 0.18 W m^{-2} yr^{-1}. The increasing global mean H predicted by the MEP model is consistent with the GLDAS but opposite to the MERRA estimates (see Figure 4.5(c)). The trend of MEP H is opposite to that of CERES T_s as shown in Figure 4.5(d). Yet it has been shown that the decreasing trend of CERES T_s (also surface upward longwave radiation LWu (in magnitude)) is an artifact caused by the switch of the assimilated atmospheric temperature and humidity profile data between 2007 and 2008 (from GEOS-4.1 to GEOS-5.2.0, see CERES_SYN1deg_Ed3A data quality summary available at https://ceres.larc.nasa.gov/documents/DQ_summaries/-CERES_SYN1deg_Ed3A_DQS.pdf, see also Figure 4.5(d)). The MEP estimated global annual mean Q has a positive trend of 0.16 W m^{-2} yr^{-1} consistent with the increasing trend of CERES R_n. The 95% CI of the trend is 0.13 W m^{-2} yr^{-1}. The results of trend analyses are also listed in Table 4.10. An analysis of the impacts of the artifact in CERES T_s and radiation data on the trends of MEP estimated global surface heat fluxes is given in Secion 4.6.

The spatial distribution of the trends of MEP surface heat fluxes compared to those of the MERRA and GLDAS data are shown in Figure 4.6. The trends of MEP E and H agree more closely with those of MERRA as opposed to GLDAS estimates. The trend of MEP Q is positive over most of the land areas, while those of MERRA and GLDAS Q are essential zero as the corresponding annual means are nearly zero. The spatial pattern of the trend of MEP E (Figure 4.6(a)) is consistent with that of CERES R_n (Figure 4.6(j)) and MERRA q_s (Figure 4.6(l)), which again illustrates that E is dominated by the surface

radiation energy and humidity conditions in the MEP model. Figure 4.6(k) clearly shows that CERES T_s has an overall decreasing trend over lands, which is, however, due to the artifact of switching the source of atmospheric temperature and humidity profile datasets used in the meteorological assimilation system as mentioned previously.

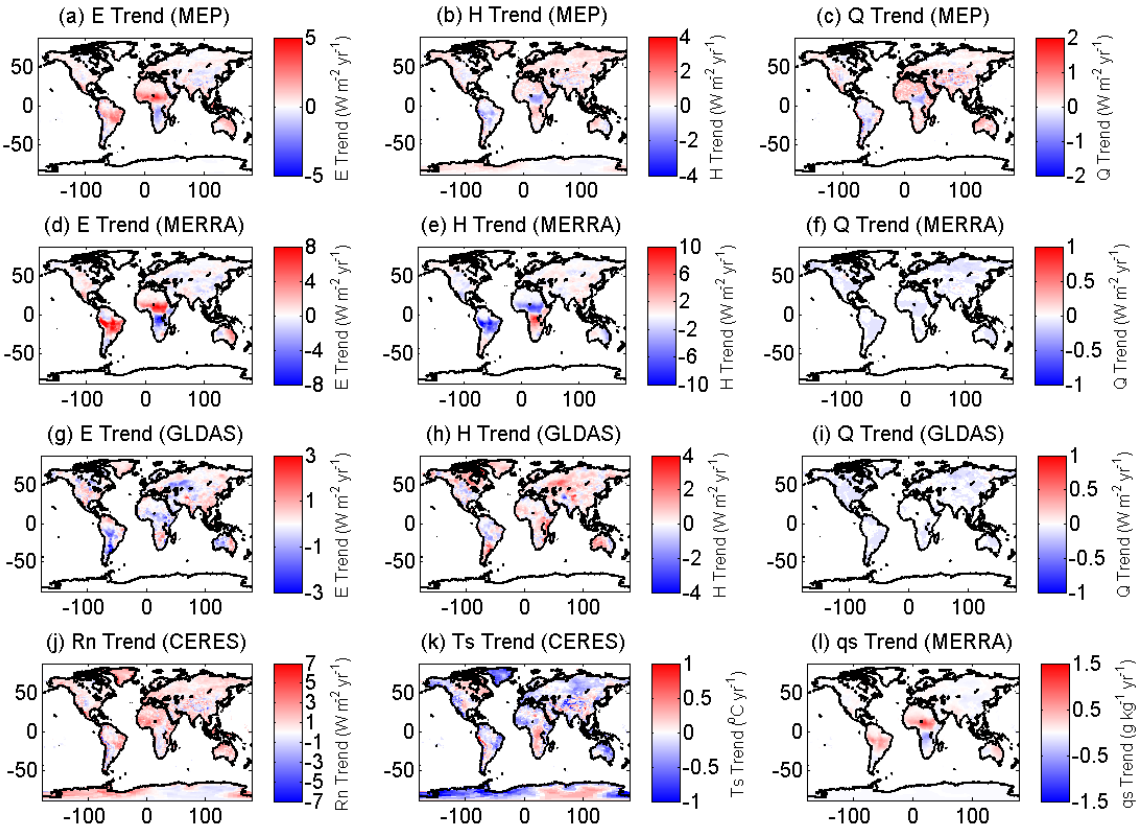

Figure 4.6: Annual trends (2001-2010) of MEP estimated (a) E (b) H (c) Q versus those of MERRA (d) E (e) H (f) Q and GLDAS (g) E (h) H (i) Q with those of CERES (j) R_n (k) T_s and MERRA (l) q_s over lands.

A comparison of the trend of MEP E with previous estimates is shown in Figure 4.7. The spatial pattern of the trend of MEP E is qualitatively consistent with those reported by (Jung et al., 2010; Yan et al., 2013; Zhang et al., 2016), while its magnitude is greater than previous estimates. It is speculated that the relatively large trend in MEP E might be

partially affected by the artifact in CERES radiation data (i.e., the abrupt increased in R_n (decreased LWu) due to the decreased T_s between 2007 and 2008, see Figure 4.5(d)).

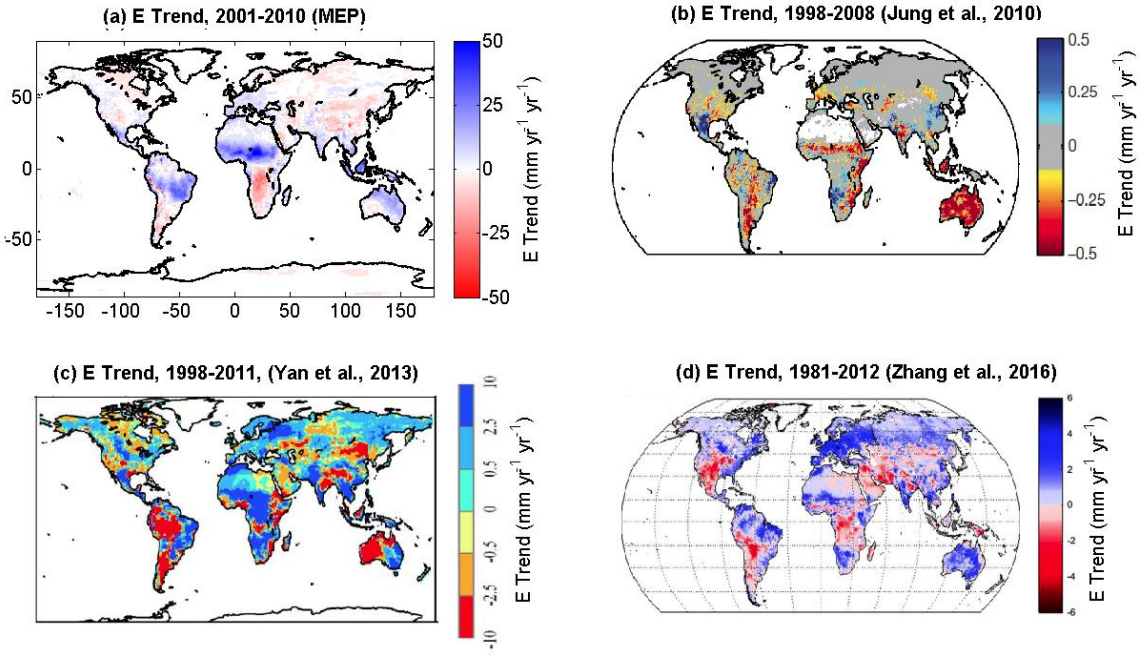

Figure 4.7: Annual trend (2001-2010) of MEP *E* over lands compared with previous studies. (a) is the same with Figure 4.6(a) with different units (mm yr^{-1} yr^{-1} vs. W m^{-2} yr^{-1}). Note that (a) uses revered color bar with Figure 4.6(a) to be consistent with previous studies.

4.5.2 Global Oceans

Figure 4.8 shows the 2001-2010 climatology of MEP estimated *E* and *H* over oceans using the 3-hourly CERES radiation fluxes and sea surface temperature (SST) data for the period 2001-2010 compared with those of the MERRA and OAFlux data. The spatial pattern of MEP *E* is consistent with both MERRA and OAFlux data, while the spatial distribution of MEP *H* is substantially different from the MERRA and OAFlux data. The spatial patterns of the MEP *E* and *H* are consistent with that of CERES R_n. The MEP

E and H are constrained by R_n, while the MERRA and OAFlux E and H over several regions, such as western and northern Pacific and Atlantic oceans, are unrealistically large (greater than R_n violating the conservation of energy). The MEP E is lower than the MERRA E for most areas, while the MEP H is in general greater than the MERRA H as shown in Figure 4.8. The global annual means of MEP ocean surface heat fluxes versus other previous estimates are summarized in Table 4.5. The MEP modeled annual mean E over oceans is 747±88 mm yr^{-1} (61±7 W m^{-2}), which is lower than the previous estimates ranging from 1130-1370 mm yr^{-1} (90-109 W m^{-2}). The global annual mean MEP H over oceans is 30±3 W m^{-2}, which is higher than the previous estimates of ~10-20 W m^{-2}.

Previous studies have shown that the MERRA E and H are subject to large uncertainty caused by the biases of model inputs, especially wind and vertical temperature/humidity gradient (Brunke et al., 2011; Roberts et al., 2012). The large uncertainty in the MERRA data makes it difficult to validate the discrepancy between the MEP and MERRA estimates. Roberts et al. (2012) compared the MERRA E and H over oceans with direct measurements and observational-based datasets. They found that the MERRA E is generally overestimated, while the MERRA H is often underestimated. The overestimates of MERRA E mainly result from the positive biases of wind speed and vertical humidity gradient. The underestimation of MERRA H is primarily caused by the negative bias of estimated vertical temperature gradient, while the areas with high H are presumably due to large positive bias of wind speed data.

Roberts et al. (2012) also pointed out that the biases of MERRA E and H vary with the magnitudes of E and H. The MERRA overestimates E about 25 W m^{-2} when observed

E below 50 W m^{-2}, while MERRA underestimates *E* up to 100 W m^{-2} when the observed greater than 250 W m^{-2}. For most densely observed regions where observed *E* ranges from 50-100 W m^{-2}, the MERRA *E* is overestimated by approximately 10 W m^{-2}. MERRA overestimates *H* by 50% to 75% when observations are less than -15 W m^{-2}, while MERRA underestimates *H* by 20-50 W m^{-2} when observed *H* is greater than 40 W m^{-2}. The large variable biases of MERRA *E* and *H* lead to seemingly small overall biases relative to observations due to error cancellation.

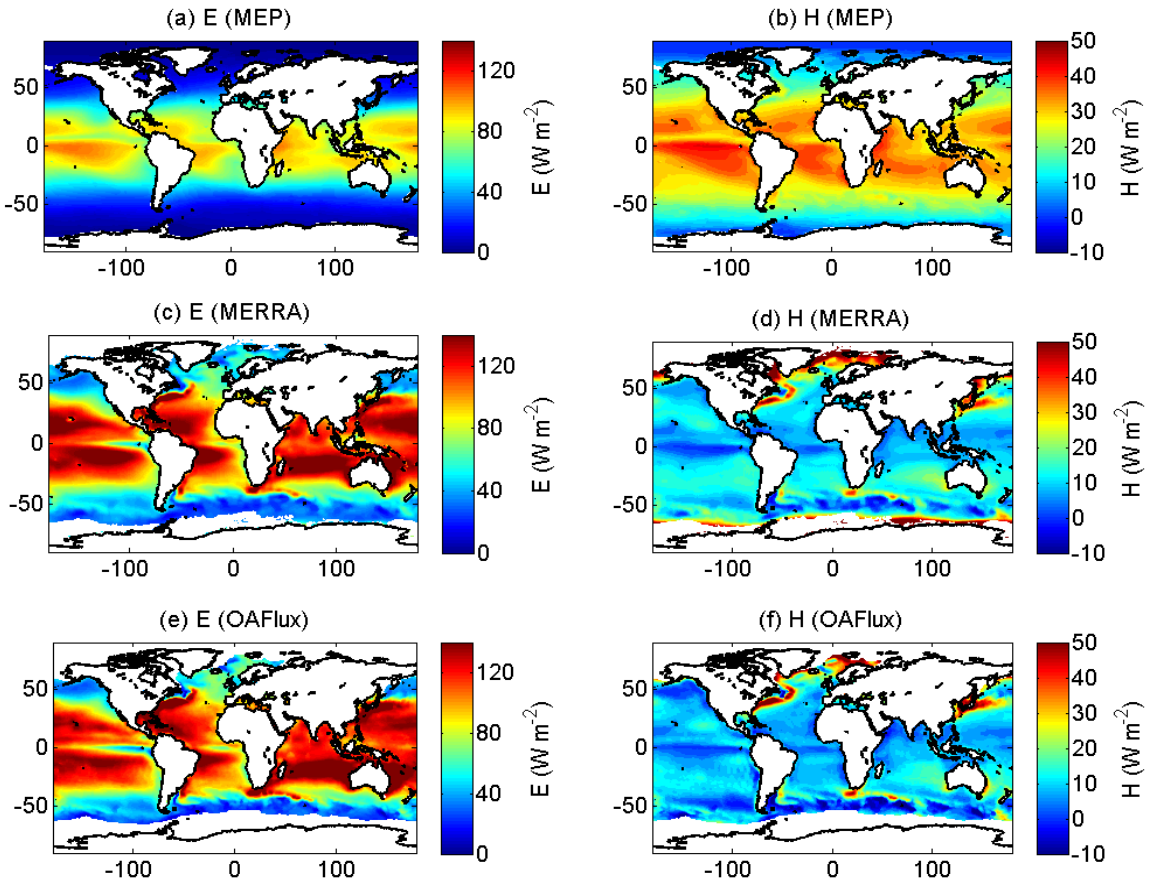

Figure 4.8: The 2001-2010 climatology of the MEP modeled annual mean (a) latent *E* and (b) sensible *H* heat fluxes over oceans (top panel) derived using the 3-hourly surface net radiation and net long-wave radiation from CERES SYN1deg-3Hour data and sea surface temperature (SST) from GMAO GEOS versus the MERRA (c) *E*, (d) *H* (central panel) and OAFlux (c) *E*, (d) *H* (bottom panel) estimates.

Table 4.5: Global annual means of ocean surface heat fluxes estimated by the MEP model according to Eq.(4.2). CERES surface net and net longwave radiation, and products from Objectively Analyzed Air-Sea Fluxes (OAFlux), NCEP reanalysis, JRA, Hamburg Ocean Atmosphere Parameters and Fluxes from Satellite Data (HOAPS), SeaFlux data, and other published studies. $R_0 = SWd - SWu$ is defined in Eq. (2.2). (Unit: W m^{-2})

Source of Products	E	H	Q	R_n	R_n^L	$R_n - E - H$ $(= R_0 + Q)$
MEP (2001-2010)	61±6	30±3	-143±9	131±14	-53±12	40±6
MEP (2001-2010, with polar regions)	56	28	-136	122	-52	38
Trenberth et al. (2009)	97	12	-166[b]	110	-57	1
MERRA (2001-2010)	92	16	-171[b]	118	-63	15
OAFlux (2001-2010)	98±7	10±1	-161[b]	134	-52	25
NCEP-NCAR[1]	94	11	-161[b]	109	-56	4
NCEP-DOE II[1]	106	6	-163[b]	116	-51	4
CFSR[1]	103	9	-166[b]	124	-54	12
JRA[2]	109	17	-194[b]	107	-68	-19
HOAPS[2]	104	15	-	-	-	-
SeaFlux[3]	90±14	18±6	-	-	-	-

b: Q calculated as the residual of the energy balance equation as in Eq. (2.2)
1: Wang et al. (2011)
2: Trenberth et al. (2009)
3: Clayson et al. (2013)

The OAFlux E and H are computed using the COARE bulk algorithm version 3.0. The OAFlux estimates are subject to errors and uncertainties from model inputs and parameters, which are difficult to validate and quantify given existing technology (Fairall et al., 2003). For example, the near-surface profile functions under stable conditions used in the COARE 3.0 bulk algorithm are based on, however, the observations over the Arctic ice cap (Beljaars and Holtslag, 1991; Persson et al, 2002). The bulk transfer coefficients under high wind speed (> 10 m s^{-1}) were calibrated using only a few quality observations. More importantly, the bulk algorithm used in MERRA and OAFlux as well as other

existing global flux products attempts to balance $E + H$ with R_n at annual scale according to Eq. (2.3), which is problematic (as discussed in Section 2.1).

Table 4.6: (a) Representative values of the partial derivatives and uncertainties of variables in Eq. (4.2) calculated at the global annual mean radiation fluxes and temperature over oceans, and (b) relative contributions of uncertainties (%) of the independent variables R_n, σ, and β_s to the uncertainties of MEP ocean surface heat fluxes according to Eqs. (4.5)-(4.16).

	E	H	Q
(a)			
$\lvert\partial X/\partial R_n\rvert$	**0.40**	**0.20**	**0.39**
ΔR_n		**14**	
$\lvert\partial X/\partial \sigma\rvert$	**13.67**	**3.50**	**10.17**
$\Delta\sigma$		**0.02**	
$\lvert\partial X/\partial \beta_s\rvert$	**4.74**	**2.38**	**7.12**
$\Delta\beta_s$		**0**	
(b)			
R_n	**96**	**98**	**97**
σ	**4**	**2**	**3**
β_s	**0**	**0**	**0**

The MEP model gives the first directly modeled global ocean surface (conductive) heat flux Q as shown in Figure 4.9(a) (positive $-Q$ indicates that thermal energy is transferred from the ocean to the atmosphere). The annual mean Q obtained from MERRA and OAFlux, as shown in Figures 4.9(b) and 4.9(c), are calculated as the residual of the ocean surface energy balance equation as in Eq. (2.2). The corresponding E, H, and R_n^L data are from the MERRA reanalysis, OAFlux, and ISCCP (radiation data used for OAFlux) data. Note that the climatology of OAFlux Q was calculated using data from 2001-2009 due to the availability of ISCCP radiation data. Spatial patterns of MEP Q are largely consistent with those of MERRA and OAFlux Q. The global annual mean Q

estimated by the MEP model is -143±10 W m^{-2}, which is 10-15% smaller (in magnitude) than the estimates from NCEP, ECMWF, JRA, as well as previously reported (also derived as the residual of energy balance equation) as shown in Table 4.5.

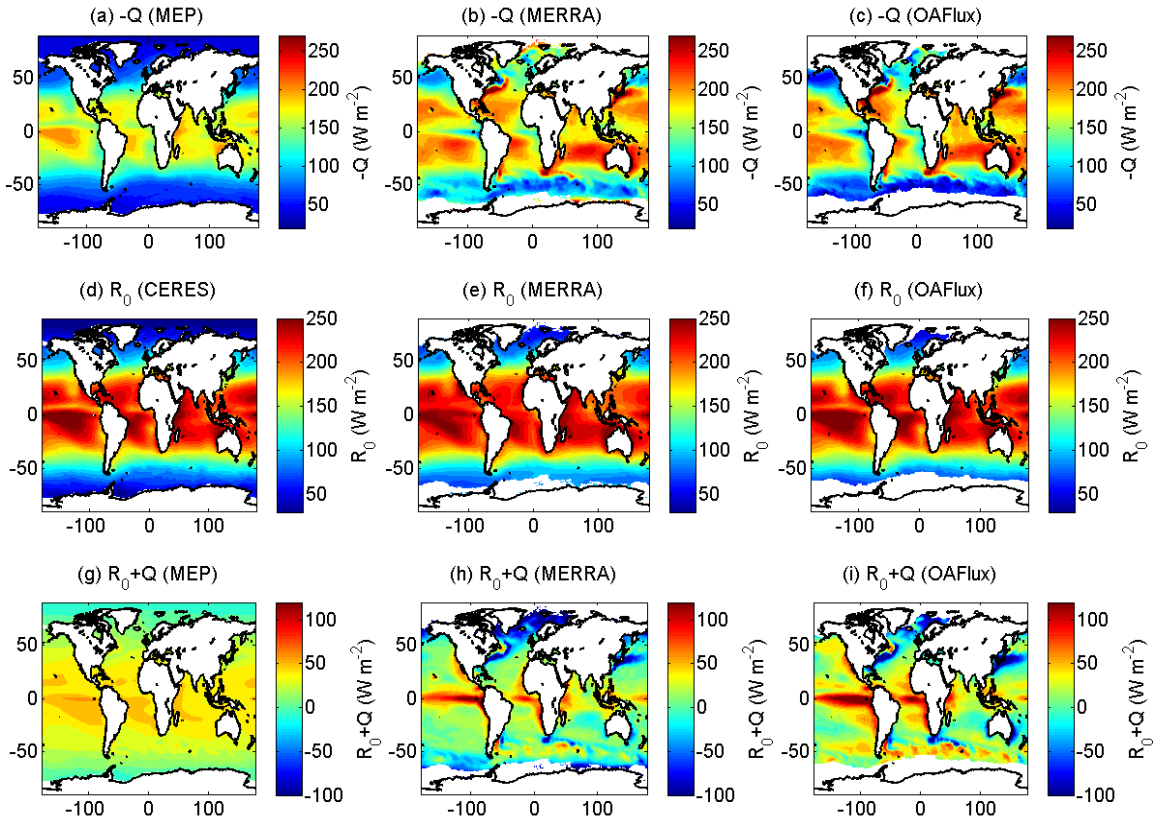

Figure 4.9: The 2001-2010 climatology of the (a) MEP modeled annual mean ocean surface heat flux Q (-Q is shown), (c) CERES net solar radiation R_0, and (e) net ocean heat flux (ocean heat uptake) $R_0 + Q$ $(= R_n - E - H)$ derived using the same input data as in Figure 4.8 vs. the corresponding MERRA reanalysis (central panel) and OAFlux data (right panel).

Figures 4.9(d)-4.9(f) show that the spatial patterns of the CERES, MERRA, and ISCCP ocean surface net solar radiation R_0 are consistent with each other. Figures 4.9(g)-4.9(i) show the comparison of the MEP-based estimates of net ocean heat flux $R_0 + Q = R_n - E - H$ with the MERRA and OAFlux data. The spatial patterns of the MEP-based estimates of $R_0 + Q$ are consistent with that of CERES R_n as shown in Figure 4.10. The

MEP-based estimates of $R_0 + Q$ have similar, yet a smoother spatial distribution compared to MERRA and OAFlux data resulting mainly from the lower estimates of MEP Q compared to MERRA and OAFlux data.

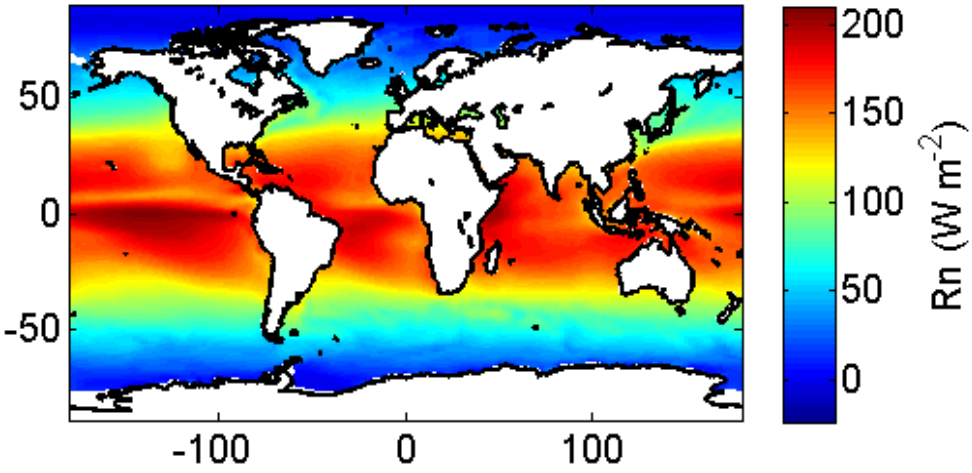

Figure 4.10: The 2001-2010 climatology of CERES R_n over oceans

The positive global annual mean $R_0 + Q$ (40±6 W m^{-2}) by the MEP model indicates that oceans gain thermal energy at an annual scale. This result is qualitatively in agreement with previous estimates ranging from 3 to 33 W m^{-2} (Yu and Weller, 2012) and most of other data products listed in Table 4.5 except for the Japan reanalysis (JRA). The non-zero $R_0 + Q$ is arguably realistic rather than a numerical artifact due to modeling errors and uncertainties of model parameters as discussed in Section 2.1. Further quantitative analysis of energy dissipation in oceans is needed but beyond the scope of this study. The uncertainties of the global annual mean of MEP heat fluxes over oceans are dominated by the uncertainty of R_n measurements ($\geq$ 96%) as shown in Table 4.6(b). The corresponding representative values of the partial derivatives and uncertainties of model input/parameter are given in Table 4.6(a).

Table 4.5 shows that the global annual mean MEP E, H, and Q over oceans, when including the PoRs, decrease (in magnitude) by about 5, 2, 7 W m^{-2}, respectively. The MEP-based estimates of global annual mean net ocean heat flux decrease slightly from 40 to 38 W m^{-2} as a result of a relatively large decrease of R_n compared to E and H. Figure 4.11 shows the global annual means of MEP, MERRA, and OAFlux estimated ocean surface heat fluxes with the corresponding surface radiations and net ocean heat flux (ocean heat uptake) shown on the right panel. The MEP modeled global annual mean ocean E and H have negative trends of -0.06 and -0.04 W m^{-2} yr^{-1} with the corresponding uncertainties estimated as 0.06 and 0.04 W m^{-2} yr^{-1}, respectively. The negative trends of are consistent with the MERRA and OAFlux data as shown in Figure 4.11. Note that the annual mean of MEP $E + H$, 91 W m^{-2}, is not equal to the CERES annual mean R_n, 131 W m^{-2}, resulting in a positive net ocean heat flux $R_n - E - H$, for the reason discussed in Section 2.1.

The global annual mean MEP Q has a trend of -0.08 W m^{-2} yr^{-1} associated with a trend of R_n^L -0.17 W m^{-2} yr^{-1} as shown in Figures 4.11(e) and 4.11(d). Note that the positive/negative trends of Q and R_n^L indicate the decrease/increase in magnitudes as Q and R_n^L are always negative over oceans. The uncertainty of global annual mean MEP Q is estimated as 0.16 W m^{-2} yr^{-1}. The trends and uncertainties of MEP estimated global annula mean ocean heat fluxes are also listed in Table 4.13. The increases (in magnitude) of MEP Q and net ocean heat flux ($R_0 + Q$) during 2001-2010 are consistent with the OAFlux but opposite to MERRA estimates as shown in Figures 4.11(e) and 4.11(f). The abrupt increase (in magnitude) of OAFlux Q from 2001 to 2002 is mainly caused by the large corresponding increase (in magnitude) of ISCCP R_n^L, which may be unreliable. The abrupt increase of ISCCP R_n^L between 2001 and 2002 may be related to the global decrease in

cloud amounts recorded by the ISCCP cloudiness data. Evan et al. (2007) found a nearly 20% reduction in the ISCCP recorded cloud amount from 1983 to mid 2001. However, this decrease was demonstrated to be satellite viewing geometry artifacts rather than physical changes in the atmosphere. Evan et al. (2007) further state that "The ISCCP data may not be appropriate for certain long-term global studies, especially those focused on trends."

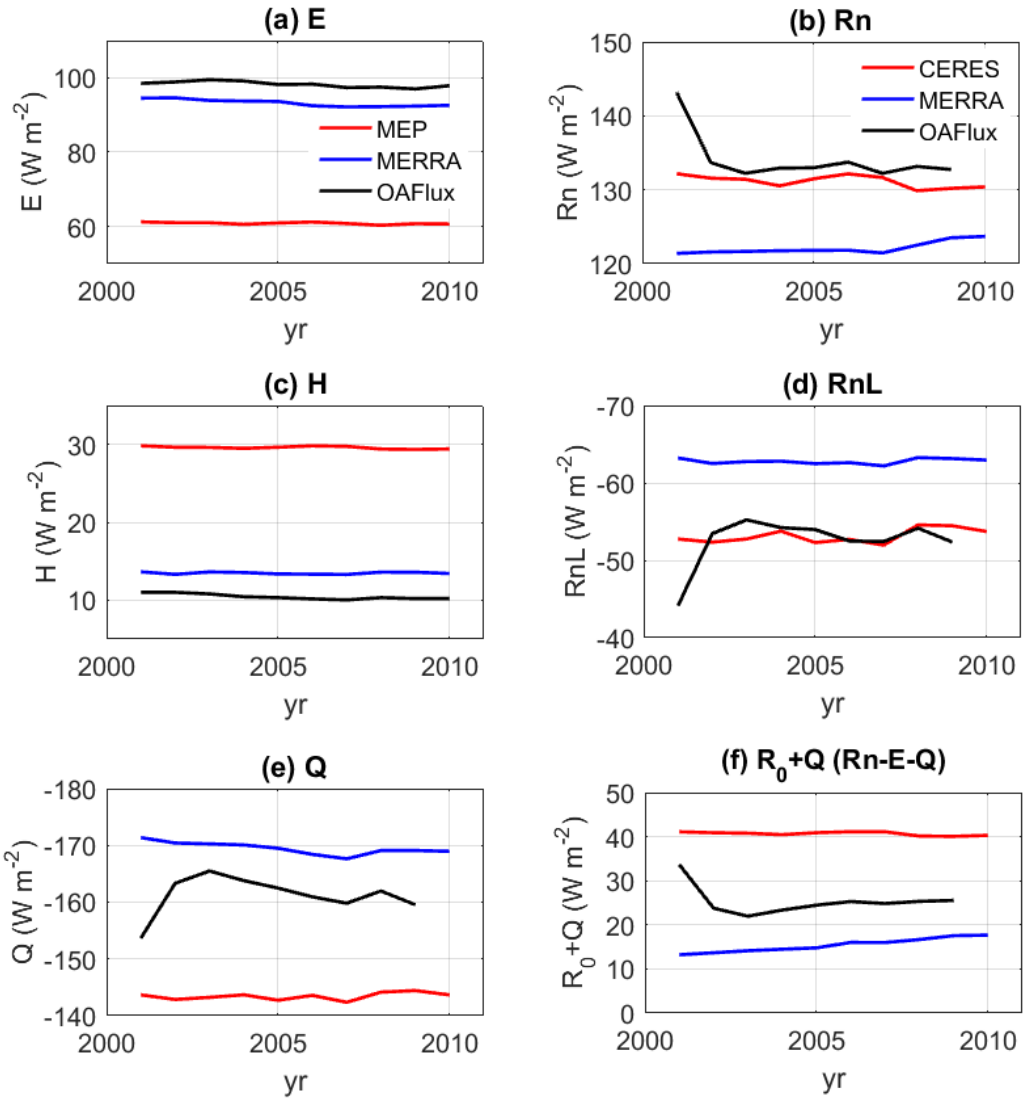

Figure 4.11: Global annual mean ocean (a) E, (c) H, and (e) Q estimated by the MEP (red), MERRA (blue), and OAFlux (black); (b) R_n (d) R_n^L (f) $R_0 + Q$ data from CERES (red), MERRA (blue), and OAFlux (ISCCP radiation data) (black) over 2001-2010 (except for ISCCP radiation data from 2001-2009).

Since direct measurements of surface heat fluxes over oceans are limited, the MEP heat fluxes may be validated indirectly by comparing the net ocean heat flux with the change of ocean heat content (ΔOHC) of the top ocean layer of certain depth since ΔOHC is expected to be positively correlated with $R_n - E - H$. Figure 4.12 shows that the MEP modeled global annual mean $R_n - E - H$ has a decreasing trend during 2001-2010 qualitatively consistent, as expected, associated with the decreasing trend of the ΔOHC of the top 700-m layer from the NCDC data (Levitus et al., 2012). One explanation for the large values MEP $R_n - E - H$ relative to ΔOHC is that part of the absorbed solar radiation by the oceans is transferred into deeper ocean layers and dissipated through other physical, chemical and biological processes within the oceans.

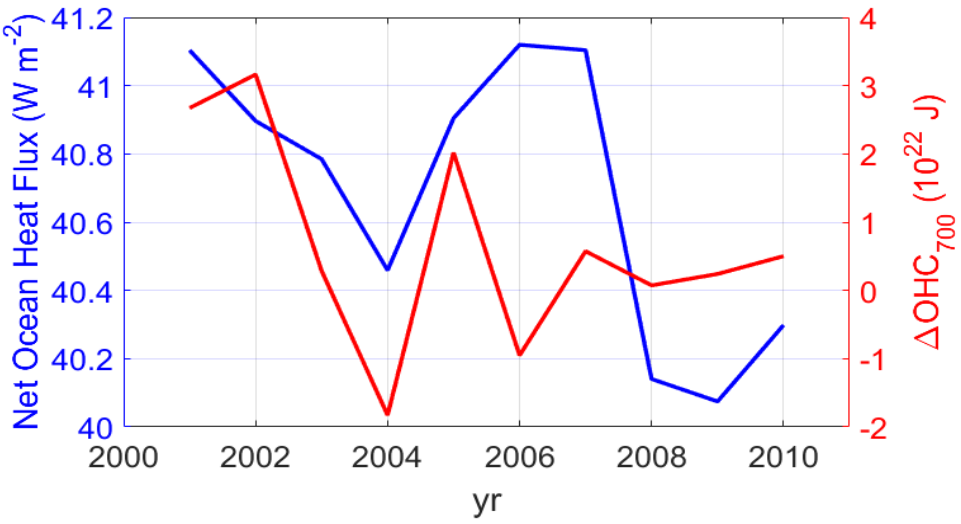

Figure 4.12: The annual mean MEP modeled net ocean heat flux (ocean heat uptake) $R_n - E - H$ vs. the change in the top 700 m ocean heat content (ΔOHC) from the National Climatic Data Center (NCDC). The correlation between $R_n - E - H$ and ΔOHC is 0.4.

Figure 4.13 shows the spatial patterns of the trends of ocean surface heat fluxes obtained from the MEP, MERRA, and OAFlux associated with those of model inputs shown on the bottom panel. The trends of MEP modeled ocean surface heat fluxes are

qualitatively consistent with those of MERRA and OAFlux but with different magnitudes. Spatial patterns of the MEP E trend are consistent with those of CERES R_n trend. Over oceans, the artifacts in CERES radiation and T_s data (i.e., negative trends of T_s resulting in decreasing LWu and increasing R_n) are smaller than those over lands (see Figures 4.13(j)-4.13(l)).

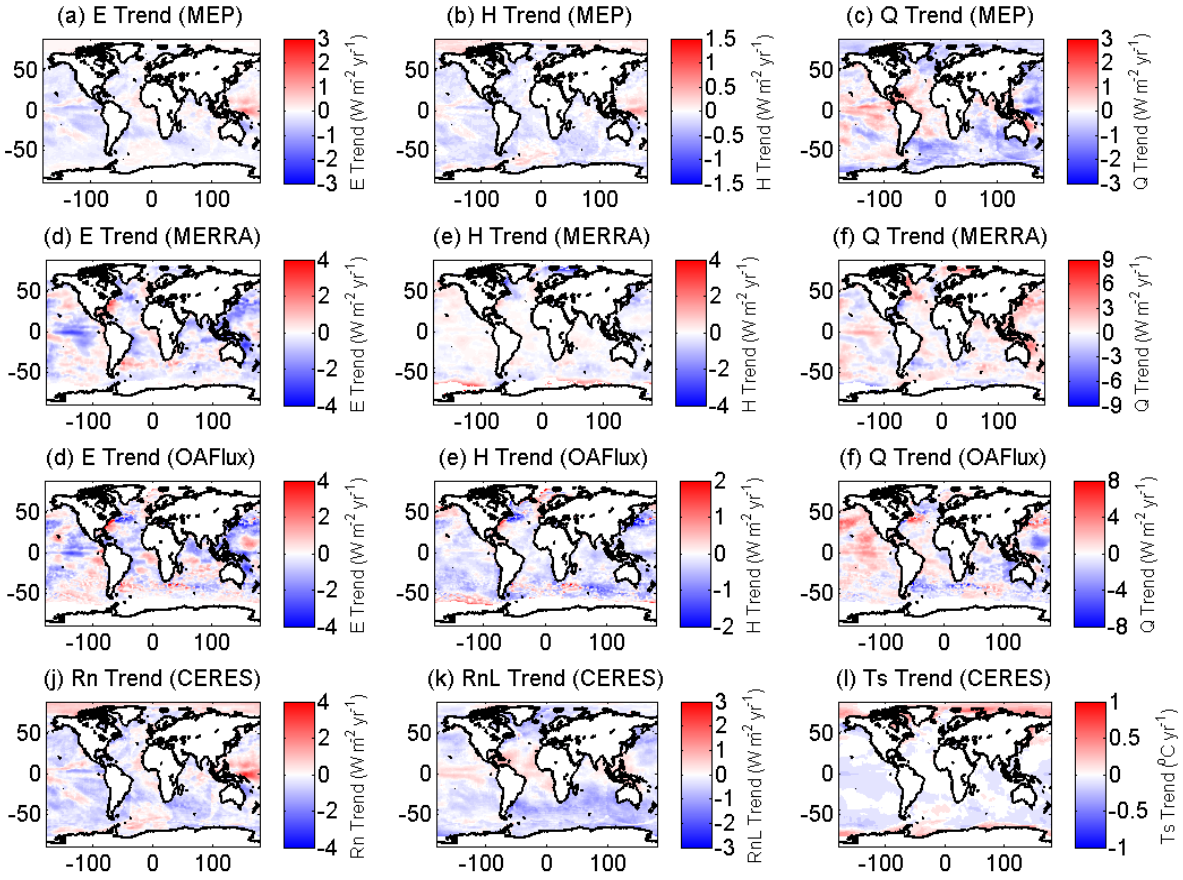

Figure 4.13: Annual trends (2001-2010) of MEP estimated (a) E (b) H (c) Q versus those of MERRA (d) E (e) H (f) Q and GLDAS (g) E (h) H (i) Q with those of CERES (j) R_n (k) R_n^L, and (l) T_s over oceans.

4.5.3 Global (Land and Ocean)

In this study, the MEP estimates of global annual mean surface heat fluxes are calculated as an area-weighted average of MEP land and ocean heat fluxes. The results are summarized in Table 4.7. The corresponding uncertainties estimates using Eqs. (4.5)-(4.16) are shown in Table 4.8. The newly estimated global annual mean E, 54±6 W m^{-2} (682±76 mm yr^{-1}), is lower than previous estimates of 80-90 W m^{-2} largely due to the lower MEP E over oceans. The new estimate of global annual mean H is 31±3 W m^{-2}, while previously reported annual mean H has a range of 8-24 W m^{-2}. The MEP estimate of global annual net surface heat flux is ~33±6 W m^{-2} consistent with most of existing products as shown in Table 4.7 except for JRA. Note that the existing reanalysis products (1) produce nearly zero annual mean Q over lands and (2) do not have direct estimates of Q over oceans (see Tables 4.3 and 4.5). Decreases of MEP-based estimates of global surface heat fluxes and CERES surface radiations by including the PoRs are also shown in Table 4.7.

Table 4.7: Global (land and ocean) annual means of surface heat fluxes estimated by the MEP model, CERES surface net and net longwave radiation, and products from MERRA reanalysis, NCEP reanalysis, JRA, and other published studies. (Unit: W m^{-2})

Variable	E	H	R_n	R_n^L	$R_n - E - H$ $(= R_0 + Q)$
MEP (2001-2010)	54±6	31±3	118±12	-58±10	33±6
MEP (2001-2010, with polar regions)	50	29	110	-56	31
Stephens et al. (2012a)	88±10	24±7	113±15	-57±14	1
Trenberth et al. (2009)	80	17	98	-63	0
MERRA (2001-2010)	79	19	110	-64	12
NCEP/NCAR[1]	81	16	100	-61	3
NCEP/DOE II[1]	91	8	103	-57	4
CFSR[1]	84	16	110	-57	10
JRA[2]	90	19	97	-73	-12

1: Wang et al. (2011)
2: Trenberth et al. (2009)

The uncertainties of the global annual mean MEP heat fluxes are dominated by those of R_n measurements as shown in Table 4.8(b). The corresponding representative values of the partial derivatives and uncertainties of model input/parameter given in Table 4.8(a). The MEP modeled surface heat fluxes have reduced uncertainties compared to the existing data products as the bulk gradients of temperature/humidity gradients, wind speed, and surface roughness subject to large uncertainties are not used in the MEP model. The uncertainties of the MEP heat fluxes caused by model parameters are limited compared to previous estimates which use conventional methods (Bourras, 2006; Yu et al., 2008; Yuan et al., 2010; Mueller et al., 2011, 2013; Vinukollu et al., 2011a; Stephens et al., 2012a; Clayson et al., 2013). Uncertainties of the MEP heat fluxes can be further reduced with the improved accuracy of radiation measurements.

Table 4.8: (a) The representative values of the partial derivatives and uncertainties of variables calculated at the global annual mean radiation fluxes, temperature, and (b) relative contributions of uncertainties (%) of the independent variables R_n, σ, and β_s to the uncertainties of the MEP land surface heat fluxes according to Eqs. (4.5)-(4.16).

	E	H	$R_n - E - H$
(a)			
$\lvert\partial X/\partial R_n\rvert$	**0.40**	**0.23**	**0.38**
ΔR_n		**12**	
$\lvert\partial X/\partial \sigma\rvert$	**14.56**	**4.22**	**10.34**
$\Delta \sigma$		**0.03**	
$\lvert\partial X/\partial \beta_s\rvert$	**4.91**	**2.79**	**7.70**
$\Delta \beta_s$		**0.15**	
(b)			
R_n	**80**	**83**	**76**
σ	**7**	**4**	**5**
β_s	**12**	**13**	**19**

4.6 Regional Analysis

4.6.1 Continents

The climatology of the MEP surface heat fluxes and CERES surface radiative fluxes evaluated at continental scale, derived from the results presented in Section 4.5.1, is shown in Table 4.9. Also shown in Table 4.9 are the estimates of continental scale surface energy budgets reported by L'Ecuyer et al. (2015) (shown in parentheses). The radiative fluxes between the CERES (used in this study) and those reported in L'Ecuyer et al. (2015) obtained from multiple products are comparable over most of the continents with the exception of Antarctica.

The MEP E and H are slightly lower than the estimates reported by L'Ecuyer et al. (2015) (except for Australia and Antarctica) obtained from Princeton ET, MERRA, and GLDAS reanalysis products. The annual means of MEP Q over continents is positive (i.e., land mass is gaining thermal energy), while those reported by L'Ecuyer et al. (2015) are exactly zero globally. The discrepancies result mainly from the use of different underlying surface energy balance equations between the MEP and other existing products (Eq. (2.1) vs. Eq. (2.3)). The annual mean E and H over Antarctica reported by L'Ecuyer et al. (2015) have opposite signs indicating a violation of the surface energy balance assuming that the same turbulent mixing is responsible for the transport of heat and water vapor within the atmospheric boundary layer. Furthermore, the corresponding surface energy budgets do not close. The discrepancies of E and H between the MEP and previous estimates may partially result from the use of different radiative flux data in the MEP model (i.e., CERES)

and other data products. The effects of using various radiative flux inputs on the MEP estimates of global mean surface heat fluxes requires further tests.

Table 4.9: The 2001-2010 climatology of continental scale MEP modeled surface heat fluxes, CERES radiative fluxes, and the 2000-2009 climatology reported by L'Ecuyer et al. (2015) shown in the parenthesis.

Continent	E	H	Q	R_n	R_n^L
Global Land (with polar regions)	35 (38)	30 (38)	12 (-)	78 (76)	-66 (-67)
North America	30 (33)	29 (32)	12 (-)	72 (65)	-58 (-60)
South America	66 (77)	42 (52)	14 (-)	124 (129)	-60 (-57)
Africa	45 (44)	38 (58)	17 (-)	102 (102)	-87 (-90)
Australia	41 (26)	42 (77)	21 (-)	105 (103)	-100 (-94)
Antarctica	0.18 (1)	0.34 (-16)	0 (-)	-3.1 (-20)	-35 (-44)
Eurasia	30 (33)	28 (34)	12 (-)	70 (67)	-64 (-64)
Asia	31	28	13	73	-67
Europe	26	25	11	63	-55

Figure 4.14 shows the annual and seasonal trends associated with the corresponding uncertainty estimates (95% CI) of the MEP land surface heat fluxes as well as model inputs for each continent (see also Table 4.10). The results showed that the trends of MEP E on each continent are consistent with those of CERES R_n and MERRA q_s indicating that MEP E is dominated by surface radiation energy and humidity conditions. Trends of MEP E over continents are also consistent with those of surface layer soil moisture θ_s from MERRA, which is reasonable as evapotranspiration and soil moisture are expected to be positively correlated. Figures 4.14(a) and 4.14(d) show that over half of the increased R_n were used to enhance E (except for Antarctica).

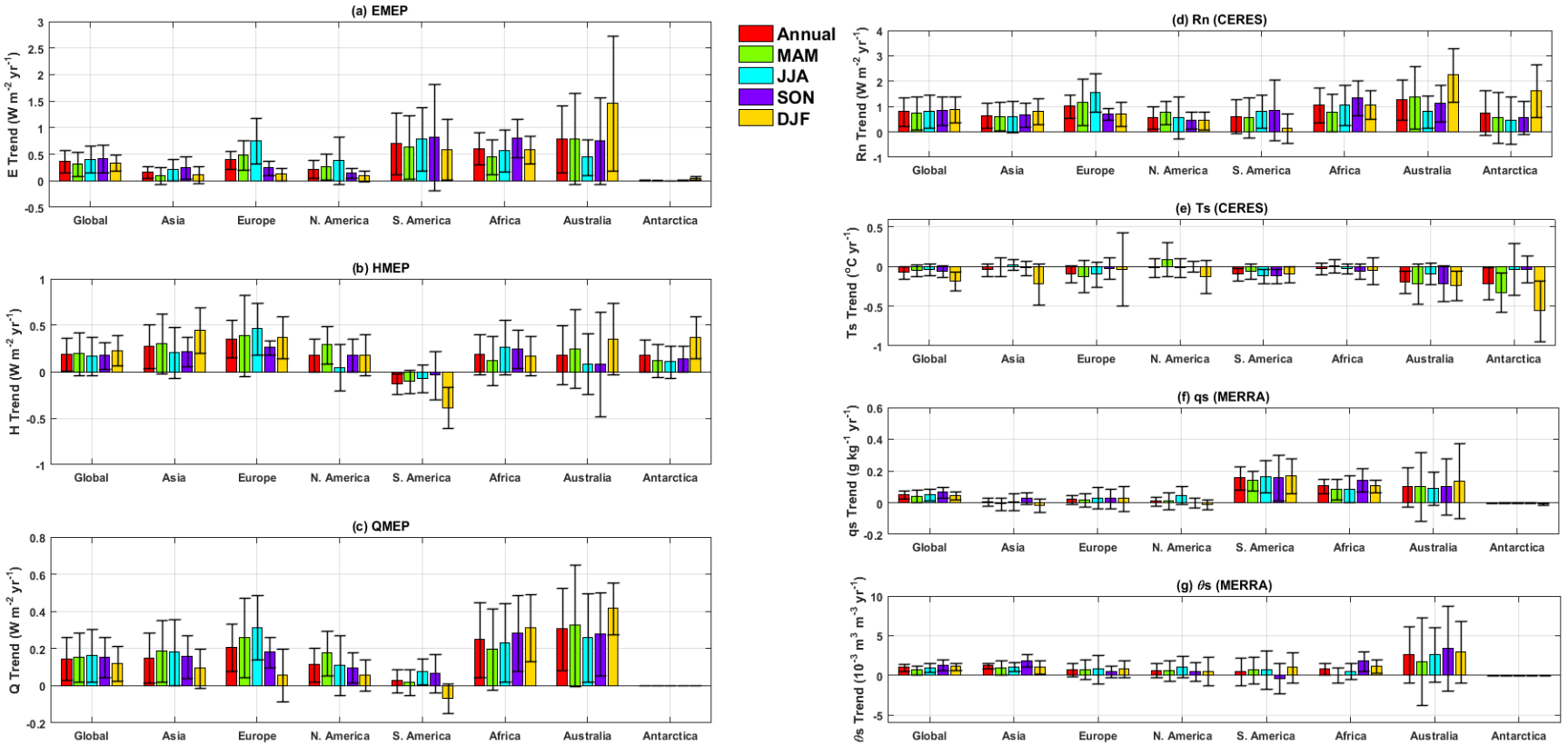

Figure 4.14: The trends and uncertainties (2001-2010) of the MEP estimated (a) E (b) H (c) Q and CERES (d) R_n (e) T_s and MERRA (f) q_s (g) θ_s for the continents (MAM: March–April–May; JJA: June–July–August; SON: September–October–November; DJF: December–January–February).

Table 4.10: The annual and seasonal trends of the MEP modeled surface heat fluxes and model inputs for the continents associated with the corresponding uncertainties (95% CI). The numbers in each grid from top to bottom are the annual trend followed by seasonal trends (in the order of MAM, JJA, SON, DJF). The calculations are based on the data over 2001-2010. (Unit: heat and radiative fluxes (W m^{-2} yr^{-1}), T_s (^oC yr^{-1}), q_s (g kg^{-1} yr^{-1}), θ_s (10^{-3} m^3 m^{-3} yr^{-1})).

Continent	E	H	Q	R_n	T_s	q_s	θ_s
Global Land (with polar regions)	0.37±0.20	0.19±0.18	0.14±0.12	0.80±0.57	-0.07±0.08	0.05±0.02	0.99±0.46
	0.32±0.23	0.19±0.23	0.15±0.13	0.74±0.64	-0.05±0.08	0.04±0.04	0.70±0.56
	0.40±0.25	0.17±0.21	0.16±0.14	0.80±0.66	-0.04±0.07	0.05±0.04	0.96±0.53
	0.42±0.26	0.18±0.14	0.15±0.11	0.84±0.56	-0.06±0.07	0.06±0.03	1.32±0.67
	0.34±0.16	0.23±0.17	0.12±0.09	0.90±0.51	-0.18±0.12	0.05±0.02	1.11±0.43
Global Land (without polar regions)	0.41±0.23	0.18±0.18	0.16±0.13	0.79±0.54	-0.05±0.06	0.06±0.03	1.00±0.46
	0.35±0.25	0.20±0.24	0.17±0.15	0.75±0.60	-0.01±0.07	0.05±0.04	0.70±0.56
	0.45±0.28	0.17±0.21	0.18±0.16	0.82±0.63	-0.03±0.05	0.06±0.04	0.97±0.53
	0.47±0.29	0.18±0.14	0.17±0.12	0.85±0.55	-0.05±0.06	0.07±0.04	1.33±0.67
	0.38±0.17	0.21±0.17	0.13±0.11	0.81±0.46	-0.14±0.10	0.05±0.03	1.12±0.43
Asia	0.17±0.11	0.28±0.24	0.15±0.13	0.65±0.49	-0.04±0.08	0.01±0.03	1.22±0.38
	0.10±0.15	0.30±0.32	0.18±0.17	0.62±0.58	0.00±0.11	-0.01±0.04	0.97±0.93
	0.21±0.21	0.21±0.28	0.18±0.18	0.61±0.60	0.03±0.06	0.01±0.05	1.09±0.61
	0.24±0.21	0.22±0.16	0.16±0.12	0.66±0.48	-0.02±0.09	0.03±0.04	1.86±0.82
	0.11±0.16	0.44±0.25	0.09±0.10	0.80±0.52	-0.22±0.26	-0.02±0.04	1.01±0.84
Europe	0.40±0.17	0.36±0.21	0.21±0.13	1.02±0.47	-0.09±0.11	0.02±0.03	0.71±0.88
	0.49±0.28	0.39±0.44	0.26±0.21	1.18±0.91	-0.12±0.20	0.02±0.04	0.75±1.21
	0.75±0.43	0.46±0.28	0.31±0.17	1.56±0.76	-0.09±0.16	0.03±0.07	0.77±1.80
	0.24±0.14	0.26±0.08	0.18±0.08	0.71±0.22	-0.02±0.14	0.03±0.06	0.49±0.71
	0.12±0.12	0.37±0.23	0.06±0.14	0.72±0.48	-0.03±0.46	0.03±0.08	0.79±1.07
Eurasia	0.20±0.12	0.29±0.22	0.16±0.13	0.71±0.48	-0.05±0.08	0.01±0.02	1.15±0.39
	0.16±0.16	0.32±0.31	0.20±0.16	0.71±0.59	-0.02±0.12	0.00±0.03	0.97±0.81
	0.28±0.22	0.26±0.26	0.21±0.17	0.76±0.60	0.01±0.07	0.01±0.05	1.04±0.65
	0.23±0.18	0.23±0.14	0.16±0.11	0.65±0.42	-0.02±0.08	0.03±0.04	1.63±0.75
	0.12±0.14	0.44±0.23	0.08±0.10	0.79±0.49	-0.20±0.29	-0.01±0.04	1.03±0.79

Table 4.10: continued

Continent	E	H	Q	R_n	T_s	q_s	θ_s
North America	0.22±0.17	0.18±0.18	0.11±0.09	0.56±0.44	-0.01±0.12	0.01±0.03	0.65±0.89
	0.27±0.24	0.29±0.20	0.18±0.12	0.77±0.46	0.09±0.21	0.01±0.05	0.58±1.28
	0.39±0.45	0.05±0.25	0.11±0.16	0.56±0.83	-0.02±0.12	0.05±0.06	1.08±1.31
	0.15±0.09	0.18±0.18	0.10±0.08	0.47±0.33	0.00±0.07	0.00±0.03	0.50±1.16
	0.09±0.10	0.18±0.22	0.06±0.08	0.45±0.37	-0.13±0.21	-0.01±0.03	0.53±1.86
South America	0.70±0.58	-0.13±0.11	0.03±0.06	0.61±0.67	-0.10±0.08	0.16±0.07	0.44±1.74
	0.64±0.60	-0.11±0.13	0.02±0.07	0.56±0.78	-0.06±0.09	0.14±0.06	0.65±1.69
	0.79±0.60	-0.07±0.15	0.08±0.07	0.81±0.66	-0.12±0.09	0.17±0.10	0.70±2.40
	0.82±1.00	-0.04±0.26	0.07±0.10	0.86±1.20	-0.12±0.09	0.16±0.14	-0.37±1.96
	0.59±0.58	-0.39±0.22	-0.07±0.08	0.14±0.59	-0.10±0.10	0.17±0.11	1.01±1.89
Africa	0.61±0.30	0.19±0.22	0.25±0.20	1.06±0.68	-0.03±0.07	0.11±0.05	0.86±0.72
	0.45±0.33	0.12±0.26	0.20±0.22	0.77±0.73	0.00±0.08	0.09±0.06	0.05±0.97
	0.57±0.39	0.26±0.29	0.23±0.21	1.07±0.80	-0.02±0.06	0.09±0.08	0.50±1.02
	0.81±0.36	0.24±0.20	0.28±0.20	1.35±0.69	-0.06±0.10	0.14±0.07	1.79±1.22
	0.59±0.25	0.17±0.21	0.31±0.18	1.08±0.55	-0.05±0.17	0.11±0.04	1.77±0.88
Australia	0.78±0.63	0.18±0.32	0.31±0.22	1.28±0.80	-0.19±0.14	0.10±0.13	2.61±3.52
	0.79±0.86	0.25±0.42	0.32±0.33	1.37±1.23	-0.22±0.25	0.10±0.22	1.75±5.50
	0.45±0.34	0.09±0.33	0.26±0.24	0.81±0.64	-0.09±0.13	0.09±0.11	2.61±3.44
	0.75±0.81	0.08±0.56	0.28±0.22	1.12±0.71	-0.22±0.23	0.10±0.18	3.40±5.38
	1.46±0.26	0.36±0.39	0.42±0.14	2.25±1.06	-0.24±0.18	0.14±0.24	2.98±3.92
Antarctica	0.02±0.01	0.17±0.17	0.00±0.00	0.76±0.87	-0.21±0.21	0.00±0.00	
	0.01±0.00	0.12±0.18	0.00±0.00	0.57±1.01	-0.32±0.25	0.00±0.00	
	0.00±0.00	0.11±0.18	0.00±0.00	0.46±0.95	-0.03±0.32	0.00±0.00	N/A
	0.01±0.01	0.14±0.14	0.00±0.00	0.57±0.66	-0.03±0.17	0.00±0.00	
	0.05±0.03	0.37±0.23	0.00±0.00	1.63±1.03	-0.56±0.39	-0.01±0.01	

The trends of MEP H over continents are weakly positive (except for South America) owing to the relatively large uncertainties that are comparable to the magnitude of trends as shown in Figure 4.14(b). The trends of MEP Q is positive globally except for Antarctica. Q over Antarctica (permanent ice surface) is essentially zero throughout the study period, leading to a zero trend, due to the insulating effect of ice cover as discussed in Section 4.5.1. The results also show that the seasonal trends of MEP heat fluxes are mostly consistent with the annual trends. The CERES T_s has a decreasing trend globally due to the data artifact as discussed previously (see Figure 4.14(e)). The artifact in CERES radiation data is more significant over Antarctica compared to the other areas (see also Figure 4.6(k)). The questionable increasing trend of CERES R_n (Figure 4.14(d)) leads to the increasing trend of MEP H as shown in Figure 4.14(b), which is less reliable.

To assess the effects of CERES data artifacts on the trends of MEP estimated surface energy budgets, a trend analysis was re-done using the data only from 2001 to 2007 (i.e., before switching the assimilated meteorological data in CERES products). The results, as shown in Figure 4.15 (also Table 4.11), show that the trends of all three MEP heat fluxes as well as model inputs from CERES (i.e.,R_n and T_s) become insignificant as CERES R_n remains approximately stationary (Figure 4.15(d)). The large uncertainties of the heat flux trends may partially be associated with large (temporal) scale extreme climate events that cause large variations of heat fluxes at interannual scale. For example, the large uncertainty of the trend of MEP E over Australia is partially caused by the abrupt drop of E estimates during 2002-2004, which are related to the reported severe drought over Australia (Horridge et al., 2005; van Dijk et al., 2013). Connections between the changes in surface heat fluxes and regional/global climate variability deserve further investigations.

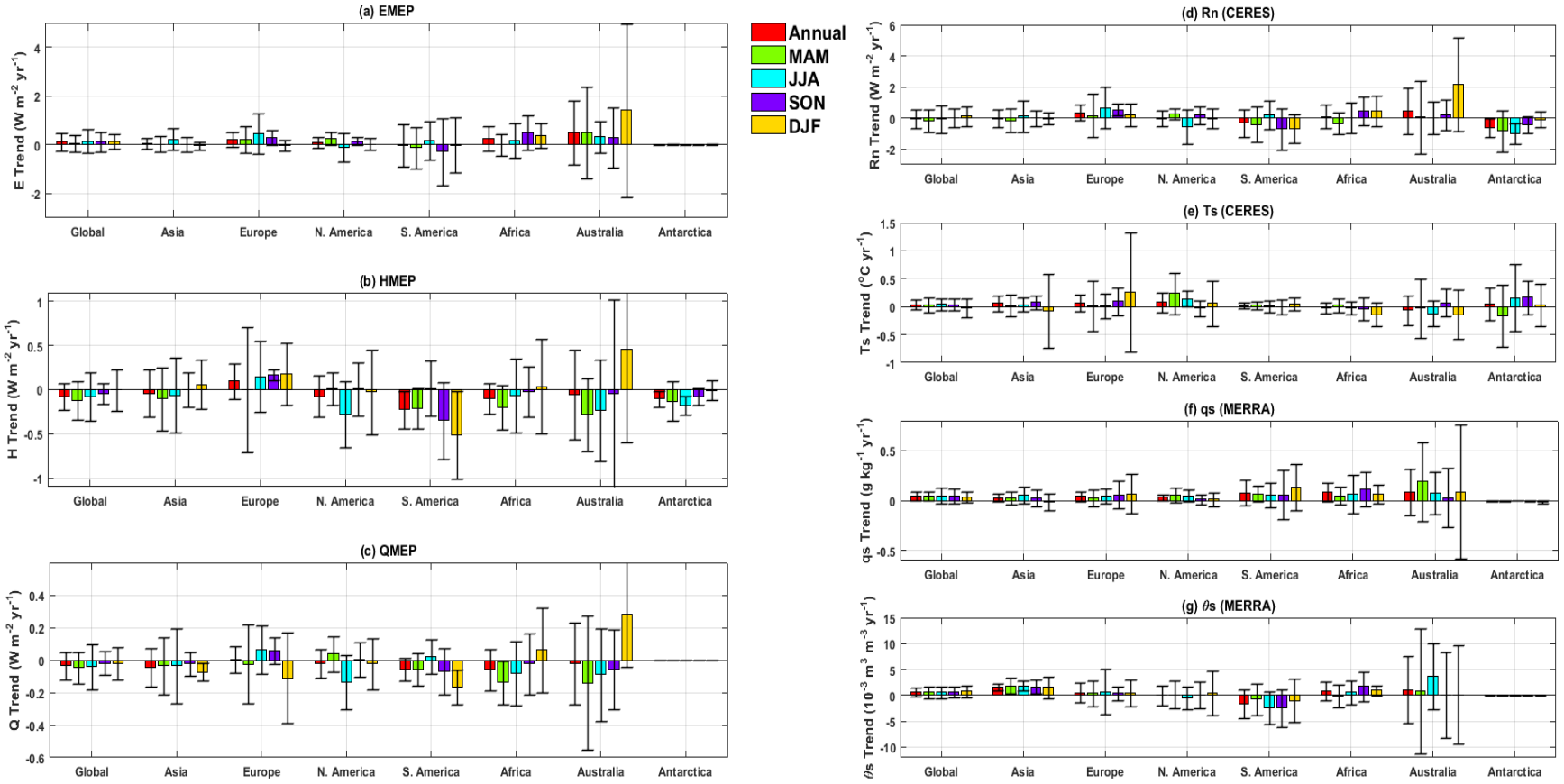

Figure 4.15: The trends and uncertainties (2001-2007) of the MEP estimated (a) E (b) H (c) Q and CERES (d) R_n (e) T_s and MERRA (f) q_s (g) θ_s for the continents (MAM: March–April–May; JJA: June–July–August; SON: September–October–November; DJF: December–January–February).

Table 4.11: The annual and seasonal trends of the MEP modeled surface heat fluxes and model inputs for the continents associated with the corresponding uncertainties (95% CI). The numbers in each grid from top to bottom are the annual trend followed by seasonal trends (in the order of MAM, JJA, SON, DJF). The calculations are based on the data over 2001-2007. (Unit: heat and radiative fluxes (W m^{-2} yr^{-1}), T_s (^{o}C yr^{-1}), q_s (g kg^{-1} yr^{-1}), θ_s (10^{-3} m^3 m^{-3} yr^{-1})).

Continent	E	H	Q	R_n	T_s	q_s	θ_s
Global Land (with polar regions)	0.12±0.35	-0.08±0.15	-0.03±0.08	-0.05±0.62	0.03±0.09	0.05±0.05	0.63±0.92
	0.06±0.35	-0.12±0.22	-0.05±0.10	-0.20±0.74	0.03±0.13	0.05±0.05	0.59±1.10
	0.14±0.48	-0.08±0.27	-0.04±0.14	-0.07±0.87	0.04±0.11	0.05±0.08	0.62±1.13
	0.12±0.42	-0.04±0.11	-0.02±0.07	0.02±0.61	0.03±0.10	0.05±0.07	0.66±1.07
	0.14±0.31	-0.01±0.24	-0.02±0.10	0.11±0.62	-0.03±0.16	0.04±0.05	0.76±1.08
Global Land (without polar regions)	0.13±0.40	-0.07±0.17	-0.04±0.09	0.02±0.65	0.03±0.07	0.05±0.05	0.64±0.92
	0.07±0.39	-0.12±0.23	-0.05±0.11	-0.12±0.71	0.05±0.12	0.05±0.05	0.59±1.10
	0.16±0.54	-0.07±0.30	-0.0.5±0.16	0.04±0.93	0.02±0.07	0.05±0.09	0.62±1.13
	0.13±0.47	-0.04±0.13	-0.02±0.08	0.07±0.66	0.03±0.09	0.05±0.08	0.66±1.07
	0.16±0.34	0.00±0.26	-0.03±0.11	0.14±0.67	-0.03±0.21	0.04±0.06	0.77±1.08
Asia	0.06±0.21	-0.04±0.27	-0.05±0.12	-0.03±0.59	0.06±0.13	0.03±0.04	1.64±0.68
	0.02±0.31	-0.10±0.36	-0.04±0.18	-0.15±0.75	0.02±0.20	0.03±0.06	1.83±1.53
	0.21±0.44	-0.06±0.42	-0.04±0.23	0.11±1.01	0.04±0.13	0.06±0.08	1.86±0.92
	0.01±0.31	0.00±0.19	-0.02±0.07	-0.01±0.51	0.08±0.13	0.02±0.09	1.66±1.34
	-0.04±0.17	0.06±0.28	-0.07±0.05	-0.04±0.39	-0.08±0.66	-0.01±0.08	1.51±2.12
Europe	0.22±0.31	0.10±0.21	0.00±0.08	0.34±0.51	0.06±0.15	0.04±0.05	0.54±1.95
	0.22±0.55	0.00±0.71	-0.03±0.24	0.17±1.41	0.01±0.44	0.03±0.08	0.40±2.47
	0.44±0.83	0.15±0.40	0.07±0.15	0.67±1.31	0.01±0.22	0.05±0.07	0.73±4.33
	0.28±0.30	0.17±0.06	0.06±0.08	0.52±0.38	0.10±0.25	0.06±0.14	0.41±1.36
	-0.03±0.22	0.18±0.35	-0.11±0.28	0.19±0.71	0.25±1.07	0.07±0.20	0.43±2.62
Eurasia	0.08±0.23	-0.01±0.24	-0.03±0.11	0.04±0.56	0.06±0.13	0.03±0.03	1.44±0.79
	0.06±0.35	-0.07±0.32	-0.02±0.15	-0.06±0.75	0.01±0.23	0.02±0.06	1.62±1.40
	0.23±0.51	-0.01±0.37	-0.01±0.20	0.22±1.05	0.03±0.13	0.05±0.07	1.65±1.21
	0.04±0.28	0.04±0.17	-0.01±0.07	0.07±0.47	0.09±0.11	0.03±0.09	1.39±1.13
	-0.05±0.14	0.08±0.28	-0.08±0.08	-0.01±0.41	-0.02±0.72	0.00±0.10	1.38±2.03

Table 4.11: continued

Continent	E	H	Q	R_n	T_s	q_s	θ_s
North America	0.09±0.22	-0.07±0.23	-0.02±0.09	-0.03±0.53	0.08±0.18	0.03±0.03	0.02±1.89
	0.25±0.26	0.01±0.19	0.04±0.11	0.26±0.36	0.24±0.37	0.05±0.07	0.14±2.60
	-0.01±0.60	-0.28±0.37	-0.14±0.16	-0.54±1.12	0.14±0.14	0.05±0.06	-0.47±2.25
	0.15±0.18	0.01±0.30	0.00±0.10	0.17±0.57	-0.03±0.14	0.02±0.05	0.05±2.56
	0.03±0.25	-0.03±0.48	-0.02±0.16	-0.02±0.64	0.06±0.40	0.01±0.07	0.50±4.26
South America	-0.04±0.87	-0.23±0.22	-0.06±0.07	-0.33±0.90	0.02±0.05	0.08±0.13	-1.60±2.76
	-0.13±0.86	-0.21±0.23	-0.06±0.10	-0.41±1.16	0.02±0.08	0.07±0.08	-0.78±3.08
	0.16±0.79	0.02±0.31	0.02±0.11	0.20±0.94	0.01±0.11	0.05±0.12	-2.38±3.17
	-0.29±1.38	-0.35±0.44	-0.07±0.14	-0.71±1.31	0.00±0.13	0.06±0.25	-2.43±3.58
	-0.02±1.14	-0.51±0.50	-0.17±0.10	-0.71±0.92	0.04±0.11	0.13±0.23	-1.01±4.13
Africa	0.26±0.51	-0.10±0.18	-0.06±0.13	0.10±0.75	-0.02±0.10	0.08±0.09	0.82±1.73
	0.00±0.45	-0.20±0.25	-0.14±0.13	-0.34±0.68	0.02±0.13	0.05±0.09	-0.13±2.27
	0.17±0.72	-0.07±0.42	-0.08±0.20	0.01±0.97	-0.02±0.12	0.06±0.19	0.56±2.30
	0.49±0.71	-0.02±0.29	-0.02±0.19	0.45±0.93	-0.03±0.20	0.12±0.17	1.71±2.90
	0.36±0.50	0.04±0.54	0.06±0.26	0.46±1.00	-0.14±0.21	0.07±0.09	1.00±0.96
Australia	0.50±1.30	-0.05±0.51	-0.02±0.25	0.43±1.49	-0.07±0.27	0.08±0.23	1.10±6.43
	0.49±1.89	-0.28±0.42	-0.14±0.41	0.07±2.35	-0.03±0.53	0.19±0.39	0.81±12.06
	0.32±0.64	-0.23±0.57	-0.09±0.28	-0.01±1.04	-0.12±0.22	0.08±0.21	3.67±6.43
	0.29±1.22	-0.04±1.06	-0.06±0.25	0.20±0.96	0.07±0.25	0.03±0.30	0.15±8.26
	1.42±3.55	0.46±1.05	0.28±0.33	2.18±3.01	-0.14±0.44	0.09±0.67	0.17±9.59
Antarctica	0.00±0.00	-0.10±0.09	0.00±0.00	-0.63±0.58	0.05±0.29	0.00±0.00	
	0.00±0.01	-0.13±0.23	0.00±0.00	-0.83±1.34	-0.17±0.56	0.00±0.01	
	0.00±0.00	-0.18±0.11	0.00±0.00	-1.02±0.67	0.16±0.59	0.00±0.00	N/A
	0.00±0.01	-0.08±0.10	0.00±0.00	-0.46±0.54	0.17±0.30	0.00±0.00	
	-0.01±0.02	-0.01±0.11	0.00±0.00	-0.10±0.52	0.03±0.38	-0.01±0.01	

4.6.2 Oceans

Table 4.12 shows the climatology (2001-2010) of the MEP estimated surface heat fluxes and model inputs from CERES for the major ocean basins associated with those reported by L'Ecuyer et al. (2015) (shown in parentheses). The surface water (conductive) heat flux Q from L'Ecuyer et al. (2015) is computed as the residual of surface energy equation as in Eq. (2.2). The annual mean CERES R_n and R_n^L over the major ocean basins are comparable to the estimates reported by L'Ecuyer et al. (2015). Compared to the results of L'Ecuyer et al. (2015), the MEP E and Q over ocean basins are about one-third and 15-20% lower, respectively, while the MEP H is higher than the estimates made by L'Ecuyer et al. (2015). The reason responsible for the discrepancies is caused by the use of a different underlying surface energy equation at annual scale in L'Ecuyer et al. (2015).

Figure 4.16 shows the annual and seasonal trends associated with the corresponding uncertainty estimates (95% CI) of the MEP ocean surface heat fluxes and model inputs at ocean basin scale (see also Table 4.13). The weakly negative trends of MEP E and H over the major ocean basins (i.e., Pacific, Atlantic, and Indian Ocean) are consistent with the trends of R_n, R_n^L, and Q. Note that the positive/negative trends of R_n^L and Q, as shown in Figures 4.16(e) and 4.16(c), represent the decrease/increase in magnitudes due to R_n^L and Q being consistently negative over oceans, i.e., Q enters the surface from water body and R_n^L points upward leaving the surface. The artifacts in CERE T_s data over oceans are small as shown in Figure 4.16(f). Figures 4.16(c) and 4.16(e) show that the added ocean surface thermal energy Q (toward the surface) over the major ocean basins during 2001-2010 are mostly utilized to enhance R_n^L rather than E and H.

Table 4.12: The climatology (2001-2010) of the MEP modeled surface heat fluxes, CERES radiative fluxes for the ocean basins, and the 2000-2009 climatology reported by L'Ecuyer et al. (2015) shown in the parenthesis.

Continent	E	H	Q	R_n	R_n^L
Global Ocean (with polar regions)	56 (98)	28 (19)	-136 (-172*)	122 (117)	-52 (-55)
North Pacific	66 (105)	30 (18)	-147 (-182*)	138 (126)	-51 (-59)
South Pacific	57 (99)	28 (20)	-138 (-178*)	124 (116)	-53 (-59)
Pacific	61 (102)	29 (19)	-142 (-180*)	129 (121)	-52 (-59)
North Atlantic	58 (98)	27 (20)	-137 (-174*)	121 (115)	-53 (-55)
South Atlantic	49 (83)	27 (19)	-126 (-149*)	113 (112)	-50 (-47)
Atlantic	51 (90)	27 (20)	-130 (-161*)	115 (114)	-52 (-51)
Indian Ocean	57 (106)	28 (21)	-138 (-181*)	124 (119)	-53 (-54)
Mediterranean Sea	53 (111)	28 (23)	-154 (-208*)	121 (131)	-74 (-73)
Caribbean Sea	83 (124)	33 (12)	-172 (-191*)	162 (177)	-58 (-55)
Black Sea	39 (85)	23 (21)	-126 (-170)	94 (106)	-65 (-64)
Arctic Ocean	4.9 (10)	4.6 (7)	-46 (-46)	13 (17)	-37 (-30)

To evaluate the effects of CERES data artifacts on the trends of MEP heat fluxes, Figure 4.17 shows the same trend analyses as those in Figure 4.16 but excluding the data from 2008-2010 (see also Table 4.14). The results show that the MEP modeled heat fluxes are virtually stationary during 2001-2007 as a result of the corresponding nearly stationary R_n. Removing the contaminated CERES data does not affect the trends of MEP ocean heat fluxes significantly as evidenced by the close estimates of trends shown in Figures 4.16 and 4.17.

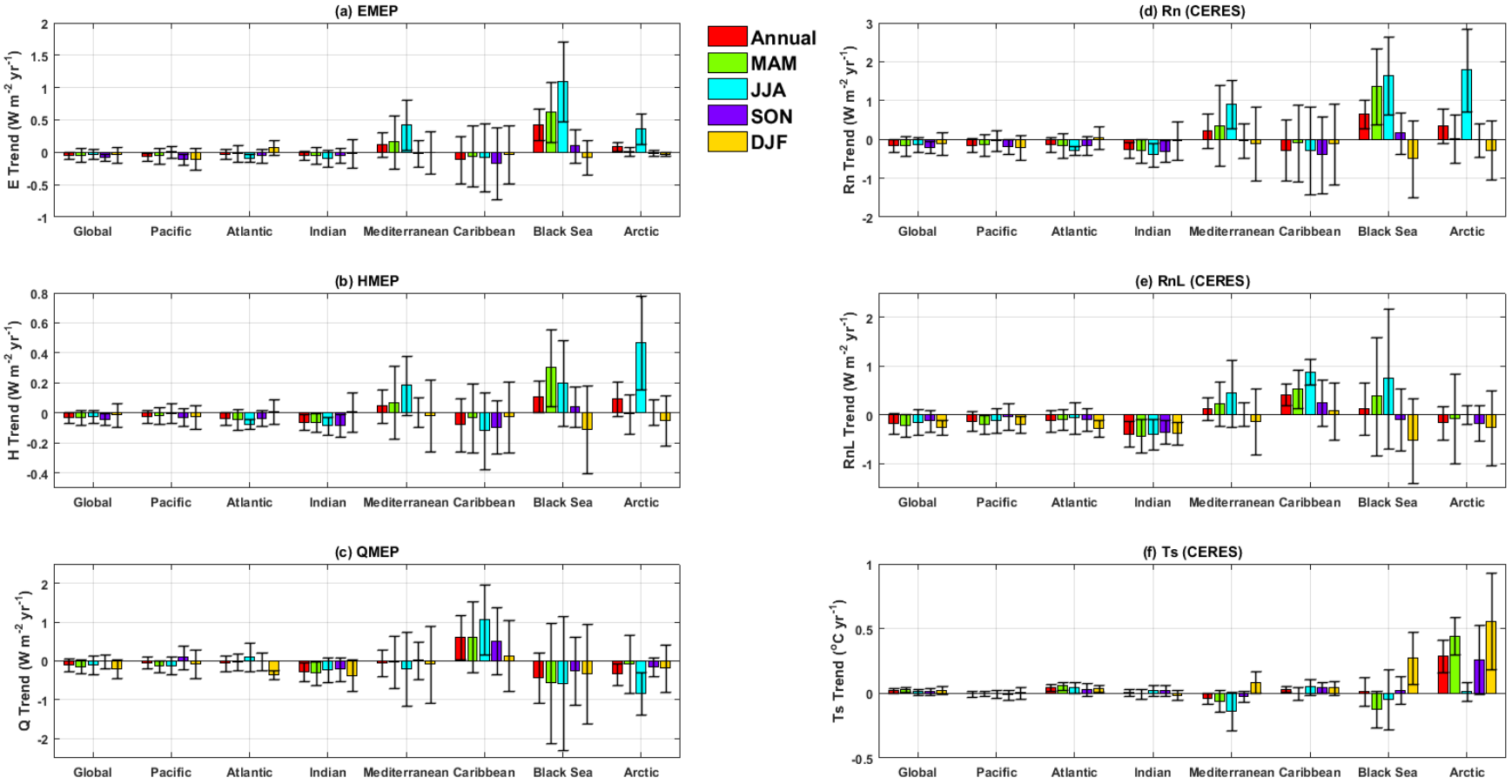

Figure 4.16: The trends and uncertainties (2001-2010) of the MEP estimated (a) E (b) H (c) Q and CERES (d) R_n (e) R_n^L (f) T_s for the ocean basins (MAM: March–April–May; JJA: June–July–August; SON: September–October–November; DJF: December–January–February).

Table 4.13: The annual and seasonal trends of the MEP modeled surface heat fluxes and model inputs for the ocean basins associated with the corresponding uncertainties (95% CI). The numbers in each grid from top to bottom are the annual trend followed by seasonal trends (in the order of MAM, JJA, SON, DJF). The calculations are based on the data over 2001-2010. (Unit: heat and radiative fluxes (W m^{-2} yr^{-1}), T_s (^{o}C yr^{-1})).

Ocean Basin	E	H	Q	R_n	R_n^L	T_s
Global Ocean (with polar regions)	-0.05±0.06 -0.04±0.11 -0.03±0.07 -0.08±0.05 -0.04±0.12	-0.03±0.04 -0.03±0.05 -0.03±0.04 -0.04±0.04 -0.01±0.08	-0.10±0.16 -0.14±0.18 -0.10±0.24 -0.00±0.18 -0.21±0.24	-0.16±0.17 -0.17±0.26 -0.13±0.19 -0.20±0.16 -0.11±0.29	-0.18±0.21 -0.22±0.23 -0.15±0.26 -0.12±0.22 -0.26±0.15	0.02±0.02 0.03±0.02 0.01±0.02 0.01±0.03 0.02±0.03
Global Ocean (without polar regions)	-0.06±0.06 -0.05±0.12 -0.04±0.08 -0.08±0.05 -0.04±0.12	-0.04±0.04 -0.03±0.05 -0.04±0.04 -0.04±0.04 -0.02±0.07	-0.08±0.16 -0.13±0.18 -0.06±0.26 0.02±0.19 -0.20±0.24	-0.18±0.17 -0.17±0.26 -0.17±0.20 -0.20±0.16 -0.13±0.26	-0.17±0.21 -0.20±0.22 -0.14±0.27 -0.10±0.23 -0.26±0.14	0.01±0.02 0.01±0.02 0.01±0.02 0.00±0.02 0.01±0.03
Pacific	-0.07±0.06 -0.05±0.12 0.01±0.09 -0.11±0.08 -0.10±0.17	-0.02±0.04 -0.02±0.05 0.00±0.07 -0.03±0.06 -0.03±0.08	-0.04±0.15 -0.14±0.16 -0.12±0.22 0.09±0.30 -0.08±0.37	-0.15±0.18 -0.14±0.28 -0.03±0.26 -0.19±0.20 -0.20±0.32	-0.13±0.20 -0.21±0.19 -0.11±0.25 -0.04±0.27 -0.21±0.17	0.00±0.02 0.00±0.02 0.00±0.03 -0.01±0.04 0.00±0.04
Atlantic	-0.03±0.08 -0.02±0.13 -0.09±0.07 -0.05±0.11 0.07±0.12	-0.04±0.04 -0.04±0.07 -0.07±0.03 -0.04±0.05 0.01±0.08	-0.06±0.19 -0.03±0.22 0.10±0.37 -0.01±0.22 -0.36±0.11	-0.15±0.19 -0.16±0.31 -0.29±0.12 -0.16±0.25 0.04±0.30	-0.13±0.22 -0.09±0.21 -0.06±0.31 -0.10±0.23 -0.28±0.17	0.04±0.03 0.06±0.03 0.04±0.04 0.03±0.05 0.04±0.03
Indian	-0.05±0.07 -0.05±0.13 -0.09±0.13 -0.05±0.12 -0.02±0.22	-0.06±0.05 -0.06±0.06 -0.08±0.06 -0.08±0.07 0.01±0.13	-0.28±0.23 -0.32±0.29 -0.23±0.33 -0.21±0.32 -0.37±0.41	-0.27±0.20 -0.30±0.29 -0.40±0.30 -0.31±0.28 -0.04±0.49	-0.39±0.26 -0.43±0.33 -0.41±0.31 -0.35±0.25 -0.38±0.23	0.01±0.03 0.00±0.04 0.02±0.04 0.02±0.04 -0.01±0.04
Mediterranean Sea	0.12±0.19 0.16±0.41 0.42±0.39 -0.01±0.21 0.00±0.33	0.05±0.11 0.07±0.24 0.18±0.20 0.00±0.10 -0.02±0.24	-0.04±0.35 -0.02±0.67 -0.20±0.96 0.02±0.48 -0.09±1.00	0.22±0.44 0.35±1.04 0.90±0.63 -0.03±0.44 -0.11±0.96	0.13±0.23 0.23±0.45 0.44±0.69 0.01±0.24 -0.13±0.68	-0.04±0.04 -0.06±0.08 -0.14±0.15 -0.02±0.04 0.09±0.08

Table 4.13: continued

Ocean Basin	E	H	Q	R_n	R_n^L	T_s
Caribbean Sea	-0.11±0.36 -0.06±0.48 -0.08±0.53 -0.17±0.55 -0.03±0.45	-0.08±0.18 -0.03±0.23 -0.12±0.26 -0.09±0.18 -0.02±0.24	0.60±0.57 0.62±0.91 1.07±0.89 0.52±0.87 0.13±0.91	-0.28±0.79 -0.09±1.00 -0.29±1.14 -0.39±0.99 -0.11±1.04	0.42±0.23 0.53±0.39 0.88±0.27 0.26±0.48 0.08±0.59	0.03±0.02 0.00±0.05 0.05±0.06 0.04±0.04 0.04±0.06
Black Sea	0.43±0.24 0.62±0.46 1.09±0.61 0.10±0.26 -0.08±0.26	0.11±0.11 0.30±0.26 0.20±0.28 0.04±0.14 -0.11±0.29	-0.43±0.66 -0.57±1.55 -0.58±1.73 -0.25±0.88 -0.32±1.28	0.66±0.37 1.36±0.97 1.64±1.01 0.16±0.54 -0.50±1.00	0.12±0.54 0.38±1.21 0.74±1.44 -0.10±0.64 -0.53±0.87	0.01±0.11 -0.13±0.14 -0.04±0.23 0.02±0.11 0.28±0.20
Arctic Ocean	0.08±0.07 0.01±0.06 0.36±0.24 -0.01±0.05 -0.03±0.03	0.10±0.12 -0.01±0.13 0.47±0.31 0.00±0.09 -0.05±0.17	-0.34±0.28 -0.08±0.76 -0.83±0.54 -0.16±0.25 -0.18±0.60	0.34±0.44 0.02±0.63 1.79±1.07 -0.02±0.42 -0.27±0.76	-0.16±0.34 -0.07±0.92 -0.00±0.20 -0.17±0.36 -0.27±0.77	0.29±0.12 0.44±0.14 0.01±0.07 0.26±0.27 0.56±0.37
North Pacific	-0.03±0.08 -0.01±0.07 0.07±0.16 -0.10±0.08 -0.07±0.11	0.00±0.04 0.01±0.08 0.04±0.09 -0.02±0.04 -0.05±0.03	-0.08±0.16 -0.16±0.28 -0.14±0.30 0.10±0.31 -0.08±0.29	-0.05±0.19 -0.01±0.36 0.15±0.38 -0.16±0.11 -0.23±0.13	-0.11±0.18 -0.16±0.14 -0.04±0.26 -0.02±0.28 -0.20±0.19	0.01±0.03 0.01±0.03 0.00±0.03 0.00±0.04 0.04±0.05
South Pacific	-0.10±0.07 -0.08±0.13 -0.05±0.08 -0.11±0.14 -0.13±0.26	-0.04±0.05 -0.04±0.06 -0.04±0.05 -0.03±0.08 -0.02±0.12	0.01±0.19 -0.11±0.29 0.07±0.18 0.11±0.34 -0.04±0.57	-0.23±0.20 -0.23±0.31 -0.19±0.22 -0.21±0.32 -0.19±0.50	-0.13±0.24 -0.23±0.29 -0.15±0.26 -0.03±0.29 -0.19±0.25	-0.02±0.02 -0.01±0.03 -0.01±0.03 -0.02±0.04 -0.03±0.05
North Atlantic	-0.05±0.09 0.04±0.08 -0.09±0.14 -0.04±0.16 -0.11±0.10	-0.05±0.06 -0.01±0.12 -0.08±0.08 -0.04±0.07 -0.07±0.06	0.13±0.24 -0.03±0.48 0.42±0.49 0.07±0.27 0.06±0.35	-0.18±0.22 0.03±0.44 -0.26±0.27 -0.16±0.35 -0.32±0.24	0.03±0.19 0.01±0.24 0.25±0.33 -0.01±0.27 -0.11±0.35	0.05±0.02 0.06±0.04 0.04±0.04 0.02±0.03 0.06±0.03
South Atlantic	-0.03±0.10 -0.11±0.19 -0.11±0.06 -0.09±0.12 0.24±0.16	-0.04±0.07 -0.09±0.11 -0.08±0.04 -0.04±0.06 0.07±0.16	-0.19±0.22 0.03±0.23 -0.14±0.34 -0.04±0.28 -0.74±0.33	-0.16±0.29 -0.36±0.49 -0.39±0.22 -0.21±0.27 0.38±0.48	-0.25±0.27 -0.17±0.31 -0.33±0.38 -0.18±0.29 -0.42±0.13	0.04±0.04 0.05±0.05 0.05±0.06 0.03±0.07 0.02±0.04

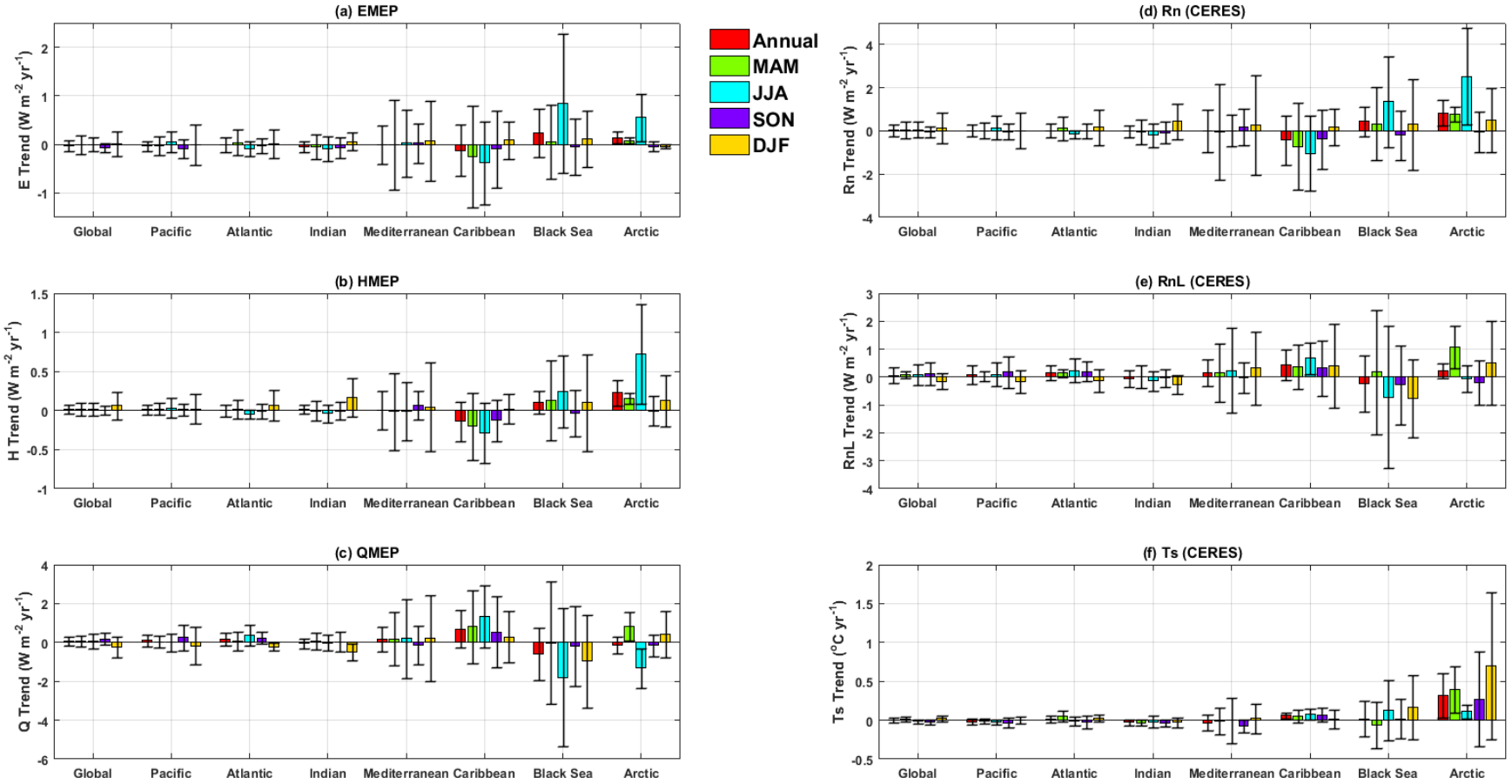

Figure 4.17: The trends and uncertainties (2001-2007) of the MEP estimated (a) E (b) H (c) Q and CERES (d) R_n (e) R_n^L (f) T_s for the ocean basins (MAM: March–April–May; JJA: June–July–August; SON: September–October–November; DJF: December–January–February).

Table 4.14: The annual and seasonal trends of the MEP modeled surface heat fluxes and model inputs for the ocean basins associated with the corresponding uncertainties (95% CI). The numbers in each grid from top to bottom are the annual trend followed by seasonal trends (in the order of MAM, JJA, SON, DJF). The calculations are based on the data over 2001-2007. (Unit: heat and radiative fluxes (W m^{-2} yr^{-1}), T_s (^{o}C yr^{-1})).

Ocean Basin	E	H	Q	R_n	R_n^L	T_s
Global Ocean (with polar regions)	-0.03±0.10 -0.01±0.19 0.00±0.15 -0.07±0.09 0.01±0.26	0.01±0.06 0.02±0.08 0.01±0.08 0.00±0.06 0.06±0.18	0.08±0.24 0.08±0.27 0.06±0.38 0.19±0.33 -0.23±0.54	-0.16±0.17 0.04±0.39 0.05±0.37 -0.04±0.26 0.15±0.71	0.07±0.28 0.08±0.12 0.08±0.38 0.12±0.40 -0.16±0.29	0.00±0.03 0.01±0.03 -0.01±0.03 -0.02±0.03 0.02±0.04
Global Ocean (without polar regions)	-0.04±0.11 -0.02±0.21 -0.01±0.17 -0.07±0.10 0.00±0.26	0.01±0.06 0.01±0.09 -0.01±0.09 0.00±0.07 0.04±0.16	0.11±0.25 0.09±0.29 0.10±0.42 0.23±0.34 -0.22±0.53	-0.01±0.29 0.02±0.43 -0.01±0.40 -0.04±0.29 0.08±0.66	0.08±0.29 0.08±0.14 0.08±0.40 0.15±0.42 -0.18±0.28	-0.01±0.02 -0.01±0.02 -0.01±0.02 -0.02±0.04 0.00±0.02
Pacific	-0.04±0.11 -0.03±0.19 0.06±0.21 -0.09±0.20 -0.01±0.41	0.01±0.06 0.02±0.08 0.03±0.13 0.01±0.08 0.02±0.19	0.10±0.30 0.04±0.29 -0.00±0.46 0.25±0.65 -0.17±0.97	0.01±0.28 0.02±0.38 0.15±0.54 -0.03±0.36 0.00±0.82	0.07±0.34 0.03±0.18 0.09±0.42 0.17±0.57 -0.16±0.41	-0.02±0.04 -0.01±0.04 -0.02±0.03 -0.03±0.07 0.00±0.05
Atlantic	-0.01±0.15 0.04±0.26 -0.09±0.15 -0.03±0.15 0.02±0.30	0.00±0.08 0.02±0.12 -0.05±0.06 -0.01±0.09 0.06±0.19	0.16±0.33 0.08±0.47 0.37±0.55 0.24±0.31 -0.22±0.18	0.02±0.33 0.12±0.54 -0.16±0.20 -0.01±0.36 0.16±0.83	0.15±0.26 0.14±0.14 0.24±0.41 0.21±0.34 -0.14±0.41	0.01±0.05 0.06±0.07 -0.01±0.06 -0.02±0.09 0.03±0.04
Indian	-0.04±0.11 -0.05±0.25 -0.09±0.25 -0.07±0.22 0.06±0.18	0.01±0.06 -0.01±0.12 -0.04±0.11 -0.01±0.11 0.17±0.25	-0.04±0.26 0.07±0.44 -0.01±0.41 0.04±0.49 -0.49±0.44	-0.01±0.26 -0.06±0.58 -0.20±0.55 -0.07±0.49 0.45±0.82	-0.07±0.30 0.02±0.40 -0.14±0.36 -0.04±0.32 -0.27±0.32	-0.03±0.04 -0.03±0.04 -0.02±0.08 -0.04±0.04 -0.03±0.06
Mediterranean Sea	-0.01±0.40 -0.01±0.92 0.03±0.69 0.03±0.41 0.07±0.82	0.00±0.225 -0.01±0.49 -0.01±0.37 0.07±0.18 0.05±0.57	0.16±0.63 0.19±1.35 0.21±2.03 -0.12±0.99 0.20±2.22	0.00±0.97 -0.04±2.22 0.02±0.72 0.17±0.84 0.26±2.30	0.16±0.47 0.17±1.04 0.24±1.53 -0.02±0.54 0.32±1.31	-0.03±0.10 -0.01±0.17 0.00±0.29 -0.07±0.08 0.02±0.19

Table 4.14: continued

Continent	E	H	Q	R_n	R_n^L	T_s
Caribbean Sea	-0.12±0.53 -0.26±1.05 -0.38±0.85 -0.10±0.80 0.09±0.39	-0.14±0.25 -0.20±0.43 -0.29±0.39 -0.12±0.27 0.02±0.19	0.70±0.96 0.81±1.88 1.33±1.59 0.54±1.83 0.29±1.31	-0.43±1.14 -0.72±2.01 -1.03±1.75 -0.38±1.37 0.17±0.86	0.44±0.55 0.35±0.79 0.67±0.56 0.32±1.00 0.40±1.50	0.06±0.04 0.05±0.08 0.08±0.07 0.07±0.09 0.02±0.12
Black Sea	0.23±0.50 0.05±0.76 0.85±1.43 -0.05±0.58 0.11±0.58	0.10±0.15 0.13±0.51 0.24±0.46 -0.04±0.29 0.10±0.61	-0.57±1.34 -0.01±3.16 -1.79±3.54 -0.19±2.07 -0.96±2.39	0.44±0.69 0.34±1.67 1.35±2.10 -0.21±1.14 0.31±2.10	-0.24±1.01 0.17±2.22 -0.71±2.56 -0.28±1.42 -0.76±1.40	0.02±0.23 -0.07±0.30 0.13±0.39 0.02±0.25 0.16±0.41
Arctic Ocean	0.14±0.12 0.08±0.06 0.55±0.48 -0.04±0.10 -0.04±0.04	0.23±0.17 0.16±0.07 0.72±0.64 0.00±0.19 0.13±0.33	-0.15±0.42 0.83±0.74 -1.32±1.02 -0.15±0.55 0.43±1.20	0.83±0.59 0.78±0.35 2.53±2.25 -0.05±0.92 0.50±1.50	0.22±0.27 1.07±0.77 -0.05±0.46 -0.20±0.80 0.51±1.51	0.31±0.28 0.40±0.30 0.11±0.09 0.27±0.61 0.70±0.95
North Pacific	0.00±0.08 0.02±0.29 0.11±0.32 -0.12±0.16 -0.08±0.17	0.02±0.07 0.04±0.13 0.06±0.22 -0.01±0.06 -0.06±0.09	-0.03±0.36 -0.18±0.53 -0.11±0.63 0.25±0.70 -0.03±0.55	0.05±0.29 0.11±0.60 0.29±0.88 -0.13±0.19 -0.26±0.32	-0.01±0.40 -0.12±0.28 0.07±0.53 0.12±0.61 -0.17±0.39	0.00±0.05 -0.01±0.06 -0.01±0.05 0.00±0.07 0.02±0.09
South Pacific	-0.07±0.16 -0.08±0.24 0.00±0.16 -0.07±0.31 0.05±0.61	0.01±0.06 -0.01±0.12 0.00±0.06 0.04±0.12 0.08±0.28	0.20±0.30 0.25±0.41 0.11±0.30 0.23±0.73 -0.30±1.30	-0.04±0.30 -0.09±0.53 0.01±0.33 0.05±0.58 0.22±1.22	0.13±0.31 0.16±0.16 0.11±0.39 0.20±0.59 -0.17±0.45	-0.03±0.04 -0.02±0.05 -0.03±0.04 -0.05±0.07 -0.01±0.05
North Atlantic	-0.08±0.14 0.00±0.41 -0.17±0.26 -0.05±0.21 -0.20±0.19	-0.05±0.08 -0.22±0.22 -0.10±0.13 -0.02±0.13 -0.09±0.15	0.33±0.43 0.10±1.00 0.70±0.90 0.23±0.49 0.33±0.82	-0.19±0.33 -0.02±0.90 -0.36±0.43 -0.08±0.55 -0.43±0.65	0.20±0.38 0.08±0.43 0.43±0.66 0.17±0.55 0.04±0.92	0.04±0.05 0.07±0.05 0.03±0.08 0.01±0.07 0.06±0.06
South Atlantic	0.04±0.19 0.03±0.29 -0.03±0.09 -0.01±0.19 0.27±0.45	0.04±0.10 0.05±0.09 -0.01±0.03 0.00±0.12 0.23±0.28	0.04±0.39 0.13±0.53 0.12±0.42 0.27±0.43 -0.80±0.82	0.19±0.38 0.21±0.50 -0.04±0.08 0.05±0.39 0.80±1.04	0.12±0.20 0.22±0.30 0.08±0.35 0.26±0.22 -0.31±0.14	-0.01±0.05 0.04±0.11 -0.05±0.04 -0.04±0.12 0.00±0.07

4.7 Global Heat Fluxes over Snow-ice and Sea Ice Surfaces

This section provides an analysis of MEP-based estimates of global land snow-ice and sea ice surface heat fluxes and the corresponding contributions to global surface heat flux budgets. The effects of land snow and sea ice on the global surface heat flux budgets were evaluated by comparing two separate MEP simulations in terms of including and excluding time-varying snow and sea ice extent (i.e. fractional snow and sea ice cover data from MERRA). The simulation including snow and sea ice extent is referred to as the Control run and used in the performed analysis in Sections 4.5 and 4.6, while that excluding snow and sea ice extent is referred to as the NoSI run. In the Control run, the surface type, assigned based on the IGBP surface classification climatology, was updated daily according to the MERRA fractional snow/sea ice cover data. By contrast, surface types in the NoSI run were determined based on the IGBP surface classification climatology alone. The sublimation ESI, sensible heat HSI, and surface snow-ice heat QSI fluxes obtained from the NoSI run represent the heat fluxes over permanent ice surfaces such as polar regions (PoRs) and alpine regions (e.g., Himalayas). The contributions from non-PoRs and PoRs will be evaluated by computing the global ESI, HSI, and QSI taking/not taking the PoRs into account.

4.7.1 Global Heat Fluxes over Land Snow-ice Surfaces

Figure 4.18 shows the climatology (2001-2010, the left panel) and global annual means of MEP modeled ESI, HSI, and QSI over global land obtained from the Control run (red curves shown on the right panel). The shaded area over the non-PoRs in Figures 4.18

(a), 4.18(c), and 4.18(e) represents the grid points in which the MERRA snow data are available, referred to as the Non-PoR-Snow-Covered (NPSC) area (MERRA snow data are not available over the PoRs). The global mean land snow-ice surface heat fluxes obtained from the NoSI run and those by excluding the PoRs are shown on the right panel of Figure 4.18. The global annual means of MEP modeled ESI, HSI, and QSI evaluated under different scenarios in terms of including/excluding snow cover and the PoRs are listed in Table 4.15. The global annual mean MEP ESI, HSI, and QSI obtained from the Control run taking the PoRs into account are 0.6, 0.2, and -8.8 W m^{-2}, respectively (see Table 4.15). Negative Q indicates thermal energy from the snow-ice surface into the atmosphere.

Figure 4.18(b) shows that the global mean ESI becomes slightly higher by excluding the PoRs (blue curve) as the ESI over the PoRs is nearly zero resulting from the corresponding low R_n and T_s (i.e., low q_s). ESI over permanent ice-covered areas is small (NoSI run, black curve) suggesting that global ESI is mainly contributed by the non-PoRs (blue curve) (see also Table 4.15). The global annual means of MEP HSI over lands obtained from the Control and NoSI runs are both small (< 0.2 W m^{-2}) during 2001 to 2007 as shown in Figure 4.18(d). The abrupt increases of global mean HSI (also ESI) between 2007 and 2008 in both runs are caused presumably by the corresponding increase of CERES R_n due to the artifact (see discussions in Section 4.5.1). Excluding the PoRs leads to a slightly higher global mean HSI (blue curve) due to the exclusion of the small but negative HSI over permanent ice-covered areas (black curve, NoSI run) before 2007. In contrast, excluding the positive HSI over the PoRs (black curve) during 2008 to 2010 leads to the corresponding lower global mean HSI (blue vs. red curve). Yet the positive HSI over the PoRs may be less reliable as the corresponding CERES R_n is potentially biased as a

result of the artifact in CERES T_s (also LWu). Figure 4.18(e) shows that the MEP estimated QSI (-QSI is shown) over the PoRs is greater than that over the non-PoRs. The reason is that the non-PoRs are free of or only partially covered by snow in non-winter season, while the PoRs are permanently ice-covered. The contributions of QSI over the PoRs and non-PoRs at annual scale are comparable as shown in Figure 4.18(f) (see also Table 4.15).

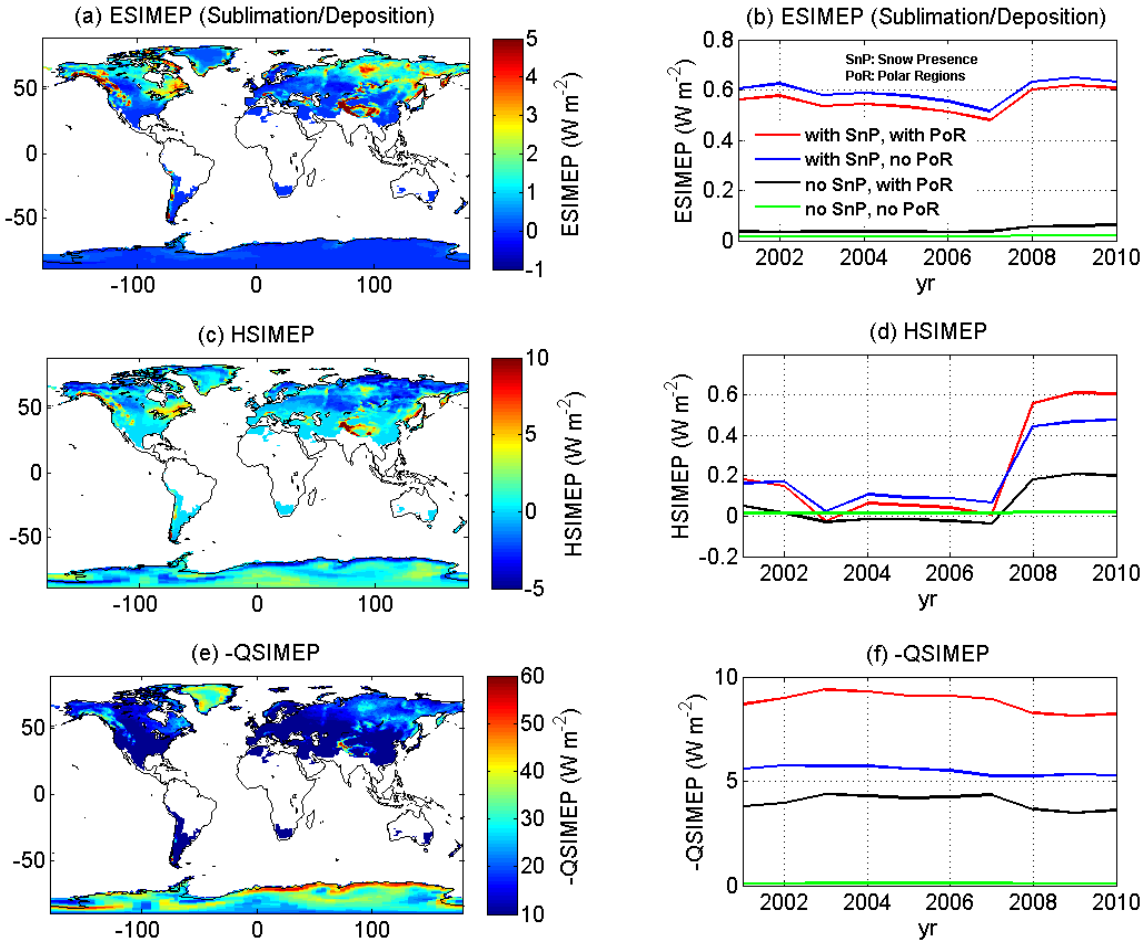

Figure 4.18: The 2001-2010 climatology of the MEP estimated (a) *ESI* (c) *HSI* (e) *QSI* (- *QSI* is shown) over lands according to Eq. (4.2) with the snow properties derived from Eqs. (4.3) and (4.4) and MERRA snow data, and global annual means of land (b) *ESI* (d) *HSI* (f) *QSI* calculated with/without snow presence (SnP) and polar regions (PoR) taken into account.

The trends of global annual mean MEP ESI, HSI, and QSI over lands are estimated as 0.01, 0.06, and 0.1 W m^{-2} yr^{-1} and have corresponding uncertainties of 0.01, 0.05, and 0.09 W m^{-2} yr^{-1}, respectively. Note that all three heat fluxes vanish when excluding both snow cover (i.e., NoSI run) and PoRs as shown in the green curves in Figures 4.18(b), 4.18(d), and 4.18(f). This is expected as the alpine areas, which account for only a small part of global land area, are the only source of snow-ice surface heat fluxes under this scenario.

Table 4.15: The 2001-2010 climatology of the MEP estimated global annual mean snow-ice surface heat fluxes (W m^{-2}) over lands according to Eq. (4.2) calculated with/without snow presence (SnP) and polar regions (PoR) taken into account.

Scenario	*ESI*	*HSI*	*QSI*
With SnP, with PoR	0.6	0.2	-8.8
With SnP, no PoR	0.6	0.2	-5.5
No SnP, with PoR	~0	0.1	-4.0
No SnP, no PoR	~0	~0	-0.1

Figure 4.19 shows the effects of snow cover on the MEP estimated global land surface heat flux budgets by comparing the estimates of the Control and NoSI runs. The discrepancies between the two simulations only exist over the NPSC areas, indicated by the shaded area in Figures 4.19(a), 4.19(c), and 4.19(e). This is because the model inputs and parameters of the two simulations over the snow-free areas and PoRs are identical. Figures 4.19(a) and 4.19(c) show that the differences of E and H between the two simulations over most of the NPSC areas are insignificant except for alpine areas (permanence ice-covered). Several reasons might be responsible for the small discrepancies. First, the surface R_n tends to be low over the NPSC areas. Second, the low

T_s over the NPSC areas leads to almost the same q_s inputs in the two simulations (saturation for the Control run vs. MERRA q_s for the NoSI run). Third, E and H estimated by the two simulations are identical or close to each other when the NPSC areas are free of or partially covered by snow (i.e., outside the cold season). The differences between green/blue and red/black curves in Figures 4.19(b), 4.19(d), and 4.19(f) represent the contributions of heat fluxes over the PoRs to the global surface heat flux budgets. The decreases of global mean MEP surface heat fluxes caused by excluding the PoRs are shown in Table 4.3.

Figures 4.19(a) and 4.19(c) show that the Control run produces higher E and H over alpine areas (e.g. Himalayas) as compared to the NoSI run. The discrepancies are presumably resulting from the switch of surface type of alpine areas between the Control and NoSI runs. Over alpine areas, the surface type was set as snow in the Control run whenever MERRA snow data are available, while permanent ice surface was prescribed in the NoSI run according to the IGBP data. The smaller thermal inertia of snow (< 900 tiu) compared to ice (1920 tiu) leads to larger E and H given the same model input and other parameters according to Eq. (4.2). Figure 4.19(e) shows that the annual mean Q obtained from the Control run is slightly higher than that obtained from the NoSI run over the NPSC areas (see also Figure 4.19(f) for the global annual mean). In the Control run, Q over the NPSC areas is zero during winter due to snow cover, while winter Q over the NPSC areas was found to be negative in the NoSI run for bare soil surfaces (i.e., no snow).

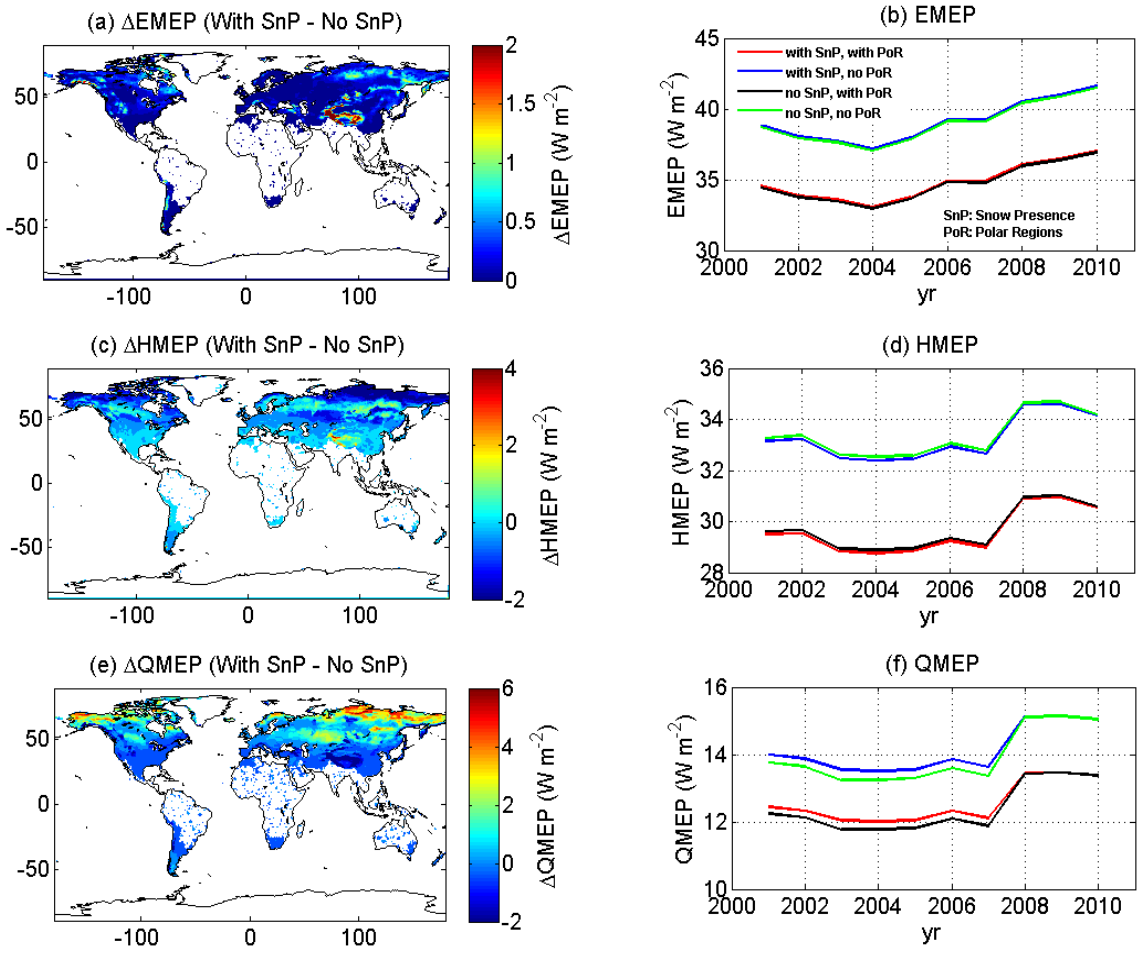

Figure 4.19: The differences in the MEP estimated climatology of (a) *E*, (c) *H*, and (e) *Q* over global land caused by the snow presence and annual means of MEP (b) *E*, (d) *H*, and (f) *Q* calculated with/without snow presence (SnP) and polar regions (PoR) taken into account.

4.7.2 Global Heat Fluxes over Sea Ice Surfaces

Figure 4.20 shows the 2001-2010 climatology (left panel) and annual means (right panel) of MEP estimated *ESI*, *HSI*, and *QSI* over global oceans obtained from the Control run. The sea ice surface heat fluxes become zero by either excluding sea ice cover (NoSI run) or the PoRs as the MERRA sea ice data are available only over the PoRs. The global

annual means of ESI, HSI, and QSI over sea ice surfaces are estimated as 0.17, 0.13, and -2.4 W m^{-2}, respectively. The decrease of HSI between 2007 and 2008 results from the corresponding decrease of CERES R_n (due to the increase of R_n^L (in magnitude)) over the PoRs (see Figure 4.13(k)). Figure 4.20(b) shows that the effects of CERES data artifact on ESI are insignificant. Over the PoRs, ESI is dominated and constrained by q_s, which is persistently low (about 2 g kg^{-1}). The low q_s keeps the ESI stationary between 2007 and 2008 even though the corresponding R_n decreases.

The MEP estimates of global ocean ESI and QSI have trends of 0.01 and -0.05 W m^{-2} yr^{-1}, while those of global ocean HSI stay stationary during 2001-2010. The uncertainties of the trends of global ocean MEP ESI and HSI are small (<0.01 W m^{-2} yr^{-1}). The trend uncertainty of global ocean MEP QSI is estimated as 0.03 W m^{-2} yr^{-1}. Figure 4.21 shows the comparisons of global annual mean MEP ocean surface heat fluxes obtained from the Control (with sea ice cover) and NoSI run (without sea ice cover). The results show that the MEP modeled ocean surface heat fluxes are insensitive to sea ice cover. The reason is that the MEP models over water and ice surfaces are identical when using slightly different thermal inertia parameters (1560 and 1920 tiu for water and ice, respectively), which is not sensitive to the MEP simulations given the same model inputs and other parameters.

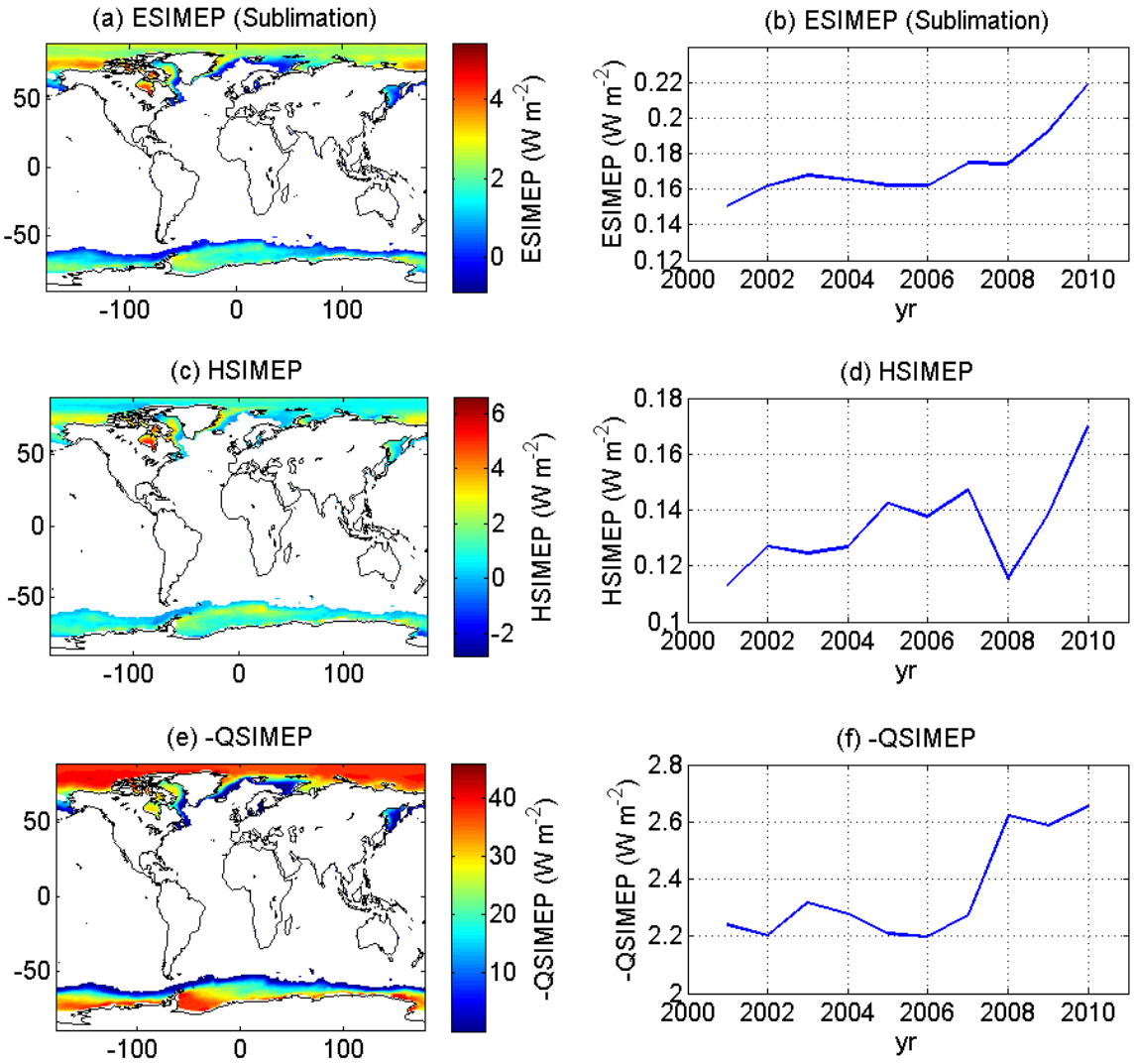

Figure 4.20: The 2001-2010 climatology of the MEP estimated (a) *ESI* (c) *HSI* (e) *QSI* (-*QSI* is shown) over oceans (Eq. (4.2)) with the corresponding global annual means shown on the right panel.

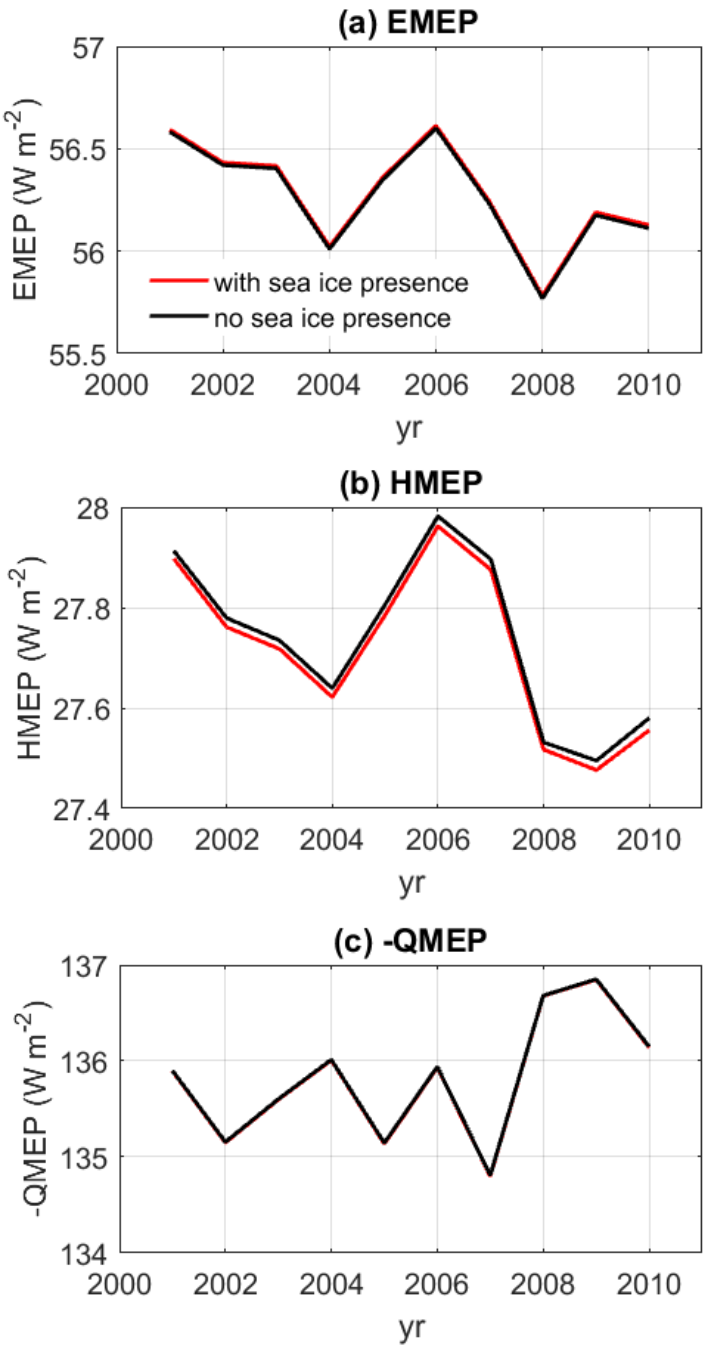

Figure 4.21: The global annual means (2001-2010) of the MEP estimated (a) E, (b) H, and (c) Q (-Q is shown) over oceans calculated with/without sea ice presence taken into account.

4.8 Summary

In this study, global climatology of surface heat fluxes is re-evaluated using the MEP model and input data of surface radiation, temperature data from NASA CERES supplemented by the (land) surface specific humidity and soil moisture data from the MERRA without explicit use of near-surface temperature and moisture gradient, wind speed and surface roughness lengths data. The MEP modeled surface heat fluxes have reduced uncertainty (limited by the uncertainty of surface net radiation) compared to the existing estimates. The MEP model produces the first direct estimate of global ocean surface water-snow-ice heat flux that is not available from existing data products.

The MEP model produces new estimates of global annual mean evaporation of 682±76 mm yr^{-1} and sensible heat flux of 31±3 W m^{-2}. The surface heat fluxes over land and ocean domains are examined separately. The MEP estimated terrestrial evapotranspiration (39±10 W m^{-2}) is in close agreement with previous estimates, while the estimate of ocean evaporation is about one-third lower than bulk-based estimates (61±6 vs. 90-100 W m^{-2}). The MEP estimated global annual mean of sensible heat flux (33±7 W m^{-2}) over lands is consistent with previous estimates, while that of ground heat flux (14±10 W m^{-2}) is higher than previous estimates. The MEP estimate of global annual mean ocean sensible heat flux, 30±3 W m^{-2}, is higher than previous estimates that ranged from 6-18 W m^{-2}. The global annual mean of MEP ocean surface (conductive) heat flux is -143±9 W m^{-2} (through conductive cool-skin), which is 15-20% smaller than the existing estimates. The relative proportions of the MEP and the existing estimates of heat flux budgets at regional (continental and ocean basin) scales are consistent with those at global scale. The MEP estimate of the global annual mean net ocean heat flux (or ocean heat uptake) is positive

(40±6 W m^{-2}), which is consistent with most of the existing estimates. The discrepancies between the MEP and existing estimates mainly result from the use of different surface energy balance equations at annual scale.

The annual and seasonal trends associated with the corresponding uncertainties of the MEP surface heat fluxes were analyzed at global and continental- and ocean-basin scales. The global annual means of MEP estimates over lands have increasing trends of 0.41±0.23, 0.18±0.18, and 0.16±0.13 W m^{-2} for latent, sensible, and ground heat fluxes, respectively. The increasing land surface radiative energy during 2001-2010 was mainly used to enhance evapotranspiration. The trends of global annual mean ocean surface evaporation, sensible and conductive heat fluxes are estimated as -0.06±0.06, -0.04±0.04, and -0.08±0.16 W m^{-2}, respectively, consistent with those of R_n and R_n^L. The increasing ocean surface conductive heat flux over the major ocean basins are mainly dissipated through R_n^L. The regional and seasonal trends are largely consistent with the global and annual trends, respectively. The effects of the artifact in CERES data on the trends of MEP estimated global/regional surface heat fluxes were evaluated by excluding the contaminated data (after 2008). The results suggest that the trends of global/regional mean MEP surface heat fluxes become either small or negligible over both lands and oceans.

The global land snow-ice and sea ice surface heat fluxes are produced using the MEP model with the snow and sea ice data from MERRA. The MEP modeled global terrestrial sublimation is 0.6 W m^{-2} with the major contributions from the non-polar regions. The global annual mean of land snow-ice surface sensible heat flux estimated by the MEP model is 0.2 W m^{-2}. The MEP-based estimates of global mean of (land) snow-ice surface conductive heat flux is -8.8 W m^{-2} with comparable contributions of the polar and

non-polar regions. The MEP modeled global snow-ice surface heat fluxes have positive trends (2001-2010) estimated as 0.01±0.01, 0.06±0.05, and 0.10±0.09 W m^{-2} yr^{-1} for sublimation, sensible, and conductive heat flux, respectively.

The effects of snow cover on the MEP estimates of global land surface heat fluxes were evaluated in this study. The results showed that the global means of MEP modeled latent heat and sensible heat fluxes remain approximately the same, while that of MEP modeled ground heat flux decreases slightly when excluding the snow covered areas. The MEP estimates of global sea ice surface sublimation, sensible, and conductive heat fluxes are 0.17, 0.13, and -2.4 W m^{-2}, respectively. The annual trends of MEP global sea ice surface sublimation and conductive heat fluxes are estimated as 0.01 and -0.05 W m^{-2} yr^{-1}, while the corresponding sensible heat flux stayed stationary. The trend uncertainties of the global sea ice surface sublimation and sensible heat flux are small (< 0.01 W m^{-2} yr^{-1}). The uncertainty of the annual trend of MEP modeled global sea-ice surface conductive heat flux is estimated as 0.03 W m^{-2} yr^{-1}. The results suggest that the MEP modeled ocean surface heat fluxes are insensitive to sea ice cover.

The discrepancies between the MEP-based heat flux estimates and those based on traditional approaches arise from multiple sources including uncertainties of input variables and model parameters. However, these uncertainties are difficult to quantify as part of inputs (e.g., wind speed) and parameters (e.g., SRLs), which are required in the conventional flux models, are not explicitly used in the MEP model. These issues are further exacerbated by the difficulties in obtaining “ground-truth” of heat fluxes over oceans and uncertainties in deriving surface radiative fluxes through radiative transfer calculations (e.g., in the presence of clouds).

CHAPTER 5. CONCLUSIONS AND FUTURE RESEARCH

5.1 Research Contributions and Findings

This dissertation aims to investigate the improvements of land surface model and global surface energy budget estimates by introducing an innovative parameterization of surface heat flux, the maximum entropy production (MEP) model. The expected improvements result from theoretical and technical advantages of the MEP model compared to the traditional bulk transfer model (BTM). An operational modeling framework, together with the quantitative analyses of applying the MEP model to the development of (1) an improved parameterizations of surface temperature, surface soil moisture, and near-surface air temperature, and (2) estimates of global surface energy budgets, are summarized in this chapter.

In this study, a coupled land surface model for predicting surface temperature, soil moisture, and near-surface air temperature was formulated based on the force-restore method (FRM) incorporating the MEP model of surface heat fluxes (FRMEP). The FRMEP model is driven by surface radiation and precipitation data without using other meteorological variables such as air temperature, humidity, wind speed and surface roughness lengths among others. In the FRMEP model, the surface soil moisture equation was revised by taking the gravitational drainage term into account. The newly derived FRM of near-surface air temperature is driven by sensible heat flux, while the existing LSMs estimates near-surface air temperature mostly through empirical equations.

The proposed FRMEP model was evaluated using field observations with contrasting climate and soil wetness conditions. The simulations of the FRMEP model were compared with those from the classical FRMs forced by observed or modeled heat flux using conventional approaches (e.g., bulk transfer model, BTM). A one-year simulation of the FRMEP model was conducted to understand the performance of the FRMEP model for capturing the seasonal variations of surface temperature, soil moisture, near-surface air temperature and heat fluxes.

Recent studies have shown that the existing LSMs produce inconsistent estimates of global surface energy budgets and the corresponding long-term variability. The existing global data products of surface heat fluxes are subject to large errors and uncertainties resulting from the drawbacks in the conventional flux models. In this study, the MEP model was applied to reconstructing a new data set of global surface energy budgets together with the corresponding trend and uncertainty for the first decade of the twenty-first century. The model inputs are obtained from contemporary remote sensing observations, such as NASA CERES surface radiation and temperature, as well as reanalysis data from MERRA surface humidity and snow/sea ice products. The MEP modeled surface heat fluxes over land and ocean domains are examined at continental and ocean-basin scales, respectively, to quantify the corresponding global contributions.

Several achievements made in this study, which bridge the gaps in the current understanding of global surface energy budgets based on the existing data products, are benefited by the unique formalism of the MEP model. First, the MEP model produces the first directly modeled global water-snow-ice surface heat fluxes not available from the existing data products. Second, the MEP model provides an analytical expression for

estimating the uncertainties of surface heat fluxes. In contrast, the heat flux uncertainties reported by previous studies are simply a spread of various estimates or random sampling errors using limited ground observations. Finally, the MEP model gives a new estimate of global sublimation, sensible and snow-ice surface conductive heat fluxes over (land) snow/ice- and sea-ice-covered areas, together with the analyses of the effects of land snow/ice and sea ice cover on the MEP estimates of global surface energy budgets.

The accomplished work is described in Chapter 3 and 4. The major findings are summarized below.

(1) The FRMEP model

- The FRMEP model predicted surface temperature, soil moisture, and near-surface air temperature agree closely with observations under various climate and soil wetness conditions. The modeling errors of the FRMEP model predictions are lower than those of the classical FRMs driven by observed or BTM heat fluxes (bias 1~2 ^{o}C vs. ~4 ^{o}C for surface temperature, 0.02 m^3 m^{-3} vs. 0.05 m^3 m^{-3} for surface soil moisture, less than 1 ^{o}C vs. 2~3 ^{o}C for near-surface air temperature).

- The FRMEP model accurately predicts the diurnal variations of surface temperature, soil moisture, and near-surface air temperature measured by high correlations ($\geq$ 0.7) between the model predictions and observations.

- The MEP modeled surface heat fluxes agree closely with observations, while the BTM estimated heat fluxes have unrealistic fluctuations as a result of the large uncertainties and errors (theoretically unbounded) of model inputs (wind

temperature/humidity gradient) and parameters (bulk transfer coefficients). The MEP modeled surface heat fluxes have lower modeling errors and higher correlations with observations compared to the BTM modeled heat fluxes.

- The MEP modeled surface heat fluxes improve the model performance during nighttime and rainy period whenever the observed heat fluxes have large measurement errors.

- The revised FRM of soil moisture taking the gravitational drainage into account significantly improves the simulated soil moisture under high soil moisture conditions, which suggests that the drainage term cannot be neglected under wet soil condition.

- The FRMEP model is able to simulate the seasonal variations of surface temperature, soil moisture, and near-surface air temperature (correlations 0.93, 0.93, and 0.87, respectively) with mean biases of 1.7 ^{o}C, 6×10^{-3} m^3 m^{-3}, and 0.49 ^{o}C, respectively.

- Specification of FRM model parameters, such as the reference soil temperature, moisture and air temperature, has a stronger impact on long-term simulations as opposed to short-term simulations, which is a major limitation of the FRM for long-term simulations.

These encouraging results justify the use of the FRMEP as a promising data retrieval algorithm using satellite remote sensing observations. The FRMEP model may also be an attractive physical parameterization of surface soil temperature, soil moisture,

and heat fluxes in regional and global atmospheric models. The direct use of radiation and precipitation data as model forcing facilitates the application of the FRMEP model in the study of regional and global water and energy cycles as remote sensing observation missions are now capable of providing more abundant global high-resolution radiation (e.g., NASA CERES) and precipitation (e.g., NASA-The Global Precipitation Measurement Mission) data sets (Wielicki et al., 1996; Hou et al., 2014). Additionally, the FRMEP model expands applications of the MEP model of surface heat fluxes in situations where remote sensing observations of surface temperature and moisture have substantial gaps in space and time coverage and uncertainties.

(2) MEP-based Estimates of Global Surface Energy Budgets

- The MEP estimate of global land evapotranspiration 492 mm yr^{-1} (39±10 W m^{-2}) agrees closely with previous estimates, while that of ocean evaporation (61±7 W m^{-2}) is lower than the existing estimates produced by the bulk-formula-based algorithms (90-100 W m^{-2}).

- The MEP estimated global annual mean sensible heat flux over lands is 33±7 W m^{-2} consistent with previous estimates, while that over oceans, 30±3 W m^{-2}, is higher than the previous estimates ranging from 6-18 W m^{-2}.

- The global annual mean ground heat flux estimated by the MEP model is 14±10 W m^{-2}, while most of the existing estimates are nearly zero assuming there is no net energy absorbed/released by the Earth's surface at annual scale. The MEP modeled

global ocean surface conductive heat flux is -143±9 W m^{-2}, which is 15-20% lower than the existing estimates derived from a residual of surface energy balance. The MEP-based estimates of net ocean heat flux (or ocean heat uptake) is positive (40±6 W m^{-2}) consistent with most of the previous estimates.

- The MEP model produced new estimates of global annual mean evaporation, 682±76 mm yr^{-1}, is lower than the existing estimates, while that of global annual mean sensible heat flux is higher than previously reported. This is mainly caused by the lower (higher) estimates of evaporation (sensible heat flux) over oceans. The overall positive net surface heat fluxes (33±6 W m^{-2}) suggests that the Earth's is gaining thermal energy at annual scale.

- The uncertainties of the MEP modeled climatology of global land and ocean surface heat fluxes are smaller than the existing estimates. The uncertainties of MEP surface heat fluxes are evaluated analytically and constrained by that of surface (net) radiation.

- Land surface heat fluxes have increasing trends globally as estimated by the MEP model, while MEP modeled ocean surface heat fluxes show decreasing trends during 2001-2010. The trends of the MEP heat fluxes are consistent with those of CERES surface net radiation data. The regional (continental and ocean basin scale) and seasonal trends are largely consistent with the global and annual trends, respectively. The positive trends of MEP land surface heat fluxes may be overestimated and is thought to be caused by the artifact in the CERES surface temperature (and upward longwave radiation) data resulting in abrupt increase of

CERES surface net radiation between 2007 and 2008. The trends of MEP heat fluxes become stationary if excluding the contaminated data.

- The added surface radiation energy over lands is largely used to enhance evapotranspiration, while the increase of ocean surface thermal energy over oceans is mostly dissipated through longwave radiation.

- The MEP estimated global land sublimation is 0.6 W m^{-2} mostly contributed by the non-polar-snow-covered areas. The global annual mean of land snow-ice surface sensible heat flux estimated by the MEP model is 0.2 W m^{-2}. The snow-ice surface conductive heat flux over global land is estimated as -8.8 W m^{-2} with comparable contributions of polar and non-polar regions. The global annual means of MEP modeled terrestrial latent and sensible heat flux are insensitive to snow cover, while those of MEP ground heat flux slightly increase if excluding snow cover.

- The MEP-based estimates of global sea ice sublimation, sensible, and surface conductive heat flux are 0.17, 0.13, and -2.4 W m^{-2}, respectively. The MEP modeled ocean surface heat fluxes are insensitive to sea ice cover.

The MEP modeled surface heat fluxes not only close surface energy budgets at all space-time scales by definition, but also avoid explicit use of temperature/moisture gradients, wind speed and surface roughness lengths as model inputs and parameters. These unique properties make the MEP model a powerful tool that can be used in facilitating the monitoring and evaluating regional and global surface water and energy budgets, especially over sparsely instrumented polar regions, sea ice surfaces, and remote continental areas.

The MEP model may serve as an effective physical parameterization of land-ocean-atmosphere interaction in regional and global weather prediction and climate models, contributing to the study of changes of water-energy-carbon cycles in response to radiative forcing perturbations of both natural and anthropogenic origins. Constructing a new global surface energy budget based on the MEP model facilitates the understanding of the climate system's energy cycle from a surface perspective.

5.2 Recommendations for Future Work

Based on the findings described above, several topics deserve further investigation:

(1) The FRMEP model

- Further tests of the FRMEP model over various surface types and conditions are required for characterizing model parameters (e.g., reference temperature in the FRM of surface temperature/near-surface air temperature and wetness function for determining surface specific humidity).

- Tests of the FRMEP model at larger spatial (mesoscale, regional) scales are needed for regional scale model simulations. The effects of temporal resolution of input data on the MEP modeled surface heat fluxes over different surface types and conditions also require further tests and validation due to the nonlinearity of the MEP model.

- The FRMEP model is a promising new physically-based algorithm for downscaling and gap-filling (temporal and spatial) satellite remote sensing observations of surface hydro-meteorological variables and heat fluxes. By combining with the latest high resolution satellite observations (e.g., CERES radiation, MODIS surface temperature, SMAP surface soil moisture, NASA Global Precipitation Measurement (GPM) precipitation), the FRMEP model can produce surface state variables and heat fluxes with the highest resolution of the input data down to sub-daily and km resolution.

- The FRMEP model can be further expanded by incorporating root zone soil moisture and temperature models for simulating root zone soil temperature and moisture, as well as subsurface heat and hydrologic fluxes in the study of regional and global energy and water cycles.

(2) MEP-based Estimates of Global Surface Energy Budgets

- Further improvements of the MEP simulations could be achieved by using more accurate model parameters. For example, the thermal inertia of dry soil of ~ 800 (J m^{-2} K^{-1} $s^{-1/2}$) was used in this study as a representative value of the dominant soil types of the Earth. The thermal inertia parameters can be estimated more accurately by introducing high resolution soil property data from e.g., the International Soil Reference and Information Centre (ISRIC) (1 km resolution).

- The estimated trends of the MEP modeled global/regional land surface heat flux budgets presented in this study are subject to biases due to the artifact in CERES radiation data. The performance of the MEP simulations can be further improved

by using model inputs either with bias corrections or from alternative data products (e.g., reanalysis data products).

- The MEP model may be used as an alternative parameterization of surface heat fluxes in the atmospheric models for studying heat-flux-driven processes such as the atmospheric moisture transport between lands and oceans as well as the sea level rise and climate change in response to the changes in net ocean heat flux or ocean heat uptake.

APPENDIX. COPYRIGHT PERMISSION

Figures 4.2(b), 4.7(b), 4.7(c), and 4.7(d) in this study are reprinted from Jung et al. (2010), Yan et al. (2013), and Zhang et al. (2016). The requested copyright permission for using these figures in this dissertation are attached below. All content in Zhang et al. (2016) has been distributed under a Creative Commons CC-BY license and can be reused without obtaining permission from Nature Publishing Group.

(1) Copyright permission of Figures 4.2(b) and 4.7(b) reprinted from Figures 1(a) and 3(a) in Jung et al. (2010)

NATURE PUBLISHING GROUP LICENSE TERMS AND CONDITIONS

Oct 15, 2017

This Agreement between Shihyu Huang ("You") and Nature Publishing Group ("Nature Publishing Group") consists of your license details and the terms and conditions provided by Nature Publishing Group and Copyright Clearance Center.

License Number	4210330709962
License date	Oct 15, 2017
Licensed Content Publisher	Nature Publishing Group
Licensed Content Publication	Nature
Licensed Content Title	Recent decline in the global land evapotranspiration trend due to limited moisture supply
Licensed Content Author	Martin Jung, Markus Reichstein, Philippe Ciais, Sonia I. Seneviratne, Justin Sheffield, Michael L. Goulden
Licensed Content Date	Oct 10, 2010
Licensed Content Volume	467
Licensed Content Issue	7318
Type of Use	reuse in a dissertation / thesis
Requestor type	academic/educational

Format	print and electronic
Portion	figures/tables/illustrations
Number of figures/tables/illustrations	2
High-res required	no
Figures	Figure 1a and Figure 3a
Author of this NPG article	no
Your reference number	
Title of your thesis / dissertation	A modeling study of land surface processes and surface energy budgets using the maximum entropy production theory
Expected completion date	Dec 2017
Estimated size (number of pages)	230
Requestor Location	Shih-Yu Huang 790 ATLANTIC DR NW ATLANTA, GA 30332 United States Attn: Shih-Yu Huang
Billing Type	Invoice
Billing Address	Shih-Yu Huang 790 ATLANTIC DR NW ATLANTA, GA 30332 United States Attn: Shih-Yu Huang
Total	**0.00 USD**
Terms and Conditions	

Terms and Conditions for Permissions

Nature Publishing Group hereby grants you a non-exclusive license to reproduce this material for this purpose, and for no other use,subject to the conditions below:

1. NPG warrants that it has, to the best of its knowledge, the rights to license reuse of this material. However, you should ensure that the material you are requesting is original to Nature Publishing Group and does not carry the copyright of another entity (as credited in the published version). If the credit line on any part of the material you have requested indicates that it was reprinted or adapted by NPG with permission from another source, then you should also seek permission from that source to reuse the material.

2. Permission granted free of charge for material in print is also usually granted for any electronic version of that work, provided that the material is incidental to the work as a whole and that the electronic version is essentially equivalent to, or substitutes for, the print version.Where print permission has been granted for a fee, separate permission must be obtained for any additional, electronic re-use (unless, as in the case of a full paper, this has already been accounted for during your initial request in the calculation of a print run).NB: In all cases, web-based use of full-text articles must be authorized separately through the 'Use on a Web Site' option when requesting permission.

3. Permission granted for a first edition does not apply to second and subsequent editions and for editions in other languages (except for signatories to the STM Permissions Guidelines, or where the first edition permission was granted for free).

4. Nature Publishing Group's permission must be acknowledged next to the figure, table or abstract in print. In electronic form, this acknowledgement must be visible at the same time as the figure/table/abstract, and must be hyperlinked to the journal's homepage.

5. The credit line should read:
   Reprinted by permission from Macmillan Publishers Ltd: [JOURNAL NAME] (reference citation), copyright (year of publication)
   For AOP papers, the credit line should read:
   Reprinted by permission from Macmillan Publishers Ltd: [JOURNAL NAME], advance online publication, day month year (doi: 10.1038/sj.[JOURNAL ACRONYM].XXXXX)

   Note: For republication from the *British Journal of Cancer*, the following credit lines apply.
   Reprinted by permission from Macmillan Publishers Ltd on behalf of Cancer Research UK: [JOURNAL NAME] (reference citation), copyright (year of publication)For AOP papers, the credit line should read:
   Reprinted by permission from Macmillan Publishers Ltd on behalf of Cancer Research UK: [JOURNAL NAME], advance online publication, day month year (doi: 10.1038/sj.[JOURNAL ACRONYM].XXXXX)

6. Adaptations of single figures do not require NPG approval. However, the adaptation should be credited as follows:

   Adapted by permission from Macmillan Publishers Ltd: [JOURNAL NAME] (reference citation), copyright (year of publication)

   Note: For adaptation from the *British Journal of Cancer*, the following credit line applies.
   Adapted by permission from Macmillan Publishers Ltd on behalf of Cancer Research UK: [JOURNAL NAME] (reference citation), copyright (year of publication)

7. Translations of 401 words up to a whole article require NPG approval. Please visit http://www.macmillanmedicalcommunications.com for more information.Translations of up to a 400 words do not require NPG approval. The translation should be credited as follows:

   Translated by permission from Macmillan Publishers Ltd: [JOURNAL NAME] (reference citation), copyright (year of publication).

   Note: For translation from the *British Journal of Cancer*, the following credit line applies.
   Translated by permission from Macmillan Publishers Ltd on behalf of Cancer Research UK: [JOURNAL NAME] (reference citation), copyright (year of publication)

We are certain that all parties will benefit from this agreement and wish you the best in the use of this material. Thank you.

Special Terms:

v1.1

(2) Copyright permission of Figure 4.7(c) reprinted from Figure 2(e) in Yan et al. (2013)

JOHN WILEY AND SONS LICENSE TERMS AND CONDITIONS

Oct 15, 2017

This Agreement between Shihyu Huang ("You") and John Wiley and Sons ("John Wiley and Sons") consists of your license details and the terms and conditions provided by John Wiley and Sons and Copyright Clearance Center.

License Number	4210331022424
License date	Oct 15, 2017
Licensed Content Publisher	John Wiley and Sons
Licensed Content Publication	Journal of Geophysical Research: Atmospheres
Licensed Content Title	Diagnostic analysis of interannual variation of global land evapotranspiration over 1982–2011: Assessing the impact of ENSO
Licensed Content Author	Hao Yan,Qin Yu,Zai-Chun Zhu,Ranga B. Myneni,Hui-Min Yan,Shao-Qiang Wang,Herman H. Shugart
Licensed Content Date	Aug 27, 2013
Licensed Content Pages	15
Type of Use	Dissertation/Thesis
Requestor type	University/Academic
Format	Print and electronic
Portion	Figure/table
Number of figures/tables	1
Original Wiley figure/table number(s)	Figure 2e
Will you be translating?	No
Title of your thesis / dissertation	A modeling study of land surface processes and surface energy budgets using the maximum entropy production theory
Expected completion date	Dec 2017
Expected size (number of pages)	230
Requestor Location	Shihyu Huang 790 ATLANTIC DR NW

	ATLANTA, GA 30332 United States Attn: Shih-Yu Huang
Publisher Tax ID	EU826007151
Billing Type	Invoice
Billing Address	Shih-Yu Huang 790 ATLANTIC DR NW ATLANTA, GA 30332 United States Attn: Shih-Yu Huang
Total	**0.00 USD**

Terms and Conditions

TERMS AND CONDITIONS

This copyrighted material is owned by or exclusively licensed to John Wiley & Sons, Inc. or one of its group companies (each a"Wiley Company") or handled on behalf of a society with which a Wiley Company has exclusive publishing rights in relation to a particular work (collectively "WILEY"). By clicking "accept" in connection with completing this licensing transaction, you agree that the following terms and conditions apply to this transaction (along with the billing and payment terms and conditions established by the Copyright Clearance Center Inc., ("CCC's Billing and Payment terms and conditions"), at the time that you opened your RightsLink account (these are available at any time at http://myaccount.copyright.com).

Terms and Conditions

- The materials you have requested permission to reproduce or reuse (the "Wiley Materials") are protected by copyright.
- You are hereby granted a personal, non-exclusive, non-sub licensable (on a stand-alone basis), non-transferable, worldwide, limited license to reproduce the Wiley Materials for the purpose specified in the licensing process. This license, **and any CONTENT (PDF or image file) purchased as part of your order,** is for a one-time use only and limited to any maximum distribution number specified in the license. The first instance of republication or reuse granted by this license must be completed within two years of the date of the grant of this license (although copies prepared before the end date may be distributed thereafter). The Wiley Materials shall not be used in any other manner or for any other purpose, beyond what is granted in the license. Permission is granted subject to an appropriate acknowledgement given to the author, title of the material/book/journal and the publisher. You shall also duplicate the copyright notice that appears in the Wiley publication in your use of the Wiley Material. Permission is also granted on the understanding that nowhere in the text is a previously published source acknowledged for all or part of this Wiley Material. Any third party content is expressly excluded from this permission.
- With respect to the Wiley Materials, all rights are reserved. Except as expressly granted by the terms of the license, no part of the Wiley Materials may be copied, modified, adapted (except for minor reformatting required by the new Publication), translated, reproduced, transferred or distributed, in any form or by any means, and no derivative works may be made based on the Wiley Materials without the prior permission of the respective copyright owner.**For STM Signatory Publishers clearing permission under the terms of the STM Permissions Guidelines only, the terms of the license are extended to include subsequent editions and for editions in other languages, provided such editions are for the work as a whole in situ and does not involve the separate exploitation of the permitted figures or extracts,** You may not alter, remove or suppress in any manner any copyright, trademark or other notices displayed by the Wiley Materials. You may not

license, rent, sell, loan, lease, pledge, offer as security, transfer or assign the Wiley Materials on a stand-alone basis, or any of the rights granted to you hereunder to any other person.

- The Wiley Materials and all of the intellectual property rights therein shall at all times remain the exclusive property of John Wiley & Sons Inc, the Wiley Companies, or their respective licensors, and your interest therein is only that of having possession of and the right to reproduce the Wiley Materials pursuant to Section 2 herein during the continuance of this Agreement. You agree that you own no right, title or interest in or to the Wiley Materials or any of the intellectual property rights therein. You shall have no rights hereunder other than the license as provided for above in Section 2. No right, license or interest to any trademark, trade name, service mark or other branding ("Marks") of WILEY or its licensors is granted hereunder, and you agree that you shall not assert any such right, license or interest with respect thereto

- NEITHER WILEY NOR ITS LICENSORS MAKES ANY WARRANTY OR REPRESENTATION OF ANY KIND TO YOU OR ANY THIRD PARTY, EXPRESS, IMPLIED OR STATUTORY, WITH RESPECT TO THE MATERIALS OR THE ACCURACY OF ANY INFORMATION CONTAINED IN THE MATERIALS, INCLUDING, WITHOUT LIMITATION, ANY IMPLIED WARRANTY OF MERCHANTABILITY, ACCURACY, SATISFACTORY QUALITY, FITNESS FOR A PARTICULAR PURPOSE, USABILITY, INTEGRATION OR NON-INFRINGEMENT AND ALL SUCH WARRANTIES ARE HEREBY EXCLUDED BY WILEY AND ITS LICENSORS AND WAIVED BY YOU.

- WILEY shall have the right to terminate this Agreement immediately upon breach of this Agreement by you.

- You shall indemnify, defend and hold harmless WILEY, its Licensors and their respective directors, officers, agents and employees, from and against any actual or threatened claims, demands, causes of action or proceedings arising from any breach of this Agreement by you.

- IN NO EVENT SHALL WILEY OR ITS LICENSORS BE LIABLE TO YOU OR ANY OTHER PARTY OR ANY OTHER PERSON OR ENTITY FOR ANY SPECIAL, CONSEQUENTIAL, INCIDENTAL, INDIRECT, EXEMPLARY OR PUNITIVE DAMAGES, HOWEVER CAUSED, ARISING OUT OF OR IN CONNECTION WITH THE DOWNLOADING, PROVISIONING, VIEWING OR USE OF THE MATERIALS REGARDLESS OF THE FORM OF ACTION, WHETHER FOR BREACH OF CONTRACT, BREACH OF WARRANTY, TORT, NEGLIGENCE, INFRINGEMENT OR OTHERWISE (INCLUDING, WITHOUT LIMITATION, DAMAGES BASED ON LOSS OF PROFITS, DATA, FILES, USE, BUSINESS OPPORTUNITY OR CLAIMS OF THIRD PARTIES), AND WHETHER OR NOT THE PARTY HAS BEEN ADVISED OF THE POSSIBILITY OF SUCH DAMAGES. THIS LIMITATION SHALL APPLY NOTWITHSTANDING ANY FAILURE OF ESSENTIAL PURPOSE OF ANY LIMITED REMEDY PROVIDED HEREIN.

- Should any provision of this Agreement be held by a court of competent jurisdiction to be illegal, invalid, or unenforceable, that provision shall be deemed amended to achieve as nearly as possible the same economic effect as the original provision, and the legality, validity and enforceability of the remaining provisions of this Agreement shall not be affected or impaired thereby.

- The failure of either party to enforce any term or condition of this Agreement shall not constitute a waiver of either party's right to enforce each and every term and condition of this Agreement. No breach under this agreement shall be deemed waived or excused by either party unless such waiver or consent is in writing signed by the party granting such waiver or consent. The waiver by or consent of a party to a breach of any provision of this Agreement shall not operate or be construed as a waiver of or consent to any other or subsequent breach by such other party.

- This Agreement may not be assigned (including by operation of law or otherwise) by you without WILEY's prior written consent.

- Any fee required for this permission shall be non-refundable after thirty (30) days from receipt by the CCC.

- These terms and conditions together with CCC's Billing and Payment terms and conditions (which are incorporated herein) form the entire agreement between you and WILEY concerning this licensing transaction and (in the absence of fraud) supersedes all prior agreements and representations of the parties, oral or written. This Agreement may not be amended except in writing signed by both parties. This Agreement shall be binding upon and inure to the benefit of the parties' successors, legal representatives, and authorized assigns.

- In the event of any conflict between your obligations established by these terms and conditions and those established by CCC's Billing and Payment terms and conditions, these terms and conditions shall prevail.

- WILEY expressly reserves all rights not specifically granted in the combination of (i) the license details provided by you and accepted in the course of this licensing transaction, (ii) these terms and conditions and (iii) CCC's Billing and Payment terms and conditions.

- This Agreement will be void if the Type of Use, Format, Circulation, or Requestor Type was misrepresented during the licensing process.

- This Agreement shall be governed by and construed in accordance with the laws of the State of New York, USA, without regards to such state's conflict of law rules. Any legal action, suit or proceeding arising out of or relating to these Terms and Conditions or the breach thereof shall be instituted in a court of competent jurisdiction in New York County in the State of New York in the United States of America and each party hereby consents and submits to the personal jurisdiction of such court, waives any objection to venue in such court and consents to service of process by registered or certified mail, return receipt requested, at the last known address of such party.

WILEY OPEN ACCESS TERMS AND CONDITIONS

Wiley Publishes Open Access Articles in fully Open Access Journals and in Subscription journals offering Online Open. Although most of the fully Open Access journals publish open access articles under the terms of the Creative Commons Attribution (CC BY) License only, the subscription journals and a few of the Open Access Journals offer a choice of Creative Commons Licenses. The license type is clearly identified on the article.

The Creative Commons Attribution License

The Creative Commons Attribution License (CC-BY) allows users to copy, distribute and transmit an article, adapt the article and make commercial use of the article. The CC-BY license permits commercial and non-

Creative Commons Attribution Non-Commercial License

The Creative Commons Attribution Non-Commercial (CC-BY-NC)License permits use, distribution and reproduction in any medium, provided the original work is properly cited and is not used for commercial purposes.(see below)

Creative Commons Attribution-Non-Commercial-NoDerivs License

The Creative Commons Attribution Non-Commercial-NoDerivs License (CC-BY-NC-ND) permits use, distribution and reproduction in any medium, provided the original work is properly cited, is not used for commercial purposes and no modifications or adaptations are made. (see below)

Use by commercial "for-profit" organizations

Use of Wiley Open Access articles for commercial, promotional, or marketing purposes requires further explicit permission from Wiley and will be subject to a fee.

Further details can be found on Wiley Online Library http://olabout.wiley.com/WileyCDA/Section/id-410895.html

Other Terms and Conditions:

v1.10 Last updated September 2015

Questions? customercare@copyright.com or +1-855-239-3415 (toll free in the US) or +1-978-646-2777.

---

(3) Copyright permission of Figure 4.7(d) reprinted from Figure 5(a) in Zhang et al. (2016)

Title:	Multi-decadal trends in global terrestrial evapotranspiration and its components
Author:	Yongqiang Zhang, Jorge L. Peña-Arancibia, Tim R. McVicar, Francis H. S. Chiew, Jai Vaze et al.
Publication:	Scientific Reports
Publisher:	Nature Publishing Group
Date:	Jan 11, 2016

Logged in as:

Shihyu Huang

Account #:

3000992164

LOGOUT

Creative Commons

The article for which you have requested permission has been distributed under a Creative Commons CC-BY license (please see the article itself for the license version number). You may reuse this material without obtaining permission from Nature Publishing Group, providing that the author and the original source of publication are fully acknowledged, as per the terms of the license.
For license terms, please see http://creativecommons.org/

REFERENCES

Abramopoulos, F., C. Rosenzweig, and B. Choudhury (1988), Improved ground hydrology calculations for Global Climate Models (GCMs): Soil water movement and evapotranspiration, *J. Climate*, **1**(9), 921-941, doi:10.1175/1520-0442(1988)001<0921:IGHCFG>2.0.CO;2.

Ács, F., D. T. Mihailović, and B. Rajković (1991), A coupled soil moisture and surface temperature prediction model, *J. Appl. Meteor.*, **30**(6), 812-822, doi:10.1175/1520-0450(1991)030<0812:ACSMAS>2.0.CO;2.

Adler, R. F., G. Gu, and G. J. Huffman (2012), Estimating climatological bias errors for the Global Precipitation Climatology Project (GPCP), *J. Appl. Meteor. Climatol.*, **51**(1), 84-99, doi:10.1175/JAMC-D-11-052.1.

Adler, R. F., G. J. Huffman, A. Chang, R. Ferraro, P.-P. Xie, J. Janowiak, B. Rudolf, U. Schneider, S. Curtis, D. Bolvin, A. Gruber, J. Susskind, P. Arkin, and E. Neikin (2003), The Version-2 Global Precipitation Climatology Project (GPCP) monthly precipitation analysis (1979–Present), *J. Hydrometeorol.*, **4**(6), 1147-1167, doi:10.1175/1525-7541(2003)004<1147:TVGPCP>2.0.CO;2.

Allen, R. G., L. S. Pereira, D. Raes, and M. Smith (1998), Crop evapotranspiration—Guidelines for computing crop water requirements, *FAO Irrigation and drainage paper 56*, Food and Agriculture Organization of the United Nations, Rome, Italy.

Alves, I., and L. S. Pereira (2000), Modelling surface resistance from climatic variables?, *Agric. Water. Manag.*, **42**(3), 371-385, doi:10.1016/S0378-3774(99)00041-4.

Andersson, A., K. Fennig, C. Klepp, S. Bakan, H. Graßl, and J. Schulz (2010), The Hamburg Ocean Atmosphere Parameters and Fluxes from Satellite Data – HOAPS-3, *Earth Syst. Sci. Data*, **2**(2), 215-234, doi:10.5194/essd-2-215-2010.

Andersson, A., C. Klepp, K. Fennig, S. Bakan, H. Grassl, and J. Schulz (2011), Evaluation of HOAPS-3 ocean surface freshwater flux components, *J. Appl. Meteor. Climatol.*, **50**(2), 379-398, doi:doi:10.1175/2010JAMC2341.1.

Andersson, E., P. Bauer, A. Beljaars, F. Chevallier, E. Hólm, M. Janisková, P. Kållberg, G. Kelly, P. Lopez, A. McNally, E. Moreau, A. J. Simmons, J.-N. Thépaut, and A. M. Tompkins (2005), Assimilation and modeling of the atmospheric hydrological cycle in the ECMWF forecasting system, *Bull. Amer. Meteor. Soc.*, **86**(3), 387-402, doi:doi:10.1175/BAMS-86-3-387.

Andreas, E. L., and B. Murphy (1986), Bulk transfer coefficients for heat and momentum over leads and polynyas, *J. Phys. Oceanogr.*, **16**(11), 1875-1883, doi:10.1175/1520-0485(1986)016<1875:BTCFHA>2.0.CO;2.

Assouline, S., and D. M. Tartakovsky (2001), Unsaturated hydraulic conductivity function based on a soil fragmentation process, *Water Resour. Res.*, **37**(5), 1309-1312, doi:10.1029/2000WR900332.

Assouline, S., D. Tessier, and A. Bruand (1998), A conceptual model of the soil water retention curve, *Water Resour. Res.*, **34**(2), 223-231, doi:10.1029/97WR03039.

Arakawa, A. (1972), Design of the UCLA general circulation model, *Tech. Rep. 7*. 116 pp., Dep. of Meteorol., Univ. of Calif., Los Angeles, CA, United States.

Arya, S. (1988), *Introduction to micrometeorology*, 307 pp., Academic Press, New York.

Avissar, R., and Y. Mahrer (1988), Mapping frost-sensitive areas with a three-dimensional local-scale numerical model. Pad II: Comparison with observations, *J. Appl. Meteor.*, **27**(4), 414-426, doi:10.1175/1520-0450(1988)027<0414:MFSAWA>2.0.CO;2.

Avissar, R., and R. A. Pielke (1989), A parameterization of heterogeneous land surfaces for atmospheric numerical models and its impact on regional meteorology, *Mon. Wea. Rev.*, **117**(10), 2113-2136, doi:10.1175/1520-0493(1989)117<2113:APOHLS>2.0.CO;2.

Badgley, F. (1966), Heat balance at the surface of the Arctic Ocean, in *Proc. Symp. Arctic Heat Budget and Atmos. Circ.*, edited by J. O. Fletcher, pp. 267-277, Rand Corp. Rep. RM-5233-NSF, Santa Monica, CA.

Bai, Y., T. A. Scott, and Q. Min (2014), Climate change implications of soil temperature in the Mojave Desert, USA, *Frontiers of Earth Science*, **8**(2), 302-308, doi:10.1007/s11707-013-0398-3.

Balsamo, G., A. Beljaars, K. Scipal, P. Viterbo, B. van den Hurk, M. Hirschi, and A. K. Betts (2009), A revised hydrology for the ECMWF model: Verification from field site to terrestrial water storage and impact in the integrated forecast system, *J. Hydrometeorol.*, **10**(3), 623-643, doi:10.1175/2008JHM1068.1.

Baker, D. G., Skaggs, R. H., and Ruschy, D. L. (1991), Snow depth required to mask the underlying surface, *Journal of Applied Meteorology*, **30**(3), 387-392, doi:10.1175/1520-0450(1991)030<0387:SDRTMT>2.0.CO;2

Balsamo, G., A. Beljaars, K. Scipal, P. Viterbo, B. van den Hurk, M. Hirschi, and A. K. Betts (2009), A revised hydrology for the ECMWF model: Verification from field site to terrestrial water storage and impact in the integrated forecast system, *J. Hydrometeorol*., **10**(3), 623-643, doi:10.1175/2008JHM1068.1.

Barkstrom, B., E. Harrison, G. Smith, R. Green, J. Kibler, R. Cess, and t. E. S. Team (1989), Earth Radiation Budget Experiment (ERBE) archival and April 1985 results, *Bull. Amer. Meteor. Soc.*, **70**, 19.

Barr, A. G., K. Morgenstern, T. A. Black, J. H. McCaughey, and Z. Nesic (2006), Surface energy balance closure by the eddy-covariance method above three boreal forest stands and implications for the measurement of the CO2 flux, *Agric. For. Meteorol.*, **140**(1–4), 322-337, doi:10.1016/j.agrformet.2006.08.007.

Beers, N. R. (1944), Temperature and turbulence in the lower atmosphere, *J. Meteorol.*, **1**(3), 78-88, doi:10.1175/1520-0469(1944)001<0078:TATITL>2.0.CO;2.

Behrangi, A., G. L. Stephens, R. F. Adler, G. J. Huffman, B. Lambrigtsen, and M. Lebsock (2014), An update on the oceanic precipitation rate and its zonal distribution in light of advanced observations from space, *J. Climate*, **27**(11), 3957-3965, doi:10.1175/JCLI-D-13-00679.1.

Behrenfeld, M. J., and P. G. Falkowski (1997), Photosynthetic rates derived from satellite-based chlorophyll concentration, *Limnol. Oceanogr.*, **42**(1), 1-20, doi:10.4319/lo.1997.42.1.0001.

Beltrami, H. (2001), Surface heat flux histories from geothermal data: Inferences from inversion, *Geophys. Res. Lett.*, **28**(4), 655-658, doi:10.1029/2000GL012238.

Beljaars, A. C. M., and A. A. M. Holtslag (1991), Flux parameterization over land surfaces for atmospheric models, *J. Appl. Meteor*., **30**(3), 327-341, doi:10.1175/1520-0450(1991)030<0327:FPOLSF>2.0.CO;2.

Benoit, R. (1976), *A comprehensive parameterization of the atmospheric boundary layer for general circulation models*, Ph.D. thesis, Dep. of Meteorol., McGill Univ., Montreal, Que., Canada.

Bentamy, A., K. B. Katsaros, A. M. Mestas-Nuñez, W. M. Drennan, E. B. Forde, and H. Roquet (2003), Satellite estimates of wind speed and latent heat flux over the global oceans, *J. Climate*, **16**(4), 637-656, doi:10.1175/1520-0442(2003)016<0637:SEOWSA>2.0.CO;2.

Berbigier, P., J.-M. Bonnefond, and P. Mellmann (2001), CO2 and water vapour fluxes for 2 years above Euroflux forest site, *Agric. For. Meteorol.*, **108**(3), 183-197, doi:10.1016/S0168-1923(01)00240-4.

Berris, S. N., and R. D. Harr (1987), Comparative snow accumulation and melt during rainfall in forested and clear-cut plots in the western Cascades of Oregon. *Water Resour. Res*. **23**(1), 135-142, doi:10.1029/WR023i001p00135.

Berrisford, P., P. Kållberg, S. Kobayashi, D. Dee, S. Uppala, A. J. Simmons, P. Poli, and H. Sato (2011), Atmospheric conservation properties in ERA-Interim, *Q. J. R. Meteorol. Soc.*, **137**(659), 1381-1399, doi:10.1002/qj.864.

Bhumralkar, C. M. (1975), Numerical experiments on the computation of ground surface temperature in an atmospheric general circulation model, *J. Appl. Meteor.*, **14**(7), 1246-1258, doi:10.1175/1520-0450(1975)014<1246:NEOTCO>2.0.CO;2.

Blackadar, A. K. (1976), Modeling the nocturnal boundary layer, in *Proc. Third Symp. Atmos. Turbul., Diffus., and Air Qual*., pp. 46-49, Amer. Meteor. Soc, Raleigh, NC.

Blackadar, A. K. (1979), High resolution models of the planetary boundary layer, in *Adv. Environ. Sci. Eng*., Vol. 1, edited by J. Pfafflin and E. Ziegler, pp. 50-85, Gordon and breach, New York.

Bloom, S. C., L. L. Takacs, A. M. da Silva, and D. Ledvina (1996), Data assimilation using incremental analysis updates, *Mon. Wea. Rev.*, **124**(6), 1256-1271, doi:10.1175/1520-0493(1996)124<1256:DAUIAU>2.0.CO;2.

Boike, J., K. Roth, and O. Ippisch (2003), Seasonal snow cover on frozen ground: Energy balance calculations of a permafrost site near Ny-Ålesund, Spitsbergen, *J. Geophys. Res. Atmos*., **108**(D2), ALT 4-1-ALT 4-11, doi:10.1029/2001JD000939.

Bonan, G. B. (1996), A land surface model (LSM version 1.0) for ecological, hydrological, and atmospheric studies: Technical description and user's guide, *NCAR Technical Note NCAR/TN-417+STR*, 150 pp., National Center for Atmospheric Research, Boulder, Colorado.

Bondeau, A., P. C. Smith, S. Zaehle, S. Schaphoff, W. Lucht, W. Cramer, D. Gerten, H. Lotze-Campen, C. Müller, M. Reichstein, and B. Smith (2007), Modelling the role of agriculture for the 20th century global terrestrial carbon balance, *Glob. Chang. Biol.*, **13**(3), 679-706, doi:10.1111/j.1365-2486.2006.01305.x.

Boone, A., P. de Rosnay, G. Balsamo, A. Beljaars, F. Chopin, B. Decharme, C. Delire, A. Ducharne, S. Gascoin, M. Grippa, F. Guichard, Y. Gusev, P. Harris, L. Jarlan, L.

Kergoat, E. Mougin, O. Nasonova, A. Norgaard, T. Orgeval, C. Ottlé, I. Poccard-Leclercq, J. Polcher, I. Sandholt, S. Saux-Picart, C. Taylor, and Y. Xue (2009), The AMMA Land Surface Model Intercomparison Project (ALMIP), *Bull. Amer. Meteor. Soc.*, **90**(12), 1865-1880, doi:10.1175/2009BAMS2786.1.

Boone, A., V. Masson, T. Meyers, and J. Noilhan (2000), The Influence of the inclusion of soil freezing on simulations by a Soil–Vegetation–Atmosphere Transfer scheme, *J. Appl. Meteor.*, **39**(9), 1544-1569, doi:10.1175/1520-0450(2000)039<1544:TIOTIO>2.0.CO;2.

Bosilovich, M., S. Akella, L. Coy, R. Cullather, C. Draper, R. Gelaro, P. Kabat, Q. Liu, A. Molod, P. Norris, K. Wargan, W. Chao, R. Reichle, L. Takacs, Y. Vikhliaev, S. C. Bloom, A. Collow, S. Firth, G. Labow, G. Partyka, S. Pawson, O. Reale, S. D. Schubert, and M. Suarez (2015) MERRA-2: Initial evaluation of the climate, *NASA Tech. Rep. Series on Global Modeling and Data Assimilation*, Vol. 43 (NASA/TM–2015-104606), 139. pp., NASA Goddard Space Flight Center, Greenbelt, Maryland.

Bosilovich, M. G., J. Chen, F. R. Robertson, and R. F. Adler (2008), Evaluation of global precipitation in reanalyses, *J. Appl. Meteor. Climatol.*, **47**(9), 2279-2299, doi:10.1175/2008JAMC1921.1.

Bosilovich, M. G., F. R. Robertson, and J. Chen (2011), Global energy and water budgets in MERRA, *J. Climate*, **24**(22), 5721-5739, doi:10.1175/2011JCLI4175.1.

Bosilovich, M. G., and W.-Y. Sun (1995), Formulation and verification of a land surface parameterization for atmospheric models, *Bound.-Lay. Meteorol.*, **73**(4), 321-341, doi:10.1007/bf00712676.

Bounoua, L., R. DeFries, G. J. Collatz, P. Sellers, and H. Khan (2002), Effects of land cover conversion on surface climate, *Clim. Chang.*, **52**(1), 29-64, doi:10.1023/A:1013051420309.

Bourras, D. (2006), Comparison of five satellite-derived latent heat flux products to moored buoy data, *J. Climate*, **19**(24), 6291-6313, doi:10.1175/JCLI3977.1.

Bouttier, F., J.-F. Mahfouf, and J. Noilhan (1993), Sequential assimilation of soil moisture from atmospheric low-level parameters. Part I: Sensitivity and calibration studies, *J. Appl. Meteor.*, **32**(8), 1335-1351, doi:10.1175/1520-0450(1993)032<1335:SAOSMF>2.0.CO;2.

Brooks, R. H., and A. T. Corey (1964), Hydraulic properties of porous media, *Hydrol. Pap.*, **3**, 27 pp., Colo. State Univ., Fort Collins.

Brunke, M. A., C. W. Fairall, X. Zeng, L. Eymard, and J. A. Curry (2003), Which bulk aerodynamic algorithms are Least problematic in computing ocean surface turbulent fluxes?, *J. Climate*, **16**(4), 619-635, doi:10.1175/1520-0442(2003)016<0619:WBAAAL>2.0.CO;2.

Brunke, M. A., Z. Wang, X. Zeng, M. Bosilovich, and C.-L. Shie (2011), An assessment of the uncertainties in ocean surface turbulent fluxes in 11 reanalysis, satellite-derived, and combined global datasets, *J. Climate*, **24**(21), 5469-5493, doi:10.1175/2011JCLI4223.1.

Brunke, M. A., X. Zeng, and S. Anderson (2002), Uncertainties in sea surface turbulent flux algorithms and data sets, *J. Geophys. Res. Oceans*, **107**(C10), 5-1-5-21, doi:10.1029/2001JC000992.

Brutsaert, W. (2000), A concise parameterization of the hydraulic conductivity of unsaturated soils, *Adv. Water Resour.*, **23**(8), 811-815, doi:10.1016/S0309-1708(00)00019-1.

Brutsaert, W., and D. Chen (1995), Desorption and the two stages of drying of natural tallgrass prairie, *Water Resour. Res.*, **31**(5), 1305-1313, doi:10.1029/95WR00323.

Budyko, M. I. (1982), *The Earth's Climate: Past and Future*, 307 pp., Academic Press, New York, doi:10.1002/qj.49710946218.

Bunker, A. F. (1976), Computations of surface energy flux and annual air–sea interaction cycles of the North Atlantic Ocean, *Mon. Wea Rev.*, **104**(9), 1122-1140, doi:10.1175/1520-0493(1976)104<1122:COSEFA>2.0.CO;2.

Burda, G. (2013), *Eddy covariance method for scientific, industrial, agricultural and regulatory applications: A field book on measuring ecosystem gas exchange and areal emission rates*, 331 pp., LI-COR Biosciences, Lincoln, NE, United States.

Burke, E. J., S. J. Brown, and N. Christidis (2006), Modeling the recent evolution of global drought and projections for the twenty-first century with the Hadley Centre climate model, *J. Hydrometeorol.*, **7**(5), 1113-1125, doi:10.1175/JHM544.1.

Businger, J. A. (1988), A note on the Businger-Dyer profiles, *Bound.-Lay. Meteorol.*, **42**(1–2), 145-151, doi:10.1007/BF00119880.

Businger, J. A., J. C. Wyngaard, K. Izumi, and E. F. Bradley (1971), Flux-profile relationships in the atmospheric surface layer, *J. Atmos. Sci.*, **28**(2), 181-189, doi:10.1175/1520-0469(1971)028<0181:FPRITA>2.0.CO;2.

Calvet, J.-C., J. Noilhan, and P. Bessemoulin (1998), Retrieving the root-zone soil moisture from surface soil soisture or temperature estimates: A feasibility study based on field measurements, *J. Appl. Meteor.*, **37**(4), 371-386, doi:10.1175/1520-0450(1998)037<0371:RTRZSM>2.0.CO;2.

Campbell, G. S. (1974), A simple method for determining unsaturated conductivity from moisture retention data *Soil Sci.*, **117**(6), 311-314.

Carslaw, H. S., and J. C. Jaeger (1959), *Conduction of heat in solids (2nd ed.)*, 510 pp., Oxford University Press, New York.

Celia, M. A., E. T. Bouloutas, and R. L. Zarba (1990), A general mass-conservative numerical solution for the unsaturated flow equation, *Water Resour. Res.*, **26**(7), 1483-1496, doi:10.1029/WR026i007p01483.

Ceppi, P., Y.-T. Hwang, D. M. W. Frierson, and D. L. Hartmann (2012), Southern Hemisphere jet latitude biases in CMIP5 models linked to shortwave cloud forcing, *Geophys. Res. Lett.*, **39**(19), L19708, doi:10.1029/2012GL053115.

Chang, E. K. M., Y. Guo, and X. Xia (2012), CMIP5 multimodel ensemble projection of storm track change under global warming, *J. Geophys. Res. Atmos.*, **117**, D23118, doi:10.1029/2012JD018578.

Chen, B., W. C. Chao, and X. Liu (2003), Enhanced climatic warming in the Tibetan Plateau due to doubling CO2: a model study, *Clim. Dyn.*, **20**(4), 401-413, doi:10.1007/s00382-002-0282-4.

Chen, D., and W. Brutsaert (1995), Diagnostics of land surface spatial variability and water vapor flux, *J. Geophys. Res. Atmos.*, **100**(D12), 25595-25606, doi:10.1029/95JD00973.

Chen, F., and R. Avissar (1994a), The impact of land-surface wetness heterogeneity on mesoscale heat fluxes, *J. Appl. Meteor.*, **33**(11), 1323-1340, doi:10.1175/1520-0450(1994)033<1323:TIOLSW>2.0.CO;2.

Chen, F., and R. Avissar (1994b), Impact of land-surface moisture variability on local shallow convective cumulus and precipitation in large-scale models, *J. Appl. Meteor.*, **33**(12), 1382-1401, doi:10.1175/1520-0450(1994)033<1382:IOLSMV>2.0.CO;2.

Chen, F., and J. Dudhia (2001), Coupling an advanced land surface–hydrology model with the Penn State–NCAR MM5 modeling system. Part I: Model implementation and

sensitivity, *Water Resour. Res.*, **129**(4), 569-585, doi:10.1175/1520-0493(2001)129<0569:CAALSH>2.0.CO;2.

Chen, F., K. Mitchell, J. Schaake, Y. Xue, H.-L. Pan, V. Koren, Q. Y. Duan, M. Ek, and A. Betts (1996), Modeling of land surface evaporation by four schemes and comparison with FIFE observations, *J. Geophys. Res. Atmos.*, **101**(D3), 7251-7268, doi:10.1029/95JD02165.

Chou, S.-H., E. Nelkin, J. Ardizzone, R. M. Atlas, and C.-L. Shie (2003), Surface turbulent seat and momentum fluxes over Global oceans based on the Goddard Satellite retrievals, Version 2 (GSSTF2), *J. Climate*, **16**(20), 3256-3273, doi:10.1175/1520-0442(2003)016<3256:STHAMF>2.0.CO;2.

Clapp, R. B., and G. M. Hornberger (1978), Empirical equations for some soil hydraulic properties, *Water Resour. Res.*, **14**(4), 601-604, doi:10.1029/WR014i004p00601.

Clarizia, M. P., C. Gommenginger, M. D. Bisceglie, C. Galdi, and M. A. Srokosz (2012), Simulation of L-Band bistatic returns from the ocean surface: A facet approach with application to ocean GNSS reflectometry, *IEEE T. Geosci. Remote*, **50**(3), 960-971, doi:10.1109/TGRS.2011.2162245.

Clayson, C. A., and A. S. Bogdanoff (2013), The effect of diurnal sea surface temperature warming on climatological air–sea fluxes, *J. Climate*, **26**(8), 2546-2556, doi:10.1175/JCLI-D-12-00062.1.

Clayson, C. A., J. B. Roberts, and A. S. Bogdanoff (2012), The SeaFlux turbulent flux dataset version 1.0 documentation, *Tech. Rep*., 5 pp., Woods Hole Oceanographic Institution, MA.

Clayson, C. A., J. B. Roberts, and A. S. Bogdanoff (2013), SeaFlux Version 1: A new satellite-based ocean-atmosphere turbulent flux dataset., *Int. J. of Climatology (submitted)*.

Cogley, J. G., A. J. Pitman, and A. Henderson-Sellers (1990), A land surface for large scale climate models., *Trent University Tech. Note 90-1*, 124 pp., Dep. of Geography, Trent Unicersity, Peterborough, Ontario, Canada.

Collatz, G. J., L. Bounoua, S. O. Los, D. A. Randall, I. Y. Fung, and P. J. Sellers (2000), A mechanism for the influence of vegetation on the response of the diurnal temperature range to changing climate, *Geophys. Res. Lett*., **27**(20), 3381-3384, doi:10.1029/1999GL010947.

Corby, G. A., A. Gilchrist, and R. L. Newson (1972), A general circulation model of the atmosphere suitable for long period integrations, *Q. J. R. Meteorol. Soc.*, **98**(418), 809-832, doi:10.1002/qj.49709841808.

Culf, A. D., T. Foken, and J. H. C. Gash (2004), The energy balance closure problem, in *Vegetation, Water, Humans and the Climate: A New Perspective on an Interactive System*, edited by P. Kabat, M. Claussen, P. A. Dirmeyer, J. H. C. Gash, L. B. de Guenni, M. Meybeck, R. A. Pielke, C. I. Vörösmarty, R. W. A. Hutjes and S. Lütkemeier, pp. 159-166, Springer Berlin Heidelberg, Berlin, Heidelberg, doi:10.1007/978-3-642-18948-7_13.

Curry, J. A., A. Bentamy, M. A. Bourassa, D. Bourras, E. F. Bradley, M. Brunke, S. Castro, S. H. Chou, C. A. Clayson, W. J. Emery, L. Eymard, C. W. Fairall, M. Kubota, B. Lin, W. Perrie, R. A. Reeder, I. A. Renfrew, W. B. Rossow, J. Schulz, B. Smith, P. J. Webster, G. A. Wick, and X. Zeng (2004), SeaFlux, *Bull. Amer. Meteor. Soc.*, **85**(3), 409-424, doi:10.1175/BAMS-85-3-409.

Dai, Y., X. Zeng, R. E. Dickinson, I. Baker, G. B. Bonan, M. G. Bosilovich, A. S. Denning, P. A. Dirmeyer, P. R. Houser, G. Niu, K. W. Oleson, C. A. Schlosser, and Z.-L. Yang (2003), The Common Land Model, *Bull. Amer. Meteor. Soc.*, **84**(8), 1013-1023, doi:10.1175/BAMS-84-8-1013.

Dankers, R., N. W. Arnell, D. B. Clark, P. D. Falloon, B. M. Fekete, S. N. Gosling, J. Heinke, H. Kim, Y. Masaki, Y. Satoh, T. Stacke, Y. Wada, and D. Wisser (2014), First look at changes in flood hazard in the Inter-Sectoral Impact Model Intercomparison Project ensemble, *Proc. Nat. Acad. Sci.*, **111**(9), 3257-3261.

Davidson, J. M., L. R. Stone, D. R. Nielsen, and M. E. Larue (1969), Field measurement and use of soil-water properties, *Water Resour. Res.*, **5**(6), 1312-1321, doi:10.1029/WR005i006p01312.

Deardorff, J. W. (1968), Dependence of air-sea transfer coefficients on bulk stability, *J. Geophys. Res.*, **73**(8), 2549-2557, doi:10.1029/JB073i008p02549.

Deardorff, J. W. (1977), A parameterization of ground-surface moisture content for use in atmospheric prediction models, *J. Appl. Meteor.*, **16**(11), 1182-1185, doi:10.1175/1520-0450(1977)016<1182:APOGSM>2.0.CO;2.

Deardorff, J. W. (1978), Efficient prediction of ground surface temperature and moisture, with inclusion of a layer of vegetation, *J. Geophys. Res. Oceans*, **83**(C4), 1889-1903, doi:10.1029/JC083iC04p01889.

Dee, D. P., S. M. Uppala, A. J. Simmons, P. Berrisford, P. Poli, S. Kobayashi, U. Andrae, M. A. Balmaseda, G. Balsamo, P. Bauer, P. Bechtold, A. C. M. Belijaars, L. van de

Berg, J. Bidlot, N. Bormann, C. Delsol, R. Dragani, M. Fuentes, A. J. Geer, L. Haimberger, S. B. Healy, H. Hersbach, E. V. Hólm, L. Isaksen, P. Kållberg, M. Köhler, M. Matricardi, A. P. McNally, B. M. Monge-Sanz, J. J. Morcrette, B. K. Park, C. Peubey. P. de Rosnay, C. Tavolato, J. N. Thépaut, and F. Vitart (2011), The ERA-Interim reanalysis: Configuration and performance of the data assimilation system, *Q. J. R. Meteorol. Soc.*, **137**(656), 553-597, doi:10.1002/qj.828.

Derber, J., D. Parrish, and S. Lord (1991), The new global operational analysis system at the National Meteorological Center, *Wea. Forecasting*, **6**, 538-547.

Dickinson, R. E. (1988), The force–restore model for surface temperatures and its generalizations, *J. Climate*, **1**(11), 1086-1097, doi:10.1175/1520-0442(1988)001<1086:TFMFST>2.0.CO;2.

Dickinson, R. E., A. Henderson-Sellers, and P. J. Kennedy (1993), Biosphere-atmosphere Transfer Scheme (BATS) version 1e as coupled to the NCAR community climate model, *NCAR Technical Note NCAR/TN-387+STR*, 72 pp., National Center for Atmospheric Research, Boulder, Colorado.

Dickinson, R. E., A. Henderson-Sellers, P. J. Kennedy, and M. F. Wilson (1986), Biosphere-atmosphere Transfer Scheme (BATS) for the NCAR Community climate model, *NCAR Technical Note NCAR/TN-275-+STR*, 69 pp., National Center for Atmospheric Research, Boulder, Colorado.

Dickinson, R. E., A. Henderson-Sellers, C. Rosenzweig, and P. J. Sellers (1991), Evapotranspiration models with canopy resistance for use in climate models, a review, *Agric. For. Meteorol.*, **54**(2), 373-388, doi:10.1016/0168-1923(91)90014-H.

Dines, W. H. (1917), The heat balance of the atmosphere, *Q. J. R. Meteorol. Soc.*, **43**(182), 151-158, doi:10.1002/qj.49704318203.

Dirmeyer, P. A., A. J. Dolman, and N. Sato (1999), The pilot phase of the Global Soil Wetness Project, *Bull. Amer. Meteor. Soc.*, **80**(5), 851-878, doi:10.1175/1520-0477(1999)080<0851:TPPOTG>2.0.CO;2.

Dirmeyer, P. A., X. Gao, M. Zhao, Z. Guo, T. Oki, and N. Hanasaki (2006), GSWP-2: Multimodel analysis and implications for our perception of the land surface, *Bull. Amer. Meteor. Soc.*, **87**(10), 1381-1397, doi:10.1175/BAMS-87-10-1381.

Ek, M. B., K. E. Mitchell, Y. Lin, E. Rogers, P. Grunmann, V. Koren, G. Gayno, and J. D. Tarpley (2003), Implementation of Noah land surface model advances in the

National Centers for Environmental Prediction operational mesoscale Eta model, *J. Geophys. Res. Atmos.*, **108**(D22), doi:10.1029/2002JD003296.

Entekhabi, D., and P. S. Eagleson (1989), Land surface hydrology parameterization for atmospheric general circulation models including subgrid scale spatial variability, *J. Climate*, **2**(8), 816-831, doi:10.1175/1520-0442(1989)002<0816:LSHPFA>2.0.CO;2.

Evan, A. T., A. K. Heidinger, and D. J. Vimont (2007), Arguments against a physical long-term trend in global ISCCP cloud amounts, *Geophys. Res. Lett.*, **34**(4), doi:10.1029/2006GL028083.

Fairall, C. W., E. F. Bradley, J. S. Godfrey, G. A. Wick, J. B. Edson, and G. S. Young (1996a), Cool-skin and warm-layer effects on sea surface temperature, *J. Geophys. Res. Oceans*, **101**(C1), 1295-1308, doi:10.1029/95JC03190.

Fairall, C. W., E. F. Bradley, J. E. Hare, A. A. Grachev, and J. B. Edson (2003), Bulk parameterization of air–sea fluxes: updates and verification for the COARE algorithm, *J. Climate*, **16**(4), 571-591, doi:10.1175/1520-0442(2003)016<0571:BPOASF>2.0.CO;2.

Fairall, C. W., E. F. Bradley, D. P. Rogers, J. B. Edson, and G. S. Young (1996b), Bulk parameterization of air-sea fluxes for Tropical Ocean-Global Atmosphere Coupled-Ocean Atmosphere Response Experiment, *J. Geophys. Res. Oceans*, **101**(C2), 3747-3764, doi:10.1029/95JC03205.

Falkowski, P., and J. Raven (2007), Aquatic photosynthesis: second edition., Princeton University Press.

Famiglietti, J. S., and E. F. Wood (1994), Multiscale modeling of spatially variable water and energy balance processes, *Water Resour. Res.*, **30**(11), 3061-3078, doi:10.1029/94WR01498.

Farouki, O. (1982), Thermal properties of soils, *CRREL Monogr No. 81-1*, U.S. Army Cold Regions Research and Engineering Laboratory, Hanover, New Hampshire.

Fisher, J. B., T. A. DeBiase, Y. Qi, M. Xu, and A. H. Goldstein (2005), Evapotranspiration models compared on a Sierra Nevada forest ecosystem, *Environ. Model. Softw.*, **20**(6), 783-796, doi:10.1016/j.envsoft.2004.04.009.

Fisher, J. B., K. P. Tu, and D. D. Baldocchi (2008), Global estimates of the land–atmosphere water flux based on monthly AVHRR and ISLSCP-II data, validated at

16 FLUXNET sites, *Remote Sens. Environ.*, **112**(3), 901-919, doi:10.1016/j.rse.2007.06.025.

Foken, T. (2008), The energy balance closure problem: An overview, *Eco. Appl.*, **18**(6), 1351-1367, doi:10.1890/06-0922.1.

Foken, T., F. Wimmer, M. Mauder, C. Thomas, and C. Liebethal (2006), Some aspects of the energy balance closure problem, *Atmos. Chem. Phys.*, **6**(12), 4395-4402, doi:10.5194/acp-6-4395-2006.

Frey, C. M., and C. Kuenzer (2014), Land-surface temperature dynamics in the Upper Mekong Basin derived from MODIS time series, *Int. J. Remote Sens.*, **35**(8), 2780-2798, doi:10.1080/01431161.2014.890304.

Friedl, M. A. (2002), Forward and inverse modeling of land surface energy balance using surface temperature measurements, *Remote Sens. Environ.*, **79**(2–3), 344-354, doi:10.1016/S0034-4257(01)00284-X.

Friend, A. D., and N. Y. Kiang (2005), Land surface model development for the GISS GCM: Effects of improved canopy physiology on simulated climate, *J. Climate*, **18**(15), 2883-2902, doi:10.1175/JCLI3425.1.

Fu, Q., and K. N. Liou (1993), Parameterization of the radiative properties of cirrus clouds, *J. Atmos. Sci.*, **50**(13), 2008-2025, doi:10.1175/1520-0469(1993)050<2008:POTRPO>2.0.CO;2.

Fuchs, M., and A. Hadas (1973), Analysis of performance of an improved soil heat-flux transducer, *Soil Sci. Soc. Am. J.*, **37**(2), 173-175.

Fujita, K., and Y. Ageta (2000), Effect of summer accumulation on glacier mass balance on the Tibetan Plateau revealed by mass-balance model, *J. Glaciol.*, **46**(153), 244-252, doi:10.3189/172756500781832945.

Gądek, B., and J. Leszkiewicz (2010), Influence of snow cover on ground surface temperature in the zone of sporadic permafrost, Tatra Mountains, Poland and Slovakia, *Cold. Reg. Sci. Technol.*, **60**(3), 205-211, doi:10.1016/j.coldregions.2009.10.004.

Gallage, C., J. Kodikara, and T. Uchimura (2013), Laboratory measurement of hydraulic conductivity functions of two unsaturated sandy soils during drying and wetting processes, *Soils Found.*, **53**(3), 417-430, doi:10.1016/j.sandf.2013.04.004.

Gao, Z., N. Chae, J. Kim, J. Hong, T. Choi, and H. Lee (2004), Modeling of surface energy partitioning, surface temperature, and soil wetness in the Tibetan prairie using the Simple Biosphere Model 2 (SiB2), *J. Geophys. Res. Atmos.*, **109**, D06102, doi:10.1029/2003JD004089.

Gao, Z., R. Horton, L. Wang, H. Liu, and J. Wen (2008), An improved force-restore method for soil temperature prediction, *Eur. J. Soil Sci.*, **59**(5), 972-981, doi:10.1111/j.1365-2389.2008.01060.x.

Garratt, J. R. (1993), Sensitivity of climate simulations to land-surface and atmospheric boundary-layer treatments-a review, *J. Climate*, **6**(3), 419-448, doi:10.1175/1520-0442(1993)006<0419:SOCSTL>2.0.CO;2.

Gates, W. L., E. S. Batten, A. B. Kahle, and A. B. Nelson (1971), A documentation of the Mintz-Arakawa two-level atmospheric general circulation model, *Rep. R-877-ARPA*, 408. pp., Rand Corp., Santa Monica, Calif.

Gates, W. L., and M. E. Schlesinger (1977), Numerical simulation of the January and July global climate with a two-level atmospheric model, *J. Atmos. Sci.*, **34**(1), 36-76, doi:10.1175/1520-0469(1977)034<0036:NSOTJA>2.0.CO;2.

Gavilán, P., J. Berengena, and R. G. Allen (2007), Measuring versus estimating net radiation and soil heat flux: Impact on Penman–Monteith reference ET estimates in semiarid regions, *Agric. Water Manag.*, **89**(3), 275-286, doi:10.1016/j.agwat.2007.01.014.

Gentine, P., D. Entekhabi, and B. Heusinkveld (2012), Systematic errors in ground heat flux estimation and their correction, *Water Resour. Res.*, **48**, W09541, doi:10.1029/2010WR010203.

Georgakakos, K. P., and O. W. Baumer (1996), Measurement and utilization of on-site soil moisture data, *J. Hydrol.*, **184**(1–2), 131-152, doi:10.1016/0022-1694(95)02971-0.

Gibson, J. K., P. Kållberg, S. Uppala, A. Hernandez, A. Nomura, and E. Serrano (1999), ERA-15 description (version 2 – January 1999), *ECMWF Re-Analysis Project Report Series 1*, 84 pp., Eur. Cent. for Med.-Range Weather Forecasts, Reading, United Kingdom.

Gilichinsky, D. A., R. Barry, S. S. Bykhovets, V. A. Sorokovikov, T. Zhang, S. L. Zudin, and D. G. Fedorov-Davydov (1998), A century of temperature observations of soil climate: Methods of analysis and long-term trends, *in Proceedings of the 7th International Conference on Permafrost, June 23–27, 1998*, edited by A. G. Lewkowicz and M. Allard, pp. 313-317, Univ. Laval, Quebec, Yellowknife, Canada.

Gleckler, P. J., and B. C. Weare (1997), Uncertainties in global ocean surface heat flux dlimatologies derived fromship observations, *J. Climate*, **10**, 2764-2781.

Golombek, R., S. A. C. Kittelsen, and I. Haddeland (2012), Climate change: impacts on electricity markets in Western Europe, *Clim. Chang.*, **113**(2), 357-370, doi:10.1007/s10584-011-0348-6.

Grachev, A. A., E. L. Andreas, C. W. Fairall, P. S. Guest, and P. O. G. Persson (2007), SHEBA flux–profile relationships in the stable atmospheric boundary layer, *Bound.-Lay. Meteorol.*, **124**(3), 315-333, doi:10.1007/s10546-007-9177-6.

Grassl, H., J. V., K. R., S. J., B. P., and P. Schlüssel (2000), The Hamburg ocean-atmosphere parameters and fluxes from satellite data (HOAPS): A climatological atlas of satellite-derived air-sea-interaction parameters over the oceans, *Rep. 312*, Max-Planck-Inst, für Meteorol,, Hamburg, Germany.

Gregory, J. M., J. F. B. Mitchell, and A. J. Brady (1997), Summer drought in northern midlatitudes in a time-dependent CO2 climate experiment, *J. Climate*, **10**(4), 662-686, doi:10.1175/1520-0442(1997)010<0662:SDINMI>2.0.CO;2.

Grenfell, T. C. and G. A. Maykut (1977) The optical properties of ice and snow in the Arctic Basin, *Journal of Glaciology*, **18**(80). 445–463.

Grise, K. M., and L. M. Polvani (2014), Southern Hemisphere cloud–dynamics biases in CMIP5 models and their Implications for climate projections, *J. Climate*, **27**(15), 6074-6092, doi:10.1175/JCLI-D-14-00113.1.

Guswa, A. J., M. A. Celia, and I. Rodriguez-Iturbe (2002), Models of soil moisture dynamics in ecohydrology: A comparative study, *Water Resour. Res.*, **38**(9), 5-1-5-15, doi:10.1029/2001WR000826.

Haddeland, I., D. B. Clark, W. Franssen, F. Ludwig, F. Voß, N. W. Arnell, N. Bertrand, M. Best, S. Folwell, D. Gerten, S. Gomes, S. N. Gosling, S. Hagemann, N. Hanasaki, R. Harding, J. Heinke, P. Kabat, S. Koirala, T. Oki, J. Polcher, T. Stacke, P. Viterbo, G. P. Weedon, and P. Yeh (2011), Multimodel estimate of the global terrestrial water balance: Setup and first results, *J. Hydrometeorol.*, **12**(5), 869-884, doi:10.1175/2011JHM1324.1.

Hagemann, S., K. Arpe, and L. Bengtsson (2005), Validation of the hydrological cycle of ERA-40, *ERA-40 Project Rep. 24*, 42 pp., Eur. Cent. for Med.-Range Weather Forecasts, Reading, United Kingdom.

Hanasaki, N., S. Kanae, T. Oki, K. Masuda, K. Motoya, N. Shirakawa, Y. Shen, and K. Tanaka (2008), An integrated model for the assessment of global water resources – Part 1: Model description and input meteorological forcing, *Hydrol. Earth Syst. Sci.*, **12**(4), 1007-1025, doi:10.5194/hess-12-1007-2008.

Hansen, J., G. Russell, D. Rind, P. Stone, A. Lacis, S. Lebedeff, R. Ruedy, and L. Travis (1983), Efficient three-simensional global models for climate studies: Models I and II, *Mon. Wea. Rev.*, **111**(4), 609-662, doi:10.1175/1520-0493(1983)111<0609:ETDGMF>2.0.CO;2.

Hanson, R. T., M. D. Dettinger, and M. W. Newhouse (2005), Relations between climatic variability and hydrologic time series from four alluvial basins across the southwestern United States, *Hydrogeol. J.*, **14**, 1122-1146.

Harada, Y., H. Kamahori, C. Kobayashi, H. Endo, S. Kobayashi, Y. Ota, H. Onoda, K. Onogi, K. Miyaoka, and K. Takahashi (2016), The JRA-55 Reanalysis: Representation of atmospheric circulation and climate variability, *J. Meteor. Soc. Japan. Ser. II*, **94**(3), 269-302, doi:10.2151/jmsj.2016-015.

Harrison, S. P., P. J. Bartlein, K. Izumi, G. Li, J. Annan, J. Hargreaves, P. Braconnot, and M. Kageyama (2015), Evaluation of CMIP5 palaeo-simulations to improve climate projections, *Nat. Clim. Change*, **5**(8), 735-743, doi:10.1038/nclimate2649.

Hay, S. I., J. Cox, D. J. Rogers, S. E. Randolph, D. I. Stern, G. D. Shanks, M. F. Myers, and R. W. Snow (2002), Climate change and the resurgence of malaria in the East African highlands, *Nature*, **415**, 905-909, doi:10.1038/415905a.

Haynes, J. M., T. S. L'Ecuyer, G. L. Stephens, S. D. Miller, C. Mitrescu, N. B. Wood, and S. Tanelli (2009), Rainfall retrieval over the ocean with spaceborne W-band radar, *J. Geophys. Res. Atmos.*, **114**, D00A22, doi:10.1029/2008JD009973.

Heitman, J. L., R. Horton, T. J. Sauer, T. S. Ren, and X. Xiao (2010), Latent heat in soil heat flux measurements, *Agric. For. Meteorol.*, **150**(7–8), 1147-1153, doi:10.1016/j.agrformet.2010.04.017.

Heitman, J. L., X. Xiao, R. Horton, and T. J. Sauer (2008), Sensible heat measurements indicating depth and magnitude of subsurface soil water evaporation, *Water Resour. Res.*, **44**(4), W00D05, doi:10.1029/2008WR006961.

Henderson-Sellers, A., K. McGuffie, and A. J. Pitman (1996), The Project for Intercomparison of Land-surface Parametrization Schemes (PILPS): 1992 to 1995, Clim. Dyn., **12**(12), 849-859, doi:10.1007/s003820050147.

Henderson-Sellers, A., A. J. Pitman, P. K. Love, P. Irannejad, and T. H. Chen (1995), The Project for Intercomparison of Land Surface Parameterization Schemes (PILPS): Phases 2 and 3, *Bull. Amer. Meteor. Soc.*, **76**(4), 489-503, doi:10.1175/1520-0477(1995)076<0489:TPFIOL>2.0.CO;2.

Henderson-Sellers, A., Z.-L. Yang, and R. E. Dickinson (1993), The Project for Intercomparison of Land-surface Parameterization Schemes, *Bull. Amer. Meteor. Soc.*, **74**(7), 1335-1349, doi:10.1175/1520-0477(1993)074<1335:TPFIOL>2.0.CO;2.

Hengl, T., J. M. de Jesus, R. A. MacMillan, N. H. Batjes, G. B. M. Heuvelink, E. Ribeiro, A. Samuel-Rosa, B. Kempen, J. G. B. Leenaars, M. G. Walsh, and M. R. Gonzalez (2014), SoilGrids1km – Global soil information based on automated mapping, *PLOS ONE*, **9**(8), e105992, doi:10.1371/journal.pone.0105992.

Herman, A. (2015), Trends and variability of the atmosphere–ocean turbulent heat flux in the extratropical Southern Hemisphere, *Sci. Rep.*, **5**, 14900, doi:10.1038/srep14900.

Higgins, R. W., V. E. Kousky, V. B. S. Silva, E. Becker, and P. Xie (2010), Intercomparison of daily precipitation statistics over the United States in observations and in NCEP reanalysis products, *J. Climate*, **23**(17), 4637-4650, doi:10.1175/2010JCLI3638.1.

Hirabayashi, Y., R. Mahendran, S. Koirala, L. Konoshima, D. Yamazaki, S. Watanabe, H. Kim, and S. Kanae (2013), Global flood risk under climate change, *Nat. Clim. Change*, **3**(9), 816-821, doi:10.1038/nclimate1911.

Hirota, T., M. Fukumoto, R. Shirooka, and K. Muramatu (1995), Simple method of estimating daily mean soil temperature by using the force-restore model, *J. Agric. Meteorol.*, **51**(3), 269-277, doi:10.2480/agrmet.51.269.

Hirota, T., J. W. Pomeroy, R. J. Granger, and C. P. Maule (2002), An extension of the force-restore method to estimating soil temperature at depth and evaluation for frozen soils under snow, *J. Geophys. Res. Atmos.*, **107**(D24), ACL 11-11-ACL 11-10, doi:10.1029/2001JD001280.

Hoelzle, M., C. Mittaz, B. Etzelmüller, and W. Haeberli (2001), Surface energy fluxes and distribution models of permafrost in European mountain areas: an overview of current developments, *Permafrost Periglac. Process.*, **12**(1), 53-68, doi:10.1002/ppp.385.

Högström, U. (1988), Non-dimensional wind and temperature profiles in the atmospheric surface layer: A re-evaluation, *Bound.-Lay. Meteorol.*, **42**(1), 55-78, doi:10.1007/bf00119875.

Hong, S.-Y., and H.-L. Pan (1996), Nonlocal boundary layer vertical diffusion in a medium-range forecast model, *Mon. Wea. Rev.*, **124**(10), 2322-2339, doi:10.1175/1520-0493(1996)124<2322:NBLVDI>2.0.CO;2.

Horridge, M., J. Madden, and G. Wittwer (2005), The impact of the 2002–2003 drought on Australia, *J. Policy Model*., **27**(3), 285-308, doi:10.1016/j.jpolmod.2005.01.008.

Hou, A. Y., R. K. Kakar, S. Neeck, A. A. Azarbarzin, C. D. Kummerow, M. Kojima, R. Oki, K. Nakamura, and T. Iguchi (2014), The Global Precipitation Measurement mission, *Bull. Amer. Meteor. Soc*., **95**(5), 701-722, doi:10.1175/BAMS-D-13-00164.1.

Hu, Z., and S. Islam (1995), Prediction of ground surface temperature and soil moisture content by the force-restore method, *Water Resour. Res.*, **31**(10), 2531-2539, doi:10.1029/95WR01650.

Huang, S., Y. Deng, and J. Wang (2014), Re-evaluation of the Earth's surface energy balance using a new method of heat fluxes, *American Geophysical Union Fall Meeting*, San Francisco, A41B-3022.

Hunt, G. E., R. Kandel, and A. T. Mecherikunnel (1986), A history of presatellite investigations of the Earth's radiation budget, *Rev. Geophys.*, **24**(2), 351-356, doi:10.1029/RG024i002p00351.

IPCC (2007), *Contribution of working groups I, II and III to the fourth assessment report of the Intergovernmental Panel on Climate Change*, edited by Core writing team, R. K. Pachauri and A. Reisinger, IPCC, Geneva, Switzerland.

IPCC (2013), *Climate Change 2013: The Physical Science Basis. Contribution of Working Group I to the Fifth Assessment Report of the Intergovernmental Panel on Climate Change*, 1535 pp., Cambridge Univ. Press, Cambridge, United Kingdom and New York, NY, United States, doi:10.1017/CBO9781107415324.

Ines, A. V. M., J. W. Hansen, and A. W. Robertson (2011), Enhancing the utility of daily GCM rainfall for crop yield prediction, *Int. J. Climatol.*, **31**(14), 2168-2182, doi:10.1002/joc.2223.

Iwata, Y., M. Hayashi, and T. Hirota (2008), Effects of snow cover on soil heat flux and freeze-thaw processes, *J. Agric. Meteorol*., **64**(4), 301-309, doi:10.2480/agrmet.64.4.12.

Jacobs, A. F. G., B. G. Heusinkveld, and S. M. Berkowicz (2000), Force-restore technique for ground surface temperature and moisture content in a dry desert system, *Water Resour. Res.*, **36**(5), 1261-1268, doi:10.1029/2000WR900016.

Jaeger, L. (1976), Monatskarten des niederschlags für die ganze Erde, *Ber. Dt' kch. Wetterdienstes*, **18**(139), 38 pp.

Jaeger, L. (1983), Monthly and areal patterns of mean global precipitation, in *Variations in the Global Water Budget*, edited by A. Street-Perrott, M. Beran and R. Ratcliffe, pp. 129-140, Springer Netherlands, Dordrecht, doi:10.1007/978-94-009-6954-4_9.

Järvinen, O., and M. Leppäranta (2013), Solar radiation transfer in the surface snow layer in Dronning Maud Land, Antarctica, *Polar Science*, **7**(1), 1-17, doi:10.1016/j.polar.2013.03.002.

Ji, F., Z. Wu, J. Huang, and E. P. Chassignet (2014), Evolution of land surface air temperature trend, *Nat. Clim. Change*, **4**(6), 462-466, doi:10.1038/nclimate2223.

Jiménez, C., C. Prigent, B. Mueller, S. I. Seneviratne, M. F. McCabe, E. F. Wood, W. B. Rossow, G. Balsamo, A. K. Betts, P. A. Dirmeyer, J. B. Fisher, M. Jung, M. Kanamitsu, R. H. Reichle, M. Reichstein, M. Rodell, J. Sheffield, K. Tu, and K. Wang (2011), Global intercomparison of 12 land surface heat flux estimates, *J. Geophys. Res. Atmos.*, **116**(D02102), doi:10.1029/2010JD014545.

Jones, P. D., D. H. Lister, T. J. Osborn, C. Harpham, M. Salmon, and C. P. Morice (2012), Hemispheric and large-scale land-surface air temperature variations: An extensive revision and an update to 2010, *J. Geophys. Res. Atmos.*, **117**(D5), doi:10.1029/2011JD017139.

Jones, P. D., M. New, D. E. Parker, S. Martin, and I. G. Rigor (1999), Surface air temperature and its changes over the past 150 years, *Rev. Geophys.*, **37**(2), 173-199, doi:10.1029/1999RG900002.

Jung, M., M. Reichstein, P. Ciais, S. I. Seneviratne, J. Sheffield, M. L. Goulden, G. Bonan, A. Cescatti, J. Chen, R. de Jeu, A. J. Dolman, W. Eugster, D. Gerten, D. Gianelle, N. Gobron, J. Heinke, J. S. Kimball, B. E. Law, L. Montagnani, Q. Mu, B. Mueller, K. Oleson, D. Papale, A. D. Richardson, O. Roupsard, S. Running, E. Tomelleri, N. Viovy, U. Weber, C. Williams, E. Wood, S. Zaehle, and K. Zhang (2010), Recent decline in the global land evapotranspiration trend due to limited moisture supply, *Nature*, **467**, 951-954, doi:10.1038/nature09396.

Kahan, D. S., Y. Xue, and S. J. Allen (2006), The impact of vegetation and soil parameters in simulations of surface energy and water balance in the semi-arid sahel: A case

study using SEBEX and HAPEX-Sahel data, *J. Hydrol.*, **320**(1–2), 238-259, doi:10.1016/j.jhydrol.2005.07.011.

Kållberg, P. (1997), Aspects of the re-analysed climate, *ECMWF ERA-15 Project Report Series, No. 2*, Eur. Cent. for Med.-Range Weather Forecasts, Shinfield, Reading, United Kingdom.

Kalnay, E., M. Kanamitsu, R. Kistler, W. Collins, D. Deaven, L. Gandin, M. Iredell, S. Saha, G. White, J. Woollen, Y. Zue, M. Chelliah, W. Ebisuzaki, W. Higgins, J. Janowiak, K. C. Mo, C. Ropelewski, J. Wang, A. Leetmaa, R. Reynolds, R. Jenne, and D. Joseph (1996), The NCEP/NCAR 40-year reanalysis project, *Bull. Amer. Meteor. Soc.*, **77**(3), 437-471, doi:10.1175/1520-0477(1996)077<0437:TNYRP>2.0.CO;2.

Kalnay, E. (2003), *Atmospheric modeling, data assimilation and predictability*, 341 pp., Cambridge Univ. Press, New York.

Kanamitsu, M., W. Ebisuzaki, J. Woollen, S.-K. Yang, J. J. Hnilo, M. Fiorino, and G. L. Potter (2002), NCEP–DOE AMIP-II reanalysis (R-2), *Bull. Amer. Meteor. Soc.*, **83**(11), 1631-1643, doi:10.1175/BAMS-83-11-1631.

Kasahara, A., and W. M. Washington (1971), General circulation experiments with a six-layer NCAR model, including orography, cloudiness and surface temperature calculations, *J. Atmos. Sci.*, **28**(5), 657-701, doi:10.1175/1520-0469(1971)028<0657:GCEWAS>2.0.CO;2.

Kato, H., M. Rodell, F. Beyrich, H. Cleugh, E. van Gorsel, H. Liu, and T. P. Meyers (2007), Sensitivity of land surface simulations to model physics, land characteristics, and forcings, at four CEOP sites, *J. Meteor. Soc. Japan. Ser. II*, **85A**, 187-204, doi:10.2151/jmsj.85A.187.

Kato, S., N. G. Loeb, F. G. Rose, D. R. Doelling, D. A. Rutan, T. E. Caldwell, L. Yu, and R. A. Weller (2013), Surface irradiances consistent with CERES-derived top-of-atmosphere shortwave and longwave irradiances, *J. Climate*, **26**(9), 2719-2740, doi:doi:10.1175/JCLI-D-12-00436.1.

Kato, S., N. G. Loeb, D. A. Rutan, F. G. Rose, S. Sun-Mack, W. F. Miller, and Y. Chen (2012), Uncertainty estimate of surface irradiances computed with MODIS-, CALIPSO-, and CloudSat-derived cloud and aerosol properties, *Surv. Geophys.*, **33**(3), 395-412, doi:10.1007/s10712-012-9179-x.

Kato, S., F. G. Rose, S. Sun-Mack, W. F. Miller, Y. Chen, D. A. Rutan, G. L. Stephens, N. G. Loeb, P. Minnis, B. A. Wielicki, D. M. Winker, T. P. Charlock, P. W. Stackhouse, K.-M. Xu, and W. D. Collins (2011), Improvements of top-of-

atmosphere and surface irradiance computations with CALIPSO-, CloudSat-, and MODIS-derived cloud and aerosol properties, *J. Geophys. Res. Atmos.*, **116**(D19209), doi:10.1029/2011JD016050.

Kato, S., S. Sun-Mack, W. F. Miller, F. G. Rose, Y. Chen, P. Minnis, and B. A. Wielicki (2010), Relationships among cloud occurrence frequency, overlap, and effective thickness derived from CALIPSO and CloudSat merged cloud vertical profiles, *J. Geophys. Res.-Atmos.*, **115**(D00H28), doi:10.1029/2009JD012277.

Katul, G. G., R. Oren, S. Manzoni, C. Higgins, and M. B. Parlange (2012), Evapotranspiration: A process driving mass transport and energy exchange in the soil-plant-atmosphere-climate system, *Rev. Geophys.*, **50**(3), doi:10.1029/2011RG000366.

Katzberg, S. J., and J. Dunion (2009), Comparison of reflected GPS wind speed retrievals with dropsondes in tropical cyclones, *Geophys. Res. Lett.*, **36**, L17602, doi:10.1029/2009GL039512.

Katzberg, S. J., R. A. Walker, J. H. Roles, T. Lynch, and P. G. Black (2001), First GPS signals reflected from the interior of a tropical storm: Preliminary results from Hurricane Michael, *Geophys. Res. Lett.*, **28**(10), 1981-1984, doi:10.1029/2000GL012823.

Keefer, T. O., M. S. Moran, and G. B. Paige (2008), Long-term meteorological and soil hydrology database, Walnut Gulch Experimental Watershed, Arizona, United States, *Water Resour. Res.*, **44**, W05S07, doi:10.1029/2006WR005702.

Kennedy, A. D., X. Dong, B. Xi, S. Xie, Y. Zhang, and J. Chen (2011), A comparison of MERRA and NARR reanalyses with the DOE ARM SGP Data, *J. Climate*, **24**(17), 4541-4557, doi:10.1175/2011JCLI3978.1.

Kiehl, J. T., and K. E. Trenberth (1997), Earth's annual global mean energy budget, *Bull. Amer. Meteor. Soc.*, **78**(2), 197-208, doi:10.1175/1520-0477(1997)078<0197:EAGMEB>2.0.CO;2.

Kimball, B. A., R. D. Jackson, F. S. Nakayama, S. B. Idso, and R. J. Reginato (1976), Soil-heat flux determination: Temperature gradient method with computed thermal conductivities, *Soil Sci. Soc. Am. J.*, **40**(1), 25-28, doi:10.2136/sssaj1976.03615995004000010011x.

Kleidon, A., M. Renner, and P. Porada (2014), Estimates of the climatological land surface energy and water balance derived from maximum convective power, *Hydrol. Earth Syst. Sci.*, **18**(6), 2201-2218, doi:10.5194/hess-18-2201-2014.

Kobayashi, S., Y. Ota, Y. Harada, A. Ebita, M. Moriya, H. Onoda, K. Onogi, H. Kamahori, C. Kobayashi, H. Endo, K. Miyaoka, and K. Takahashi (2015), The JRA-55 reanalysis: General specifications and basic characteristics, *J. Meteor. Soc. Japan. Ser. II*, **93**(1), 5-48, doi:10.2151/jmsj.2015-001.

Kohsiek, W., C. Liebethal, T. Foken, R. Vogt, S. P. Oncley, C. Bernhofer, and H. A. R. Debruin (2007), The Energy Balance Experiment EBEX-2000. Part III: Behaviour and quality of the radiation measurements, *Bound.-Lay. Meteorol.*, **123**(1), 55-75, doi:10.1007/s10546-006-9135-8.

Koirala, S. (2010), *Explicit representation of groundwater process in a global-scale land surface model to improve hydrological predictions*, 208 pp, Ph.D. thesis, University of Tokyo, Japan.

Komjathy, A., M. Armatys, D. Masters, P. Axelrad, V. Zavorotny, and S. J. Katzberg (2004), Retrieval of ocean surface wind speed and wind direction using reflected GPS signals, *J. Atmos. Oceanic Technol.*, **21**(3), 515-526, doi:10.1175/1520-0426(2004)021<0515:ROOSWS>2.0.CO;2.

Kondo, J. (1975), Air-sea bulk transfer coefficients in diabatic conditions, *Bound.-Lay. Meteorol.*, **9**(1), 91-112, doi:10.1007/bf00232256.

Kondo, J., N. Saigusa, and T. Sato (1990), A parameterization of evaporation from bare soil surfaces, *J. Appl. Meteor.*, **29**(5), 385-389, doi:10.1175/1520-0450(1990)029<0385:APOEFB>2.0.CO;2.

Koster, R. D., and P. C. D. Milly (1997), The interplay between transpiration and runoff formulations in land surface schemes used with atmospheric models, *J. Climate*, **10**(7), 1578-1591, doi:10.1175/1520-0442(1997)010<1578:TIBTAR>2.0.CO;2.

Koster, R. D., and M. J. Suarez (1996), Energy and water balance calculations in the Mosaic LSM, *NASA Tech. Memo. 104606*, **9**, National Aeronautics and Space Administration, Greenbelt, Maryland, United States.

Koster, R. D., M. J. Suarez, A. Ducharne, M. Stieglitz, and P. Kumar (2000), A catchment-based approach to modeling land surface processes in a general circulation model: 1. Model structure, *J. Geophys. Res. Atmos.*, **105**(D20), 24809-24822, doi:10.1029/2000JD900327.

Kowalczyk, E. A., J. R. Garratt, and P. B. Krummel (1991), A soil-canopy scheme for use in a numerical model of the atmosphere-1D stand-alone model, *Tech. Rep. 23*, 60 pp., Commonw. Sci. and Ind. Res. Org., Div. of Atmos. Res., Melbourne, Victoria, Australia.

Kuhlbrodt, T., and J. M. Gregory (2012), Ocean heat uptake and its consequences for the magnitude of sea level rise and climate change, *Geophys. Res. Lett.*, **39**, L18608, doi:10.1029/2012GL052952.

Kumar, R., V. Shankar, and M. K. Jat (2013), Soil moisture dynamics modeling considering multi-layer root zone, *Water Sci Technol.*, **67**(8), 1778-1785, doi: 10.2166/wst.2013.054.

Laio, F., A. Porporato, L. Ridolfi, and I. Rodriguez-Iturbe (2001), Plants in water-controlled ecosystems: active role in hydrologic processes and response to water stress: II. Probabilistic soil moisture dynamics, *Adv. Water Resour.*, **24**(7), 707-723, doi:10.1016/S0309-1708(01)00005-7.

Lakshmi, V. (2013), Remote sensing of soil moisture, *ISRN Soil Sci.*, **2013**, 33 pp., doi:10.1155/2013/424178.

LaMontagne, A. (2009), *Characterization and quantification of ground heat flux for late season shallow snow*, 69 pp., Master thesis, Dep. of Geosciences, Boise State Univ., Boise, Idaho, United States.

Laurent, L., and H. Simmons (2006), Estimates of power consumed by mixing in the ocean interior, *J. Climate*, **19**(19), 4877-4890, doi:10.1175/JCLI3887.1.

L'Ecuyer, T. S., H. K. Beaudoing, M. Rodell, W. Oleson, B. Lin, S. Kato, C. A. Clayson, E. Wood, J. Sheffield, R. Adler, G. Huffman, M. Bosilovich, G. Gu, F. Robertson, P. R. Houser, D. Chambers, J. S. Famiglietti, E. Fetzer, W. T. Liu, X. Gao, C. A. Schlosser, E. Clark, D. P. Lettenmaier, and K. Hilburn (2015), The observed state of the energy budget in the early twenty-first century, *J. Climate*, **28**(21), 8319-8346, doi:10.1175/JCLI-D-14-00556.1.

L'Ecuyer, T. S., and G. L. Stephens (2002), An uncertainty model for Bayesian Monte Carlo retrieval algorithms: Application to the TRMM observing system, *Q. J. R. Meteorol. Soc.*, **128**(583), 1713-1737, doi:10.1002/qj.200212858316.

L'Ecuyer, T. S., and G. L. Stephens (2003), The tropical oceanic energy budget from the TRMM perspective. Part I: Algorithm and uncertainties, *J. Climate*, **16**(12), 1967-1985, doi:10.1175/1520-0442(2003)016<1967:TTOEBF>2.0.CO;2.

Lee, T. J., and R. A. Pielke (1992), Estimating the soil surface specific humidity, *J. Appl. Meteor.*, **31**(5), 480-484, doi:10.1175/1520-0450(1992)031<0480:ETSSSH>2.0.CO;2.

Legates, D. R. (1995), Global and terrestrial precipitation: A comparative assessment of existing climatologies, *Int. J. Climatol.*, **15**(3), 237-258, doi:10.1002/joc.3370150302.

Legates, D. R., and C. J. Willmott (1990), Mean seasonal and spatial variability in gauge-corrected, global precipitation, *Int. J. Climatol.*, **10**(2), 111-127, doi:10.1002/joc.3370100202.

Leovy, C. B. (1969), Bulk transfer coefficient for heat transfer, *J. Geophys. Res.*, **74**(13), 3313-3321, doi:10.1029/JC074i013p03313.

Levitus, S., J. I. Antonov, T. P. Boyer, O. K. Baranova, H. E. Garcia, R. A. Locarnini, A. V. Mishonov, J. R. Reagan, D. Seidov, E. S. Yarosh, and M. M. Zweng (2012), World ocean heat content and thermosteric sea level change (0–2000 m), 1955–2010, *Geophys. Res. Lett.*, **39**, L10603, doi:10.1029/2012GL051106.

Lewis, J. M. (1995), The story behind the Bowen Ratio, *Bull. Amer. Meteor. Soc.*, **76**(12), 2433-2443, doi:10.1175/1520-0477(1995)076<2433:TSBTBR>2.0.CO;2.

Li, J. L. F., D. E. Waliser, G. Stephens, S. Lee, T. L'Ecuyer, S. Kato, N. G. Loeb, and H.-Y. Ma (2013), Characterizing and understanding radiation budget biases in CMIP3/CMIP5 GCMs, contemporary GCM, and reanalysis, *J. Geophys. Res. Atmos.*, **118**(15), 8166-8184, doi:10.1002/jgrd.50378.

Liang, X., D. P. Lettenmaier, E. F. Wood, and S. J. Burges (1994), A simple hydrologically based model of land surface water and energy fluxes for general circulation models, *J. Geophys. Res. Atmos.*, **99**(D7), 14415-14428, doi:10.1029/94JD00483.

Liang, X., E. F. Wood, D. P. Lettenmaier, D. Lohmann, A. Boone, S. Chang, F. Chen, Y. Dai, C. Desborough, R. E. Dickinson, Q. Duan, M. Ek, Y. M. Gusev, F. Habets, P. Irannejad, R. Koster, K. E. Mitchell, O. N. Nasonova, J. Noilhan, J. Schaake, A. Schlosser, Y. Shao, A. B. Shmakin, D. Verseghy, K. Warrach, P. J. Wetzel, Y. Xue, Z.-L. Yang, and Q.-c Zeng (1998), The Project for Intercomparison of Land-surface Parameterization Schemes (PILPS) phase 2(c) Red-Arkansas River basin experiment:: 2. Spatial and temporal analysis of energy fluxes, *Glob. Planet. Chang.*, **19**(1–4), 137-159, doi:10.1016/S0921-8181(98)00045-9.

Lin, J. D. (1980), On the force-restore method for prediction of ground surface temperature, *J. Geophys. Res. Oceans*, **85**(C6), 3251-3254, doi:10.1029/JC085iC06p03251.

Liou, K. N. (1992), *Radiation and cloud processes in the atmosphere: Theory, observation, and modeling*, 487 pp., Oxford University Press, New York, NY, United States.

Liu, H., W. Lin, and M. Zhang (2010), Heat budget of the upper ocean in the South-Central Equatorial Pacific, *J. Climate*, **23**(7), 1779-1792, doi:10.1175/2009JCLI3135.1.

Lucchesi, R. (2008), File specification for MERRA products, *GMAO Office Note*, 96 pp.

Lucchesi, R. (2012), File specification for MERRA products, *GMAO Office Note No. 1 (Version 2.3)*, 82 pp. available from http://gmao.gsfc.nasa.gov/pubs/office_notes.

Luce, C. H., and D. G. Tarboton (2010), Evaluation of alternative formulae for calculation of surface temperature in snowmelt models using frequency analysis of temperature observations, *Hydrol. Earth Syst. Sci.*, **14**(3), 535-543, doi:10.5194/hess-14-535-2010.

Lüers, J., and J. Bareiss (2010), The effect of misleading surface temperature estimations on the sensible heat fluxes at a high Arctic site – the Arctic Turbulence Experiment 2006 on Svalbard (ARCTEX-2006), *Atmos. Chem. Phys.*, **10**(1), 157-168, doi:10.5194/acp-10-157-2010.

Lund, M., C. Stiegler, J. Abermann, M. Citterio, B. U. Hansen, and D. van As (2017), Spatiotemporal variability in surface energy balance across tundra, snow and ice in Greenland, *Ambio*, **46**(1), 81-93, doi:10.1007/s13280-016-0867-5.

Lynch, A. H., F. S. Chapin, L. D. Hinzman, W. Wu, E. Lilly, G. Vourlitis, and E. Kim (1999), Surface energy balance on the arctic tundra: Measurements and models, *J. Climate*, **12**(8), 2585-2606, doi:10.1175/1520-0442(1999)012<2585:sebota>2.0.co;2.

Mahfouf, J. F., and J. Noilhan (1991), Comparative study of various formulations of evaporations from bare soil using in situ data, *J. Appl. Meteor.*, **30**(9), 1354-1365, doi:10.1175/1520-0450(1991)030<1354:CSOVFO>2.0.CO;2.

Mahfouf, J.-F., E. Richard, and P. Mascart (1987), The influence of soil and vegetation on the development of mesoscale circulations, *J. Clim. Appl. Meteor.*, **26**(11), 1483-1495, doi:10.1175/1520-0450(1987)026<1483:TIOSAV>2.0.CO;2.

Mahrt, L., and H. Pan (1984), A two-layer model of soil hydrology, *Bound.-Lay. Meteorol.*, **29**(1), 1-20, doi:10.1007/bf00119116.

Male, D. H., and D. M. Gray (1981), Snowcover ablation and runoff, in *Handbook of snow: Principles, processes, management & use*, edited by D. H. Gray and D. M. Male, pp. 360-430, Permagon Press, Willowdale, Canada.

Manabe, S. (1969), Climate and the ocean circulation: I. The atmospheric circulation and the hydrology of the Earth's surface, *Mon. Wea. Rev.*, **97**(11), 739-774, doi:10.1175/1520-0493(1969)097<0739:CATOC>2.3.CO;2.

Manabe, S., D. G. Hahn, and H. J. L. Jr. (1974), The seasonal variation of the tropical circulation as simulated by a global model of the atmosphere, *J. Atmos. Sci.*, **31**(1), 43-83, doi:10.1175/1520-0469(1974)031<0043:TSVOTT>2.0.CO;2.

Manabe, S., R. T. Wetherald, P. C. D. Milly, T. L. Delworth, and R. J. Stouffer (2004), Century-scale change in water availability: CO2-quadrupling experiment, *Clim. Chang.*, **64**(1), 59-76, doi:10.1023/B:CLIM.0000024674.37725.ca.

Margulis, S. A., and D. Entekhabi (2001), A coupled land surface–boundary layer model and its adjoint, *J. Hydrometeorol.*, **2**(3), 274-296, doi:10.1175/1525-7541(2001)002<0274:ACLSBL>2.0.CO;2.

Markoff, M. S., and A. C. Cullen (2008), Impact of climate change on Pacific Northwest hydropower, *Clim. Chang.*, **87**(3–4), 451-469, doi:10.1007/s10584-007-9306-8.

Mauder, M., and T. Foken (2006), Impact of post-field data processing on eddy covariance flux estimates and energy balance closure, *Meteorol. Z.*, **15**(6), 597-609, doi:10.1127/0941-2948/2006/0167.

Mauder, M., C. Liebethal, M. Göckede, J.-P. Leps, F. Beyrich, and T. Foken (2006), Processing and quality control of flux data during LITFASS-2003, *Bound.-Lay. Meteorol.*, **121**(1), 67-88, doi:10.1007/s10546-006-9094-0.

Maykut, G. A. (1982), Large-scale heat exchange and ice production in the central Arctic, *J. Geophys. Res. Oceans*, **87**(C10), 7971-7984, doi:10.1029/JC087iC10p07971.

Mayocchi, C. L., and K. L. Bristow (1995), Soil surface heat flux: some general questions and comments on measurements, *Agric. For. Meteorol.*, **75**(1), 43-50, doi:10.1016/0168-1923(94)02198-S.

McDonald, R. I., and E. H. Girvetz (2013), Two challenges for U.S. irrigation due to climate change: increasing irrigated area in wet states and increasing irrigation rates in dry states, *PLoS ONE*, **8**(6), e65589, doi:10.1371/journal.pone.0065589.

Meehl, G. A., C. Covey, K. E. Taylor, T. Delworth, R. J. Stouffer, M. Latif, B. McAvaney, and J. F. B. Mitchell (2007), THE WCRP CMIP3 multimodel dataset: A new era in climate change research, *Bull. Amer. Meteor. Soc.*, **88**(9), 1383-1394, doi:10.1175/BAMS-88-9-1383.

Meigh, J. R., A. A. McKenzie, and K. J. Sene (1999), A grid-based approach to water scarcity estimates for eastern and southern Africa, *Water Resour. Manag.*, **13**(2), 85-115, doi:10.1023/a:1008025703712.

Mellor, M. (1977), Engineering properties of snow, *J. Glaciol*., **19**(81), 15-66.

Michel, D., R. Philipona, C. Ruckstuhl, R. Vogt, and L. Vuilleumier (2008), Performance and uncertainty of CNR1 net radiometers during a one-year field comparison, *J. Atmos. Oceanic Technol.*, **25**(3), 442-451, doi:10.1175/2007JTECHA973.1.

Mihailović, D. T., G. Kallos, I. D. Arsenić, B. Lalić, B. Rajković, and A. Papadopoulos (1999), Sensitivity of soil surface temperature in a force-restore equation to heat fluxes and deep soil temperature, *Int. J. Climatol.*, **19**(14), 1617-1632, doi:10.1002/(SICI)1097-0088(19991130)19:14<1617::AID-JOC448>3.0.CO;2-B.

Milly, P. C. D. (1992), Potential evaporation and soil moisture in general circulation models, *J. Climate*, **5**(3), 209-226, doi:10.1175/1520-0442(1992)005<0209:PEASMI>2.0.CO;2.

Mintz, Y. (1984), The sensitivity of numerically simulated climates to land surface boundary conditions, in *The Global Climate*, edited by J. T. Houghton, pp. 79–105, Cambridge Univ. Press, Cambridge.

Mintz, Y., and G. K. Walker (1993), Global fields of soil moisture and land surface evapotranspiration derived from observed precipitation and surface air temperature, *J. Appl. Meteor.*, **32**(8), 1305-1334, doi:10.1175/1520-0450(1993)032<1305:GFOSMA>2.0.CO;2.

Miralles, D. G., T. R. H. Holmes, R. A. M. De Jeu, J. H. Gash, A. G. C. A. Meesters, and A. J. Dolman (2011), Global land-surface evaporation estimated from satellite-based observations, *Hydrol. Earth Syst. Sci.*, **15**(2), 453-469, doi:10.5194/hess-15-453-2011.

Moghim, S., A. J. Bowen, S. Sarachi, and J. Wang (2015), Retrieval of hourly records of surface hydrometeorological variables using satellite remote sensing data, *J. Hydrometeorol.*, **16**(1), 147-157, doi:10.1175/JHM-D-13-0127.1.

Molod, A., L. Takacs, M. Suarez, J. Bacmeister, I.-S. Song, and A. Eichmann (2012), The GEOS-5 atmospheric general circulation model: Mean climate and development from MERRA to fortuna, *Technical Report Series on Global Modeling and Data Assimilation*, Vol. 28 (NASA/TM–2012-104606), 115 pp., NASA Goddard Space Flight Center, Greenbelt, Maryland.

Monin, A. S., and A. M. Obukhov (1954), Basic laws of turbelent mixing in the surface layer of the atmosphere, *Tr. Inst. Teor. Geofiz. Akad. Nauk. SSSR* **24**(151), 163-187 (English translation available in V. N. Bespalyi, Ed., 2001: Turbulence and Atmospheric Dynamics, J. L. Lumley, 2164–2194).

Monteith, J. L. (1965), Evaporation and environment, in *The state and movement of water in living organisms. Society for Experimental Biology, Swansea, Symposium No. 19*, pp. 205-234, Cambridge Univ. Press, Cambridge.

Monteith, J. L., and M. H. Unsworth (2013), Principles of environmental physics (fourth edition), Academic Press, Boston.

Moore, G. W. K., and I. A. Renfrew (2002), An assessment of the surface turbulent heat fluxes from the NCEP–NCAR reanalysis over the western boundary currents, *J. Climate*, **15**(15), 2020-2037, doi:10.1175/1520-0442(2002)015<2020:AAOTST>2.0.CO;2.

Moran, M. S., C. D. Peters-Lidard, J. M. Watts, and S. McElroy (2004), Estimating soil moisture at the watershed scale with satellite-based radar and land surface models, *Can. J. Remote Sens.*, **30**(5), 805-826, doi:10.5589/m04-043.

Mualem, Y. (1976), A new model for predicting the hydraulic conductivity of unsaturated porous media, *Water Resour. Res.*, **12**(3), 513-522, doi:10.1029/WR012i003p00513.

Mueller, B., M. Hirschi, and S. Seneviratne (2013), Benchmark products for land evapotranspiration: LandFlux-EVAL multi-dataset synthesis, *Hydrol. Earth Syst. Sci.*, **17**, 3707-3720.

Mueller, B., S. I. Seneviratne, C. Jiménez, T. Corti, M. Hirschi, G. Balsamo, P. Ciais, P. Dirmeyer, J. B. Fisher, Z. Guo, M. Jung, F. Maignan, M. F. McCabe, R. Reichle, M. Reichstein, M. Rodell, J. Sheffield, A. J. Teuling, K. Wang, E. F. Wood, and Y. Zhang (2011), Evaluation of global observations-based evapotranspiration datasets and IPCC AR4 simulations, *Geophys. Res. Lett.*, **38**, L06402, doi:10.1029/2010GL046230.

Nachtergaele, F., H. Velthuizen, L. Verelst, and W. D. (2012), Harmonized world soil database (version 1.2). *FAO, Rome, Italy and IIASA*, Laxenburg, Austria.

National Academy of Sciences (1975), *Understanding Climatic Change: A program for action*, 239 pp., National Academy of Sciences, Washington D.C..

Neale, R. B., C.-C. Chen, A. Gettelman, P. H. Lauritzen, S. Park, D. L. Williamson, A. J. Conley, R. Garcia, D. Kinnison, J.-F. Lamarque, D. Marsh, M. Mills, A. K. Smith, S. Tilmes, F. Witt, H. Morrison, P. Camaron-Smith, W. D. Collins, M. J. Iacono, R. C. Easter, S. J. Ghan, X. Liu, P. J. Rasch, and M. A. Taylor (2012), Description of the NCAR community atmosphere Model (CAM 5.0), *NCAR technical note NCAR/TN-486+STR*, 274 pp., National Center for Atmospheric Research, Boulder, Colorado.

Nearing, G. S., M. S. Moran, R. L. Scott, and G. Ponce-Campos (2012), Coupling diffusion and maximum entropy models to estimate thermal inertia, *Remote Sens. Environ.*, **119**, 222-231, doi:10.1016/j.rse.2011.12.012.

Nickerson, E. C., and V. E. Smiley (1975), Surface layer and energy budget parameterizations for mesoscale models, *J. Appl. Meteor.*, **14**(3), 297-300, doi:10.1175/1520-0450(1975)014<0297:SLAEBP>2.0.CO;2.

Noilhan, J., and J. F. Mahfouf (1996), The ISBA land surface parameterisation scheme, *Glob. Planet. Chang.*, **13**(1–4), 145-159, doi:10.1016/0921-8181(95)00043-7.

Noilhan, J., and S. Planton (1989), A simple parameterization of land surface processes for meteorological models, *Mon. Wea. Rev.*, **117**(3), 536-549, doi:10.1175/1520-0493(1989)117<0536:ASPOLS>2.0.CO;2.

Nordbo, A., L. Järvi, and T. Vesala (2012), Revised eddy covariance flux calculation methodologies – effect on urban energy balance, *Tellus B*, **64**, doi:10.3402/tellusb.v64i0.18184.

Ochsner, T., T. J. Sauer, and H. Horton (2006), Field tests of the soil heat flux plate method and some alternatives, *Agron. J.*, **98**(4), 1005-1014, doi:10.2134/agronj2005.0249.

Ochsner, T., T. J. Sauer, and H. R. (2007), Soil heat storage measurements in energy balance studies, *Agron. J.*, **99**(1), 311-319, doi:10.2134/agronj2005.0103S.

Ohmura, A. (1982), Objective criteria for rejecting data for Bowen Ratio flux calculations, *J. Agric. Meteorol.*, **21**(4), 595-598, doi:10.1175/1520-0450(1982)021<0595:OCFRDF>2.0.CO;2.

Ohmura, A., and H. Gilgen (1993), Re-evaluation of the global energy balance, in *Interactions Between Global Climate Subsystems: The legacy of Hann, Geophys. Monogr, No. 75*, pp. 93-110, Int. Union Geodesy and Geophys.

Oleson, K. W., D. M. Lawrence, G. B. Bonan, M. G. Flanner, E. Kluzek, P. J. Lawrence, S. Levis, S. C. Swenson, P. E. Thornton, A. Dai, M. Decker, R. Dicknison, J.

Feddema, C. L. Heald, F. Hoffman, J.-F. Lamarque, N. Mahowald, G.-Y. Niu, T. Qian, J. Randerson, S. Running, K. Sakaguchi, A. Slater, R. Stöckli, A. Wang, Z.-L. Yang, X. Zeng, and X. Zeng (2010), Technical description of version 4.0 of the Community Land Model (CLM), *NCAR Technical Note NCAR/TN-478+STR*, 257 pp., National Center for Atmospheric Research, Boulder, Colorado.

O'Neill, A. D. J. and D. M. Gary (1973), Solar radiation penetration through snow, *Proc. of UNESCO-WMO-IAHS Symposia on the Role of Snow and Ice in Hydrology*, IAHS Press, Wallingford, United Kingdom.

Oncley, S. P., T. Foken, R. Vogt, W. Kohsiek, H. A. R. DeBruin, C. Bernhofer, A. Christen, E. van Gorsel, D. Grantz, C. Feigenwinter, I, Lehner, C. Liebethal, H. Liu, M. Mauder, A. Pitacco, L. Ribeiro, and T. Weidinger (2007), The Energy Balance Experiment EBEX-2000. Part I: overview and energy balance, *Bound.-Lay. Meteorol.*, **123**(1), 1-28, doi:10.1007/s10546-007-9161-1.

Onogi, K., H. Koide, M. Sakamoto, S. Kobayashi, J. Tsutsui, H. Hatsushika, T. Matsumoto, N. Yamazaki, H. Kamahori, K. Kato, R. Oyama, T. Ose, S. Kadokura, and K. Wada (2005), JRA-25: Japanese 25-year re-analysis project—progress and status, *Q. J. R. Meteorol. Soc.*, **131**(613), 3259-3268, doi:10.1256/qj.05.88.

Onogi, K., J. Tsutsui, H. Koide, M. Sakamoto, S. Kobayashi, H. Hatsushika, T. Matsumoto, N. Yamazaki, H. Kamahori, K. Takahashi, S. Kadokura, K. Wada, K. Kato, R. Oyama, T. Ose, N. Mannoji, and R. Taira (2007), The JRA-25 reanalysis, *J. Meteor. Soc. Japan. Ser. II*, **85**(3), 369-432, doi:10.2151/jmsj.85.369.

Ookouchi, Y., M. Segal, R. C. Kessler, and R. A. Pielke (1984), Evaluation of soil moisture effects on the generation and modification of mesoscale circulations, *Mon. Wea. Rev.*, **112**(11), 2281-2292, doi:10.1175/1520-0493(1984)112<2281:EOSMEO>2.0.CO;2.

Owe, M., R. de Jeu, and T. Holmes (2008), Multisensor historical climatology of satellite-derived global land surface moisture, *J. Geophys. Res. Earth Surf.*, **113**, F01002, doi:10.1029/2007JF000769.

Pan, H.-L., and L. Mahrt (1987), Interaction between soil hydrology and boundary-layer development, *Bound.-Lay. Meteorol.*, **38**(1), 185-202, doi:10.1007/bf00121563.

Paulson, C. A. (1970), The mathematical representation of wind speed and temperature profiles in the unstable atmospheric surface layer, *J. Appl. Meteor.*, **9**(6), 857-861, doi:10.1175/1520-0450(1970)009<0857:TMROWS>2.0.CO;2.

Penman, H. L. (1948), Natural evaporation from open water, bare soil and grass, *Proc. Roy. Soc. London A, Math Phys. Eng. Sci.*, **193**(1032), 120-145, doi:10.1098/rspa.1948.0037.

Persson, P. O. G., C. W. Fairall, E. L. Andreas, P. S. Guest, and D. K. Perovich (2002), Measurements near the atmospheric surface flux group tower at SHEBA: Near-surface conditions and surface energy budget, *J. Geophys. Res. Oceans*, **107**(C10), SHE 21-21-SHE 21-35, doi:10.1029/2000JC000705.

Philip, J. R. (1957), Evaporation, and moisture and heat fields in the soil, *J. Meteorol.*, **14**(4), 354-366, doi:10.1175/1520-0469(1957)014<0354:EAMAHF>2.0.CO;2.

Philip, J. R. (1961), The theory of heat flux meters, *J. Geophys. Res.*, **66**(2), 571-579, doi:10.1029/JZ066i002p00571.

Pisciotta, J. M., Y. Zou, and I. V. Baskakov (2010), Light-dependent electrogenic activity of cyanobacteria, *PLoS ONE*, **5**(5), e10821, doi:10.1371/journal.pone.0010821.

Pitman, A. J. (2003), The evolution of, and revolution in, land surface schemes designed for climate models, *Int. J. Climatol.*, **23**(5), 479-510, doi:10.1002/joc.893.

Pitman, A. J., A. G. Slater, C. E. Desborough, and M. Zhao (1999), Uncertainty in the simulation of runoff due to the parameterization of frozen soil moisture using the Global Soil Wetness Project methodology, *J. Geophys. Res. Atmos.*, **104**(D14), 16879-16888, doi:10.1029/1999JD900261.

Pitman, A. J., Z. L. Yang, J. G. Cogley, and A. Henderson-Sellers (1991), Description of bare essentials of surface transfer for the Bureau of Meteorology Research Centre AGCM, *BMRC research Rep. 32*, 117 pp. BMRC, Melbourne, Australia.

Pleim, E. J., and A. Xiu (1995), Development and testing of a surface flux and planetary boundary layer model for application in mesoscale models, *J. Appl. Meteor.*, **34**(1), 16-32, doi:10.1175/1520-0450-34.1.16.

Pond, S., D. B. Fissel, and C. A. Paulson (1974), A note on bulk aerodynamic coefficients for sensible heat and moisture fluxes, *Bound.-Lay. Meteorol.*, **6**, 333-340.

Priestley, C. H. B. (1959), *Turbulent transfer in the lower atmosphere*, 130 pp., University of Chicago Press VII, doi:10.1002/qj.49708636825.

Priestley, C. H. B., and R. J. Taylor (1972), On the assessment of surface heat flux and evaporation using large-scale parameters, *Mon. Wea. Rev.*, **100**(2), 81-92, doi:10.1175/1520-0493(1972)100<0081:OTAOSH>2.3.CO;2.

Qian, B., E. G. Gregorich, S. Gameda, D. W. Hopkins, and X. L. Wang (2011), Observed soil temperature trends associated with climate change in Canada, *Journal of Geophysical Research: Atmospheres*, **116**(D02106), doi:10.1029/2010JD015012.

Reichle, R. H. (2012), The MERRA-Land data product, *GMAO Office Note No. 3 (Version 1.2)*, 38 pp.

Reichle, R. H., R. D. Koster, G. J. M. De Lannoy, B. A. Forman, Q. Liu, S. P. P. Mahanama, and A. Touré (2011), Assessment and enhancement of MERRA land surface hydrology estimates, *J. Climate*, **24**(24), 6322-6338, doi:10.1175/JCLI-D-10-05033.1.

Ren, D., and M. Xue (2004), A revised force–restore model for land surface modeling, *J. Appl. Meteor.*, **43**(11), 1768-1782, doi:10.1175/JAM2161.1.

Renfrew, I. A., G. W. K. Moore, P. S. Guest, and K. Bumke (2002), A comparison of surface layer and surface turbulent flux observations over the Labrador Sea with ECMWF analyses and NCEP reanalyses, *J. Phys. Oceanogr.*, **32**(2), 383-400, doi:10.1175/1520-0485(2002)032<0383:ACOSLA>2.0.CO;2.

Richards, L. A. (1931), Capillary conduction of liquids through porous mediums, *J. Appl. Phys.*, **1**(5), 318-333, doi:10.1063/1.1745010.

Rienecker, M. M., M. J. Suarez, R. Gelaro, R. Todling, J. Bacmeister, E. Liu, M. G. Bosilovich, S. D. Schubert, L. Takacs, G.-K. Kim, S. Bloom, J. Chen, D. Collins, A. Conaty, A. da Silva, W. Gu, J. Joiner, R. D. Koster, R. Lucchesi, A. Molod, T. Owens, S. Pawson, P. Pegion, C. R. Redder, R. Reichle, F. R. Robertson, A. G. Ruddick, M. Sienkiewicz, and J. Woollen (2011), MERRA: NASA's Modern-Era Retrospective Analysis for Research and Applications, *J. Climate*, **24**(14), 3624-3648, doi:10.1175/JCLI-D-11-00015.1.

Rienecker, M. M., M. J. Suarez, R. Todling, L. Bacmeister, L. Takacs, H.-C. Liu, W. Gu, M. Sienkiewicz, R. D. Koster, R. Gelaro, I. Stajner, and J. E. Neilsen (2008), The GEOS-5 data assimilation system - documentation of versions 5.0.1, 5.1.0, and 5.2.0, *NASA Technical Report Series on Global Modeling and Data Assimilation*, Vol. 27 (NASA/TM–2008–104606), 101 pp., NASA Goddard Space Flight Center, Greenbelt, Maryland.

Roberts, J. B., F. R. Robertson, C. A. Clayson, and M. G. Bosilovich (2012), Characterization of turbulent latent and sensible heat flux exchange between the atmosphere and ocean in MERRA, *J. Climate*, **25**(3), 821-838, doi:10.1175/JCLI-D-11-00029.1.

Robock, A., K. Y. Vinnikov, C. A. Schlosser, N. A. Speranskaya, and Y. Xue (1995), Use of midlatitude soil moisture and meteorological observations to validate soil moisture simulations with biosphere and bucket models, *J. Climate*, **8**(1), 15-35, doi:10.1175/1520-0442(1995)008<0015:UOMSMA>2.0.CO;2.

Rodell, M., H. K. Beaudoing, T. S. L'Ecuyer, W. S. Oleson, J. S. Famiglietti, P. R. Houser, R. Adler, M. G. Bosilovich, C. A. Clayson, D. Chambers, E. Clark, E. J. Fetzer, X. Gao, G. Gu, K. Hilburn, G. J. Huffman, D. P. Lettenmaier, W. T. Liu, F. R. Robertson, C. A. Schlosser, J. Sheffield, and E. F. Wood (2015), The observed state of the water cycle in the early twenty-first century, *J. Climate*, **28**(21), 8289-8318, doi:10.1175/JCLI-D-14-00555.1.

Rodell, M., P. R. Houser, U. Jambor, J. Gottschalck, K. Mitchell, C.-J. Meng, K. Arsenault, B. Cosgrove, J. Radakovich, M. Bosilovich, J. K. Entin, J. P. Walker, D. Lohmann, and D. Toll (2004), The Global Land Data Assimilation System, *Bull. Amer. Meteor. Soc.*, **85**(3), 381-394, doi:10.1175/BAMS-85-3-381.

Rodgers, C. D. (2000), *Inverse methods for atmospheric sounding*, 240 pp., World Scientific.

Romano, N., M. Palladino, and G. B. Chirico (2011), Parameterization of a bucket model for soil-vegetation-atmosphere modeling under seasonal climatic regimes, *Hydrol. Earth Syst. Sci.*, **15**(12), 3877-3893, doi:10.5194/hess-15-3877-2011.

Rossow, W. B., and Y. C. Zhang (1995), Calculation of surface and top of atmosphere radiative fluxes from physical quantities based on ISCCP data sets: 2. Validation and first results, *J. Geophys. Res. Atmos.*, **100**(D1), 1167-1197, doi:10.1029/94JD02746.

Rost, S., D. Gerten, A. Bondeau, W. Lucht, J. Rohwer, and S. Schaphoff (2008), Agricultural green and blue water consumption and its influence on the global water system, *Water Resour. Res.*, **44**, W09405, doi:10.1029/2007WR006331.

Rowntree, P. R. (1975), The representation of radiation and surface heat exchange in a general circulation model, *Tech. Note 11/58*, Meteorol. Office, Bracknell, Berkshire, England.

Rowntree, P. R. (1983), Sensitivity of GCM to land surface processes, *Proc. Workshop in Intercomparison of Large Scale Models for Extended Range Forecasts*, pp. 225-261, Eur. Cent. for Med.-Range Weather Forecasts, Reading, United Kingdom.

Rowntree, P. R. (1991), Atmospheric parameterization schemes for evaporation over land: Basic concepts and climate modeling aspects, in *Land Surface Evaporation:*

Measurement and Parameterization, edited by T. J. Schmugge and J.-C. André, pp. 5-29, Springer New York, New York, NY, doi:10.1007/978-1-4612-3032-8_2.

Rowntree, P. R., and J. A. Bolton (1983), Simulation of the atmospheric response to soil moisture anomalies over Europe, *Q. J. R. Meteorol. Soc.*, **109**(461), 501-526, doi:10.1002/qj.49710946105.

Rudolf, B., H. Hauschild, W. Rüth, and U. Schneider (1996), Comparison of raingauge analyses, satellite-based precipitation estimates and forecast model results, *Adv. Space Res.*, **18**(7), 53-62, doi:10.1016/0273-1177(95)00290-1.

Rutgersson, A., A.-S. Smedman, and A. Omstedt (2001), Measured and simulated latent and sensible heat fluxes at two marine sites In the Baltic Sea, *Bound.-Lay. Meteorol.*, **99**(1), 53-84, doi:10.1023/a:1018799227854.

Sadhuram, Y. (1991), Estimation of bulk transfer coefficient for latent heat flux (Ce), *Bound.-Lay. Meteorol.*, **54**(4), 411-414, doi:10.1007/bf00118869.

Saha, S., S. Moorthi, H.-L. Pan, X. Wu, J. Wang, S. Nadiga, P. Tripp, R. Kistler, J. Woollen, D. Behringer, H. Liu, D. Stokes, R. Grumbine, G. Gayno, J. Wang, Y.-T. Hou, H.-Y. Chuang, H.-M. H. Juang, J. Sela, M. Iredell, R. Treadon, D. Kleist, P. V. Delst, D. Keyser, M. Ek, J. Meng, H. Wei, R. Yang, S. Lord, H. V. D. Dool, A. Kumar, W. Wang, C. Long, M. Chelliah, Y. Xue, B. Huang, J.-K. Schemm, W. Ebisuzaki, R. Lin, P. Xie, M. Chen, S. Zhou, W. Higgins, C.-Z. Zou, Q. Liu, Y. Chen, Y. Han, L. Cucurull, R. W. Reynolds, G. Rutledge, and M. Goldberg (2010), The NCEP Climate Forecast System Reanalysis, *Bull. Amer. Meteor. Soc.*, **91**(8), 1015-1057, doi:10.1175/2010BAMS3001.1.

Saha, S., S. Nadiga, C. Thiaw, J. Wang, W. Wang, Q. Zhang, H. M. van den Dool, H.-L. Pan, S. Moorthi, D. Behringer, D. Stokes, M. Peña, S. Lord, G. White, W. Ebisuzaki, P. Peng, and P. Xie (2006), The NCEP Climate Forecast System, *J. Climate*, **19**(15), 3483-3517, doi:10.1175/JCLI3812.1.

Salathé, E. P. (2005), Downscaling simulations of future global climate with application to hydrologic modelling, *Int. J. Climatol.*, **25**(4), 419-436, doi:10.1002/joc.1125.

Sato, N., P. J. Sellers, D. A. Randall, E. K. Schneider, J. Shukla, J. L. Kinter, Y. T. Hou, and E. Albertazzi (1989), Effects of implementing the Simple Biosphere Model in a general circulation model, *J. Atmos. Sci.*, **46**(18), 2757-2782, doi:10.1175/1520-0469(1989)046<2757:EOITSB>2.0.CO;2.

Sauer, T. J., O. T. E., J. L. Heitman, R. Horton, B. D. Tanner, O. D. Akinyemi, G. Hern, and T. B. Moorman (2008), Careful measurements and energy balance closure - The case of soil heat flux, *Paper presented at AMS Meeting, 28th Conference on*

Agricultural and Forest Meteorology, Amer. Meteor. Soc. Committee on on Agricultural and Forest Meteorology, Orlando, FL.

Sauer, T. J., D. W. Meek, T. E. Ochsner, A. R. Harris, and R. Horton (2003), Errors in heat flux measurement by flux plates of contrasting design and thermal conductivity, *Vadose Zone J.*, **2**(4), 580-588, doi:10.2113/2.4.580.

Saunders, P. M. (1967), The temperature at the ocean-air interface, *J. Atmos. Sci.*, **24**(3), 269-273, doi:10.1175/1520-0469(1967)024<0269:TTATOA>2.0.CO;2.

Schanz, T., W. Baille, and L. Tuan (2011), Effects of temperature on measurements of soil water content with time domain reflectometry, *Geotech. Test. J.*, **34**(1), GTJ103152.

Schlosser, C. A., and P. R. Houser (2007), Assessing a satellite-era perspective of the global water cycle, *J. Climate*, **20**(7), 1316-1338, doi:10.1175/JCLI4057.1.

Schlosser, C. A., A. G. Slater, A. Robock, A. J. Pitman, K. Y. Vinnikov, A. Henderson-Sellers, N. A. Speranskaya, K. Mitchell, and T. P. Contributors (2000), Simulations of a boreal grassland hydrology at Valdai, Russia: PILPS Phase 2(d), *Mon. Wea. Rev.*, **128**(2), 301-321, doi:10.1175/1520-0493(2000)128<0301:SOABGH>2.0.CO;2.

Schröder, D., T. Vihma, A. Kerber, and B. Brümmer (2003), On the parameterization of turbulent surface fluxes over heterogeneous sea ice surfaces, *J. Geophys. Res. Oceans*, **108**(C6), 3195, doi:10.1029/2002JC001385.

Schutz, C., and W. L. Gates (1972a), Supplemental global climatic data: January, *Rand Corp., R-915/1-ARPA*, 110 pp., Santa Monica, California.

Schutz, C., and W. L. Gates (1972b), Global climatic data for surface, 800 mb, 400 mb: July, *Rand Corp., R-1029-ARPA*, 180 pp., Santa Monica, California.

Schutz, C., and W. L. Gates (1973), Global climatic data for surface, 800 mb, 400 mb: April, *Rand Corp., R-1317-ARPA*, 192 pp., Santa Monica, California.

Schutz, C., and W. L. Gates (1974), Global climatic data for surface, 800 mb, 400 mb: October, *Rand Corp., Santa Monica, R-I425-ARPA*, 192 pp., Santa Monica, California.

Scott, R. L., T. E. Huxman, W. L. Cable, and W. E. Emmerich (2006), Partitioning of evapotranspiration and its relation to carbon dioxide exchange in a Chihuahuan Desert shrubland, *Hydrol. Process.*, **20**(15), 3227-3243, doi:10.1002/hyp.6329.

Seibert, J. (1997), Estimation of parameter uncertainty in the HBV model, *Nord. Hydrol. Conference (Akureyri, Iceland - August 1996)*, **28**(4–5), 247-262.

Sela, J. G. (1980), Spectral modeling at the National Meteorological Center, *Mon. Wea. Rev.*, **108**(9), 1279-1292, doi:10.1175/1520-0493(1980)108<1279:SMATNM>2.0.CO;2.

Sellers, P. J., F. G. Hall, R. D. Kelly, A. Black, D. Baldocchi, J. Berry, M. Ryan, K. J. Ranson, P. M. Crill, D. P. Lettenmaier, H. Margolis, J. Cihlar, J. Newcomer, D. Fitzjarrald, P. G. Jarvis, S. T. Gower, D. Halliwell, D. Williams, B. Goodison, D. E. Wickland, and F. E. Guertin (1997), BOREAS in 1997: Experiment overview, scientific results, and future directions, *J. Geophys. Res. Atmos*., **102**(D24), 28731-28769, doi:10.1029/97JD03300.

Sellers, P. J., Y. Mintz, Y. C. Sud, and A. Dalcher (1986), A Simple Biosphere Model (SIB) for use within general circulation models, *J. Atmos. Sci.*, **43**(6), 505-531, doi:10.1175/1520-0469(1986)043<0505:ASBMFU>2.0.CO;2.

Sellers, P. J., D. A. Randall, G. J. Collatz, J. A. Berry, C. B. Field, D. A. Dazlich, C. Zhang, G. D. Collelo, and L. Bounoua (1996), A revised land surface parameterization (SiB2) for atmospheric GCMS. Part I: Model formulation, *J. Climate*, **9**(4), 676-705, doi:10.1175/1520-0442(1996)009<0676:ARLSPF>2.0.CO;2.

Sellers, W. D. (1965), *Physical climatology*, 272 pp., Univ. of Chicago Press, Chicago, IL.

Sen Gupta, A., L. C. Muir, J. N. Brown, S. J. Phipps, P. J. Durack, D. Monselesan, and S. E. Wijffels (2012), Climate drift in the CMIP3 models, J. Climate, 25(13), 4621-4640, doi:10.1175/JCLI-D-11-00312.1.

Seneviratne, S., J. Pal, E. Eltahir, and C. Schär (2002), Summer dryness in a warmer climate: a process study with a regional climate model, *Clim. Dyn.*, **20**(1), 69-85, doi:10.1007/s00382-002-0258-4.

Seneviratne, I. S., and R. Stöckli (2008), The role of land-atmosphere interactions for climate variability in Europe, in *Climate Variability and Extremes during the Past 100 Years*, edited by S. Brönnimann, J. Luterbacher, T. Ewen, F. H. Diaz, S. R. Stolarski and U. Neu, pp. 179-193, Springer Netherlands, Dordrecht, doi:10.1007/978-1-4020-6766-2_12.

Seneviratne, S., N. Nicholls, D. Easterling, C. Goodess, S. Kanae, J. Kossin, Y. Luo, J. Marengo, K. McInnes, and M. Rahimi (2012), Changes in climate extremes and their impacts on the natural physical environment: an overview of the IPCC SREX report, *In book: Managing the Risks of Extreme Events and Disasters to Advance*

Climate Change Adaptation (SREX), Chapter 3, Cambridge University Press, Cambridge, United Kingdom, and New York, NY, United States.

Seneviratne, S. I., T. Corti, E. L. Davin, M. Hirschi, E. B. Jaeger, I. Lehner, B. Orlowsky, and A. J. Teuling (2010), Investigating soil moisture–climate interactions in a changing climate: A review, *Earth-Sci. Rev.*, **99**(3–4), 125-161, doi:10.1016/j.earscirev.2010.02.004.

Shanafield, M., P. G. Cook, H. A. Gutiérrez-Jurado, R. Faux, J. Cleverly, and D. Eamus (2015), Field comparison of methods for estimating groundwater discharge by evaporation and evapotranspiration in an arid-zone playa, *J. Hydrol.*, **527**, 1073-1083, doi:10.1016/j.jhydrol.2015.06.003.

Shao, Y., and A. Henderson-Sellers (1996), Modeling soil moisture: A Project for Intercomparison of Land Surface Parameterization Schemes Phase 2(b), *J. Geophys. Res. Atmos.*, **101**(D3), 7227-7250, doi:10.1029/95JD03275.

Sheffield, J., E. F. Wood, and F. Munoz-Arriola (2010), Long-term regional estimates of evapotranspiration for Mexico based on downscaled ISCCP Data, *J. Hydrometeorol.*, **11**(2), 253-275, doi:10.1175/2009JHM1176.1.

Sheikh, V., S. Visser, and L. Stroosnijder (2009), A simple model to predict soil moisture: Bridging Event and Continuous Hydrological (BEACH) modelling, *Environ. Model. Softw.*, **24**(4), 542-556, doi:10.1016/j.envsoft.2008.10.005.

Simmons, A., S. M. Uppala, D. Dee, and S. Kobayashi (2007), ERA-Interim: New ECMWF reanalysis products from 1989 onwards., *Newsletter 110 - Winter 2006/07*, 11 pp., Eur. Cent. for Med.-Range Weather Forecasts, Reading, United Kingdom.

Singh, B., and R. Taillefer (1986), The effect of synoptic-scale advection on the performance of the Priestley-Taylor evaporation formula, *Bound.-Lay. Meteorol.*, **36**(3), 267-282, doi:10.1007/bf00118664.

Smirnova, T. G., J. M. Brown, and S. G. Benjamin (1997), Performance of different soil model configurations in simulating ground surface temperature and surface fluxes, *Mon. Wea. Rev.*, **125**(8), 1870-1884, doi:10.1175/1520-0493(1997)125<1870:PODSMC>2.0.CO;2.

Stephens, G. L., J. Li, M. Wild, C. A. Clayson, N. Loeb, S. Kato, T. L'Ecuyer, P. W. Stackhouse, M. Lebsock, and T. Andrews (2012a), An update on Earth's energy balance in light of the latest global observations, *Nat. Geosci.*, **5**(10), 691-696, doi:10.1038/NGEO1580.

Stephens, G. L., M. Wild, P. W. Stackhouse Jr., T. L'Ecuyer, S. Kato, and D. S. Henderson (2012b), The global character of the flux of downward longwave radiation, *J. Climate*, **25**(7), 2329-2340, doi:10.1175/JCLI-D-11-00262.1.

Strasser, U., M. Bernhardt, M. Weber, G. E. Liston, and W. Mauser (2008), Is snow sublimation important in the alpine water balance?, *The Cryosphere*, **2**(1), 53-66, doi:10.5194/tc-2-53-2008.

Strub, P. T., and T. M. Powell (1987), The exchange coefficients for latent and sensible heat flux over lakes: Dependence upon atmospheric stability, *Bound.-Lay. Meteorol.*, **40**(4), 349-362, doi:10.1007/bf00116102.

Stull, R. (1988), *An introduction to boundary layer meteorology*, 666 pp., Kluwer Academic Publishers, Dordrecht, Boston, London.

Su, Z. (2002), The Surface Energy Balance System (SEBS) for estimation of turbulent heat fluxes, *Hydrol. Earth Syst. Sci.*, **6**(1), 85-100, doi:10.5194/hess-6-85-2002.

Takata, K., S. Emori, and T. Watanabe (2003), Development of the minimal advanced treatments of surface interaction and runoff, *Glob. Planet. Chang.*, **38**(1–2), 209-222, doi:10.1016/S0921-8181(03)00030-4.

Taylor, G. I. (1915), Eddy motion in the atmosphere, *Phil. Trans. R. Soc. A: Math Phys. Eng. Sci.*, **215**(523-537), 1-26, doi:10.1098/rsta.1915.0001.

Taylor, K. E., R. J. Stouffer, and G. A. Meehl (2012), An overview of CMIP5 and the experiment design, *Bull. Amer. Meteor. Soc.*, **93**(4), 485-498, doi:10.1175/BAMS-D-11-00094.1.

Toggweiler, J. R., and B. Samuels (1998), On the ocean's large-scale circulation near the limit of no vertical mixing, *J. Phys. Oceanogr.*, **28**(9), 1832-1852, doi:10.1175/1520-0485(1998)028<1832:OTOSLS>2.0.CO;2.

Townshend, J. R. G. (1992), Improved global data for land applications. A proposal for a new high resolution data set. Report of the Land Cover Working Group of IGBP-DIS *IGBP Global Change Report no. 20*, International Geosphere–Biosphere Programme, Stockholm, Sweden.

Trenberth, K. E., and J. T. Fasullo (2010), Simulation of present-day and twenty-first-century energy budgets of the southern oceans, *J. Climate*, **23**(2), 440-454, doi:10.1175/2009JCLI3152.1.

Trenberth, K. E., J. T. Fasullo, and J. Kiehl (2009), Earth's global energy budget, *Bull. Amer. Meteor. Soc.*, **90**(3), 311-323, doi:10.1175/2008BAMS2634.1.

Trenberth, K. E., L. Smith, T. Qian, A. Dai, and J. Fasullo (2007), Estimates of the global water budget and its annual cycle using observational and model data, *J. Hydrometeorol.*, **8**(4), 758-769, doi:10.1175/JHM600.1.

Tzimopoulos, C. D., and M. Sakellariou-Makrantonaki (1996), A new analytical model to predict the hydraulic conductivity of unsaturated soils, *Water Resour. Manag.*, **10**(5), 397-414, doi:10.1007/bf00452953.

Uppala, S. M., D. Dee, S. Kobayashi, P. Berrisford, and A. Simmons (2008), Towards a climate data assimilation system: Status update of ERA-Interim, *ECMWF Newsletter*, **115**, 12-18.

Uppala, S. M., P. W. KÅllberg, A. J. Simmons, U. Andrae, V. Da Costa Bechtold, M. Fiorino, J. K. Gibson, J. Haseler, A. Hernandez, G. A. Kelly, X. Li, K. Onogi, S. Saarinen, N. Sokka, R. P. Allen, E. Anderson, K. Arpe, M. A. Balmaseda, A. C. M. Beljaars, L. van de Berg, J. Bidlot, N. Bormann, S. Caires, F. Chevallier, A. Dethof, M. Dragosavac, M. Fisher, M. Fuentes, S. Hagemann, E. Hólm, B. J. Hoskins, L. Isaksen, P. A. E. M. Janssen, R. Jenne, A. P. McNally, J. F. Mahfouf, J. J. Morcrette, N. A. Rayner, R. W. Saunders, P. Simon, A. Sterl, K. E. Trenberth, A. Untch, D. Vasiljevic, P. Viterbo, and J. Woollen (2005), The ERA-40 re-analysis, *Q. J. R. Meteorol. Soc.*, **131**(612), 2961-3012, doi:10.1256/qj.04.176.

Valiantzas, J. D. (2011), Combined Brooks-Corey/Burdine and van Genuchten/Mualem closed-form model for improving prediction of unsaturated conductivity, *J. Irrig. Drain. Eng.*, **137**(4), 223-233, doi:10.1061/(ASCE)IR.1943-4774.0000284.

van den Broeke, M., X. Fettweis, and T. Mölg (2011), Surface energy balance, in *Encyclopedia of Snow, Ice and Glaciers*, edited by V. P. Singh, P. Singh and U. K. Haritashya, pp. 1112-1123, Springer, Dordrecht, The Netherlands, doi:10.1007/978-90-481-2642-2_132.

van Dijk, A. I. J. M., H. E. Beck, R. S. Crosbie, R. A. M. de Jeu, Y. Y. Liu, G. M. Podger, B. Timbal, and N. R. Viney (2013), The millennium drought in southeast Australia (2001–2009): Natural and human causes and implications for water resources, ecosystems, economy, and society, *Water Resour. Res.*, **49**(2), 1040-1057, doi:10.1002/wrcr.20123.

van Genuchten, M. T. (1980), A closed-form equation for predicting the hydraulic conductivity of unsaturated soils, *Soil Sci. Soc. Am. J.*, **44**, 892-898, doi:10.2136/sssaj1980.03615995004400050002x.

Venkatesh, B., L. Nandagirl, B. K. Purandara, and V. B. Reddy (2011), Modelling soil moisture under different land covers in a sub-humid environment of Western Ghats, India, *J. Earth Syst. Sci.*, **120**(3), 387-398, doi:10.1007/s12040-011-0076-3.

Verseghy, D. L. (1991), Class—A Canadian land surface scheme for GCMS. I. Soil model, *Int. J. Climatol.*, **11**(2), 111-133, doi:10.1002/joc.3370110202.

Vinukollu, R. K., R. Meynadier, J. Sheffield, and E. F. Wood (2011a), Multi-model, multi-sensor estimates of global evapotranspiration: climatology, uncertainties and trends, *Hydrol. Process.*, **25**(26), 3993-4010, doi:10.1002/hyp.8393.

Vinukollu, R. K., E. F. Wood, C. R. Ferguson, and J. B. Fisher (2011b), Global estimates of evapotranspiration for climate studies using multi-sensor remote sensing data: Evaluation of three process-based approaches, *Remote Sens. Environ.*, **115**(3), 801-823, doi:10.1016/j.rse.2010.11.006.

Viterbo, P. (2002), A review of parametrization schemes for land surface processes, *Meteorol. Training Course Lecture Ser.*, 49 pp., Eur. Cent. for Med.-Range Weather Forecasts, Reading, United Kingdom.

Wada, Y., D. Wisser, S. Eisner, M. Flörke, D. Gerten, I. Haddeland, N. Hanasaki, Y. Masaki, F. T. Portmann, T. Stacke, Z. Tessler, and J. Schewe (2013), Multimodel projections and uncertainties of irrigation water demand under climate change, *Geophys. Res. Lett.*, **40**(17), 4626-4632, doi:10.1002/grl.50686.

Wang, A., and X. Zeng (2013), Development of global hourly 0.5° land surface air temperature datasets, *J. Climate*, **26**(19), 7676-7691, doi:10.1175/JCLI-D-12-00682.1.

Wang, J., and R. L. Bras (1998), A new method for estimation of sensible heat flux from air temperature, *Water Resour. Res.*, **34**(9), 2281-2288, doi:10.1029/98WR01698.

Wang, J., and R. L. Bras (2009), A model of surface heat fluxes based on the theory of maximum entropy production, *Water Resour. Res.*, **45**, W11422, doi:10.1029/2009WR007900.

Wang, J., and R. L. Bras (2010), An extremum solution of the Monin–Obukhov similarity equations, *J. Atmos. Sci.*, **67**(2), 485-499, doi:10.1175/2009JAS3117.1.

Wang, J., and R. L. Bras (2011), A model of evapotranspiration based on the theory of maximum entropy production, *Water Resour. Res.*, **47**, W11422, doi:10.1029/2010WR009392.

Wang, J., R. L. Bras, V. Nieves, and Y. Deng (2014), A model of energy budgets over water, snow, and ice surfaces, *J. Geophys. Res. Atmos.*, **119**(10), 6034-6051, doi:10.1002/2013JD021150.

Wang, J., R. L. Bras, G. Sivandran, and R. G. Knox (2010), A simple method for the estimation of thermal inertia, *Geophys. Res. Lett.*, **37**(5), L05404, doi:10.1029/2009GL041851.

Wang, K., and R. E. Dickinson (2012), A review of global terrestrial evapotranspiration: Observation, modeling, climatology, and climatic variability, *Rev. Geophys.*, **50**, RG2005, doi:10.1029/2011RG000373.

Wang, K., and S. Liang (2008), An improved method for estimating global evapotranspiration based on satellite determination of surface net radiation, vegetation index, temperature, and soil moisture, *J. Hydrometeorol.*, **9**(4), 712-727, doi:10.1175/2007JHM911.1.

Wang, W., P. Xie, S.-H. Yoo, Y. Xue, A. Kumar, and X. Wu (2011), An assessment of the surface climate in the NCEP climate forecast system reanalysis, *Clim. Dyn.*, **37**(7), 1601-1620, doi:10.1007/s00382-010-0935-7.

Wassar, F., C. Gandolfi, M. Rienzner, E. A. Chiaradia, and E. Bernardoni (2016), Predicted and measured soil retention curve parameters in Lombardy region north of Italy, *Int. Soil and Water Conserv. Res*., **4**(3), 207-214, doi:10.1016/j.iswcr.2016.05.005.

Weller, G. (1968), Heat-energy transfer through a four-layer system: Air, snow, sea ice, sea water, *J. Geophys. Res.,* **73**(4), 1209-1220, doi:10.1029/JB073i004p01209.

Westermann, S., J. Lüers, M. Langer, K. Piel, and J. Boike (2009), The annual surface energy budget of a high-arctic permafrost site on Svalbard, Norway, *The Cryosphere*, **3**(2), 245-263, doi:10.5194/tc-3-245-2009.

Wetherald, R. T., and S. Manabe (2003), Correction to "Simulation of hydrologic changes associated with global warming", *J. Geophys. Res. Atmos.*, **108**(D22), 4702, doi:10.1029/2003JD004253.

Wetzel, P. J., and J.-T. Chang (1987), Concerning the relationship between evapotranspiration and soil moisture, *J. Clim. Appl. Meteor.*, **26**(1), 18-27, doi:10.1175/1520-0450(1987)026<0018:CTRBEA>2.0.CO;2.

Wetzel, P. J., X. Liang, P. Irannejad, A. Boone, J. Noilhan, Y. Shao, C. Skelly, Y. Xue, and Z. L. Yang (1996), Modeling vadose zone liquid water fluxes: Infiltration,

runoff, drainage, interflow, *Glob. Planet. Chang.*, **13**(1), 57-71, doi:10.1016/0921-8181(95)00037-2.

Wielicki, B. A., B. R. Barkstrom, E. F. Harrison, R. B. Lee III, G. L. Smith, and J. E. Cooper (1996), Clouds and the Earth's Radiant Energy System (CERES): An Earth observing system experiment, *Bull. Amer. Meteor. Soc.*, **77**(5), 853-868, doi:10.1175/1520-0477(1996)077<0853:CATERE>2.0.CO;2.

Wielicki, B. A., K. Priestley, P. Minnis, N. Loeb, D. Kratz, T. Charlock, D. Doelling, and D. Young (2006), CERES radiation budget accuracy overview, *Preprints, 12th Conf. Atmospheric Radiation*, Madison, WI, Amer. Meteor. Soc., 9.1.

Wiernga, J. (1993), Representative roughness parameters for homogeneous terrain, *Bound.-Lay. Meteorol.*, **63**(4), 323-363, doi:10.1007/BF00705357.

Wild, M. (2005), Solar radiation budgets in atmospheric model intercomparisons from a surface perspective, *Geophys. Res. Lett.*, **32**, L07704, doi:10.1029/2005GL022421.

Wild, M. (2008), Short-wave and long-wave surface radiation budgets in GCMs: A review based on the IPCC-AR4/CMIP3 models, *Tellus A*, **60**(5), 932-945, doi:10.1111/j.1600-0870.2008.00342.x.

Wild, M., D. Folini, M. Z. Hakuba, C. Schär, S. I. Seneviratne, S. Kato, D. A. Rutan, C. Ammann, E. F. Wood, and G. König-Langlo (2015), The energy balance over land and oceans: an assessment based on direct observations and CMIP5 climate models, *Clim. Dyn.*, **44**(11), 3393-3429, doi:10.1007/s00382-014-2430-z.

Wild, M., D. Folini, C. Schär, N. Loeb, E. G. Dutton, and G. König-Langlo (2013), The global energy balance from a surface perspective, *Clim. Dyn.*, **40**(11), 3107-3134, doi:10.1007/s00382-012-1569-8.

Wild, M., A. Ohmura, H. Gilgen, E. Roeckner, M. Giorgetta, and J.-J. Morcrette (1998), The disposition of radiative energy in the global climate system: GCM-calculated versus observational estimates, *Clim. Dyn.*, **14**(12), 853-869, doi:10.1007/s003820050260.

Wild, M., and E. Roeckner (2006), Radiative fluxes in the ECHAM5 general circulation model, *J. Climate*, **19**(16), 3792-3809, doi:10.1175/JCLI3823.1.

Wilson, K., A. Goldstein, E. Falge, M. Aubinet, D. Baldocchi, P. Berbigier, C. Bernhofer, R. Ceulemans, H. Dolman, C. Field, A. Grelle, A. Ibrom, B. E. Law, A. Kowasaki, T. Meyers, J. Moncrieff, R. Monson, W. Oechel, J. Tenhunen, R. Valentini, and S.

Verma (2002), Energy balance closure at FLUXNET sites, *Agric. For. Meteorol.*, **113**(1–4), 223-243, doi:10.1016/S0168-1923(02)00109-0.

Wood, E. F., D. P. Lattenmaier, X. Liang, D. Lohmann, A. Boone, S. Chang, F. Chen, Y. Dai, R. E. Dickinson, Q. Duan, M. Ek, Y. M. Gusev, F. Habets, P. Irannejad, R. Koster, K. E. Mitchel, O. Nasonova, J. Noilhan, J. Schaake, A. Schlosser, Y. Shao, A. B. Shmakin, D. Verseghy, K. Warrach, P. J. Wetzel, Y. Xue, Z.-L. Yang, and Q.-c. Zeng (1998), The project for intercomparison of land-surface parameterization schemes (PILPS) phase 2(c) Red-Arkansas River basin experiment: 1. Experiment description and summary intercomparisons, *Glob. Planet. Chang.*, **19**(1–4), 115–135.

Xue, Y., P. J. Sellers, J. L. Kinter, and J. Shukla (1991), A simplified biosphere model for global climate studies, *J. Climate*, **4**(3), 345-364, doi:10.1175/1520-0442(1991)004<0345:ASBMFG>2.0.CO;2.

Yan, H., Q. Yu, Z.-C. Zhu, R. B. Myneni, H.-M. Yan, S.-Q. Wang, and H. H. Shugart (2013), Diagnostic analysis of interannual variation of global land evapotranspiration over 1982–2011: Assessing the impact of ENSO, *J. Geophys. Res. Atmos*., **118**(16), 8969-8983, doi:10.1002/jgrd.50693.

Yang, J., and Z.-H. Wang (2014), Land surface energy partitioning revisited: A novel approach based on single depth soil measurement, *Geophys. Res. Lett.*, **41**(23), 8348-8358, doi:10.1002/2014GL062041.

Yang, K., and J. Wang (2008), A temperature prediction-correction method for estimating surface soil heat flux from soil temperature and moisture data, *Sci. China Ser. D*, **51**(5), 721-729, doi:10.1007/s11430-008-0036-1.

Yang, Q., H. Tian, M. A. M. Friedrichs, M. Liu, X. Li, and J. Yang (2015), Hydrological responses to climate and land-use changes along the North American east coast: A 110-Year historical reconstruction, *J. Am. Water Resour. Assoc.*, **51**(1), 47-67, doi:10.1111/jawr.12232.

Yang, Z.-L. (2004), Modeling land surface processes in short-term weather and climate studies, in *Observation, Theory and Modeling of Atmospheric Variability*, edited by X. Zhu, X. Li, M. Cai, S. Zhou, Y. Zhu, F.-F. Jin, X. Zou and M. Zhang, pp. 288-313, World Scientific Series on Meteorology of East Asia, World Scientific, New Jersey.

Yi, Y., J. S. Kimball, L. A. Jones, R. H. Reichle, and K. C. McDonald (2011), Evaluation of MERRA land surface estimates in preparation for the Soil Moisture Active Passive Mission, *J. Climate*, **24**(15), 3797-3816, doi:10.1175/2011JCLI4034.1.

Yu, L., X. Jin, and R. A. Weller (2008), Multidecade global flux datasets from the Objectively Analyzed Air-sea Fluxes (OAFlux) project: Latent and sensible heat fluxes, ocean evaporation, and related surface meteorological variables., *OAFlux Project Tech. Rep. OA-2008-01*, 64 pp., Woods Hole Oceanographic Institution, Woods Hole, MA.

Yu, L., and R. A. Weller (2007), Objectively Analyzed air–sea heat fluxes for the global ice-free oceans (1981–2005), *Bull. Amer. Meteor. Soc.*, **88**(4), 527-539, doi:10.1175/BAMS-88-4-527.

Yu, L., and R. A. Weller (2012), 50 Year global ocean surface heat flux analysis, *FY2012 Annual Report*, 12 pp., Woods Hole Oceanographic Institution, Woods Hole, MA.

Yuan, W., S. Liu, G. Yu, J.-M. Bonnefond, J. Chen, K. Davis, A. R. Desai, A. H. Goldstein, D. Gianelle, F. Rossi, A. E. Suyker, and S. B. Verma (2010), Global estimates of evapotranspiration and gross primary production based on MODIS and global meteorology data, *Remote Sens. Environ.*, **114**(7), 1416-1431, doi:10.1016/j.rse.2010.01.022.

Zaitchik, B. F., M. Rodell, and F. Olivera (2010), Evaluation of the Global Land Data Assimilation System using global river discharge data and a source-to-sink routing scheme, *Water Resour. Res.*, **46**, W06507, doi:10.1029/2009WR007811.

Zeng, X.-M., N. Wang, Y. Wang, Y. Zheng, Z. Zhou, G. Wang, C. Chen, and H. Liu (2015), WRF-simulated sensitivity to land surface schemes in short and medium ranges for a high-temperature event in East China: A comparative study, *J. Adv. Model. Earth Syst.*, **7**(3), 1305-1325, doi:10.1002/2015MS000440.

Zeng, X., M. Zhao, and R. E. Dickinson (1998), Intercomparison of bulk aerodynamic algorithms for the computation of sea surface fluxes using TOGA COARE and TAO data, *J. Climate*, **11**(10), 2628-2644.

Zhao, W., and A. Li (2015), A review on land surface processes modelling over complex terrain, *Adv. Meteorol.*, **17**, 607181, doi:10.1155/2015/607181.

Zhang, D., and R. A. Anthes (1982), A high-resolution model of the planetary boundary layer—Sensitivity tests and comparisons with SESAME-79 data, *J. Appl. Meteor.*, **21**(11), 1594-1609, doi:10.1175/1520-0450(1982)021<1594:AHRMOT>2.0.CO;2.

Zhang, C., D. A. Dazlich, D. A. Randall, P. J. Sellers, and A. S. Denning (1996), Calculation of the global land surface energy, water and CO2 fluxes with an off-line version of SiB2, *J. Geophys. Res. Atmos.*, **101**(D14), 19061-19075, doi:10.1029/96JD01449.

Zhang, D., and W.-Z. Zheng (2004), Diurnal cycles of surface winds and temperatures as simulated by five boundary layer parameterizations, *J. Appl. Meteor.*, **43**(1), 157-169, doi:10.1175/1520-0450(2004)043<0157:DCOSWA>2.0.CO;2.

Zhang, K., J. S. Kimball, R. R. Nemani, and S. W. Running (2010a), A continuous satellite-derived global record of land surface evapotranspiration from 1983 to 2006, *Water Resour. Res.*, **46**, W09522, doi:10.1029/2009WR008800.

Zhang, T. (2005), Influence of the seasonal snow cover on the ground thermal regime: An overview, *Rev. Geophys.*, **43**(4), doi:10.1029/2004RG000157.

Zhang, Y., C. N. Long, W. B. Rossow, and E. G. Dutton (2010b), Exploiting diurnal variations to evaluate the ISCCP-FD flux calculations and radiative-flux-analysis-processed surface observations from BSRN, ARM, and SURFRAD, *J. Geophys. Res. Atmos.*, **115**, D15105, doi:10.1029/2009JD012743.

Zhang, Q., S. Wang, M. Barlage, W. Tian, and R. Huang (2011), The characteristics of the sensible heat and momentum transfer coefficients over the Gobi in Northwest China, *Int. J. Climatol.*, **31**(4), 621-629, doi:10.1002/joc.2071.

Zhang, Y., J. L. Peña-Arancibia, T. R. McVicar, F. H. Chiew, J. Vaze, C. Liu, X. Lu, H. Zhang, Y. Wang, Y. Y. Liu, D. G. Miralles, and M. Pan (2016), Multi-decadal trends in global terrestrial evapotranspiration and its components, *Sci. Rep.*, **6**, 19124, doi:10.1038/srep19124.

Zhang, Y., W. B. Rossow, A. A. Lacis, V. Oinas, and M. I. Mishchenko (2004), Calculation of radiative fluxes from the surface to top of atmosphere based on ISCCP and other global data sets: Refinements of the radiative transfer model and the input data, *J. Geophys. Res. Atmos.*, **109**, D19105, doi:10.1029/2003JD004457.

Zhang, Y., W. B. Rossow, and P. W. Stackhouse (2006), Comparison of different global information sources used in surface radiative flux calculation: Radiative properties of the near-surface atmosphere, *J. Geophys. Res. Atmos.*, **111**, D13106, doi:10.1029/2005JD006873.

Zhang, Y., W. B. Rossow, and P. W. Stackhouse (2007), Comparison of different global information sources used in surface radiative flux calculation: Radiative properties of the surface, *J. Geophys. Res. Atmos.*, **112**, D01102, doi:10.1029/2005JD007008.